Pore Network Modelling of Fingering Phenomena during Unsteady-State Waterflooding of Heavy Oils

Mohamed Regaieg

Submitted for the degree of Doctor of Philosophy

Heriot-Watt University
School of Energy, Geoscience, Infrastructure and Society

May 2015

Abstract

Although thermal methods have been popular and successfully applied in heavy oil recovery, they are often found to be uneconomic or impractical. Therefore, alternative production protocols are being actively pursued and interesting options are water and polymer flooding.

Such techniques have been successfully tested in recent laboratory investigations, where oil recovery was found to be much higher than expected. Moreover, in some of the core scale waterflood experiments reported using 2D slabs of Bentheimer sandstone, X-ray scans performed during the flooding sequence provided evidence of an interesting new phenomenon – post breakthrough, highly dendritic water fingers were seen to thicken and coalesce, forming braided water channels and improving sweep efficiency.

However, despite encouraging results, these experimental studies show that the mechanisms governing water displacing extra heavy oil are still poorly understood. This means that the optimization of this process for eventual field applications is still somewhat problematic. Ideally, a combination of two-phase flow experiments and simulations should be put in place to help inform our understanding of the process.

To this end, a new fully dynamic network model is described. It has been developed to investigate unsteady state drainage floods and has been applied here in the context of waterfloods of heavy oil in oil-wet media. It has subsequently been used to investigate finger thickening during water flooding of extra-heavy oils. The displacement physics has been implemented at the pore scale and, following a successful benchmarking exercise against numerous micromodel experiments, a range of slab-scale (30cm x 30cm) simulations has been carried out and compared with the corresponding experimental observations. They reveal that the model is able to replicate finger architectures similar to those observed in the experiments. Subsequently, for the first time to our knowledge, finger thickening following water breakthrough is reproduced and interpreted. The simulator is then used to investigate the effects of different system parameters on finger swelling behaviour. Finally, a sensitivity study is performed to better understand the effects of different system variables upon the sweep efficiency, the displacement front stability and unsteady-state relative permeability.

Acknowledgements

I am using this opportunity to express my gratitude to everyone who helped me throughout my PhD.

First, I would like to thank my supervisor Dr Steven McDougall for his kindness, endless encouragement and advice throughout the last three years. It has been a pleasure to work with him.

I would like to thank Dr Igor Bondino for introducing me to applied research and for providing me with useful data and valuable advice during my PhD.

None of this research would have been carried out without the financial and technical assistance of Total E&P. I am also extremely grateful to Dr Gerald Hamon for his kindness and outstanding ideas.

I would like to thank my colleagues and friends in the Institute of Petroleum Engineering for their company and for all the good moments that we shared during these years especially Wissem, Morteza, Ahmed, Alfonso, Luis, Duarte, Foroogh, Diana and Martha.

Finally, I cannot thank enough my family and Myriam for their unconditional support and for being here when I needed it the most. Without you this would never have been possible.

Table of content

List of publications

Regaieg, M., McDougall, S.R., Hamon, G.(2014). Non-thermal heavy oil production: A Pore-to-core approach to investigate the impact of wettability during cold water injection into heavy oils. Paper presented at the World Heavy Oil Congress , New Orleans, Louisiana, USA.

Regaieg, M., McDougall, S.R., Bondino, I. Hamon, G.(2014). Finger thickening during extra-heavy oil waterflooding: simulation and interpretation using pore-scale modelling. SCA2014-28, Proceedings of the International Symposium of the Society of Core Analysts, Avignon, France.

Chapter 1: Introduction

Petroleum is a liquid mixture of hydrocarbons that resides in suitable rock strata and can be extracted and refined to produce a variety of fuels, including petrol, paraffin, and diesel. It is the general term used to describe all natural hydrocarbons, although in common usage it refers particularly to liquid crude oils.

Crude oil may be further divided into categories based on density and viscosity and according to the classification of Total E&P, heavy crude oil is generally defined as having a density in the range of 904 kg/m^3 to 946 kg/m^3 with a viscosity ranging from 10 cP to 100 cP. Extra-heavy oils have a density higher than 933 kg/m^3 with a viscosity up to 10,000 cP. Oils having a viscosity above 10,000 cP and a density between 1007 kg/m^3 and 1022 kg/m^3 are considered oil sands and bitumen. As the production from conventional acreage declines, while the global demand is rising steadily, extra-heavy oil could play a crucial role in reserve replacement and be a part of a future energy solution – it could extend the world's energy reserves by 15 years (Total E&P estimates).

Many heavy and extra heavy oil reservoirs contain oil that has some limited mobility under reservoir conditions and in these reservoirs, a small fraction of the oil-in-place can be recovered using the internal reservoir energy through heavy oil solution gas drive (primary recovery). At the end of the primary recovery, however, the majority of the oil is still in place, while the natural energy of the reservoir has been depleted. Furthermore, many of these reservoirs are relatively small or thin, or may be contacted by overlying gas or underlying water, making the thermal methods impractical and/or uneconomic.

As a part of the research effort in this area, several researchers have studied water injection into heavy and extra-heavy oil and some recent laboratory studies have

suggested that, under certain circumstances, water-flooding into extra-heavy oil (with viscosity up to 7000 cP) could actually result in higher than expected oil recovery (Bondino et al, 2011; Skauge et al, 2012; Skauge et al 2013; Skauge et al 2014). X-ray imaging of fluid fronts during these experiments has highlighted a finger swelling mechanism and the causes of this behaviour – as well as the physics involved in such displacements – have not been explained to date. Understanding the mechanisms involved in cold heavy and extra heavy oil recovery presents an important step in optimizing the recovery using cold production technologies.

To that end, the first objective of this study is to create a pore network simulator that is able to simulate the total range of flow regimes (stable displacement, capillary fingering and viscous fingering) associated with unsteady state drainage floodings as well as the transitions between them. In addition, the model is optimised to allow it to simulate slab experiments at the scale of tens of centimetres within a reasonable running time.

The second objective of this study is to use our network modelling tool to reproduce and help explain the finger swelling phenomenon and to achieve a more general understanding of the flow regimes and recovery mechanisms involved in waterflooding processes (with a special focus on heavy and extra heavy oil).

Another main objective of the research is to understand the effects of different system parameters upon oil recovery and sweep efficiency, including injection rate, viscosity ratio, core length and wettability. This information is extremely valuable, for example it can help to optimize recovery by choosing an approximate injection rate or can be used to infer how information obtained from core flooding experiments is representative of the behaviour in a real reservoir. Finally, understanding the effects of various rock/fluid parameters upon unsteady-state relative permeability would prove very useful in understanding the laboratory methodologies used in relative permeability determination. The model described here can be used to carry out such an investigation.

A broad outline of the thesis is as follows:

In Chapter 2, an extensive overview of the problem of viscous fingering in immiscible displacements is given. A literature review is presented that outlines the most important experimental observation in cores, micromodels, Hele Shaw cells and other artificial analogues of porous media. Then, we review some mathematical modelling approaches, including linear stability analysis (LSA) and statistical modelling techniques. Finally, we present attempts to numerically simulate viscous fingering in immiscible displacements, with a focus on digital rock physics methods.

A discussion of quasi-static pore network models available in the literature is presented in Chapter 3. These include models using statistically generated networks as well as those involving networks created from pore space images. We then go on to describe the main applications of quasi-static pore network models and conclude the chapter by discussing recent criticisms of the predictive potential of pore network simulators. Having reviewed quasi-static pore network models, we go on to present an analysis of published *dynamic* pore network simulators in Chapter 4, particularly drainage models. We discuss the main challenges faced by researchers as well as the main applications of their approaches.

A newly developed drainage pore network model that has been built to simulate the full range of unsteady state drainage processes associated with water-oil displacements in porous media is reported in Chapter 5. This model has been optimized to facilitate the simulation of slab experiments at the scale of tens of centimetres.

After building the dynamic drainage model, we go on to validate it against experimental micromodel data in Chapter 6. As a first test, a network is constructed to simulate the micromodel experiments reported in the pioneering paper of Lenormand et al. (1988) in order to check if our model is able to reproduce the same flow regimes observed in the experiments. Having gained confidence in the model after its validation, we next go on to carry out a range of slab-scale (30cm x 30cm) simulations and compare them against the corresponding experimental observations of Skauge et al. (2012) in Chapter 7.

Reproducing these experiments represents a first step towards gaining a better understanding of the physics governing water displacing extra heavy oil. This leads us

to propose a physical explanation for the causes of finger thickening following water breakthrough. Finally, we use our approach to predict the impact of varying core length, rock wettability, and injection rate upon finger swelling and post-breakthrough recovery in Bentheimer slabs.

In Chapter 9, we present a more general investigation into the effects of different system parameters upon displacement regime and front stability. We start by examining the flow regimes before breakthrough and go on to study the post-breakthrough behaviour. This provides us with information that can be useful for the optimization of waterflooding processes for field applications.

Finally, having studied the effects of different system parameters upon saturation distributions and recovery, we investigate the effects of these system parameters on one of the most important parameters for estimating the flow of reservoir fluids: unsteady-state relative permeability. In Chapter 10, we study the effects of flow rate, viscosity ratio and wettability upon unsteady state relative permeability curves for displacements involving heavy and extra heavy oil.

The final chapter of this thesis, Chapter 11, discusses the main findings of the investigation, and proposes areas for future study.

Chapter 2: Viscous fingering phenomena during immiscible displacements

2.1. INTRODUCTION

Viscous fingering is a phenomenon associated with displacement processes where the displaced fluid has a higher viscosity than that displacing it. The less viscous fluid flows more easily than the more viscous phase, resulting in the occurrence of instabilities. In the context of reservoir engineering, viscous fingering can be detrimental to recovery, as when it occurs, the injected water bypasses large areas of the reservoir, resulting in poor sweep efficiency. Therefore, it is crucial to understand this phenomenon and the physical mechanisms responsible for the initiation and development of viscous instabilities. Given the importance of water injection it is not surprising that, several researchers have been interested in studying viscous fingering and a large number of papers have been published in this area to date. In this chapter, we review the three main approaches towards understanding viscous fingering in porous media: experimental, mathematical and numerical.

2.2. EXPERIMENTAL STUDIES

One of the main challenges associated with laboratory studies of viscous fingering is the fact that “real” porous media are opaque and, moreover, only limited visualization tools have been available until recently. Hence, one of the primary concerns of the earlier studies in this area was to find a way of imaging the saturation maps in order to visualize viscous fingering during multiphase displacements. To overcome this difficulty several protocols were developed.

The first approach was to create transparent porous media that could reproduce the same flow behaviour as that associated with a real rock. Most of the pioneering studies were performed in a two dimensional transparent device named a Hele-Shaw cell (described below) governed by an equation identical to Darcy's law. The transparent nature of the apparatus made flow visualization very straightforward. An alternative technique was the use of a refractive index matching method to visualize the saturation maps. In this case, the defending fluid was chosen to have the same refractive index as the porous medium, making the model transparent to the defending phase. Other authors have employed packed glass beads as porous media allowing observation of the fluids displacements directly. Finally, a number of micromodel experiments have been reported, where the porous medium is approximated by a transparent two dimensional glass plate. In this case, researchers attempt to reproduce statistically the porous structure of a rock (through the inclusion of measured distributions of throat radii, pore bodies, nodal connectivities, etc) by using an etching procedure.

A second broad class of studies has focussed on the development of visualization techniques that can capture the fluid distributions inside a core. In this case, x-ray Computed Tomography (x-ray CT), Nuclear Magnetic Resonance (NMR) or Magnetic Resonance Imaging (MRI) have been employed to see fluid distribution while core flooding experiments are performed. We now go on to discuss these various approaches in more details.

2.2.1. Hele-Shaw cell studies

Hele-Shaw cells are the most widely used apparatus in viscous fingering studies. This device consists of a set of two parallel flat plates separated by a small gap (b) (1mm in the Chuoke et al. (1959) study). Then the average two-dimensional velocity (u) of a viscous fluid in the space between the plates is related to the pressure (p) by the formula given by Hele-Shaw (1898):

$$\vec{u} = -\frac{b^2}{12\mu} grad(p) \tag{2.1}$$

$$\text{div } \vec{u}=0 \tag{2.2}$$

This equation is similar to Darcy's law and therefore these devices are expected to behave in a similar way as porous media. Furthermore, the parallel plates are transparent; hence the flow visualization is very easy and so these devices have been very popular in viscous fingering studies.

Chuoke et al. (1959) used oil-wet Hele-Shaw cells to perform a variety of water/oil displacements with a viscosity ratio ($\frac{\mu_{oil}}{\mu_{water}}$) equal to 2.5. They observed a stable displacement at low rates but showed that, at rates higher than some critical value the flow became unstable. They noticed that the finger tips had a bulbous shape and that the deformations had a quasi-sinusoidal character. As can be seen in Figure 2.1, they observed an increase in the number of fingers with an increase in the injection rate. This behaviour is consistent with their theoretical study which predicted a higher number of instabilities at higher injection rates. This theory will be reviewed in detail later in this thesis.

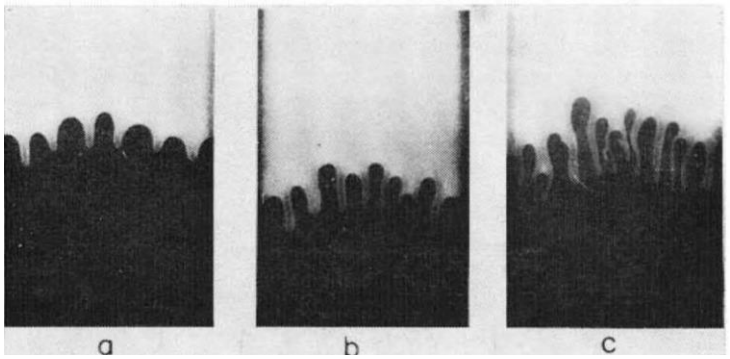

Figure 2.1: The effect of injection velocity on viscous fingering in Hele Shaw cells. Here glycerine-water solution is displacing oil at different velocities: U = 0.41 cm/s (a), U = 0.87 cm/s (b) and U = 1.66 cm/s (c). The viscosity ratio was equal to 2.5 in these experiments (Chuoke et al., 1959).

Perkins and Johnston (1969) performed water/oil displacements in Hele Shaw cells. At very unfavorable viscosity ratios (~150) and relatively high injection rates, viscous fingers were obtained. Initially, several fingers were initiated at the inlet but, as the displacement progressed, the fingers coalesced. In some experiments, only one major finger was obtained, which is similar to the tendency observed by Saffman and Taylor (1958). In another set of experiments with lower rates and less adverse viscosity ratios (20-30) the experiments were noticeably influenced by capillary forces.

In a similar study, Moore et al. (2002) observed finger width fluctuations for the first time. The magnitude of these fluctuations was proportional to $Nca^{-0.64}$ (where Nca is the capillary number) and this relation was found to be valid for all the studied aspect ratios. At higher flow rates, finger pinch-off and reconnection events were observed. and these events appeared to be caused by an interaction between the actively growing finger and suppressed fingers at the back of the channel. The maximum finger widths were obtained at low rates.

Although Hele-Shaw cells have been very popular in viscous fingering studies, some concerns have been raised about their use in immiscible displacements. For example, Perkins and Johnston (1969) preferred to use packed glass beads, as they were worried about the possible wettability heterogeneity of the surface of the Hele-Shaw cells. Moreover, Homsy (1987) pointed out that the capillary forces associated with the

propagation of menisci through pore space cannot be neglected and that such forces are not exhibited in Hele-Shaw cells. As a consequence, these devices are generally not considered suitable for immiscible displacements, which are generally governed by the competition between viscous and capillary forces.

2.2.2. Refractive index matching

Another method that has been used in viscous fingering studies is refractive index matching. This technique involves using a porous medium (usually packed granular material) and a defending fluid having the same refractive index as the porous medium. The model becomes fully transparent for the defending phase and completely opaque for the invading phase. As a result, the saturation maps can be visualized easily and directly.

Van Meurs (1957) used a model having glass walls and filled with powdered glass. The pack was then filled with oil having the same refractive index as the medium. The waterfloods showed that the viscosity ratio is an important parameter affecting the sweep efficiency ─ at low viscosity ratios, the water drive was very efficient, whilst, at high viscosity ratios, the sweep efficiency was adversely reduced as a result of viscous fingering.

Chuoke et al. (1959) used a similar approach in a Pyrex glass powder-filled model for water/oil displacements. They highlighted a viscosity effect on the finger shape and observed that instabilities became thinner as the oil viscosity increased. In addition, they observed an interfacial tension effect ─ the fingers became sharper for lower interfacial tensions.

Frette et al. (1994) performed immiscible displacements in an unconsolidated three dimensional model and for a viscosity ratio ($\frac{\mu_{defending}}{\mu_{invading}}$) equal to 14. The displacement was stable at high rates for this mobility ratio. They concluded that this may indicate that capillary effects could be important even at high displacement rates.

2.2.3. Packed glass beads

This technique involves filling transparent cells with unconsolidated glass beads. Generally, the models formed are “quasi-two-dimensional” and this makes the flow visualization easier.

Perkins and Johnston (1969) used this technique to assess the effect of connate water on water/oil displacements. They concluded that immiscible fingering in bead pack models is significantly influenced by the presence of Swi, which dampens the instabilities.

Stokes et al. (1986) studied the effect of wettability on viscous fingering by performing immiscible two phase displacements in packed glass beads using fluids with an unfavourable viscosity ratio equal to 200. They concluded that, (i) in drainage, the finger width is comparable to the pore size; (ii) in imbibition, the finger width is much larger than the pore size. Therefore, they identified the wettability as being an important parameter influencing viscous fingering phenomenon.

Løvoll et al. (2004) and Løvoll et al. (2011) performed drainage experiments in two dimensional Hele Shaw cells filled with glass beads using different injection rates. They could see the crossover between capillary and viscous fingering by increasing the injection rate (see Figure 2.2 and Figure 2.3). As the invasion rate increased, the invasion structure became thinner, which led to a lower saturation of the invading non-wetting liquid and poorer sweep efficiency. In the viscous fingering regime, the pressure drop was related to the position of the most advanced finger and to the capillary number. Furthermore, all the invasions were found to occur near the tip of the dominant finger. After measuring the pressure at several points around the invading phase, it was found to be almost constant behind the fingertip and the viscous pressure gradient in front of the invading phase was essentially constant.

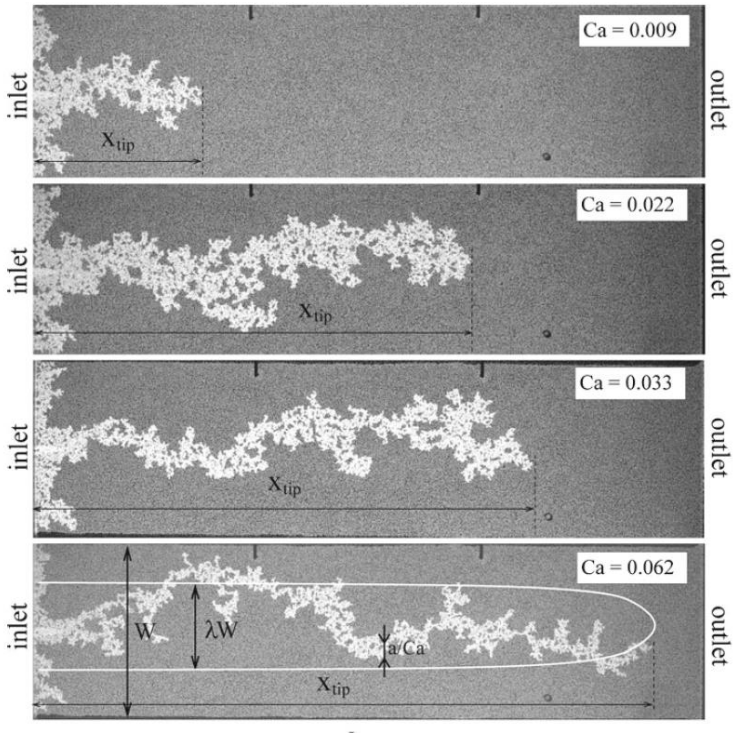

Figure 2.2: Images of experiments taken at different injection rates (Løvoll et al., 2011).

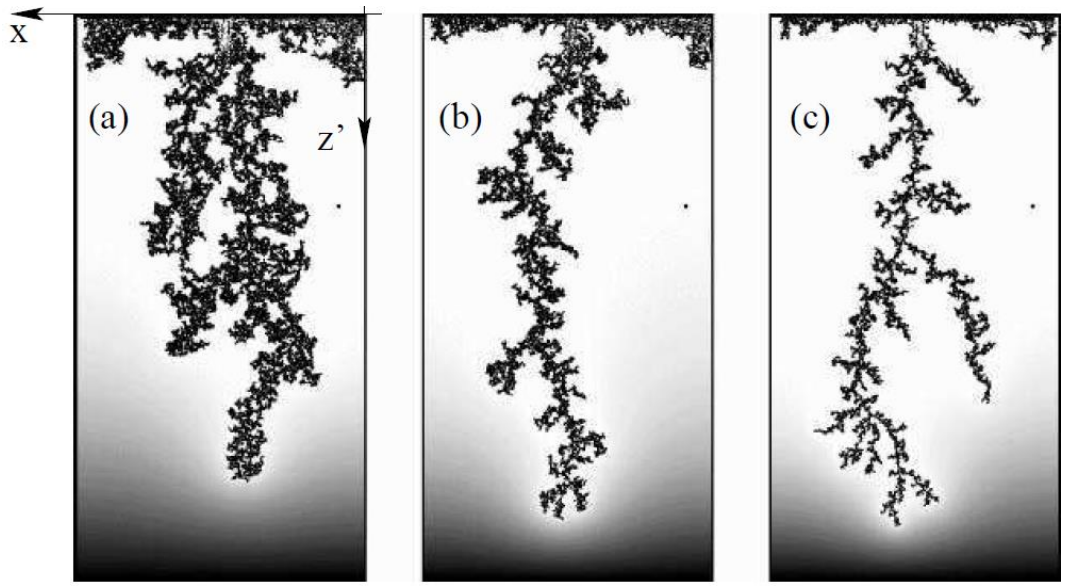

Figure 2.3: Air is injected into glycol water solution with a viscosity ratio equal to 10000 and at different capillary numbers: (a) Ca = 0.027, (b) Ca = 0.059 and (c) Ca = 0.22. (Løvoll et al., 2004) .

2.2.4. . Micromodel experiments

Micromodels are transparent two dimensional porous medium analogues that are used to simulate different processes occurring at the pore scale. They are built using an etching technique, generally on glass or silicon material, allowing the creation of a device that mimics the pore structure of a rock by reproducing it statistically on the engraved surface. Such devices have been very popular in viscous fingering studies. In fact, through the inclusion of the pore size distribution of the rock in the etched network, they provide a better representation of the capillary forces than Hele-Shaw cells or packed glass beads. Furthermore, saturation visualization is straightforward because of their transparent nature.

One of the best known applications of this technology was reported in Lenormand et al. (1988), who performed thirty five two-phase drainage experiments in micromodels using a large number of fluid combinations and flow rates. The micromodels were built using transparent resin and a photographically etched mould.

At low rates, an invasion percolation like pattern was obtained ─ the displacement was controlled by the capillary entry pressures of the pores at the interface and was characterised by invasions happening in all directions (even towards the inlet in some cases). This led to the occurrence of loops that sometimes trapped large quantities of oil. However, at high rates (and unfavourable mobility ratios) viscous fingering was observed ─ in this regime, tree shaped fingers were formed and grew towards the outlet leading to a very poor sweep efficiency. The invasion patterns in capillary and viscous dominated regimes were very different and could easily be identified from the associated saturation maps.

The authors also reported the effects of injection rate upon viscous fingering. Figure 2.4 shows that the fingers became thinner as the injection rate increased. Moreover, they could see the different stages of viscous finger development, as shown in Figure 2.5.

The results were used to build a phase diagram with three different regimes: stable displacement, viscous fingering and capillary fingering (Figure 2.6). This graph can be mapped with viscosity ratio and capillary number.

Although this groundbreaking study improved the understanding of drainage mechanisms during immiscible displacements, it was limited to the behaviour up to breakthrough.

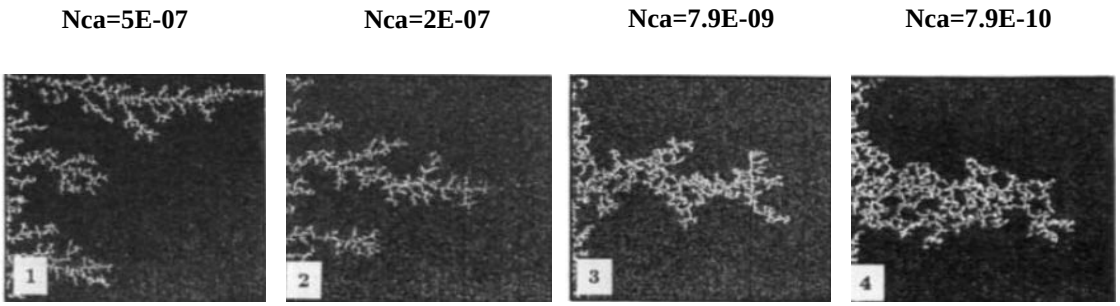

Figure 2.4: Displacement of heavy oil (black) by air (white) at capillary numbers for a viscosity ratio (M=55555)(Lenormand et al., 1988).

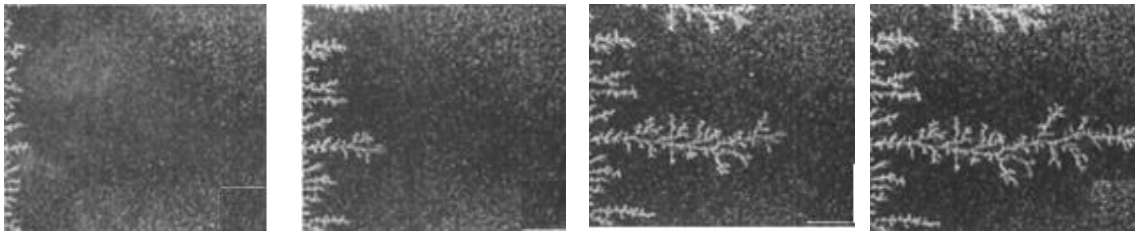

Figure 2.5: Different stages of displacement of a heavy oil (black) by air (white) for a viscosity ratio M=55555 and a capillary number Nca=5E-07 (Lenormand et al., 1988).

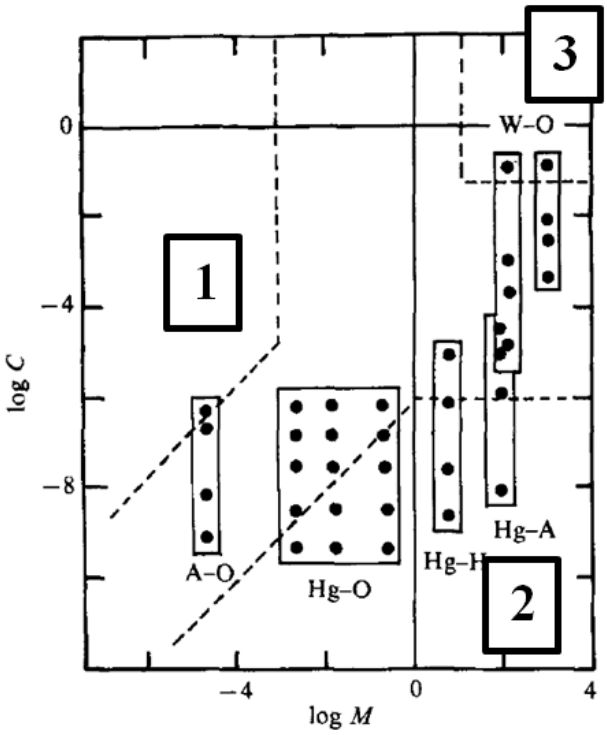

Figure 2.6: Locations of the various series of experiments in the plane M-C ($M = \frac{\mu_{invading}}{\mu_{defending}}$). The letters represent the various experiments performed. The dashed lines are the limits of the basic domains: viscous fingering (domain 1), capillary fingering (domain 2) and stable displacement (domain 3) (Lenormand et al., 1988).

Ferer et al. (2004a) used a glass micromodel to carry out immiscible two phase displacements (air/water) at different rates. The viscosity ratio of their experiments was unfavourable and equal to 62.5. They could see a change of the flow regime from capillary fingering to viscous fingering and obtained viscous instabilities as the capillary number increased.

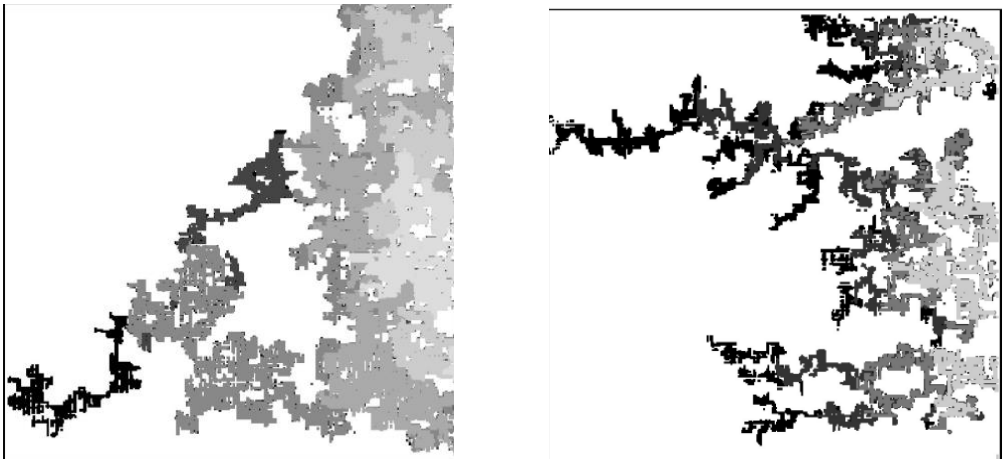

(a) (b)

Figure 2.7: Digitally converted photographs of the experiment where air was injected into water saturated flow cells for two capillary numbers Nca=8E-09 (a) and Nca=2E-05 (b).The viscosity ratio was equal to 62.5. The different shades of grey represent different time intervals, from the lightest grey near the inlet at the far right centre of the pattern to black near breakthrough at the upper left-hand side (Ferer et al., 2004a).

Buchgraber et al. (2009) performed water and polymer flooding experiments in etched silicon micromodels having the geometrical and topological properties of sandstone. Waterfloods with unfavourable mobility ratios developed viscous fingering and were characterized by early water breakthrough, poor sweep efficiency and low recovery. Finally, polymer solution was added to the injected brine resulting in a better sweep efficiency (Figure 2.8 and Figure 2.9).

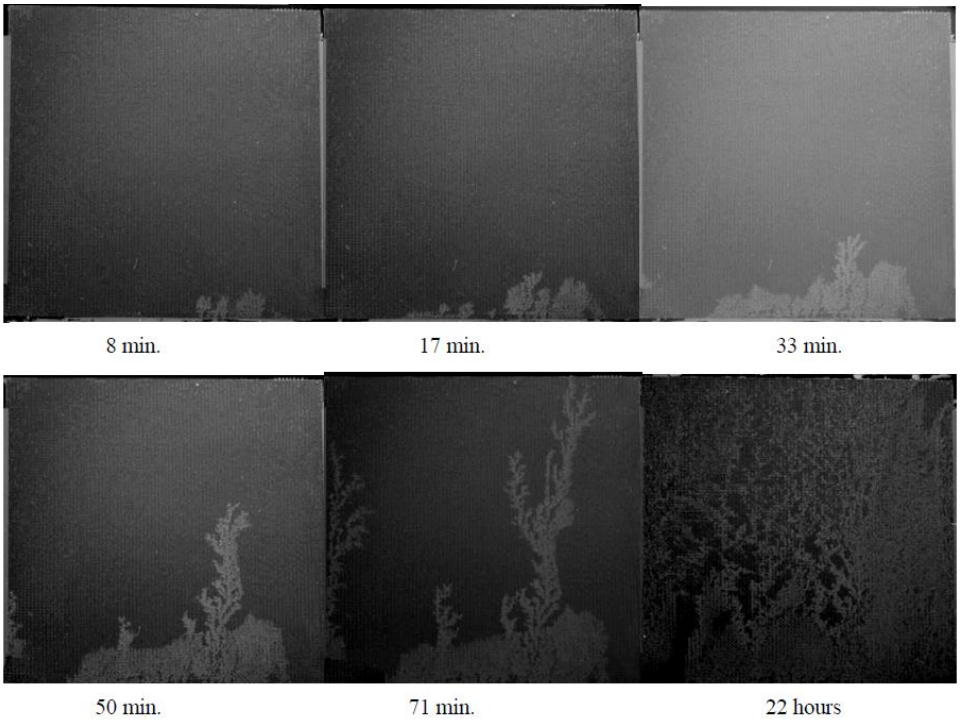

Figure 2.8: Brine flood into heavy oil ($\mu_{oil} = 210\ cP$) (Buchgraber et al., 2009).

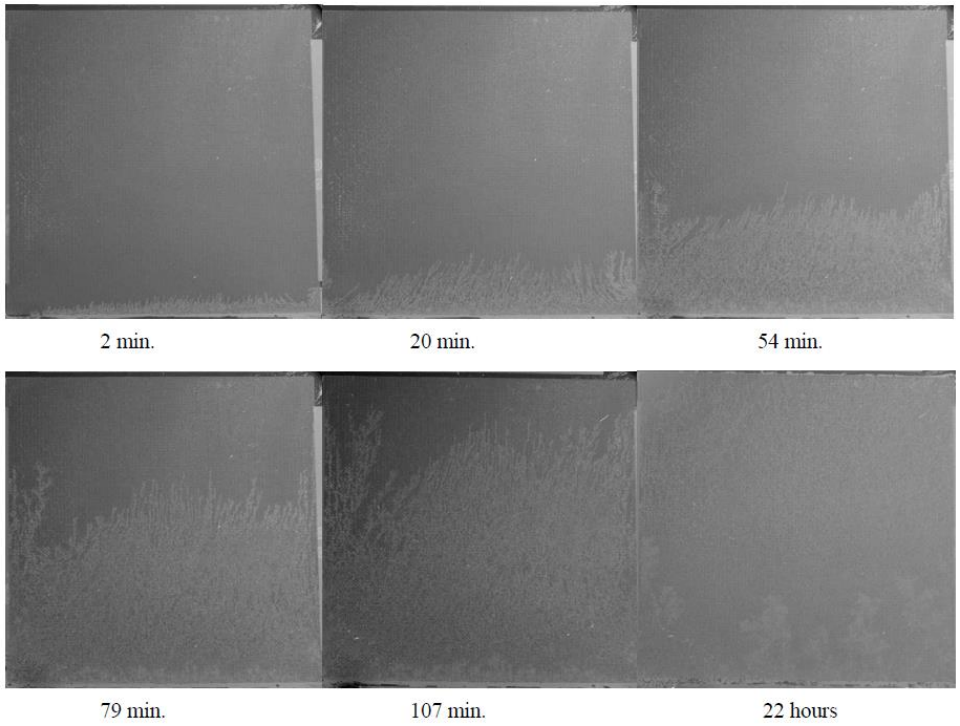

Figure 2.9: Polymer flood into heavy oil ($\mu_{oil} = 210\ cP$)(Buchgraber et al., 2009).

Doorwar and Mohanty (2011) used a similar approach to perform secondary and tertiary waterflooding and alkali-surfactant injection in very viscous oils ─ viscosities up to 10000 cP were considered. They observed that the viscosity ratio controls the finger structure during water floods and found that as the viscosity ratio increases, the number of growing fingers before breakthrough decreases. At high viscosity ratios (greater than 1000), the fingers formed are not completely random and follow the structure of a Diffusion Limited Aggregation (DLA) type pattern. In addition, they observed that an injection of alkaline-surfacant lowers the interfacial tension and forms oil in water emulsion at the sides of previously established water fingers. They also noticed that DLA simulations resemble the fingers observed for M=10000 ─ the fractal dimension of the finger pattern at M=10000 was around 1.6, compared to 1.7 for DLA (Figure 2.10).

Viscous finger patterns	Calculated fractal dimension (D_f)
 t = 1hour	1.5 ± 0.1
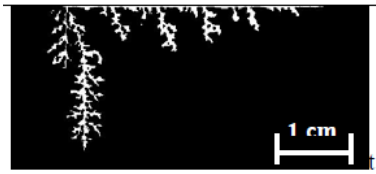 t = 2 hour	1.45 ± 0.1
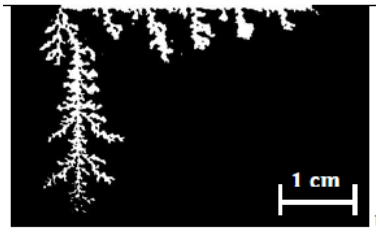 t = 3 hour	1.6 ± 0.1
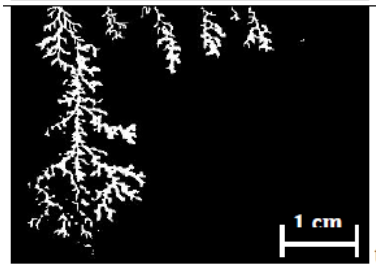 t = 4 hour	1.5 ± 0.05

Figure 2.10: Viscous fingering formed in a water injection into heavy oil (μ_{oil} = 10000) and fractal dimension calculated at each stage of the experiment (Doorwar and Mohanty, 2011).

2.2.5. . X-ray computed tomography

Instead of attempting to create a transparent porous medium having the structure of real rocks, some researchers have performed displacement experiments in opaque media and used more sophisticated imaging techniques to visualize the fluid distributions inside the system.

One of the most popular imaging technologies is x-ray computed tomography (x-ray CT). This technique consists of using computer-processed x-rays to produce images of the scanned object ─ an opaque core in this case. Another advantage of the x-ray imaging is that it can be done in real time, while the experiment is running, in order to observe the different stages of a displacement.

Wang et al. (1985) were the first to use x-ray CT imaging to visualize corefloods in time and space. They used a slow second generation CT machine tuned to a water phantom for medical applications. Figure 2.11 represents the images taken at a cross section of the core at a distance of 7 cm from the injection point. Whilst the resolution was low and the images were not very clear, the rate effect on viscous fingering and sweep efficiency could be observed inside the core. An increase in the injection rate is accompanied by a drop in the sweep efficiency and a rise in the number of fingers.

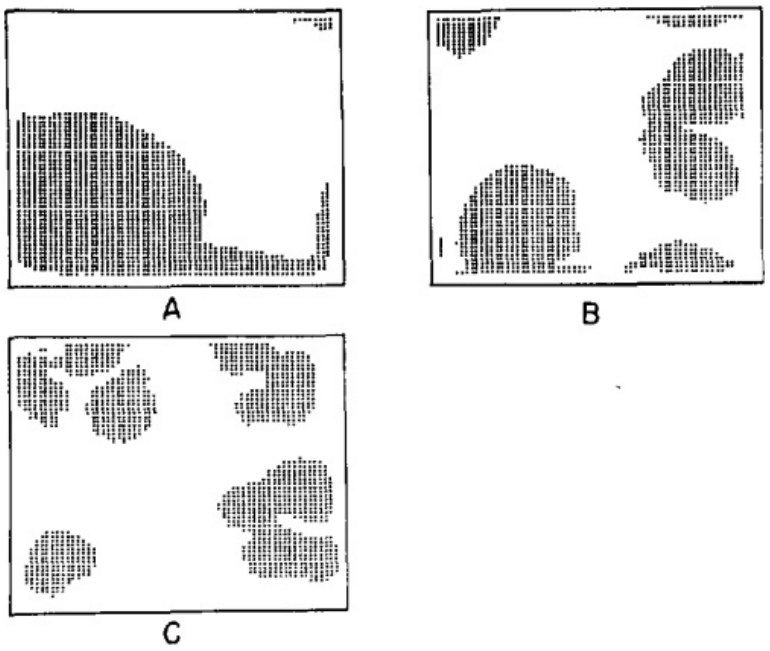

Figure 2.11: Cross section of the observed viscous fingers as a function of displacement velocity at a position 7 cm from injection point: (A) displacement rate: 19 cm^3/h; 0.155 pore volume injected;; (B) displacement rate: 90 cm^3/h; 0.204 pore volume injected; (C) displacement rate: 240 cm^3/h; 0.1051 pore volume injected (Wang et al., 1985).

Other examples of the use of x-ray CT imaging include:

Peters and Hardham (1989), who used x-ray CT imaging in a study to compare miscible and immiscible displacements with viscosity ratios varying from 62 to 360. They concluded that miscible displacements are more efficient.

Zitha et al. (2006) studied the development of foam and the subsequent flow of surfactant solution and their effect on viscous fingering and observed fluid distributions using x-ray CT.

Riaz et al. (2007), who visualized forced imbibition experiments in Berea sandstone with an x-ray imaging technique. They compared the experimental results to

simulations with continuum models to conclude that continuum models can simulate the unstable modes with reasonable accuracy ─ however they are deficient for fully developed unstable flows.

2.2.6. . Other visualization techniques

Engelberts and Klinkenberg (1951), who were the first researchers to observe viscous fingering phenomena, used cylindrical packs of granular material enclosed in steel tubes. They added fluorescein to the water phase and then took pictures in ultraviolet light after stopping the experiment and sampling the sand. They studied displacements with viscosity ratios varying from 4 to 300. They reported that (i) the higher the oil viscosity, the lower the rate of the displacement required to have an effective displacement, and (ii) that viscous fingering is caused by a high viscosity ratio.

Peters and Flock (1981) performed water/oil displacement experiments in sand packs with different wettabilities. The saturation maps were captured experimentally using a fluorescent tracer in the displacing water and by taking photos under ultraviolet lighting. They noticed that viscous fingering was rate-sensitive and that a higher rate leads to the formation of more fingers and lower recovery (Figure 2.12 and Figure 2.13)**.** In addition, the instabilities were found to decrease recovery considerably at breakthrough. Furthermore, wettability was identified as an important parameter affecting viscous instabilities. In fact, instabilities occurred in both oil-wet and water-wet media ─ however, the phenomenon emerged at lower displacement rates in an oil-wet scenario.

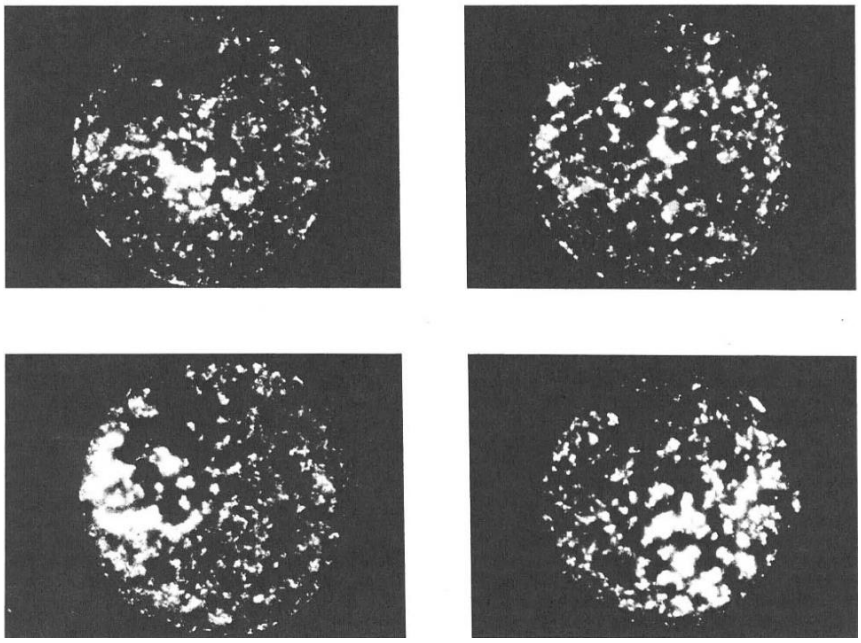

Figure 2.12: Cross section of the core showing viscous fingering in an oil-wet core and for an injection rate $Q = 3.8\,10^{-4} m/s$ (Peters and Flock, 1981).

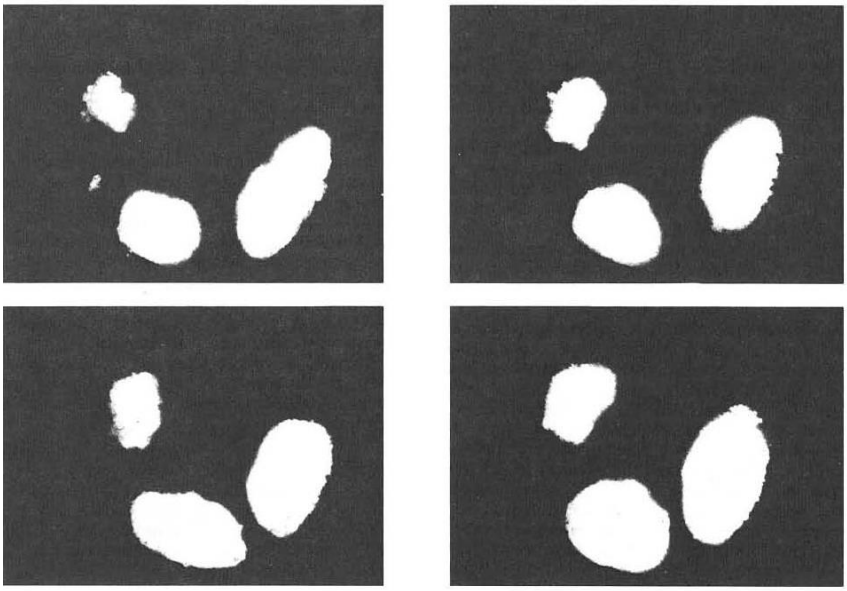

Figure 2.13: Cross section of the core showing viscous fingering in an oil-wet core and for an injection rate $Q = 1.7\,10^{-7}\, m/s$ (Peters and Flock, 1981).

Majors et al. (1997) visualized the saturation maps of corefloods during immiscible oil/water displacements with Nuclear Magnetic Resonance (NMR) technology. They noticed the influence of mobility ratio on viscous fingering and, in the adverse viscosity ratio case, the displacement was less efficient.

Romero-Zeron et al. (2009) and Romero-Zeron et al. (2010) visualized fluid distributions in core flooding experiments with a Magnetic Resonance Imaging (MRI) technique. Saturation maps, the onset of fluid instabilities, and direct determination of residual oil could be directly and accurately measured using the technique. Finally, the effect of wettability on polymer flooding experiments could be observed. They found that, in all polymer floodings, MRI fluid saturations indicated that the displacement was much more efficient in a strongly water-wet condition than in a preferentially oil-wet condition.

2.2.7. Post-breakthrough behaviour of viscous fingering

Most of the viscous fingering studies have focused on the behaviour before breakthrough and especially on finger initiation and development, and few authors have described the post-breakthrough stage of their experiments.

Van Meurs (1957) performed two phase immiscible displacements in a medium filled with powdered glass and considered fluids yielding a viscosity ratio equal to 80. As shown in Figure 2.14, the upstream instabilities grew in the outlet direction during the early stages after breakthrough. After the fingers had reached the outflow end of the system, the existing fingers started to thicken and collapse, forming water channels. The *"finger thickening"* phenomenon was described in this paper, but no physical explanation of this behaviour was given.

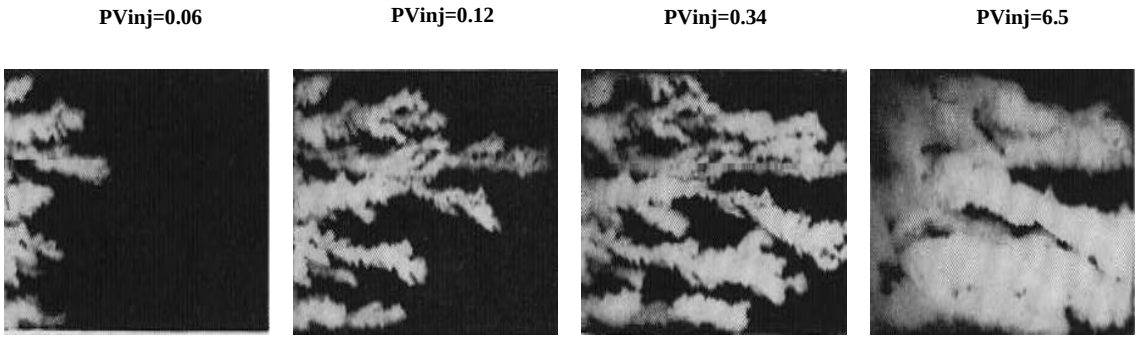

Figure 2.14: Two phase displacement of water (white) displacing oil (black) at different PV injected. The viscosity ratio $\frac{\mu_o}{\mu_w}$ was equal to 80 (Van Meurs, 1957).

Mai and Kantzas (2008) and Mai and Kantzas (2009) investigated the mechanisms governing the cold recovery of extra heavy oil in water wet cores. They performed water flooding experiments in sandstone filled with extra heavy oil. Two oil viscosities were used (4650 cP and 11500 cP) and they noticed that the oil recovery was higher at lower injection rates and that cores with lower permeability gave better recovery. To explain these results, they proposed that the viscous forces are important at early times of the experiments and that the extra recovery after breakthrough is mainly due to capillary forces. Their suggestions were based on some observations that showed an increase in recovery after shutting in the experiment for some days ─ suggesting that water imbibed into the oil during that time. However, they did not visualize the fluid distributions during the waterfloods. In a more recent paper, Mai and Kantzas (2010) performed similar experiments and used CT imaging technique to see the fluid distributions in some cross sections across the cores. They observed that, at high rates, oil was recovered from areas close to the spanning fingers. However, at low rates the water moved away from the fingers and was found in a much larger area of the core, which seems to be caused by the capillary forces.

Bondino et al. (2011), Skauge et al. (2012), Skauge et al. (2013) and Skauge et al. (2014) performed water and polymer floodings in (30cm*30cm*2cm and 15cm*15cm*2cm) non water-wet Bentheimer slabs. They used x-ray imaging technique to visualize the saturation maps and could clearly see the fluid distributions as shown in Figure 2.15. The viscous fingers developed at early stages of water injection and the

finger shape varied with mobility ratio: the instabilities were sharper for higher oil viscosiies. This study seems to contradict that performed by Stokes et al. (1986) where the finger width was found to be comparable to the pore size in drainage. In fact, at these rates, and for viscosity ratios close to those used by Stokes and co-authors (M=200), the fingers were much larger than a typical pore size in the non-water wet case. Moreover, an intriguing phenomenon was observed in this study. Continuous water injection led to the thickening of the fingers and their coalescence into channels with high water saturation. This behaviour was sensitive to the mobility ratio and the water channels were wider for less viscous oil, as can be seen in Figure 2.15. Finally, injection of polymer solution improved the oil recovery. Some of these experiments will be simulated and interpreted in Chapter 7 of this thesis.

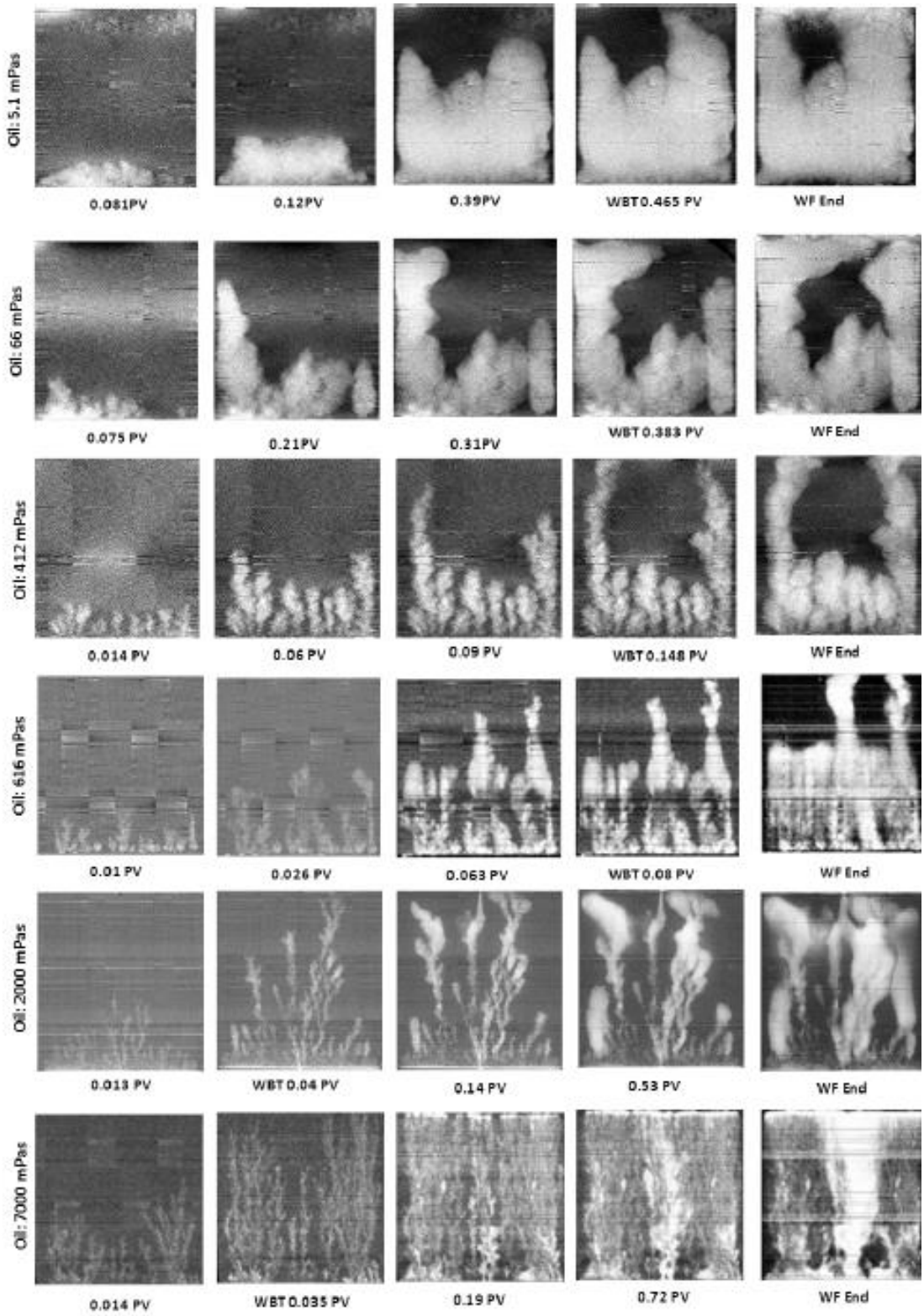

Figure 2.15: 2D x-ray images of water flood for 6 different oil-water viscosity ratios captured at different PV of injected water. White colour indicates areas with higher water saturation. The water breakthrough (WBT) for the different water floods is also indicated. As the images are contrast enhanced to better illustrate the observed finger pattern, the grayscale does not represent true water saturation (Skauge et al., 2014).

2.3. MATHEMATICAL MODELLING OF VISCOUS FINGERING

In order to better understand viscous fingering phenomena and gain an insight into the influence of rock/fluid parameters upon the instability initiation and development, a number of mathematical modelling techniques have been developed. One of the most popular approaches is named linear stability analysis, which will be discussed next.

2.3.1. Linear stability analysis (LSA)

The first rigorous one dimensional stability analysis dealing with this theory was presented by Saffman and Taylor (1958). This was followed by the paper of Chuoke et al. (1959) who published a similar analysis. According to Homsy (1987), the historical credit should probably be attributed to Chuoke et al. (1959) because of the delays involved in publishing research from an industrial laboratory.

Linear stability analysis provides a description of the variations in frontal position by means of a Fourier series approach. It transpires that, at an unfavourable mobility ratio, all perturbations below a critical wavelength are eliminated, whilst perturbations above this critical wavelength continue to grow at an unfavourable mobility ratio. We describe the study of Chuoke et al. (1959) in greater detail.

Consider two fluids that are forced under gravity and an imposed pressure gradient through a porous medium (Figure 2.16), fluid 1 (water) is displacing fluid 2 (oil) and we assume that each fluid is of infinite extent with a plane macroscopic sharp interface moving slowly through a uniform permeable medium with speed W normal to the interface.

We choose a Cartesian coordinate system with positive z axis directed from fluid 1 to fluid 2, perpendicular to the macroscopic interface and forming an angle(zz') with the z' axis directed vertically upwards. If fluid 1 is displacing fluid 2, W is positive and the component of the gravitational acceleration is $-g\cos(zz')$.

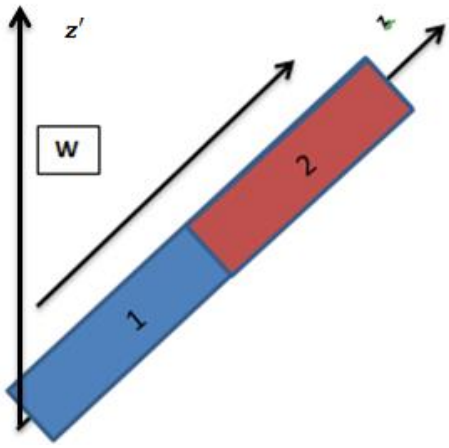

Figure 2.16: A system of water (Fluid1) displacing oil (Fluid2)

The flow of the fluids through the porous medium is described by Darcy's law:

$$\vec{v} = -\,grad\left(\frac{k}{\mu}(p + \frac{\mu}{k}Wz + \rho gzcos(zz'))\right) = -grad\phi \tag{2.3}$$

and $div(\vec{v}) = -\nabla^2\phi = 0$ (2.4)

where:

W is the velocity of the flow;

$\vec{v}$ is a perturbation velocity;

μ is the viscosity of the fluid;

ρ is the density of the fluid;

k is the permeability of the core;

g is the acceleration due to the gravity;

ϕ is the velocity potential.

After integrating equation (2.3) we have:

$$p = \frac{\mu}{k}\phi - \frac{\mu}{k}Wz - \rho gzcos(zz') \tag{2.5}$$

If we decompose an arbitrary deformation of the macroscopic interface into fundamental Fourier perturbation modes and study each separately, then every deformation can be written as:

$$\xi = \varepsilon \exp(nt + i(\alpha_x x + \alpha_y y)) \tag{2.6}$$

where $\vec{\alpha} = \alpha_x \vec{\imath} + \alpha_y \vec{\jmath}$ is the propagation vector in the x,y plane and has as a magnitude and n is the index of instability.

$$\alpha = \sqrt{{\alpha_x}^2 + {\alpha_y}^2} \tag{2.7}$$

The following boundary conditions were considered:

- Kinematical condition: the fluid particles at the interface will continue to be at the interface at later stages of the displacement;
- Dynamical condition: relates the pressure drop across the macroscopic interface to the curvature of the interface by means of an effective interfacial tension;
- The velocity of the perturbations must vanish for z infinite.

After solving equation (2.4) and applying the boundary conditions the following equation is obtained:

$$(\frac{\mu_2}{k_2}+\frac{\mu_1}{k_1})n-\left[\left(\frac{\mu_2}{k_2}-\frac{\mu_1}{k_1}\right)W+(\rho_2-\rho_1)gcos(zz')\right]\alpha+\sigma_e\alpha^3=0 \quad (2.8)$$

For α>0, a necessary and sufficient condition for instability is to have n>0 and is given by:

$$\left[\left(\frac{\mu_2}{k_2}-\frac{\mu_1}{k_1}\right)W+(\rho_2-\rho_1)gcos(zz')\right]+\sigma_e\alpha^2>0 \quad (2.9)$$

Chuoke et al. (1959) defined a critical wavelength λ_c:

$$\lambda_c=2\pi\sqrt{(\frac{\sigma_e}{(\frac{\mu_2}{k_2}-\frac{\mu_1}{k_1})(U-U_c)})} \quad (2.10)$$

and showed that $U>U_c=\frac{(\rho_1-\rho_2)g\cos(zz')}{(\frac{\mu_2}{k_2}-\frac{\mu_1}{k_1})}$ and $\lambda=\frac{2\pi}{\alpha}>\lambda_c$ combined are the necessary and sufficient conditions for instability and are equivalent to equation (2.9). This means that, if the volumetric velocity U is higher than the critical velocity U_c , the instabilities having a wavelength longer than the critical wavelength λ_c will grow and form viscous fingers.

For $U>U_c$, the index of instability, n as a function of α possesses an absolute maximum. The root of the equation $\frac{\partial n}{\partial\alpha}=0$ is named α_m and determines the wavelength of maximum instability which is defined as $\lambda_m=\sqrt{3}\lambda_c$.

This theory was extended by Outmans (1962) who considered higher order terms in the equations. He concluded that the improved method is suitable to describe the early growth of instabilities. Moreover, he identified a rate effect on the shape of viscous fingers when the gravity and interfacial tension are significant.

Further improvements to the study of Chuoke et al. (1959) were presented by Rachford (1964). A first order LSA analysis was reported and the effects of the saturation of the transition zone in water wet porous media were considered. He could successfully reproduce the instabilities in a homogenous medium and also suggested that the flow velocity effect on the instabilities could be small. He highlighted that the instabilities were sensitive to the shape of the relative permeability curves and capillary pressure functions assumed.

However, Hagoort (1974) noted that Rachford (1964) violated the nonlinearity of the perturbation equations and that the number of cases he studied was too low to draw general conclusions. He proposed a first order LSA study including the effects of the saturation of the transition zone and he used an energy method to assess the contribution to the stability of viscous and capillary effects. He proposed that the Buckley-Levrett type of displacement is unstable if the shock mobility ratio is greater than 1 and the wavelength of the instabilities is smaller than the core width. Moreover, he stressed that the predominating wavelength is proportional to the capillary number as well as other displacement characteristics.

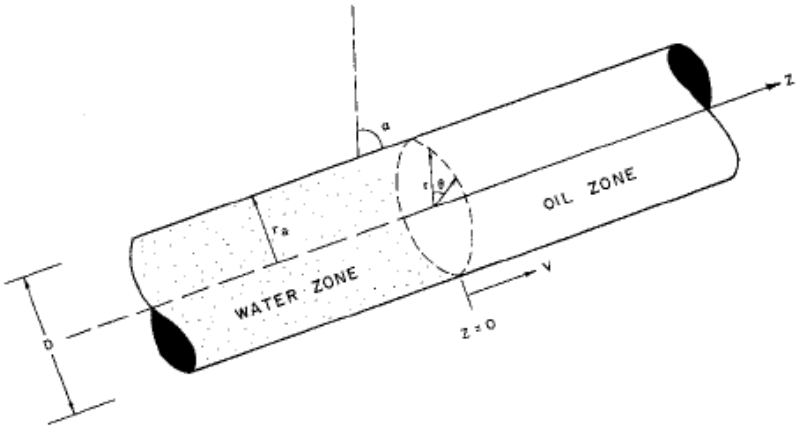

Figure 2.17: Water displacing oil in a cylindrical system (Peters and Flock, 1981).

All these studies demonstrate that several variables ─ injection velocity, wettability, mobility ratio and permeability ─ are pertinent to the onset of instabilities in two phase immiscible displacements. However, up until this point none had combined their effects into one dimensionless variable. This was achieved by Peters and Flock (1981) who extended the LSA of Chuoke et al. (1959) ─ the main feature of their paper was the addition of a fourth boundary condition to the problem. After using the Chuoke et al. (1959) methodology in a cylindrical core, they calculated the velocity potentials in fluids 1(water) and 2 (oil) as follows:

$$\phi_1 = B_1 \exp(\alpha z + nt) cosm\theta J_m(\alpha r) \tag{2.11}$$

$$\phi_2 = B_2 \exp(-\alpha z + nt) cosm\theta J_m(\alpha r) \tag{2.12}$$

where:

r, θ and z are the components of the cylindrical system ;

B_1, B_2 are random integration constants;

J_m is the Bessel function of first kind.

The perturbation was calculated as:

$$\xi = \frac{\alpha}{n} B_1 \exp(nt)\, cosm\theta J_m(\alpha r) \tag{2.13}$$

and the critical and fastest growing wavelengths were given by:

$$\lambda_c = 2\pi \sqrt{\left(\frac{\sigma_e\, k_{wor}}{(M-1)(U-U_c)\mu_w}\right)} \tag{2.14}$$

$$\lambda_m = 2\pi\sqrt{3} \sqrt{\left(\frac{\sigma_e\, k_{wor}}{(M-1)(U-U_c)\mu_w}\right)} \tag{2.15}$$

where M is the end point mobility ratio and k_{wor} is the permeability to water at S_{or}.

The fastest growing wavelength gives a qualitative idea of the fingering phenomenon as a function of injection rate. At high rates, the analysis predicts that the finger wavelength will be short and that several fingers will be seen in the core. However, at low rates, the finger wavelength will be long and only few fingers can be accommodated.

The new boundary condition assumes that the velocities normal to the core wall must vanishes and this gives the wavenumbers that will manifest themselves in an unstable displacement, given by the roots of:

$$\frac{dJ_m}{dr} = 0 \tag{2.16}$$

The instabilities will occur when the minimum root of the Bessel function is reached, obtained for m=1 and equal to 1.8412─ below the rate corresponding to this value no instability can be obtained.

This corresponds to a defined instability number:

$$I_{sc} = \frac{(M-1)(U-U_c)\mu_w D^2}{C^* \sigma k_{wor}} = 13.56 \tag{2.17}$$

Therefore, according to this study, viscous fingering occurs when the instability number I_s is higher than the critical value (13.56 for a cylindrical core). Below the critical value, the capillary forces are still strong enough to stabilize the displacement. This variable is very useful as it gives a very fast way of predicting the stability of a given displacement.

Peters and Flock (1981) confirmed their theory by performing several flooding experiments. They verified that viscous fingering occurred only when the stability number was above the critical value. In the opposite case, the displacements were stable.

An analogous study done for a rectangular core gave the following critical stability number:

$$I_{sc} = \frac{(M-1)(U-U_c)\mu_w {L_x}^2 {L_y}^2}{C^* \sigma k_{wor}({L_x}^2 + {L_y}^2)} = \pi^2 \quad (2.18)$$

Although LSA has been an important mathematical tool in viscous fingering studies, Riaz and Tchelepi (2006) emphasized that it gives only information about the initial stages of the instabilities and cannot be used to study late phases of finger development. To overcome this shortcoming, other techniques such as statistical modelling methods, have been used to predict the behaviour of viscous fingers at late stages.

2.3.2. Statistical modelling of viscous fingering

(a) Fractal nature of viscous fingering

A fractal is a curve or geometrical figure, each part of which has the same statistical character as the whole. They are useful in modelling structures (such as snowflakes) in which similar patterns recur at progressively smaller scales, and in describing partly random or chaotic phenomena such as crystal growth and galaxy formation.

Although fractals are very complex shapes, they are formed by repeating a simple process and can be found in a wide range of natural phenomena, from tiny patterns like seashells up to the giant spirals of galaxies. Trees, river networks, mountains, coastlines, lightning bolts, blood vessels, flowers are all examples of natural fractals. Examples of fractals in nature can be found in Figure 2.18 and Figure 2.19.

Figure 2.18: An example of fractals in nature. The fern is an ancient, primitive plant that is made up of the same pattern at different scales (Source: http://fractalfoundation.org/)

The complexity of fractals can be characterized by a ratio named the fractal dimension (D), which can be expressed at a time t during a radial displacement as a function of the areal sweep efficiency E_A, the radius of the displacement front r_d and a proportionality constant C as follows:

$$Ln(E_A(t)) = Ln(C) + DLn(r_d) \tag{2.19}$$

In practice, the fractal dimension is determined by plotting equation (2.19) at several stages of an experiment. The slope of the curve gives the fractal dimension.

This concept was first introduced by Mandelbrot (1967) in the description of complex geographical curves and since then, several authors have studied the fractal nature of various phenomena including viscous fingering. Van Damme et al. (1986) were the first

to propose the relationship between the area swept and the maximum finger length (radius of gyration).

Several authors used fractal geometry to characterize unstable displacements (Pons et al., 1999, Zhang and Liu, 1998, Maxworthy, 1987, Nittman et al., 1985, Daccord et al., 1986, Fanchi and Christiansen, 1989, Måløy et al., 1985, Peters and Cavalero, 1990, Doorwar and Mohanty, 2011). From these studies, it emerged that the fractal dimension of viscous fingering depends on rock and fluid properties.

(b) Diffusion limited aggregation (DLA)

Diffusion limited aggregation (DLA) is a model which represents noisy growth limited by diffusion. It has been widely used to model fractal types of natural phenomena (Vicsek, 1992) such as ice creation (Kim et al., 2004), lightning formation (Kim and Lin, 2007) and viscous fingering phenomena (Bogoyavlenskiy, 2001) .

To understand the basics, we consider colloidal particles undergoing motion in some fluid, and let them adhere irreversibly on contact with one another. We suppose that the density of the particles is quite low, so one can imagine that the aggregation process takes place one particle at a time. We are then led to the following model.

We consider a seed particle at the origin of some coordinate system, introduce another particle far away from the seed, and let it carry out a random walk ─ a mathematical formalization of a path that consists of a succession of random steps. Eventually, that second particle will either escape to infinity or contact the seed, to which it will stick irreversibly. Next, introduce a third particle and let it walk randomly until it either sticks to the two-particle cluster or escapes to infinity and so on.

Paterson (1984) was the first to notice the parallels in the behaviour of DLA and two-phase fluid flow in porous media. In fact, he noticed that both processes can be described by the application of Laplace's equation and that the boundary conditions were similar. Furthermore, he highlighted the similarities in the flow patterns between DLA and viscous fingering in porous media.

However, the original analysis neglects the effects of interfacial tension and this makes it unsuitable to simulate viscous fingering in immiscible displacements. There have been several attempts to extend DLA analysis to take into account capillary pressure, where modifications of the growth rules and conditions were proposed. For example, some authors made the random walkers evaporate from the cluster after first contact, with a probability calculated as a function of the number of nearest cluster ‘‘neighbours’’ or, more generally, as a function of front curvature (Vicsek, 1992, Banavar et al., 1986, Liang, 1986, Tao et al., 1988, Fernández and Albarrán, 1990). Others took into account a surface diffusion of growth units and the related thermodynamics (Xiao et al., 1988, Ohta and Honjo, 1991, Bogoyavlenskiy and Chernova, 2000a).

Several researchers have tried to introduce continuum approaches for the DLA model (Witten Jr and Sander, 1981, Nauenberg, 1983, Garik et al., 1985, Kantor et al., 1986, Cates, 1986, Levine and Tu, 1992, Sandow and Trimper, 1993, Levine and Tu, 1993, Kassner and Brener, 1994, Keblinski et al., 1994, Bogoyavlenskiy and Chernova, 2000b). However, Bogoyavlenskiy (2001) criticized these studies and pointed out that the vast majority suffer from a lack of *ab initio* principles. He justified this by the fact that a hypothesis on the aggregation kinetics is needed to construct a mean field theory; something that cannot be explicitly verified and justified for a purely continuum case. To avoid this difficulty Bogoyavlenskiy (2001) proposed a quasi-continuum model and used it to simulate two phase immiscible displacements in Hele Shaw cells.

(c) Dielectric breakdown model (DBM)

Dielectric breakdown (named also electrical breakdown) is a phenomenon implying the rapid reduction in the resistance of an electrical insulator when the voltage applied through it goes beyond the breakdown voltage. This results in a portion of the insulator becoming electrically conductive. The electrical discharge is a fractal pattern and looks similar to the viscous fingering phenomenon as we can see in Figure 2.19.

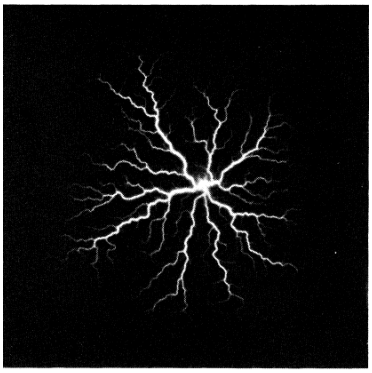

Figure 2.19: Time-integrated photograph of a surface leader discharge (Lichtenberg figure). This experiment corresponds to an equipotential channel system growing in a plane with radial electrode.(Niemeyer et al., 1984)

Niemeyer et al. (1984) introduced the dielectric breakdown model (DBM) for modelling the dielectric discharge in insulators. It consisted of a simple two-dimensional stochastic model with a basic assumption that the growth probability depends on the local electrical field. The insulator is modelled by a lattice consisting of sites and bonds. One of the electrodes is situated in the central site and the other is modelled as a circle situated far from the central site. The electrical field ϕ can be determined by solving Laplace equation:

$$\nabla^2 \emptyset = 0 \tag{2.20}$$

The boundary conditions considered are $\emptyset = 0$ at each discharge site and $\emptyset = 1$ at the external electrode.

A probability is associated with the transport of electrons from an occupied site (ij) at the interface to a neighbour site $(i'j')$ and can be calculated as:

$$P = \frac{(\emptyset_{i'j'})^{\eta}}{\sum(\emptyset_{i'j'})^{\eta}} \tag{2.21}$$

where η is a real number and is a parameter of the equation. Then, the probability is multiplied by a random number between 0 and 1 to introduce randomness to the system. The site having the highest probability is invaded by the discharge pattern.

if $\eta = 1$ the invasion pattern will be fractal whereas if $\eta = 0$ the pattern becomes homogenous and is similar to a piston like displacements (Doorwar and Mohanty, 2014).

Doorwar and Mohanty (2014) have suggested that several similarities exist between dielectric discharge and viscous fingering. For example, the discharge occurs only above a certain potential called the critical excitation potential, whilst a drainage invasion happens only above a threshold capillary entry pressure. Moreover, both viscous fingers and dielectric discharge have a higher growth probability at the tip. Indeed, Pietronero and Wiesmann (1988) have pointed out that, for $\eta = 1$, the local field and the growth probability are linear. For a porous medium, although the flow is proportional to the pressure gradient, it is not linear because of the capillary entry pressure effect. They proposed that this non linearity could be taken into account by using a value different from unity for the parameter η.

Doorwar and Mohanty (2014) proposed a slightly modified DBM model to model flow in porous media. In this model, the potential field is first calculated. Then, the movements with the highest probability are executed and the process repeated until breakthrough. They could simulate a wide range of flow regimes from piston like displacement to viscous fingering by changing the parameter η as we can see in Figure 2.20. They went on to propose a correlation between the viscosity ratio and η to have the same regime in the simulations match a couple of micromodel experiments. Finally, they used this model to simulate slab scale experiments (Skauge et al., 2012). Whilst they reproduced the same regimes seen in the experiments, they did not simulate the

post-breakthrough behaviour and it was not clear if their model could reproduce the flow post-breakthrough.

The Doorwar and Mohanty (2014) model can be criticized as being completely dependent on the value assigned to η and, furthermore, the correlation that they proposed for determining η as a function of the viscosity ratio seems too simplistic. Actually, as seen in the experimental studies of viscous fingering, viscous instabilities are complex and are sensitive not only to viscosity ratio but also to other rock/fluid parameters such as capillary number, wettability and interfacial tension. The effects of varying these parameters cannot be reproduced by their model.

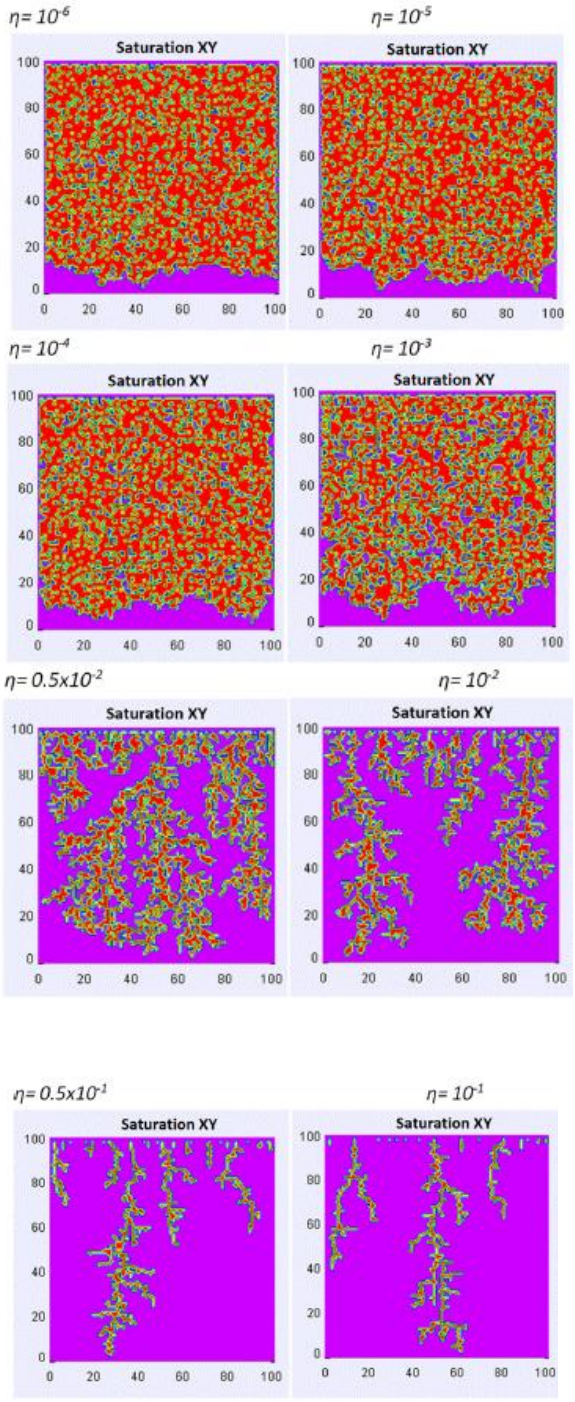

Figure 2.20: Water and oil distribution in 2D simulations for different values of parameter η (Doorwar and Mohanty, 2014).

2.4. CONTINUM APPROACH MODELLING

Very few papers exist in the literature concerning the simulation of immiscible viscous fingering using conventional reservoir simulators.

Riaz et al. (2007) investigated the possibility of reproducing unstable displacement experiments using continuum models and concluded that the onset of instability, as well as the initial unstable modes, can be determined with acceptable precision. However, such models are deficient for fully developed flows.

Gilje (2008) attempted to use the UTCHEM reservoir simulator to reproduce miscible and immiscible viscous fingering experiments ─ however, for unstable immiscible displacements, the simulated saturation profiles did not match the experimental images.

Bondino et al. (2011) simulated water and polymer flooding experiments using a Darcy law simulator. They carried out two experiments realized under the same conditions but a different geometry: one 2D experiment performed in a 30*30*2cm slab and a 1D experiment carried out in a 30 cm long core. They history matched the production data by varying the relative permeability set and the capillary pressure curve in the 2D experiment. However, the saturation maps could not be reproduced. They then used the relative permeability and capillary pressure curves that reproduced the 2D prediction to simulate the 1D case. The (kr,Pc) set could not match the production data of the 1D experiment and again the saturation maps could not be replicated.

2.5. DIGITAL ROCK PHYSICS MODELLING

2.5.1. Computational fluid dynamic (CFD)

Computational fluid dynamics, usually abbreviated to CFD, is a branch of fluid mechanics that uses numerical methods to solve problems that involves fluid flows. They generally involve solving flow equations, such as Navier-Stokes, thermal energy, and species equations and it has been widely used in numerous areas, such as automotive (Ding et al., 2006), aerospace (Fujii, 2005) and the food industry (Xia and

Sun, 2002). CFD has also been applied in the oil and gas industry for separator studies, blow out simulations, cuttings transport in wells and steam assisted gravity drainage (Erdal et al., Borello et al., 2007, Bilgesu et al., 2002). CFD is a very interesting tool to simulate flow in porous media as it raises the possibility of performing direct simulations in rock images.

Clemens et al. (2013) have developed a CFD Navier-Stokes simulator in this context. First, they took images of the porous medium by a Scanning Electron Microscope (SEM), grids were then formed from the images of a unit block, and they solved Navier-Stokes, mass conservation and momentum conservation equations. They considered as boundary conditions that no flow occurs at the boundary of the model and considered that the fluid does not slip when it is in contact with the rock. The phase saturations could be determined throughout.

This simulator was used to simulate micromodel experiments and it successfully reproduced viscous fingering during water and polymer floodings as can be seen in Figure 2.21. The model predicted severe fingering for water injection into oil and an improved recovery for the polymer flooding case.

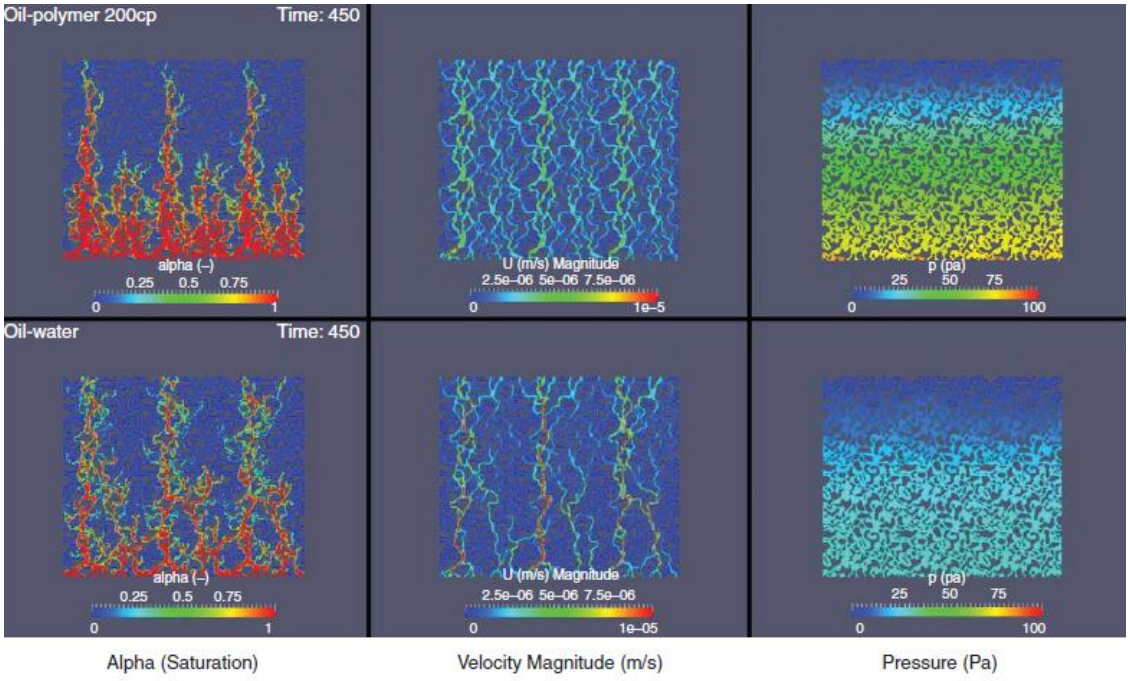

Figure 2.21: CFD simulation for water and polymer solutions displacing oil(Clemens et al., 2013)

The Lattice Boltzmann method (LBM) is another popular CFD technique. Unlike Navier-Stokes simulators, Navier–Stokes equations are not solved. Instead, the discrete Boltzmann equation is resolved to simulate the flow of a Newtonian fluid with collision rules. Compared to the conventional CFD models LBM has the advantage of being simple and effective for modelling flow in complex geometries (Chen and Doolen, 1998). Gunstensen et al. (1991) proposed a LBM for immiscible displacement simulations, where sharp interface was obtained by phenomenological collision and recoloring rules.

Early studies of LBM considered very simple models with fixed wettability condition and equal fluid viscosities (Van Kats and Egberts, 1999, Gunstensen et al., 1991). Evidently, such models could not simulate viscous fingering phenomena.

Langaas and Yeomans (2000) studied the displacement of immiscible fluids in a two-dimensional channel by means of a thermodynamically consistent Oxford model. They could see the evolution of a single finger and their results were similar to the experiments of Saffman and Taylor (1958).

Chin et al. (2002) studied viscous fingering in two dimensions using the Shan-Chen (Shan & Chen 1994) binary immiscible fluid model. Although a finger-like structure was observed in many simulations, they highlighted that they were not sure that the observed structure was actually due to viscous fingering.

None of these models considered the effect of wettability. Yiotis et al. (2007) built a model taking into account the wettability in the formulation and the model was applied to the study of two-phase immiscible displacements. However, the simulations presented in this study were performed with a maximum viscosity ratio equal to 10 and the model formulation did not consider the effect of gravity.

Dong et al. (2011) proposed a LBM taking into account both wettability and gravity. They were successful in reproducing flow experiments in Hele Shaw cells with their simulator as we can see in Figure 2.22.They analysed the effects of capillary number, viscosity ratio, bond number and wettability upon the viscous fingering phenomenon. Their simulations showed that when gravity is not considered and the fluid viscosities are similar, the displacement is not sensitive to the capillary number. In addition, the model predicted that the areal sweep efficiency decreases with an increase in the viscosity ratio. However, this model could not handle fluids with viscosity ratios higher than 5.

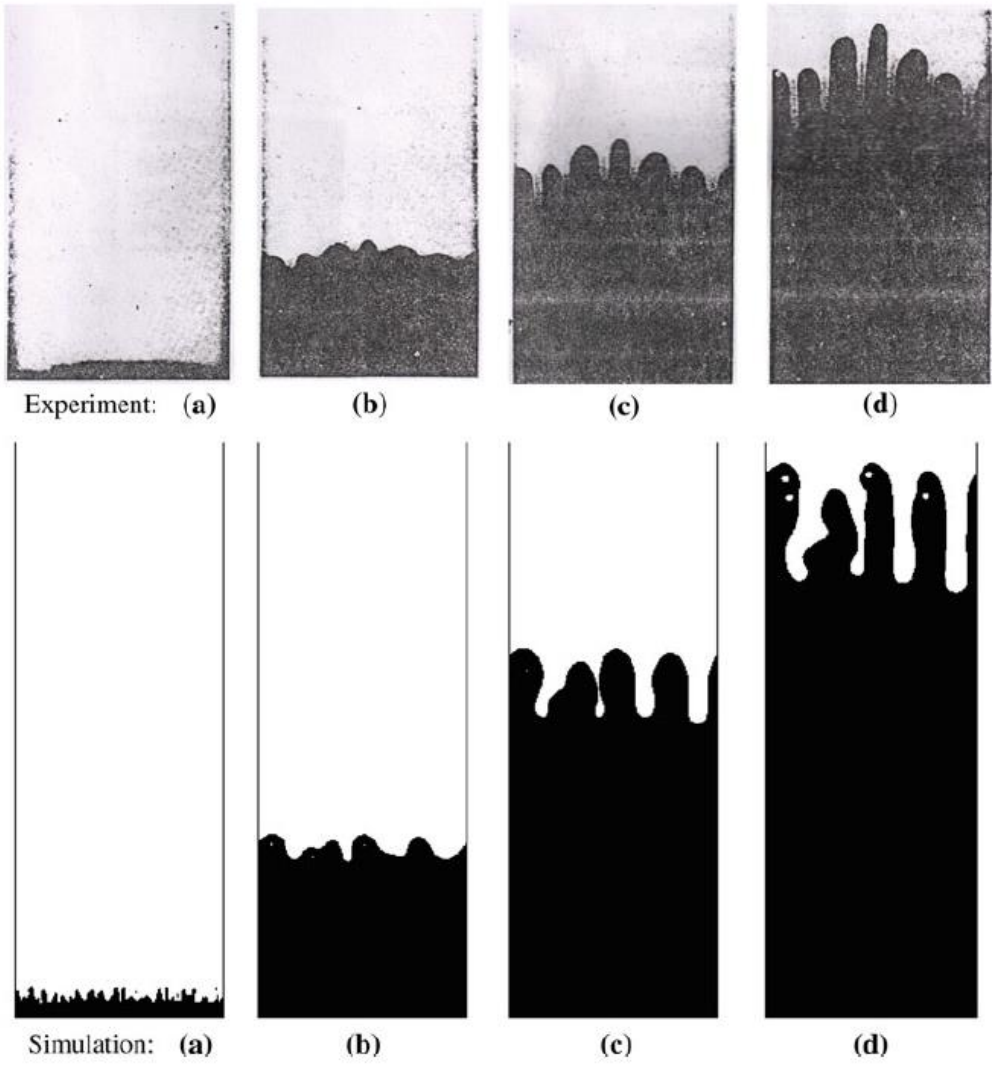

Figure 2.22: Qualitative comparison between simulations and flow in Hele Shaw cells (Dong et al., 2011)

Recently, Huang et al. (2014) proposed a lattice Boltzmann model that could handle viscosity ratios ranging from 10^{-3} to 10^{3}. This model was used to build a phase diagram qualitatively consistent with the one published by Lenormand et al. (1988).

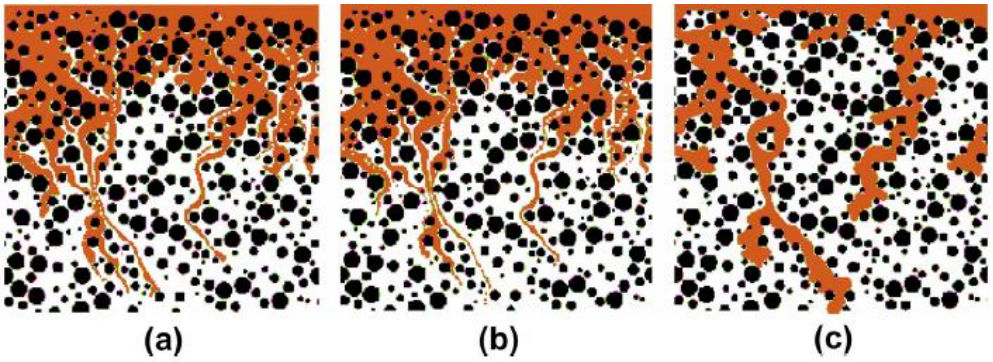

Figure 2.23: Viscous fingering simulation obtained from different combinations of different M and Nca(Huang et al., 2014).

As we can see from Figure 2.21, Figure 2.22 and Figure 2.23, whilst CFD simulators reproduced viscous instabilities, they could not simulate the characteristic tree like shape of viscous fingering.

2.5.2. Pore network models (PNM)

Pore network modelling is now a long-standing technique for the study of various pore scale phenomena that cannot be reproduced by conventional continuum-scale numerical simulators (see, for example, McDougall and Sorbie,1995; Valvatne and Blunt, 2004; Bondino et al, 2009, for details of the approach and various applications). The porous medium is modelled as a number of interconnected pore elements representing the void space in the rock. Multiphase flow models can then be developed and applied to this *in silico* network model. Several authors have used unsteady-state PNM simulators to model viscous fingering phenomenon in immiscible displacements.

Chen and Wilkinson (1985) built a simplified version of the pore network models of Koplik and Lasseter (1985) and Dias and Payatakes (1986a). They studied the effects of randomness of the porous medium on viscous fingering and performed both experiments and simulations. They used several pore size distributions generated in the interval $[1-\lambda, 1+\lambda]r$, where r is the mean radius and λ is the randomness factor. In the experiments, oil was injected into the centre of a two dimensional micromodel filled with glycerine. The viscosity ratio was unfavourable and was equal to 1200. Viscous fingering was observed experimentally and the size and pattern of fingers was

dependent on the pore size distribution. The instabilities formed almost ordered patterns and grew along the injection direction for a narrow pore size distribution. However, chaotic fingers were observed for a wide pore size distribution. A very good qualitative agreement was found between the experiments and the simulations as we can see in Figure 2.24. They found that for λ=1 the fractal dimension was equal to 1.72.

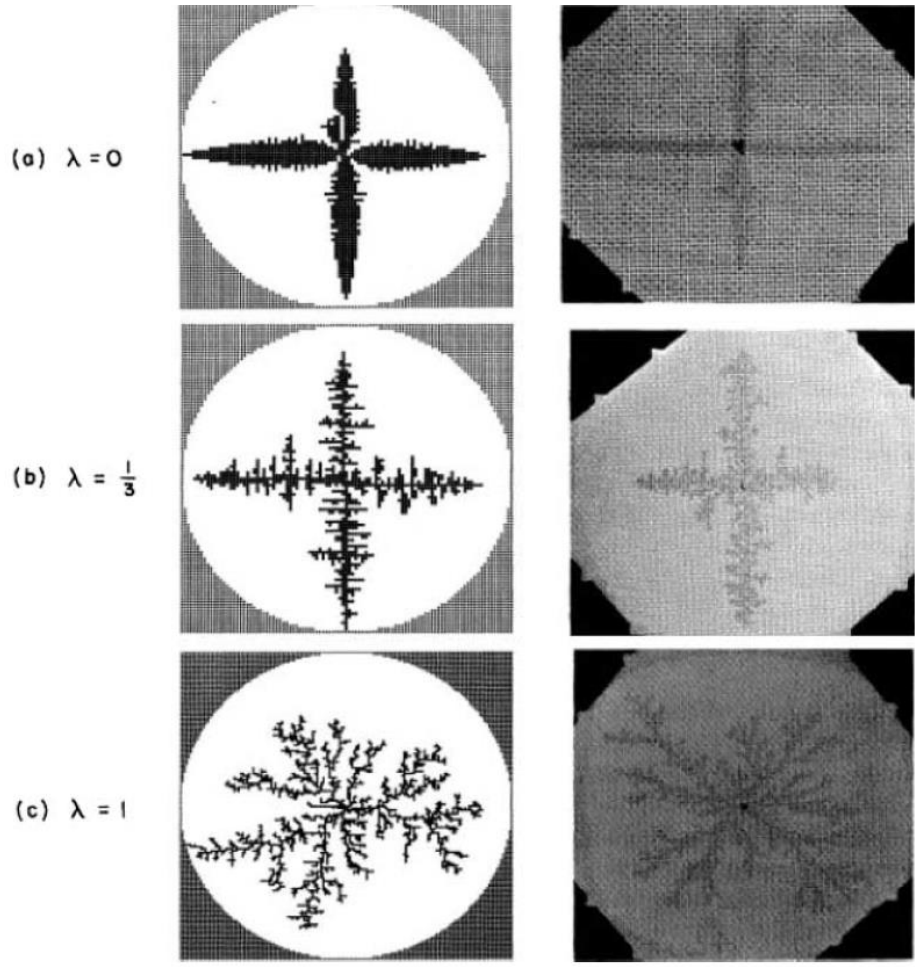

Figure 2.24: Viscous fingers for different randomness values in the network. The left column represents the simulations and the right one shows the experimental results.

Later, King (1987) used a pore network model to study the fractal behaviour of viscous fingering. He investigated the surface fractal dimension D_s assigned to the fingers at the front of a compact flow. He showed that the surface of fingers follows a fractal

phenomenon and that it is not sensitive to the disorder of the network. He found that it is dependent on the viscosity ratio.

Blunt and King (1990) have also studied the fractal behaviour of viscous fingering. The fractal dimension in their network changed from 1.82 in 2D simulations to 2.44 in 3D networks.

Lenormand et al. (1988) developed a dynamic drainage pore network model and used it to simulate micromodel experiments. They could reproduce capillary fingering, viscous fingering and frontal displacement regimes for different capillary number and mobility ratio combinations as we can see in Figure 2.25. They used these results to build a phase diagram representing the three main flow regimes and which can be mapped with the viscosity ratio and the capillary number. The biggest networks that they used in their simulations were 100*100 lattices.

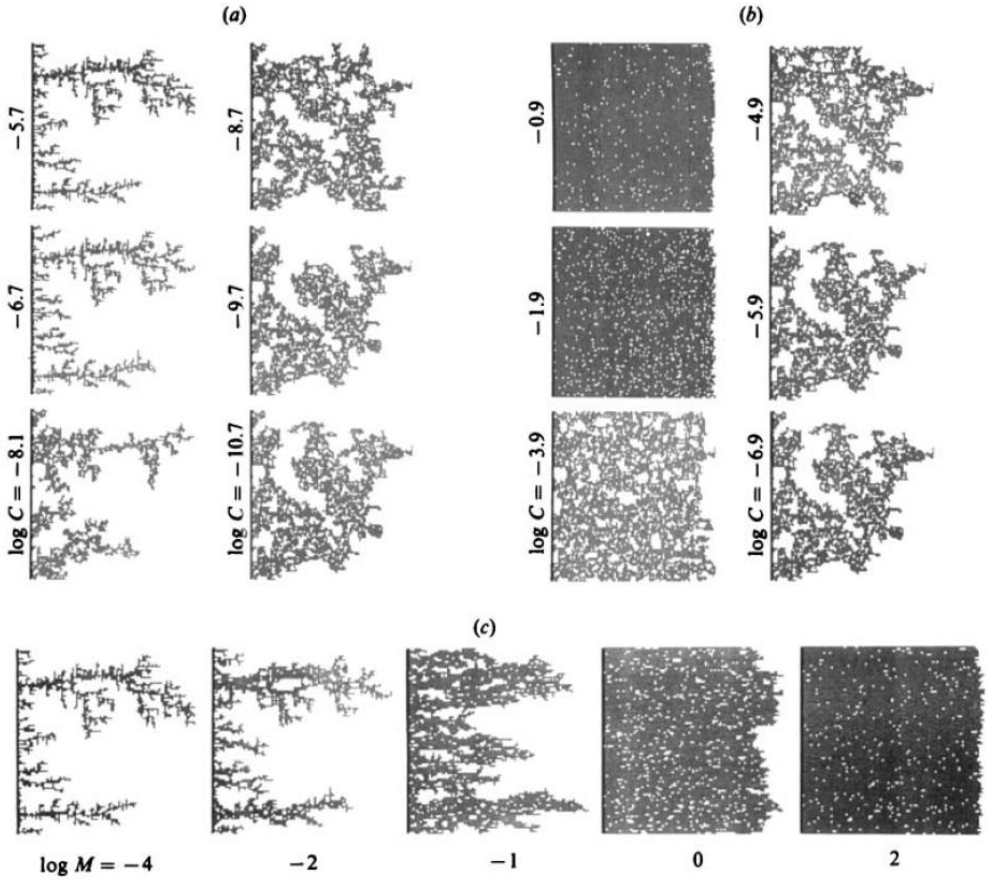

Figure 2.25: 100 x 100 simulations at various viscosity ratio and capillary numbers (a)M =50120 from viscous fingering to capillary fingering: (b) M = 0.0125, from stable displacement to capillary fingering: (c) logNca = 0, from viscous fingering to stable displacement (Lenormand et al., 1988).

Aker et al. (1998b) built an unsteady state drainage PNM simulator and used it to simulate different flow regimes patterns. They introduced a new method allowing simultaneous flow of two liquids into one pore. They could reproduce viscous fingering as we can see in Figure 2.26. However, they reported that their simulator was slow and 60*80 network was the biggest lattice that they could use.

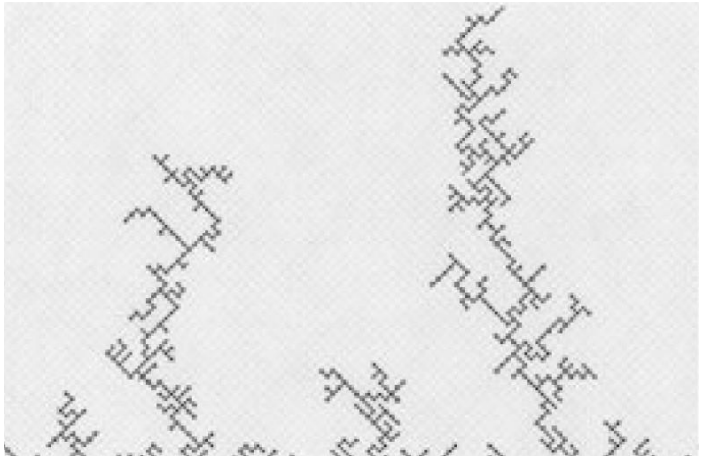

Figure 2.26: The pattern obtained of a simulation in the regime of viscous fingering on a lattice of 60*80 nodes (Aker et al., 1998a).

Singh and Mohanty (2003) performed three dimensional simulations by a dynamic drainage PNM simulator. They studied the effect of the capillary number and viscosity ratio on residual saturations. Their simulator could reproduce all the flowing regimes including viscous fingering. However, the saturation patterns that they presented in their paper were in 3D systems and it was difficult to check whether the characteristic tree like shape of viscous fingering was simulated. Furthermore, the biggest system that they used in their study was a 30*8*8 network.

Ferer et al. (2004b) were interested in the crossover between capillary fingering and viscous fingering regimes. They used a pore network model and presented two dimensional drainage simulations that were in agreement with some experiments that they performed.

Hammond and Unsal (2012) used a PNM model to study the effects of surfactant upon the flowing regimes. Their dynamic simulator could reproduce the main flowing regimes including viscous fingering. Nevertheless, it failed to simulate the finger shapes observed in experimental studies. In fact, the simulated instabilities were very thin and straight and did not have a branched form. The biggest network that they could simulate was a 70*70 lattice.

Despite the fact that that most of the PNM studies described above were performed in small networks, they showed the potential to simulate viscous fingering phenomenon and to reproduce viscous instabilities with very similar shapes to those exhibited in laboratory studies. In this study we propose to build a new pore network model fast enough to simulate viscous fingering in slab experiments at the scale of tens centimetres. We will go on to use this to examine finger behaviour post-breakthrough and suggest how it could be used as a potential screening tool.

Chapter 3: Overview of pore network modelling

3.1. INTRODUCTION

Pore network modelling is now a well-established technique for the study of various pore scale phenomena that cannot be reproduced by conventional continuum-scale numerical simulators. The porous medium is modelled as a number of interconnected pore elements representing the void space in the rock. Some researchers consider the porous media as a number of large compartments or *pores* connected by a network of narrower channels or *throats*. Others use only one type of elements (*bonds)* to build their network models.

Having built the network, fluid flow within the pore space is modelled. Mainly two approaches are used; (i) the flow is modelled by considering some simplified rules and the filling sequence depends on the pore geometry. Such models are called quasi-static and are used to simulate the flow behaviour when the flow is capillary dominated, (ii) the flow is controlled by the calculated pressure gradients in the network. These models can reproduce the flow behaviour even when viscous forces are important and are named dynamic/ unsteady state models.

Since the ground-breaking work of Fatt (1956), pore network modelling has proved to be a very promising tool. Fatt built a two dimensional regular network of cylindrical tubes, ranked the pores using their capillary entry pressure, and filled them sequentially. Subsequently, he computed the flow properties using an equivalent physical network of electrical resistors. The drainage capillary pressure and relative permeability curves computed with this very simple model were in agreement with laboratory studies.

Pore network models have subsequently been used to simulate a variety of different phenomena, such as depletion (Bondino et al., 2009), ganglia dynamics (Dias and Payatakes, 1986b), three phase flow (Al-Dhahli et al., 2012), viscous fingering (Lenormand et al., 1988) and to investigate how different fluid and rock parameters affect flow dynamics and relative permeability curves (Blunt and King, 1990, Singh and Mohanty, 2003, McDougall and Sorbie, 1993).

In recent years, rock imaging techniques have emerged as a very useful tool making possible a more precise description of porous media. This development has been greatly beneficial for pore network modelling and several researchers have been able to extract networks from images that can be used by pore network simulators. These techniques will be reviewed in the next section.

3.2. PORE SPACE DESCRIPTION

In porous media, the void spaces can be described in terms of a system of large compartments called pore bodies connected via bottlenecks named pore throats. The void spaces are very irregular in shape and size and so reproducing the exact geometry and topology is very challenging. Two different approaches have been used by researchers to model interstitial spaces ─ some have developed simple algorithms to generate simplified lattices to use in their simulations: others have been taking advantage of the advances made in imaging techniques and extracted pore networks from pore space images.

3.2.1. Statistically generated networks

This method is based on generating pore networks from statistical distributions and these networks can be composed of either large pore bodies connected by tiny pore throats or can be made of bonds only. First, a regular lattice is built and is generally described by two parameters: its coordination number (the average number of elements meeting at a common point) and a pore size distribution. This lattice can then be distorted (Figure 3.1). Finally, radii are assigned randomly to each pore element according to a statistical distribution.

Jerauld et al (1984) built networks using a Voronoi technique. Initially, the coordination number was very high and this was later reduced by removing the longest throats until an average coordination number of six was obtained. However, the relative permeability curves were similar to the ones predicted by regular grids.

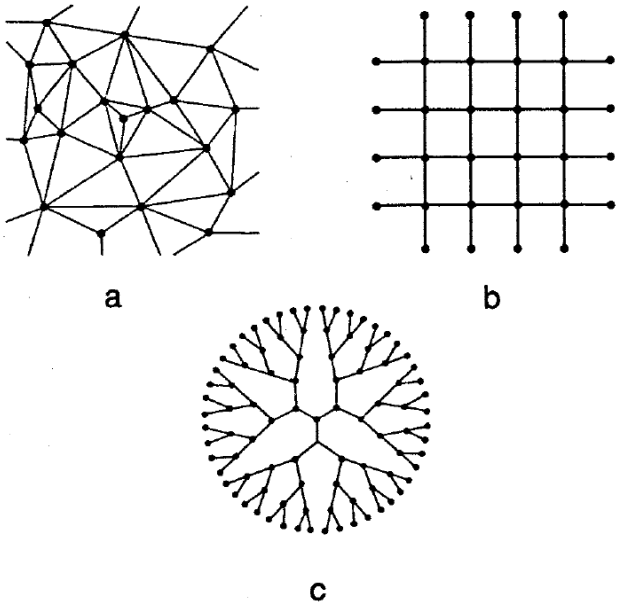

Figure 3.1: Examples of different types of networks used to represent the pore space (a) an irregular network generated from Voronoi Diagram (b) regular network (c) Bethe network (Helba et al., 1992)

Although they used a simple cubic lattice with circular tubes, Jerauld and Salter (1990) could still reproduce some features of relative permeability curves observed experimentally.

Using a similar approach, Lin and Slattery (1982) had a reasonable success in matching the capillary pressure and relative permeability data of Leverett (1939). Helba et al. (1992) used a Bethe lattice in their simulator (Figure 3.1) and predicted relative permeability sets that were a good fit to Talash (1976) experimental data.

An equivalent network of a given real porous media can be obtained by adjusting the network coordination number by randomly removing pores to match the coordination number of a specific sample. Early networks of unconsolidated sandstones were tuned

this way to permit a more realistic determination of two-phase flow properties. Dixit et al (1997) found, using regular cubic lattice networks, that reducing the coordination number from 6 to 4 had a stronger influence on hysteretic relative permeability curves than varying the pore size distribution or the pore-scale displacement mechanisms (snap-off and piston-type).

Fischer and Celia (1999) tuned a regular cubic lattice to match capillary pressure – saturation data for repacked and undisturbed soils. They then used the tuned network to predict absolute and relative permeabilities. For the repacked porous media, the predicted water relative permeabilities varied from good to fair when compared with experimental data. For the undisturbed soil samples, however, the predictions were poor.

These studies showed that these simple pore network models can have a predictive potential and McDougall et al. (2002) attempted to increase the predictive capabilities of these models. In order to achieve this, they used experimental mercury injection data as lithological "anchors". The method consists of building a network of pore elements – no explicit distinction is made between pore throats and bodies ─ with each element assigned a radius, a volume and a conductance. The volume and conductance are considered to be proportional to the radius raised to some power, as follows:

$$\boldsymbol{P_c \propto \frac{1}{r}} \qquad (3.\ 1)$$

$$\boldsymbol{V(r) \propto r^{\upsilon}}$$

$$\boldsymbol{g(r) \propto r^{\lambda}}$$

where, V is the pore volume, g is the pore conductance, P_c is the capillary entry pressure, ν the volume exponent and λ the conductance exponent. The geometric parameters of the resulting networks can be tuned to match available experimental data such as mercury intrusion capillary pressure data. The exponents are found by matching a curve called the R-plot, obtained by inverting experimental mercury injection data

using the Young-Laplace equation. McDougall et al. (2002) could successfully reproduce oil/gas relative permeability sets using this methodology which was named the "3Rs" approach.

Despite the evident utility of statistically generated networks for gaining fundamental insight into pore-scale displacement mechanisms, their description of the topology of the pore space still leaves out a lot of what is known about geological porous media – such as the irregularity of pore space geometry, the random distribution of coordination number and the existence of short range pore size correlations, that introduces a high level of uncertainty into the quantitative predictive results that can be obtained with lattice models. Whilst the construction of more geologically realistic networks that incorporates the right amount of detail in a computationally efficient way is a nontrivial task, several authors have extracted networks from directly or stochastically reconstructed pore spaces (Al-Kharusi and Blunt, 2007; Silin et al, 2006, 2003; Valvatne and Blunt, 2004; Gladkikh and Bryant, 2003; Blunt et al, 2002; Øren et al, 1998). More details of this approach are presented next.

3.2.2. Networks based on pore space imaging

Instead of generating an idealised pore network from average statistics to represent the void space in a rock, some researchers have used extracted networks obtained directly from 3D images of the porous medium. This can be obtained either by X-ray computed microtomography (named also micro-CT) or by means of numerical 3D reconstructions obtained from 2D thin section images.

(a) Micro-CT images

X-ray microtomography is a technique that uses x-rays to create cross-sections of a physical object that can be used to reconstruct a virtual 3D model without destroying the original sample. The pixel sizes of the cross-sections are in the micrometre range hence the usage of the prefix micro. This technique has been used by several researchers over recent years (Coenen et al., 2004, Dunsmuir et al., 1991, Arns et al., 2004, Arns et al., 2005). The main disadvantage of micro-CT is that there should be a compromise

between the resolution and the size of the sample and it is not possible to image large samples with high resolution. This can be problematic, especially if a high resolution is needed to image carbonates for instance. In this case, two dimensional thin sections are obtained from a scanning electronic microscope (SEM), and the 2D images are used to reconstruct the 3D pore space.

(b) Digital rock reconstruction

Several algorithms exist to reconstruct a digital rock from 2D thin sections. Some of these methods are now presented.

Process-Based Algorithm

Process-based reconstruction methods account for the fact that the pore structure is the result of physical processes. Consequently, these algorithms model different rock formation processes such as sedimentation, compaction and diagenesis. Bryant et al. (1993a), (Bryant et al., 1993b, Bryant and Raikes, 1995, Bryant and Blunt, 1992) were the first to propose such methods and they used them to model a sandstone rock forming process by considering a random close packing of equal spheres. They considered compaction and diagenesis but not sedimentation. This methodology was extended later by considering sedimentation and using packing spheres of different sizes (Bakke and Øren, 1997, Øren et al., 1998, Øren and Bakke, 2002, Øren and Bakke, 2003). These algorithms produced good results ─ the reconstructed rocks had good connectivity and researchers were able to reproduce multi-phase transport properties with these digital rocks (Øren et al., 1998, Patzek and Silin, 2001, Øren and Bakke, 2003, Valvatne and Blunt, 2004, Piri and Blunt, 2005). However, the method made use of many tuning parameters and these algorithms fail when diagenetic processes are very complex. This can be the case in carbonates, where the post-depositional diagenesis often completely dominates the matrix structure (Lucia, 1999). In such situations, statistical methods can be a good alternative.

Statistical Methods

Digital 3D rocks can be reconstructed from 2D thin sections using statistical methods. This approach consists of building the 3D rock by matching single and two point statistics obtained from 2D images (Quiblier, 1984, Adler et al., 1990, Adler et al., 1992, Roberts, 1997). However, the use of two point statistics was found to be insufficient to reproduce the long-range connectivity of the original pore space and tends to underestimate the rock connectivity (Okabe and Blunt, 2004). To surmount this issue, Okabe and Blunt (2004) developed an alternative multi-point statistical method and showed that it preserved the long range connectivity of the structure. They validated their method using a sandstone rock and then applied it to a carbonate sample. They overestimated the permeability by a factor of three but mentioned that the result was good considering the size difference between the reconstructed images and the experimental sample.

However, multi-point methods can be computationally expensive and, as a consequence, Wu et al. (2006) developed a more efficient stochastic pore space reconstruction approach that uses thin section images as its main input. They used a third-order Markov mesh and introduced a new algorithm that creates the reconstruction in a single scan. They showed that their method could be applied to a range of rocks and the calculated permeabilities of their reconstructed media were very close to the experimental values. Jiang et al. (2013) used a similar approach to reconstruct a heterogeneous carbonate sample containing both macro and micro porosity.

(c) Network extraction

In contrast to some digital rock physics methods, pore network models do not involve direct flow simulation in a 3D CT image or a reconstructed digital rock. Instead, it needs a pore network that is extracted from 3D reconstructions. Various algorithms for network extraction exist to extract the *skeleton* of the 3D model that carries the essential geometric and topological information of the underlying pore system. Some of these algorithms are presented next.

Medial Axis Based Algorithm

This method was pioneered by Lindquist et al. (1996) and Lindquist and Venkatarangan (1999). The medial axis of an object is the set of all points having more than one closest point on the object boundary, for instance, the medial axis of a sphere is its centre and of a cylinder is the axis of rotation.

The first step of these algorithms consists of calculating the medial axes of the void space ─ this gives knowledge about the void space topology and geometry ─ and is obtained by "*burning"* the void space starting from the rock surface. At some point, the fire is said to directionally extinguish if two components of the flame, traveling in opposite directions arrive at the same time. The intersection represents one point of the medial axis. Then, pore bodies and pore throats are identified by pore space partitioning. This algorithm is very good at preserving topological information, although some issues appear with the pore bodies partitioning. Hence, some cleaning procedures have been developed to overcome these problems (Sheppard et al., 2005, Sheppard et al., 2006), whereby spurious pore throats are removed and connected individual pore bodies are merged to reduce the high local coordination number.

Later, Jiang et al. (2007) improved the efficiency of the method and enhanced the pore body identification procedure.

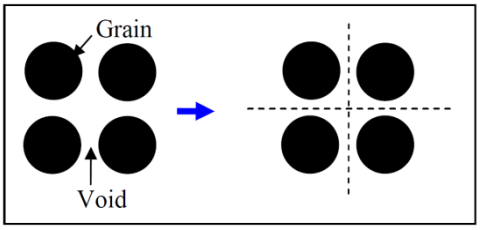

Figure 3.2: The concept of medial axis in a schematized two-dimensional binary system, the dashed lines represents the medial axis

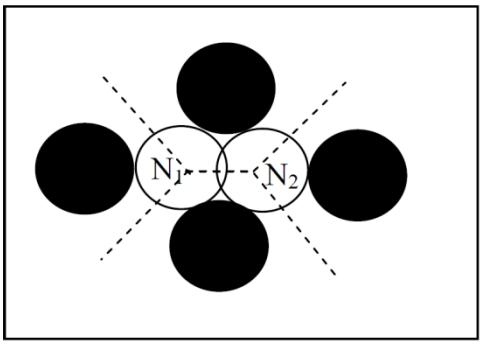

Figure 3.3: Schematic of the overlap of inscribed radius, nodes represent point of intersection of three or more medial axis branches (from Al-Raoush et al, 2003)

Maximum Ball Based Algorithm

This method consists of going through each void voxel and defining the maximum ball that can fit in the surrounding void space (Silin et al., 2003, Silin and Patzek, 2006) . The pore bodies are identified as the largest maximum balls and the throats as the smallest balls located between them (Figure 3.4). This method has been enhanced recently and several researchers have improved the way in which pore throats and bodies are identified (Al-Kharusi and Blunt, 2007, Dong et al., 2007, Dong and Blunt, 2009).

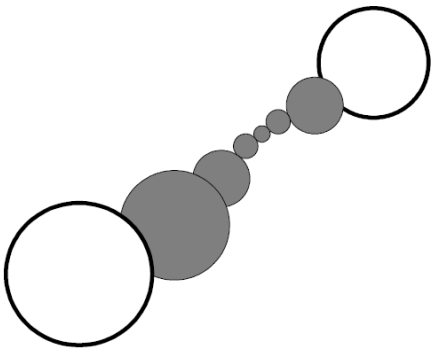

Figure 3.4: Simple pore- throat identification using the maximal ball algorithm. The shaded spheres represent a pore throats whereas the white spheres represent the pore bodies (Al-Kharusi and Blunt, 2007).

Voronoi tessellation

A Voronoi tessellation of a set of points in three dimensions divides a space into polyhedra that enclose the volume nearer to a given point than any other. The Delaunay dual of this network divides the space into tetrahedra. The edges of each tetrahedron connect four nearest-neighbour points.

This has often been used to extract networks from pore space constructed by the process-based algorithm (Gladkikh and Bryant, 2003; Mason and Mellor, 1995; Bryant et al, 1992, 1993), the coordinates of all the grain centres are known and this information is used to extract the pore space skeleton using Delaunay triangulation algorithms. Pore bodies and throats are defined by the voids formed between the surfaces of four nearest spheres. Prior knowledge of sphere coordinates permits easy calculation of pore and throat geometric properties such as areas and volumes.

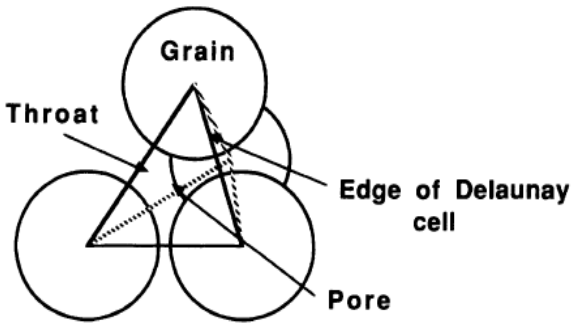

Figure 3.5: Delaunay cell in a random close packing of spheres. A void space or pore is situated in the centre of the tetrahedral cell and crossing each face are four narrower restrictions called throats (Bryant and Blunt, 1992).

3.3. MODELLING FLOW IN PORE NETWORKS

The main application of pore network models is the simulation of multiphase flow phenomena and the calculation of macroscopic flow properties. These can be used in qualitative studies to understand the effect of pore scale mechanisms on the macroscopic flow features. Furthermore, some researchers claim that they can provide quantitative predictions of relative permeability and capillary desaturation curves using pore network models (Valvatne and Blunt (2004) and Ryazanov et al. (2010)). However, once the network has been extracted or built, it is important to define the appropriate flow rules governing the multiphase displacements of interest.

Two phase immiscible flow in porous media is governed by a complex interaction between capillary, viscous and gravity forces. As the flow rate decreases, the displacement tends to become dominated by capillary forces and this means that, during drainage, the pores having the lowest capillary entry pressure will be filled first. Conversely, during imbibition, the pores having the highest capillary entry pressure will be invaded initially. In this case, simple flow rules can be defined instead of computing local flow rates and pressure gradients (which can be complicated and computationally expensive). These simplified models are named quasi-static and can be only used when viscous and gravity forces are small ─ otherwise, a dynamic model is needed. In this chapter we will focus on quasi-static models and dynamic models will be reviewed in Chapter 4. We begin with same theoretical background.

3.1. Theoretical background

a. Surface and interfacial tension

Within the bulk of a liquid, the molecules attract each other, keeping the fluid as a single cohesive mass. However, at an interface between two different fluids, the attractive forces are different within each liquid and the net effect is that the system behaves as if the surface separating the fluids is covered with a stretched elastic membrane. This phenomenon can be characterised by a net tensile force, which can be defined as the work required to increase the area of a surface isothermally by a unit

amount; commonly used units are dynes/cm or N/m. This force is named *surface tension* if a liquid/air system is considered and *interfacial tension* in a liquid/liquid system.

The interfacial tension of a two liquid system is one of the most important parameters governing multiphase flow in porous media and generally lies between the surface tensions of the individual components: for crude-oil/water systems, typical values are in the range 10-30mN/m (Donaldson et al, 1969).

b. Wettability

If a solid surface is contacted by a pair of fluids, one of them will tend to have a greater affinity for that surface than the other. This phase is identified as the wetting phase, whilst the other is known as the nonwetting phase.

When two fluids are in contact with a solid surface, the equilibrium configuration of the two fluid phases (say air and water) depends on the relative values of the surface tension between each pair of the three phases (Equation (3. 2)). Let us denote surface tension as ɣ, and solid, liquid and gas as s, l, and g respectively. Each surface tension acts upon its respective interface, and defines the angle θ at which the liquid contacts the surface. This is known as the wetting or contact angle of the liquid to the solid in the presence of the gas and can be used to quantify the wettability (Figure 3.7). Equilibrium considerations allow us to calculate the wetting angle from the surface tensions:

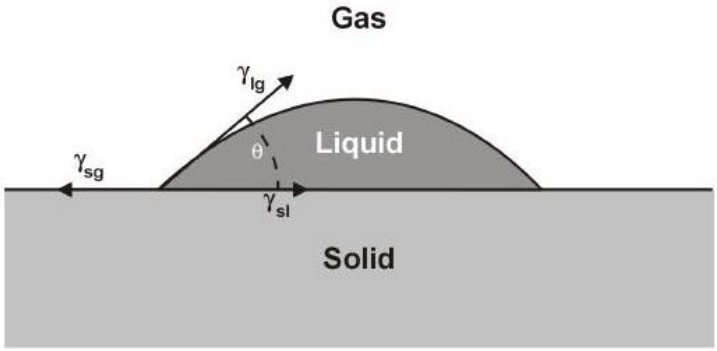

Figure 3.6: liquid solid gas wetting angle

$$\gamma_{lg} cos\theta = \gamma_{sg} - \gamma_{sl} \quad (3.\ 2)$$

For a water oil system we have the following possible scenarios:

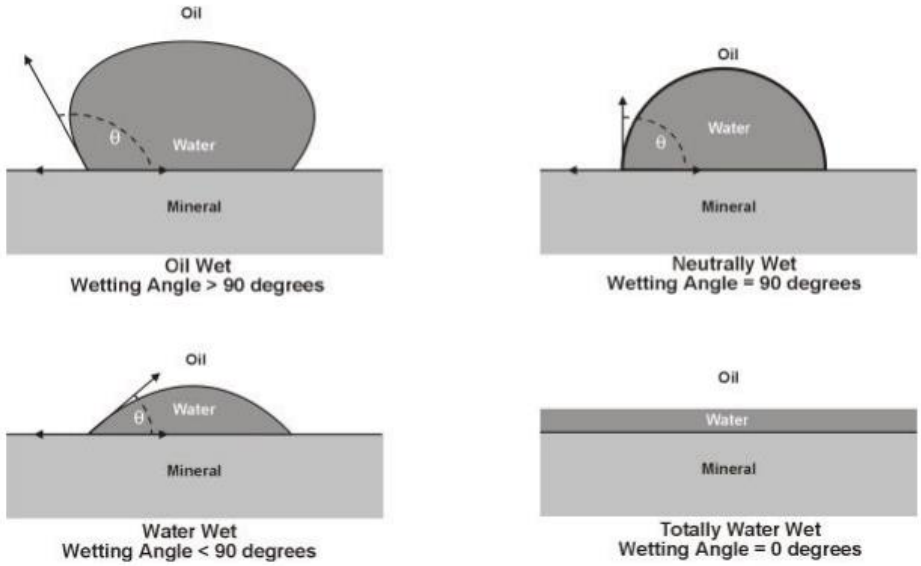

Figure 3.7: possible scenarios for a water oil system

In two phase displacements, if the non-wetting phase is displacing the wetting phase, the process is named drainage. In the opposite situation, it is called imbibition.

c. Capillary pressure

If we consider a rubber balloon that has been inflated to a certain pressure ($\boldsymbol{P_i}$) in an environment at atmospheric pressure equal to ($\boldsymbol{P_o}$), then, at equilibrium, the elastic force acting around the circular perimeter of the balloon should counterbalance the difference in pressure. Similarly, if we consider a spherical gas bubble placed in oil (

Figure 3.8) the interfacial tension σ should compensate the difference in pressures between gas and oil and it is possible to write:

$$\left(P_{gas} - P_{oil}\right) = \frac{2\sigma}{R} \tag{3. 3}$$

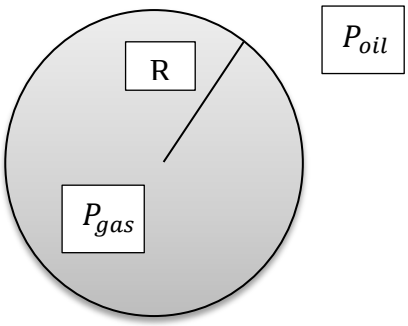

Figure 3.8: A spherical gas bubble placed in oil

where R is the principal radius of curvature of the spherical bubble.

More generally, an interface may have two different principal radii of curvature (a sausage shaped bubble for instance). In this case equation (3. 3) becomes:

$$\left(P_{gas} - P_{oil}\right) = \sigma\left(\frac{1}{R_1} + \frac{1}{R_2}\right) \tag{3. 4}$$

where R_1 and R_2 are the principal radii of curvature characterising the interface.

In a cylindrical tube of radius r and contact angle θ, equation (3. 4) can be simplified after using some trigonometry rules and is reduced to the Young-Laplace equation defined as follows:

$$\left(P_{gas} - P_{oil}\right) = \frac{2\sigma cose\ \theta}{r} \quad (3.5)$$

3.2 Quasi static models

Quasi-static models were made to simulate flows occurring at low rates, where, the viscous and gravity forces can be neglected and the flow is governed only by equilibrium capillary pressure. Thus, simply knowing the distribution of capillary entry pressures (which can be calculated from the geometry of the network) is sufficient to determine the invasion order. As a consequence, calculating the local flow rates and the pressure gradient (which is computationally intensive) can be avoided. In drainage, the capillary entry pressure acts as a resistance to flow, and so the larger pores (having a low capillary entry pressure) are filled first. This can be modelled by considering discrete capillary pressure steps, starting from a low initial value that will be increased sequentially. At each step, the pore elements having a capillary entry pressure lower than the current capillary pressure value and situated between the wetting and non-wetting phases (or at the inlet of the network) are filled. This approach was first introduced by Chandler et al (1982) and Wilkinson and Willemson (1983) and is similar to the displacement mechanism governing mercury porosimetry experiments.

In imbibition, the capillary entry pressure acts as a driving force and so the small pores having a high capillary entry pressure are filled first. This can be modelled by considering discrete capillary pressure steps and starting from a high initial value that is decreased in steps. At each step, pore elements having a capillary entry pressure higher than the current capillary pressure value are invaded.

Jerauld and Salter (1990) investigated the effect of pore structure hysteresis on two-phase relative permeability and capillary pressure curves. They found that the pore to throat aspect ratio was an important structural determinant of the hysteresis behaviour. They also found that the correlation between pore throat sizes affects the relative permeability curves.

Many other researchers have generated regular and non-regular networks and quasi-static models to predict absolute and relative permeability, investigate relative permeability hysteresis, wettability and heterogeneity effects (Koplik, 1982, Blunt, 1997, Dixit et al., 1998, Fenwick and Blunt, 1998, Fischer and Celia, 1999) and numerous other aspects of multiphase flow in porous media.

More realistic wettability scenarios were considered by McDougall and Sorbie (1995), who modelled fractionally wet and mixed-wet porous media using a steady state pore network model and they proposed a test that can be used to distinguish between them experimentally.

Starting with a network generated from a reconstructed Berea sandstone, Valvatne and Blunt (2004) successfully reproduced flow properties for water- and oil-wet datasets using quasi-static models. However, for mixed-wet datasets, although the calculated Amott water and oil indices reasonably matched the experimental values and same oil recovery trend were reproduced, quantitative match with experiment was poor. Maximum recovery was predicted to occur at lower initial water saturation, Swi, and the variation in recovery with Swi was predicted to be less than what was observed experimentally. Their results showed the difficulty associated with determining wettability variations at the pore scale.

Behbahani and Blunt (2004) adjusted the contact angles and oil-wet volume fraction parameters in a quasi-static model and matched experimental waterflood recovery and wettability index for Berea samples aged in crude oil for different times. The computed relative permeability and capillary pressure were then used in a conventional simulator to predict oil recovery from countercurrent imbibition in mixed-wet Berea. Their simulated results reproduced the experimental oil recovery trends of Zhou et al. (2000) but the quantitative agreement was poor. Their results again showed the difficulty in determining, wettability variation at the pore scale.

During imbibition, several displacement mechanisms may occur. Lenormand and Zarcone (1984) identified three main types of displacements: snap-off, piston like displacement and pore body filling (Figure 3.9). Snap off occurs when a wetting phase

is brought in contact with the rock: first, it imbibes via film flow along irregularities on the pore surfaces. As this imbibition process continues, the thin films begin to swell; eventually the thinnest pores will become completely filled with the wetting phase and the non-wetting phase will be displaced if an escape route exists.

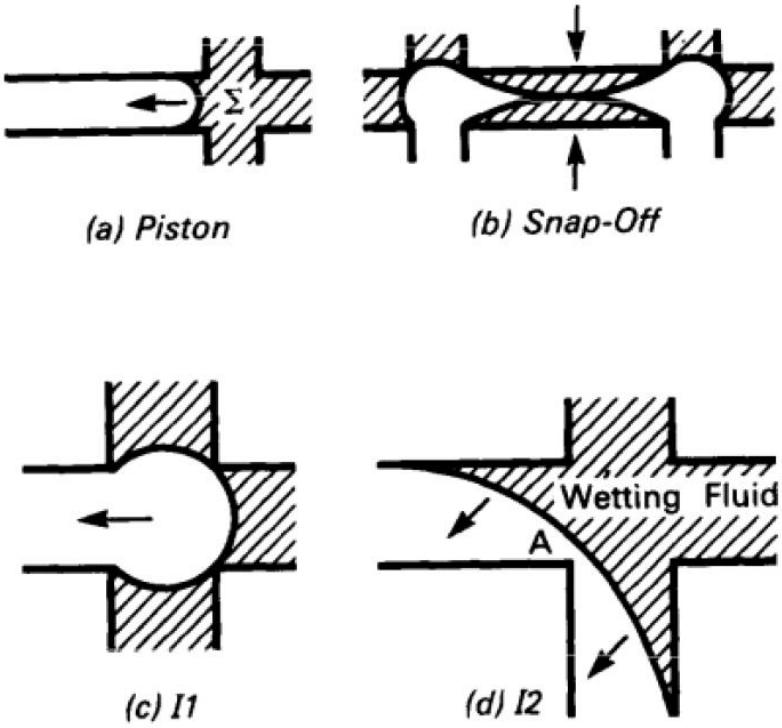

Figure 3.9: Snap-off (choke-off) displacement mechanism. The (water) wetting films are swelling to form a "collar" and then cause the non-wetting fluid (oil) to snap-off (Lenormand and Zarcone, 1984)

Valvatne and Blunt (2004) proposed a pore network model that takes into account film flow and snap-off and successfully reproduced flow properties for water-wet and oil-wet datasets using their quasi-static model.

Other researchers have extended quasi-static models to take into account 3 phase flow. Heiba et al, (1984) presented one of the first network models to simulate three-phase flow (oil, water, and gas). Using a regular lattice network, they showed that gas and water relative permeabilities were functions of their saturation only. However, oil

isoperms had curvatures which suggested that oil relative permeability is also a function of the saturation of other phases.

Piri and Blunt (2005) presented a quasi-static network capable of simulating three phase flow. Their model was able to reproduce two-phase and three-phase relative permeability for Berea sandstone as reported by Oak (1990).

van Dijke and Sorbie (2006) presented thermodynamic criteria of three-fluid configurations in angular pores of non-uniform wettability and Al-Dhahli et al. (2012) used these thermodynamic criteria to account for film/layer flow and layer collapse in a three-phase network model which they used to make predictions of three-phase relative permeability for a reconstructed carbonate rock of mixed-wettability.

These apparently successful quantitative relative permeability studies make some researchers think that pore network models can be a *"numerical laboratory"* and that they represent an alternative to experiments in the prediction of some rocks properties. However, Sorbie and Skauge (2011) and Bondino et al. (2012) have criticized this opinion. In fact, Sorbie and Skauge (2011) went through the "prediction" workflow used by researchers to estimate the petrophysical properties of a rock from images. They showed that, at each stage, several tuning parameters are involved and that there are more parameters than the data itself. Furthermore, they estimated that in the full workflow there are between 15 and 26 parameters fixed by the researchers making their predictions effectively meaningless (Table 3.1). They also concluded that it is not possible to predict relative permeability capillary pressure and residual oil saturation from a mixed-wet system, as choosing the wettability scenario is the most uncertain stage. They suspected that, even for strongly water-wet rocks, such predictions are not possible and cited the papers of Valvatne and Blunt (2004) and Ryazanov et al. (2010), who "predicted" the experimental oil/water relative permeability curves in strongly water-wet Berea sandstone measured by Oak (1990). They showed that the initial water saturation was not really predicted and that it depended upon the amount of clay assigned to Berea rock (i.e. one of the tuning parameters).

Stage	Parameter Count	Comment
Construction of digital rock	2 - 4	Probably least parameterised stage in workflow
Extraction of network	4 – 6	Several decisions must be made in this stage
Wetting assignment of the network	7 – 12	Most complex and least validated stage
Physics of the pore scale displacement	2 - 4	Quite well understood for simple pore geometries
	Min. no. parameters = 15 Max. no. parameters = 26	

Table 3.1: Estimated number of parameters required for each stage of 2 phase petrophysical "prediction" workflow (Sorbie and Skauge, 2011).

Bondino et al. (2012) investigated further the predictivity of pore network models. They divided a rock sample into 4 parts and they sent each to a different contractor to image and extract pore networks. A different extraction method was used by each contractor and each a pore network model was used to compute the relative permeability curves from each extracted network. Different wettability scenarios were considered: drainage, water-wet imbibition and oil-wet imbibition. Although only one rock sample was used, large variations in the relative permeabilities were observed when different extraction methods were used, as we can see in Figure 3.10. They concluded that quantitative multiphase flow prediction using pore network models is not possible unless substantial progress is made in wettability characterisation at the pore scale.

Sorbie and Skauge (2011) concluded their paper by stating that pore network models can still be used in a variety of useful ways that bring great understanding of multi-phase flow through porous media. In this thesis, we will present an example of how pore scale modelling can help to understand post-breakthrough viscous thickening phenomena that are observed experimentally during water injection into extra heavy oil. This modelling technique also provides insights into the underlying mechanisms involved in water injection into heavy oil.

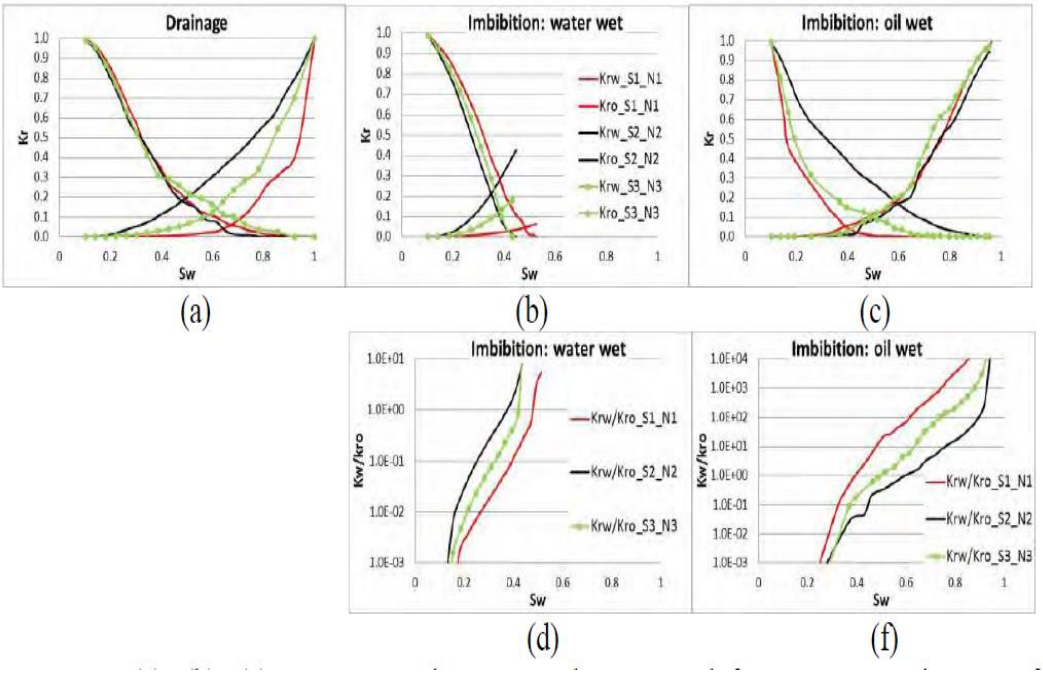

Figure 3.10: (a), (b), (c) Computed relative permeability on networks extracted from sandstone using different extraction methods, (d), (f) Ratios Krw/Kro for the waterflooding simulations (Bondino et al., 2012).

Chapter 4: :Dynamic pore network models

4.1. INTRODUCTION

In several situations, viscous and gravity forces cannot be neglected and the flow is governed by the interplay of capillary, viscous and gravity forces. Examples include: fracture flow, where flow rates might be very large, often of the order of hundreds of meters a day; displacements with very low interfacial tension that substantially reduce capillary forces, such as near-miscible gas injection, gas condensate reservoirs and surfactant flooding; near well-bore flow; flow involving polymers, gels and foams where very large pressure gradients are found; and some cases where wetting layer flow and formation is significant, such as spontaneous wetting into a dry soil.

In such cases, a quasi-static model is unsuitable to model the flow and a dynamic pore network model is needed. In this chapter, we describe dynamic pore network models, with a special focus on drainage simulators, and, we will present some main applications.

4.2. PORE NETWORK STRUCTURE

As discussed in the previous chapter, in pore network models, the void space in the porous medium can be described in terms of a system of large compartments or *pore bodies* connected by a network of narrower channels or *throats.* In reality, the menisci curvatures change from a pore throat to a pore body and may also vary as the fluid advances inside the pore body itself. The value of this curvature determines the capillary pressure inside each pore element, which is a major parameter affecting fluid displacement. Taking account of all of these changes is clearly complex and

computationally intensive. Therefore, researchers have used simplifying assumptions in dynamic simulators. Some have considered networks of volumeless throats and non-resistant bodies. Others modelled porous media using one equivalent element.

4.2.1. Models with pore bodies and pore throats

In most dynamic models, the pore throats are considered volumeless ─ they are filled instantly ─ and pore body resistance is neglected. The most common shapes used have been cylindrical throats and spherical sites (Koplik and Lasseter, 1985, Dias and Payatakes, 1986a, Dias and Payatakes, 1986b, Lenormand et al., 1988, Blunt and King, 1990, Nordhaug et al., 2003).

However, in a real rock, the wetting phase generally fills the corners of the pore space and this flow may have a significant effect on fluid distributions, especially for imbibition. Therefore, Singh and Mohanty (2003), Joekar-Niasar et al. (2010) and Mogensen and Stenby (1998) considered cubic pore bodies and pore throats with a square section. The advantage of such a geometry is that the angular cross sections explicitly allow for the existence of film flow. Mogensen and Stenby (1998) developed a dynamic model of imbibition that permits stepped interface advancement within a pore for both piston-like and snap-off displacements, whilst Singh and Mohanty (2003) built a network that accounts for wetting layers by a two-step pressure solution procedure – one for the wetting layers and the other for bulk flow. It appears that the only model where resistance and volume were assigned to both pore bodies and throats was that developed by Mogensen and Stenby (1998) for imbibition simulations.

4.2.2. Models with an equivalent pore element

The second way of modelling porous media is to use an equivalent pore element approach.

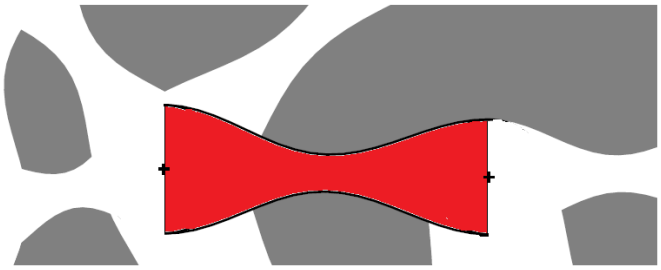

Figure 4.1: an example of a pore element with convergent divergent cross section

Dias and Payatakes (1986a) used a converging diverging geometry similar to that shown in Figure 4.1 where the cross section varies along the "*pore"* and the element represents a throat and some parts at adjacent pore bodies. Al-Gharbi and Blunt (2005) considered a similar shape but assumed that the cross section had a scalene triangular shape. As a consequence, their model could take into consideration the effects of wetting films of varying thickness – depending on the capillary pressure, by the use of equivalent hydraulic resistance to calculate pore pressures.

Aker et al. (1998a) built a bonds model with volumeless bodies but considered that the effective radii of the tubes varied as functions of the position of the meniscus. The capillary pressure is small at the edges of the pore element and is maximal when the meniscus is in the middle of the pore. This approach is very similar to that used by Dias and Payatakes (1986a) and Al-Gharbi and Blunt (2005).

Dahle and Celia (1999), Lovoll et al. (2005) , Lam and Horvath (2000) and McDougall and Sorbie (1993) have made extensive use of pore network models of bonds to simulate dynamic drainage and imbibition mechanisms and these have been used for various applications.

4.3. FLOW RULES AT NODES

One of the issues that researchers face is to decide which flow rules to set at network junctions. If we consider the situation of Figure 4.2, we can see that two different fluids are flowing towards a node.

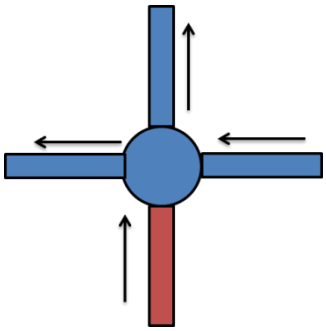

Figure 4.2: Example showing two different fluids flowing towards a node: oil (red) and water (blue)

Aker et al. (1998b) considered that both fluids will flow into the node and developed a mixing algorithm. They assumed that the simultaneous flow can be represented by a finite number of small bulbs of each liquid placed next to each other inside the tube. They used the procedure described in Figure 4.3. First, the oil meniscus is moved inside the other tubes by a distance δ – taken as 1-5% of the tube length. Then, due to the counter flow of water, the water meniscus is moved towards the node (arrangement c). The water is moved by a distance δ inside the adjacent bonds (arrangement d). The water meniscus is subsequently displaced inside the tubes and the oil meniscus is updated inside the neighbour pores. Finally, some ganglia are formed and multiple menisci exist in a tube. To simplify things, the multiple menisci are reduced to one meniscus as we can see in the arrangement d. These rules were developed for a drainage model. However, Aker et al. (1998b) mention that it can be applied to imbibition after some modifications.

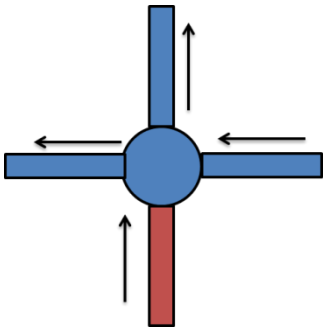

(a)

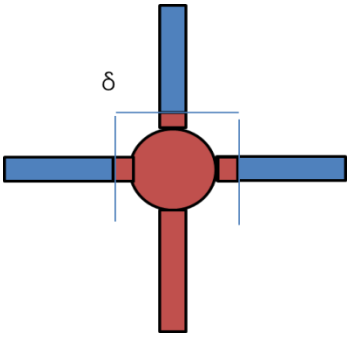

(b)

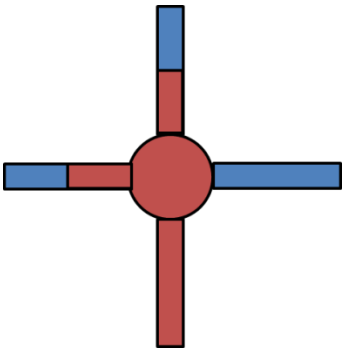

(c)

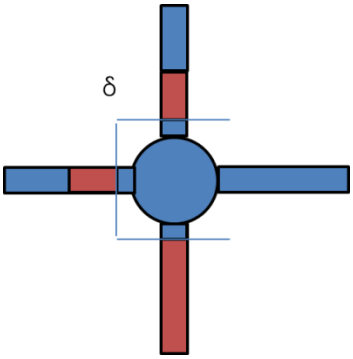

(d)

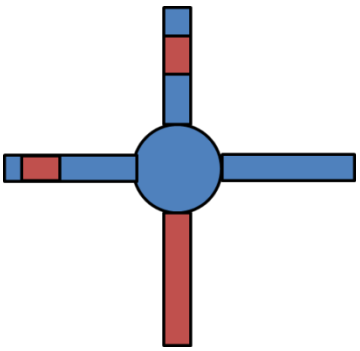

(e)

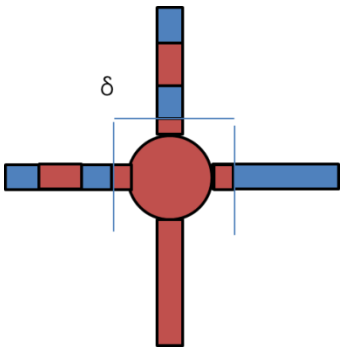

(f)

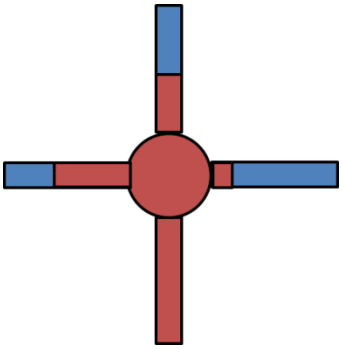

(g)

Figure 4.3: An example illustration the procedure used by Aker et al. (1998b) to mix the wetting and the non-wetting fluid at a node

Al-Gharbi and Blunt (2005) developed another algorithm to deal with the same situation. As mentioned in the previous section, they used variable-section pore elements with variable capillary pressure according to the meniscus position. This procedure is illustrated in Figure 4.4. First, the oil enters in all the throats regardless of the flow direction (arrangement b). It is distributed in each element so that there is the same capillary pressure at the interface in all the branches (arrangement c) – we should remember here that the capillary pressure in each pore depends on the position of the meniscus. To find the menisci position an iterative approach is used until there is consistency with the volumetrics and the capillary pressure is the same in all the connected pore elements.

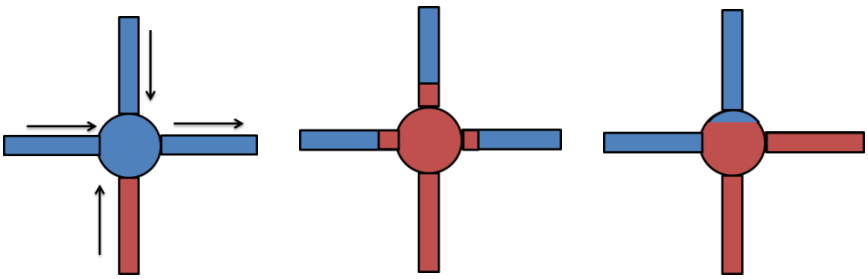

(a) (b) (c)

Figure 4.4: An example of invasion of a pore centre (Al-Gharbi and Blunt, 2005).

However, Aker et al. (1998b) have reported that their procedure can lead to numerical problems in some situations and that this results in the instability and divergence of the numerical solution. Furthermore, the Al-Gharbi and Blunt (2005) model was very slow and a simulation in a 9*9 network needed 55 hours to reach the breakthrough stage.

Other researchers have simplified the problem and simply ignored the counter flow in a node during drainage. They consider pores with counter current flow direction as being *closed* or *capillary blocked* (Lenormand et al., 1988, Blunt and King, 1990, Van Der Marck et al., 1997, Nordhaug et al., 2003, Gielen et al., 2005). This assumption makes sense for a drainage simulator ─ at a node the curvature of the meniscus increases leading to a decrease in the capillary pressure and, as a consequence, it is likely that the non-wetting fluid invades the pore body and that the wetting phase stops at the junction.

Lenormand et al. (1988) performed micromodel drainage experiments and tried to simulate some of them with a pore network simulator. They presented some simulations that reproduced the same flow regimes observed experimentally. This demonstrates that the assumption of closing the counter flow pores is reasonable in drainage simulators. We will discuss these experiments more in details in Chapter 6.

4.4. PRESSURE SOLUTION

In a dynamic pore network model, all the invasions are fully controlled by the pressure gradients across the network. Therefore, the way of solving the pressure has a major impact on the model speed and results. Since the first unsteady-state model (Koplik and Lasseter, 1985), the pressure has been solved using a mass conservation equation, where it is assumed that the mass of fluids entering to a node is equal to the mass of the fluids leaving each node. Therefore, the following equation can be written for immiscible fluids at every node i:

$$\sum_{i,j} Q_{ij} = 0 \tag{4.1}$$

where Q_{ij} is the local rate from node i to an adjacent node j.

This rate can be calculated from the nodal pressures and the pore conductances. For single phase flow:

$$Q_{ij} = G_{ij}(P_i - P_j) \tag{4.2}$$

where P_i is the pressure at node i, P_j is the pressure at node j and G_{ij} is the conductance of the bond linking nodes i and j in bond models and generally the equivalent conductance of the throat and a part of the adjacent pore bodies in models taking into account pore bodies.

In two phase flow, the flow within a pore containing an interface separating wetting and nonwetting phases must account for the capillary pressure drop across that interface, and so for these pores we have:

$$Q_{ij} = G_{ij}\left(P_i - P_j + P_c\right) \tag{4.3}$$

where the capillary entry pressure is defined using Young-Laplace law as for cylindrical tubes:

$$P_c = \frac{2\sigma cos\theta}{R} \tag{4.4}$$

Here σ is the interfacial tension, θ is the contact angle ($\theta = 180°$ for a strongly oil wet system) and R is the radius of the pore throat. It should be noted that the capillary pressure is negative for an oil wet system.

After writing the conservation equation at each node, the pressure solution problem can be written in matrix form (more details of the problem formulation can be found in the next chapter of this thesis):

$$G * p = q_b + C_s q_c \tag{4.5}$$

where G is the coefficient matrix of pore conductances, p is the column vector of non-dimensional nodal pressures, q_b is the column vector of boundary conditions, q_c is the capillary effects column vector and C_s is the capillary scale and is calculated as a function of the differential pressure.

In models that allow counter-current flow (Aker et al., 1998b, Al-Gharbi and Blunt, 2005), solving this problem is very straightforward for constant pressure simulations and computing the nodal pressures is equivalent to solving a simple linear problem. However, some difficulties can arise in constant flow simulations (more relevant for SCAL experiments) and these will be discussed in the next section.

If counter-flow invasions are not allowed, even constant pressure simulations become more involved. Here, pores with counter-current flows are closed ─however, these are not known before solving the pressure field and, to make things more complicated, the pressure solution itself is affected by the closed pores.

To overcome this difficulty, Lenormand et al. (1988) used a relaxation technique ─ at each time step, the network was swept several times and the nodal pressures were updated through the mass conservation equation.

Blunt and King (1990) simplified the problem and used an implicit-pressure explicit-saturation methodology. The counter flow pores were closed in the subsequent time step of the pressure solution. This method results in a faster code and 80000 node simulations became possible. This method was used later by other researchers (Gielen et al., 2005, Nordhaug et al., 2003, Singh and Mohanty, 2003). However, Singh and Mohanty (2003) have reported that the implicit-pressure explicit-saturation methodology creates numerical problems and that the model fails to simulate flow in an invasion percolation like regime. Therefore, they used a pseudo-invasion percolation method for low rates: at each time step, the throat with the highest *"potential"* is opened and the pressure is computed again to calculate the local rates. They considered a threshold capillary number equal to 10^{-6} and used their pseudo-invasion percolation algorithm for lower capillary numbers. However, this can be criticised, as the transition between different regimes happens at different rates for different viscosity ratios (as has been shown by Lenormand et al. (1988)). For extra heavy oil simulations, the effects of viscous forces may be important even at low capillary numbers.

Although it was not mentioned explicitly, it appears that the capillary pressure was ignored in the pressure equations in the Blunt and King (1990) model. Several other researchers have built models similar to the Blunt and King (1990) model and have not coupled the capillary pressure with the pressure solution (Gielen et al., 2005, Nordhaug et al., 2003).

The formulation of pressure equations from flow formulas that include capillary pressure could lead to nonlinear flow problems that will be discussed in Chapter 5. Therefore, McDougall and Sorbie (1993) simplified the problem and did not consider the capillary pressure in the formulation of the pressure equations which were derived using pseudo-single phase approach ─ calculating the average viscosity in each element and solving the pressure with the methodology used for single phase flow. Their model was then used for unsteady-state two-phase displacements during waterflooding for a

range of viscosity ratios, flow rates and levels of pore-scale heterogeneity. The impact of viscosity ratio and flow rate (or capillary number) largely followed a similar trend as reported by Lenormand et al (1988) ─ capillary fingering at low rates, stable displacement at high rates and favourable viscosity ratio and viscous fingering at high rates and adverse viscosity ratios.

Joekar-Niasar and Hassanizadeh (2011a) and Thompson (2002) used a completely different approach. They solved the pressure in each fluid separately and so, if two fluids are present at the same time in a pore body, each one has a different pressure. They stated that this is easier to implement than the classical approach and that it offers the possibility of including mechanisms related to the variations in local capillary pressure, such as snap-off and counter current flow. Thompson (2002) could not provide good agreement between the results of dynamic flow simulations at low rates and quasi-static simulators. However, this issue was fixed by Joekar-Niasar and Hassanizadeh (2011a), who added some numerical improvements to the pressure solver.

4.5. COUPLING DIFFERENTIAL PRESSURE AND INJECTION RATE

Considering capillary pressure in the pressure equations introduces some complexity into dynamic simulations, especially if counter-current flow invasions are ignored. The capillary pressure introduces a non-linearity between the differential pressure value and the injection rate. Several authors have used different approaches to deal with this.

Dias and Payatakes (1986a) added a segment of pores close to the outlet acting as a large resistor in series in order to damp the changes of flow rate, whilst Vizika et al. (1994) considered pore throats with very low resistivity at the outlet boundary to regulate the flow rate and damp the pressure fluctuations.

Al-Gharbi and Blunt (2005) assumed that the inlet pressure did not change significantly between time steps and used a simple approximate correction to the inlet pressure to match the fixed injection rate. Whilst it is true that their assumption is valid for viscous dominated flow, in capillary dominated regimes the differential pressure fluctuates

considerably and assuming that the pressure drop is almost constant becomes unphysical. In fact, the simulations performed by Aker et al. (1998b) showed that in capillary dominated regimes the simulated differential pressure fluctuated a great deal from one step to another. This may be one of the reasons why the Al-Gharbi and Blunt (2005) model could not reproduce saturation maps similar to those predicted by quasi-static models.

Lenormand et al. (1988) used a relaxation process to find the inlet pressure corresponding to a fixed rate. However, they did not give more details about their methodology.

Aker et al. (1998a, 1998b) developed a different approach to solve the pressure field and calculate the differential pressure at the same time. They considered that the total rate (Q) can be written in terms of the pressure drop and capillary pressure as follows:

$$Q = A\Delta P + B \tag{4.6}$$

where ΔP is the pressure drop across the system and A and B are parameters depending on the geometry of the network and fluid configuration. They are calculated for each fluid configuration by solving the nodal pressures for two different pressure drops:

$$Q' = A\Delta P' + B \tag{4.7}$$

$$Q'' = A\Delta P'' + B \tag{4.8}$$

This allows the calculation of A and B and, as a consequence, allows the differential pressure to be determined for the target rate for a particular fluid configuration.

4.6. APPLICATION OF DYNAMIC PORE NETWORK MODELS

One of the major application of unsteady-state pore network models has been the simulation of viscous fingering which is impossible to simulate with classical reservoir simulators (Riaz et al., 2007). The literature review of these applications was in Chapter 2 and so we will not mention these studies in this section.

4.6.1. Blob formation and residual saturation

Unsteady-state pore networks have also been used to study the effects of viscosity ratio and capillary number on residual oil saturation. Koplik and Lasseter (1985) performed dynamic simulations using fluids with matched viscosity and observed that, at high capillary numbers, trapped blobs could be mobilised and became smaller and their number increased. At low rates, the blobs were larger and their number lower. Similar studies have shown that, during imbibition, an increase of capillary number and/or viscosity ratio leads to an increase in residual saturation and reduced trapping occurs (Dias and Payatakes, 1986a, Vizika et al., 1994, Blunt and Scher, 1995, Mogensen and Stenby, 1998, Hughes and Blunt, 2000, DiCarlo, 2006, Nguyen et al., 2006). This has been attributed to the suppression of snap-off at high flow rates.

Singh and Mohanty (2003) developed a dynamic drainage pore network model taking into account film/corner flow by a two-step pressure solution procedure – one for the wetting layers and the other for bulk flow. They used it to study the effects of capillary number and viscosity ratio on the residual wetting phase saturation. They observed that the lowest wetting residual was obtained in stable displacements and that the highest residual was obtained for the viscous fingering case.

Al-Gharbi and Blunt (2005) developed a drainage model that accounted for the effects of wetting films of varying thickness, depending on the capillary pressure, by the use of equivalent hydraulic resistance to calculate pore pressures. Their results showed that at low capillary numbers, oil tends to flow through the pores with the lowest capillary entry pressure. When the rate increases, pores with lower entry condition become accessible. They also observed that more oil ganglia are formed by snap-off as the

capillary number increases although their contribution to the flow is insignificant except at very large capillary numbers.

4.6.2. Differential pressure

Van Der Marck et al. (1997) studied the variations of differential pressure during a drainage experiment in a micromodel. They compared the experimental pressure drop against simulations performed with a pore network model. They used fluid combinations with favourable viscosity ratios equal to 1 and $^{1}/_{12}$ and for both cases, they observed an increase in the pressure drop as the non-wetting fluid advanced in the network. After breakthrough, the pressure dropped significantly and the agreement between the simulated and observed pressure curves became poorer as the viscosity ratio became smaller.

Aker et al. (1998a) performed drainage simulations with both favourable and adverse viscosity ratios for different capillary numbers and different network sizes. In the unfavourable viscosity ratio case, they observed capillary fingering and viscous fingering regimes, although the largest network that they could simulate was composed of 60*80 nodes. They saw a decrease in the pressure drop as the non-wetting fluids progressed towards the outlet and noticed some pressure fluctuations mainly in the capillary dominated regime. In the favourable viscosity ratio case, the differential pressure built up as the invading fluid advanced towards the outflow boundary. Aker et al. (1998a) also calculated two quantities characterizing the capillary pressure ─ the first is the average front capillary pressure associated with the front menisci and calculated as a simple arithmetic average of the capillary pressures in the pores situated at the invasion front; the second is named the global capillary pressure, which is the capillary pressure associated with all the menisci in the network – equal to $\frac{B}{A}$ in their differential pressure drop equation (section 4.5). They found that, at low rates, the fluid pressure differences are equal to the global capillary pressure and that the front Pc is equal to the global Pc. They observed that this is no longer true at high rates but, did not propose a formulation relating the nonequilibirum effects to the dynamic conditions of the system. This will be discussed in details in the following section.

4.6.3. Nonequilibrium effect on capillary pressure

Capillary pressure is commonly defined as the difference between the wetting and non-wetting fluids pressures at equilibrium and this can be expressed by the following simple equation:

$$P^n - P^w = P_c(S_w) \tag{4.9}$$

However, equation (4.9) is only valid at equilibrium (Hassanizadeh et al., 2002). Furthermore, Lewalle et al. (1994) revealed that nonequilibrium effects are more significant whenever the pressure gradients and fluid velocities are large. Several researchers have suggested the following equation to calculate the difference in pressure between the wetting and non-wetting phases (Hassanizadeh and Gray, 1990, Kalaydjian, 1987):

$$P^n - P^w = P_c(S_w) - \tau \frac{\partial S_w}{\partial t} \tag{4.10}$$

where τ is a material property that may depend on the saturation.

Dahle et al. (2005) built a dynamic drainage pore network model to investigate the effects of pore size distribution and saturation on τ and concluded that a decrease of the wetting fluid saturation or an increase of the variance of the pore radii increases τ. Gielen et al. (2005) used a dynamic pore network model to perform drainage simulations for viscosity ratios equal to 0.1 and 1 and also found that a drop in the wetting phase saturation increased τ. However, their model was relatively simple with circular cross sections and did not take into account other physical processes, such as snap-off and local counter current flow. Moreover, their simulations were performed for a stable displacement.

Joekar-Niasar et al. (2010) and Joekar-Niasar and Hassanizadeh (2011a) studied nonequilibrium capillarity using a more sophisticated model. Their pore network simulator had angular cross sections and was able to model more complex phenomena like snap-off and local counter flow invasions. Furthermore, it could be used for both drainage and imbibition. They found τ values ranging from 100 to 1000 Pa.s for M=1 and mentioned that these values were in agreement with previous modelling studies. However, they considered 35*35*35 networks corresponding to 1.9*1.9*1.9mm^3 rock which is very small. Dahle et al. (2005) and Manthey et al. (2005) have shown that the magnitude of τ increases with an increase in the length of the network .

4.6.4. Interfacial velocity

Another application of dynamic models relates to average interfacial velocity (Nordhaug et al., 2003, Joekar-Niasar et al., 2010, Joekar-Niasar and Hassanizadeh, 2011b). Nordhaug et al. (2003) studied interface movements using a pore network model similar to that of Blunt and King (1990), who had assumed that the throats were filled instantaneously and did not track intrapore menisci. They performed constant pressure drop simulations in a three dimensional network with circular cylindrical elements and computed the interfacial velocity for stable and unstable displacements. The meniscus velocity was calculated in pore bodies based on invasion time and changes in local saturation and the direction of the velocity was found by averaging the directions of total inflow and outflow in the pore body. The velocity from the pore body was then upscaled to the lattice scale by averaging the local velocities weighted by local interfacial area. Nordhaug et al. (2003) compared their results with a simplified equation derived from a thermodynamic theory (Hassanizadeh and Gray, 1990), Hassanizadeh and Gray (1993) and found better agreement between theory and simulations for a stable displacement (M=0.1) compared to an unstable case (M=10). Finally, they observed that, for constant pressure drop drainage simulations, the interface velocity decreased with decreasing wetting fluid saturation (with a major drop occurring in the saturation range 0.8 to 1).

Joekar-Niasar et al. (2010) studied interfacial velocity dynamics and performed drainage simulations with five different differential pressure values and three different

viscosity ratios (M=0.1,1,10). They showed that, as the number of invading fingers decreases, the area associated with the fluid-fluid interface also decreases.

4.6.5. Relative permeability

Although steady-state models have proved to be very popular in generating relative permeability curves, they fail to simulate the effects of some system parameters ─ such as capillary number and viscosity ratio ─ on the relative permeability data sets. Therefore, several authors have attempted to use dynamic models to investigate these effects in more detail and to help explain related experiments (Wang et al., 2006, Odeh, 1959, Henderson et al., 1996).

Blunt and King (1990,1991) used a drainage pore network model to generate relative permeability sets for a range of rates and viscosity ratios. They used Darcy's law to calculate the relative permeability sets at different stages of the simulation and found the relative permeability to be sensitive to the capillary number and viscosity ratio ─ they observed that at the same saturation, the relative permeability of the defending phase increases if the injection rate increases. However, both increasing and decreasing trends were observed in the invading phase relative permeability. They proposed that, at very high rates, the invading phase can access the entire network; even small pores with a high capillary entry pressure. For lower capillary numbers, (i) flow cannot access a considerable part of the network and this tends to decrease the relative permeability to both phases and may explain a decrease in the invading phase relative permeability. Conversely, at low rates, (ii) the invading fluid will enter large pores only, thus increasing the relative permeability of the invading phase.

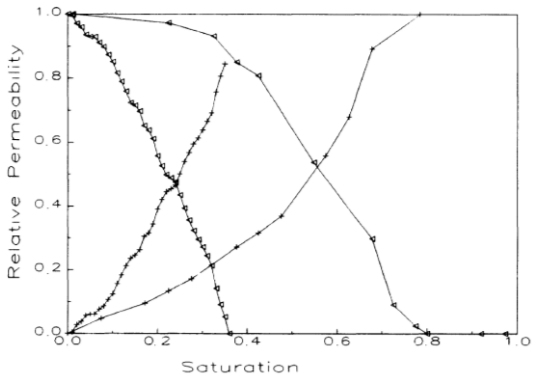

Figure 4.5: Effect of capillary number on relative permeability. The curves in the left are for a capillary dominated flow and the ones on the right represent a viscous fingering case with M=10 (Blunt and King, 1990)

Singh and Mohanty (2003) performed drainage simulations for different viscosity ratios and capillary numbers and computed relative permeability using Darcy's law in thin slices of the porous domain. At high capillary numbers, the relative permeability curves exhibited a linear shape, whilst, at low rates, they had a non-linear form. They observed that, for a unit viscosity ratio, increasing the capillary number increases the relative permeability of both wetting and non-wetting fluids. This behaviour was consistent with the experimental results of Lefebvre du Prey (1973) as we can see in Figure 4.6. They next investigated the effect of the viscosity ratio on relative permeability and found that the relative permeability of the wetting phase decreases as the viscosity ratio increases (Figure 4.7).

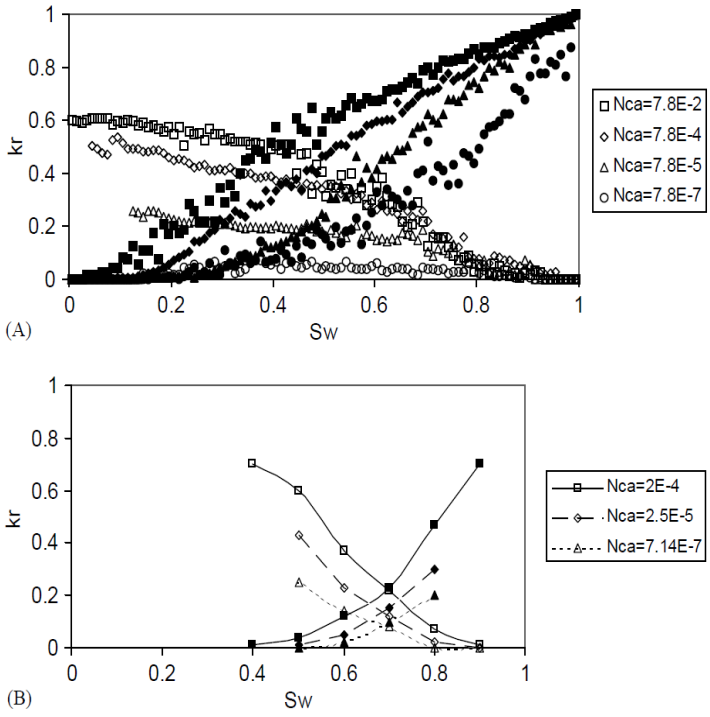

Figure 4.6: Effect of capillary number on relative permeability sets for a displacement with unit viscosity ratio for: (A) simulations performed with dynamic pore network model (Singh and Mohanty, 2003) (B) Experimental study (Lefebvre du Prey, 1973)

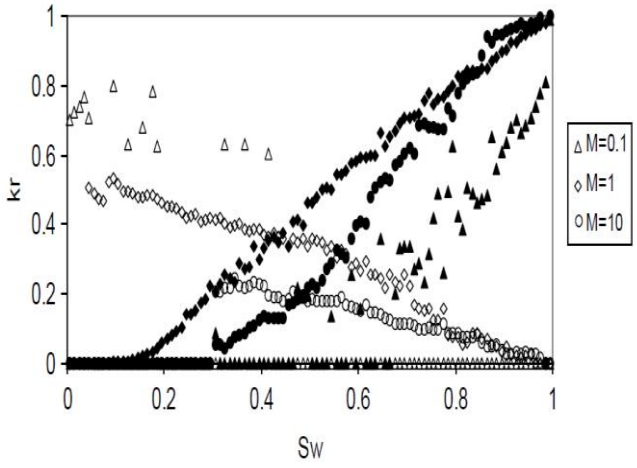

Figure 4.7: The effect of viscosity on drainage relative permeability for Nca=7.8E-4 (Singh and Mohanty, 2003).

McDougall et al. (1997) studied the effects of interfacial tension (IFT) upon gas oil relative permeability using an unsteady state pore network simulator. They calculated unsteady state relative permeability from production data using a modified version of the Jones and Roszelle method (Jones and Roszelle, 1978). They found that a decrease in IFT resulted in a marked increase of the gas relative permeability and a very small change in the oil relative permeability (Figure 4.8). This behaviour was observed in both constant rate and constant pressure drop simulations.

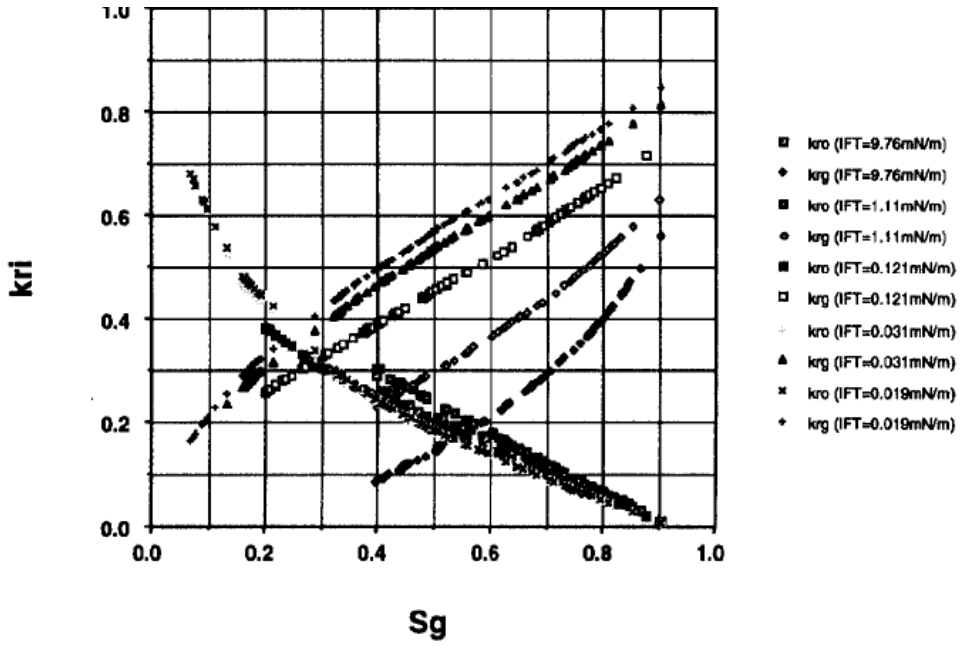

Figure 4.8: Unsteady state relative permeability predicted from pore network constant injection rate simulations (McDougall et al., 1997).

Other researchers have developed dynamic imbibition network models to investigate the effect of system parameters on relative permeability. Constantinides and Payatakes (1996) built a model that takes into account the dynamics of ganglia. They observed that an increase in the viscosity ratio decreases the relative permeability at a given saturation and they proposed that, at increased viscosity ratio, the phases tend to segregate and

create their own paths ─ the non-wetting phase is likely to flow through the large pores, thus increasing its effective permeability. Constantinides and Payatakes (1996) also investigated the effect of capillary number and found that, at the same saturation, the relative permeability increases at a higher rate.

4.7. SUMMARY

To summarize, this chapter reports the main challenges faced by researchers while developing dynamic pore network models. Considering realistic pore geometry was a big challenge because of difficulties arising from tracking the menisci inside pore bodies and throats, which is computationally too expensive. Consequently, most of the authors considered simplified approaches. Some used pore bodies without flow resistance and volumeless pore throats. Others built models with one equivalent pore element or simply developed bonds-only networks.

Another challenge has been to define the flow rules at the junctions between interconnecting pores when two different fluids are flowing towards the node. One approach is to develop a mixing algorithm, allowing both fluids to flow simultaneously. An alternative is to allow only the invading fluid to flow towards defending phase. This assumption can be justified in drainage as discussed earlier in this chapter. The simulators employing mixing algorithms that have been reported in the literature were slow and the simulations were done in relatively small networks. Unfortunately, closing the counter flowing pores makes solving the pressure more difficult.

Including capillary pressure into the formulation makes the relation between the injection rate and differential pressure non-linear and several algorithms and methods have been developed to deal with this issue (although this becomes is difficult if local counter flows are ignored).

These simulators have been used for a wide range of applications and have proved to be very useful mainly in giving physically-based insights into a range of physical phenomena. They have also been valuable in isolating the impact of each of the system variables to understand its effect on the macroscopic properties of the network;

something that would be difficult to achieve in laboratory studies. The various applications include:

- Studies on the effects of different system parameters, such as capillary number and viscosity ratio on the residual oil saturation;
- Simulation of the invasion patterns of different flow regimes – viscous fingering, capillary fingering and stable displacement, as well as the crossover between them;
- Differential pressure behaviour;
- Nonequilibrium capillarity effects;
- Interfacial velocity and dynamic effects associated with interfacial area;
- Relative permeability calculations. Unsteady-state drainage models have been used to show that the relative permeability depends on the capillary number and the viscosity ratio.

Table 4.1 summaries the main dynamic drainage models reported to date. The largest model reported in the literature was composed of 150,000 nodes. Ideally, however, we need to simulate at a much larger scale. In the next chapter we present a newly developed drainage pore network model that allows us to reproduce all the flow regimes, viscous instabilities and post-breakthrough finger thickening behaviour observed experimentally.

Table 4.1: Summary of dynamic drainage pore network models

Researchers	**Pore Geometry**	**Application**	**Boundary condition**	**Biggest network reported**	**Pc coupled with the solver**	**Rules in the junction**
King (1986)	Cylindrical bonds	Fractal patterns study	Constant differential pressure	N.A.	No	N.A
Lenormand et al(1988)	Volumeless cylindrical throats Spherical bodies without resistance	Effect of viscosity ratio and capillary number on the flowing regime and patterns	Constant rate	100*100	Yes	Closing counter flow pores
Blunt and King (1990)	Volumeless cylindrical throats Spherical bodies without resistance	invasion patterns. Effect of capillary number on fractional flow and relative permeability	Constant rate	80000 nodes	It seems that it is not coupled with the solver	Closing counter flow pores (implicit pressure explicit saturation method)

McDougall and Sorbie(1993)	Cylindrical bonds	Flow in laminated media	Constant rate		No	Allowing only invading fluid to flow towards the node (without closing counter flow pores)
Van Der Mark et al (1997)	Shape similar to the micromodel	Differential pressure simulation	Constant rate	25*25*2	Yes	Closing counter flow pores
Aker et al (1998)	Bonds model with non-uniform capillary pressure in each tube	Flow regime patterns, nonequilibrium capillarity and differential pressure studies	Constant rate	60*80	Yes	Mixing algorithm

Researchers	**Pore Geometry**	**Application**	**Boundary condition**	**Biggest network reported**	**Pc coupled with the solver**	**Rules in the junction**
Sahimi et al (1998)	Volumeless cylindrical throats Spherical bodies without resistance	Invasion patterns and fractal dimension calculation	Constant rate	100*100	Yes	Closing counter flow pores
Dahle and Celia (1999)	Cylindrical bonds	Drainage Pc curves	Constant rate	17*17*29	Yes	N.A
Singh and Mohanty (2003)	Square pore throats and cubic pore bodies	Effect of capillary number and viscosity ratio on residual saturation and relative permeability	Constant rate/ constant differential pressure	30*8*8	Yes	Closing counter flow pores (implicit pressure explicit saturation method)

Nordhaug et al(2003)	Volumeless cylindrical throats Spherical bodies without resistance	Interface velocity for different regimes	Constant differential pressure	10*10*50	No	Closing counter flow pores (implicit pressure explicit saturation method)
Gielen et al(2005)	Volumeless cylindrical throats Spherical bodies without resistance	Nonequilibrium effects in phase pressures difference	Constant differential pressure	30*30*40	No	Closing counter flow pores (implicit pressure explicit saturation method)
Al-Gharbi and Blunt(2005)	Convergent divergent pores with triangular cross section	Flow regimes patterns. Effect of capillary number on residual saturation	Constant rate	9*9	Yes	Mixing algorithm
Joekar-Niasar et al(2010)	Square throats. Cubic pore bodies	Nonequilibrium capillarity	Constant pressure	45*35*35	Yes through two phase solver	N.A

Idowu and Blunt (2010)	Several shapes and resistance assigned to pore bodies and pore throats	The effects of capillary number and mobility ratio on imbibition	Constant rate	150,000 nodes	No	They used sequential filling they did not face this issue
Hammond and Unsal (2012)	Several shapes and resistance assigned to pore bodies and pore throats	EOR application (surfactant injection)	Constant rate	70*70	Yes	They used sequential filling they did not face this issue

Chapter 5: Description of the model

5.1. INTRODUCTION

The flow in porous media is governed by the competition between viscous and capillary forces. Whilst these pore scale phenomena completely determine the flow regime, they are not explicitly taken into account by the classical reservoir simulators. As a consequence, in some situations, reservoir simulators are unable to reproduce certain flow behaviours observed experimentally, such as viscous fingering phenomena (Riaz et al., 2007). The motivation of the present work is to overcome this issue by applying a pore scale modelling technique (pore network modelling) to simulate slab experiments at the appropriate scale.

In this chapter, we describe a newly developed drainage pore network model that has been built to simulate the full range of unsteady state drainage processes associated with water-oil displacements in porous media. This model has been optimized to facilitate the simulation of slab experiments at the scale of tens centimetres.

We start by describing the motivation for building a new pore network model and proceed to give an overview of the main assumptions and the structure of the modelling algorithms. We then present the pore network reconstruction technique that was used to generate the digital rock used in the simulations and explain the methodologies used to solve the pressure field to update the nodal pressures, determine the filling events, and update the menisci in partially filled pores. Finally, we present the clustering technique used that helps to identify trapped pores.

5.2. THE NEED TO DEVELOP A NEW MODEL

In this work we present a new dynamic drainage pore network simulator that builds upon an earlier model developed by McDougall and Sorbie (1993) in the context of unsteady-state displacements in laminated media. The derivation of pressure equations from local flow laws that includes capillary pressure can lead to nonlinear issues that will be discussed later in this chapter (Section 5.5). However, McDougall and Sorbie (1993) simplified the problem and did not consider the capillary pressure in the approach and pressures were simply derived using a pseudo-single phase approach ─ calculating the average viscosity in each element and solving the pressure with the methodology used for single phase flow. Their model was then used to simulate unsteady-state two-phase displacements during waterflooding for a range of viscosity ratios, flow rates and levels of pore-scale heterogeneity. Whilst the impact of viscosity ratio and flow rate (or capillary number) largely followed a similar trend to that reported by Lenormand et al (1988) ─ capillary fingering at low rates, stable displacement at high rates and favourable viscosity ratio and viscous fingering at high rates and adverse viscosity ratio ─ some pathological results were observed. In displacements involving fluids with unfavourable viscosity ratio, a single thin finger emerged during the transition between capillary and viscous dominated regimes (Figures 5.1, 5.2 and 5.3). Such a pattern had not been observed in the experimental study of Lenormand et al (1988).

Furthermore, although viscous fingering and stable displacement regimes were simulated by the model, they were only obtained at very high (unphysical) injection rate/differential pressures and this issue was more significant as the network length increased. As we are not only interested in simulating the general behaviour, but also aim to reproduce the observed flow regimes under experimental conditions, we have investigated the causes of these pathological results.

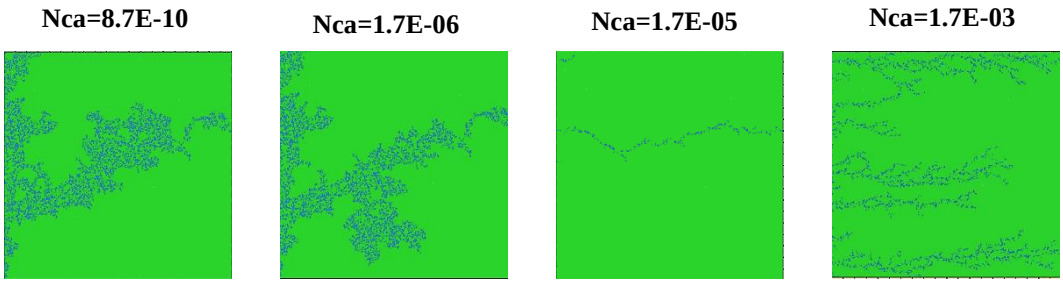

Figure 5.1 : Simulations performed without including the capillary pressure in the pressure equations that show the effect of the capillary number on waterflooding of a (400*400) network and a viscosity ratio M=100.

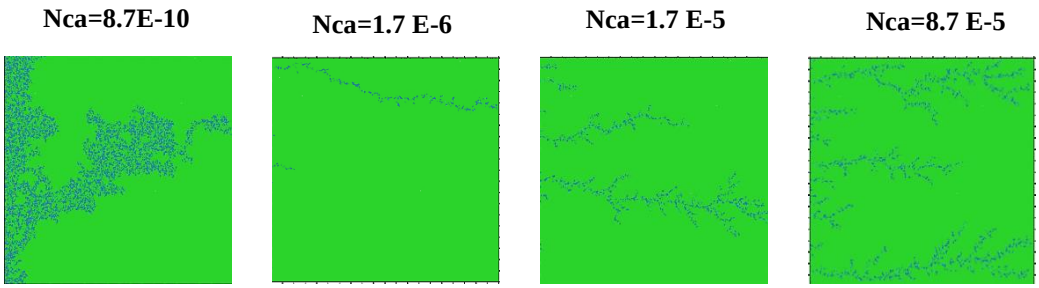

Figure 5.2 Simulations performed without including the capillary pressure in the pressure equations that show the effect of the capillary number on waterflooding of a (400*400) network and a viscosity ratio M=7000.

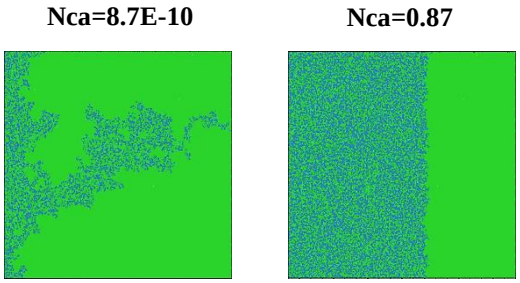

Figure 5.3: Simulations performed without including the capillary pressure in the pressure equations that show the effect of the capillary number on waterflooding of a (400*400) network and a viscosity ratio M=0.5.

At low rates, the model of McDougall and Sorbie (1993) resulted in cases where the pressure of the water phase was lower than the capillary resistance of all the pores at the interface. In such situations, they were using a "*pseudo-invasion percolation*" technique, which fills only one pore at a time, and this pore was chosen as the one having the lowest negative net entry pressure (equal to the difference between viscous pressure gradient across the pore and the absolute value of the capillary resistance of the pore element: net Pentry=ΔP viscous- |Pc entry|). Whilst this method was good at simulating capillary fingering at low rates (Figures 5.1, 5.2 and 5.3), it failed to catch the transition between the capillary dominated and viscous fingering regimes and resulted in the simulation of pathologically thin fingers. In fact, at the transition between the capillary and viscous regimes for an unfavourable viscosity ratio, when a viscous finger was initiated (i) the highest viscous pressure gradient occurred at the tip of the viscous instability (Figure 5.4 and Figure 5.5), and (ii) the viscous forces were not strong enough to switch the algorithm to the dynamic subroutine where multiple pores filling was switched on. This results in using the pseudo-invasion percolation algorithm that fills only the pore having the least negative net entry pressure ─ that is likely to be the pore situated at the tip of the already initiated finger.

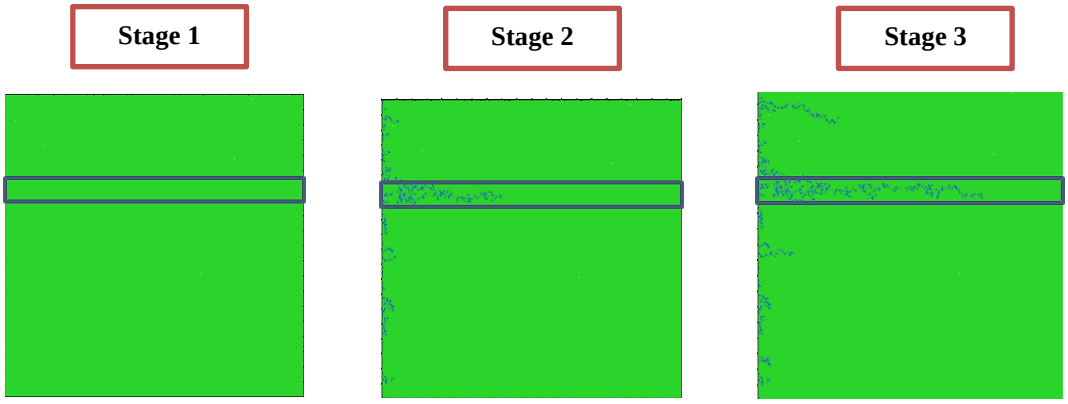

Figure 5.4: Different stages of growth of a thin finger in a constant pressure drop simulation (ΔP=1 bar) .The viscosity ratio (M=100) in this case.

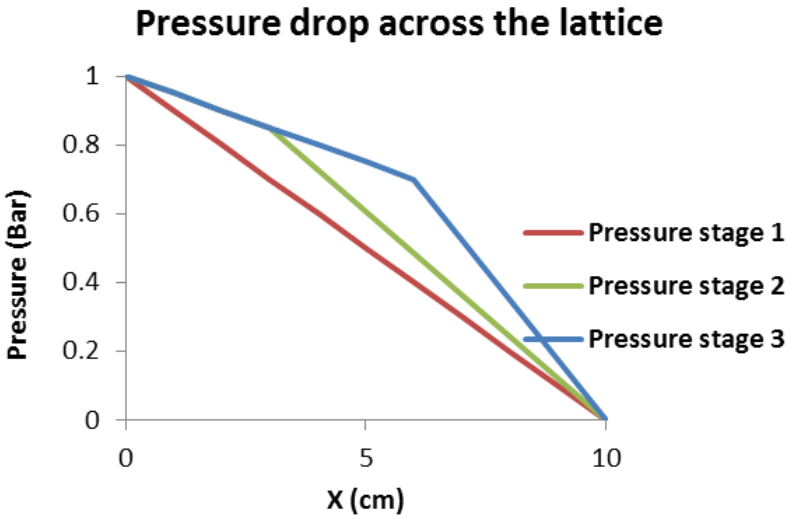

Figure 5.5: Pressure gradient at each stage of a thin finger growth observed in Figure 5.4..

Furthermore, the pseudo-single phase approach to solve the viscous pressure leads to the initiation of viscous fingers only at very high rates. To understand the causes of this behaviour we consider a system composed of a single pipe filled with matched viscosity water and oil (illustrated in Figure 5.6) and where the pressure is solved using the pseudo-one phase approach. Now, imagine that this pipe is composed of 2 bonds having equal radii, the pressure at the interface should be higher than the capillary entry pressure of the oil filled bond to dynamically fill this pore, which is equivalent in this case to:

$$\frac{\Delta P}{2} > P_{c\,entry} \tag{5.1}$$

If we consider that this pipe is composed of a number of bonds (n) having the same radii, the pressure drop in this simple system should be higher than $n * P_{c\,entry}$ to dynamically fill the pore at the interface. This means that, if we take an example of bonds having a capillary entry pressure $P_{c\,entry} = 1000$ Pa, then the initial differential pressure in the network should be at least equal to 15 bars to be able to invade a single

bond in the experiments reported by Skauge et al (2012) which is much higher than the experimental initial differential pressure equal to (1.5 bar) that we know corresponds to a viscous dominated flow. This example highlights the causes of the observed unphysical high injection rates and differential pressures required by te old model to simulate viscous dominated flow (viscous fingering or stable displacement).

To avoid these issues, it is important to consider the capillary pressure in the pressure equation formulation ─ in this case, at low rates, it is sufficient to have a differential pressure slightly higher than the capillary entry pressure of a pore to be able to invade it using a dynamic approach (Figure 5.7). Moreover, coupling the capillary pressure with the solver enables us to use only the pressure gradients to decide which the pores to invade (Figure 5.7) and so there is no longer any need to use a pseudo invasion percolation algorithm thereby avoiding the simulation of pathological thin fingers.

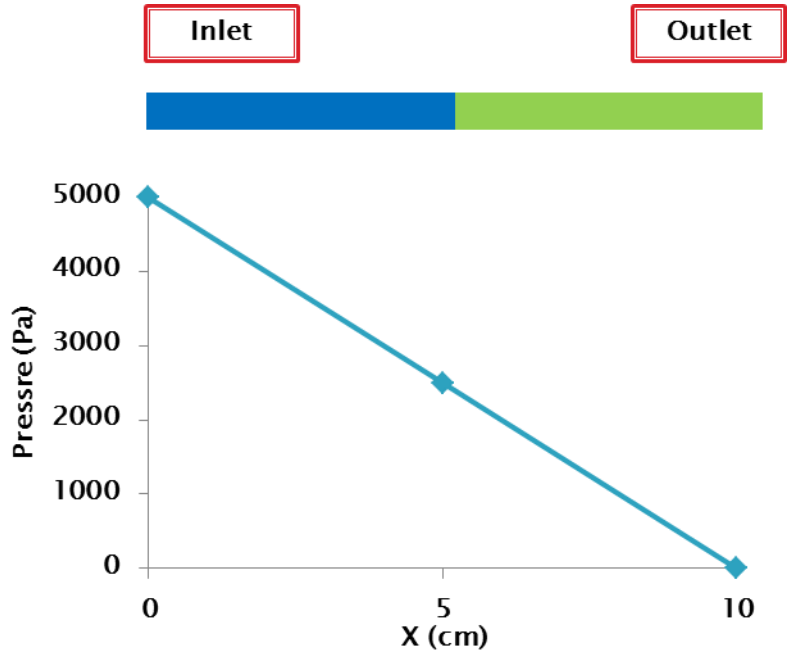

Figure 5.6: A figure illustrating the pressure solution in a simple pipe using the pseudo one phase algorithm.

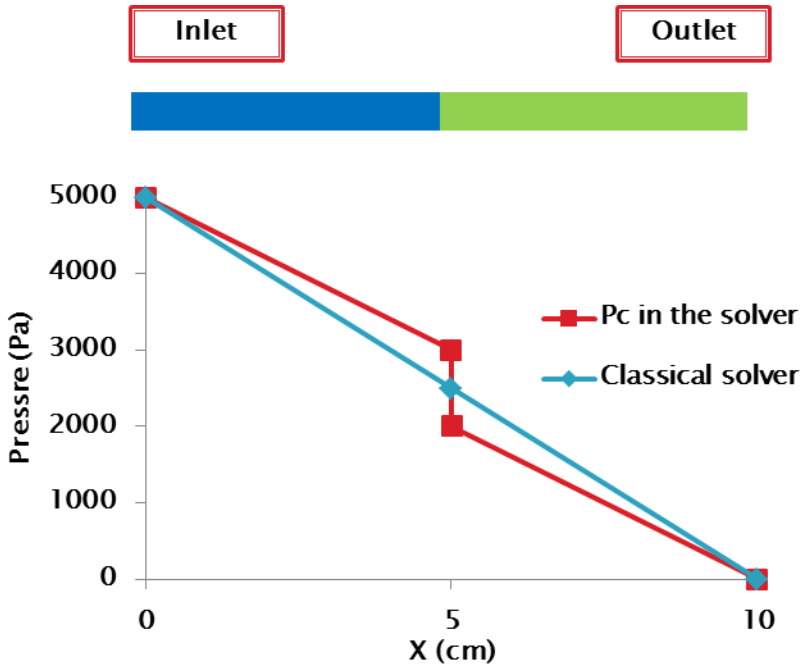

Figure 5.7: A figure illustrating the pressure solution in a simple pipe after coupling the capillary pressure with the solver.

5.3. MODEL OVERVIEW

We present in the following sections a newly developed fully dynamic drainage pore network model that includes an iterative approach to enable capillary pressure to be taken into account when solving for the global pressure field.

The main assumptions of the model are:

- Laminar flow ─ intra-pore fluid flows in parallel layers, with no cross-currents perpendicular to the direction of flow;
- Stokes/ Creeping flow ─ inertial forces are considered negligible;
- The fluids are incompressible, immiscible and Newtonian;
- Film flow and gravity are neglected;
- Counter-current imbibition events are not considered.

In the first step, a digital rock is generated from a statistical distribution or loaded from network files. The porous medium is modelled as a number of interconnected pore elements ("pores") representing the void space in the rock. We choose a simple representation that makes no distinction between pore bodies and pore throats and a methodology named the "3Rs approach", which considers the geometrical shape of the pore element itself as immaterial and focuses on modelling system behaviour instead.

Once the network is created, all the pores are filled with the defending phase (oil) and the injection of the invading phase (water) begins. The network edges are considered sealed, except for the inflow and outflow boundaries, and the simulator offers the possibility of performing constant pressure drop and constant injection rate simulations. The first step in simulating the network flow consists of solving the pressure field, which becomes a more complex task when considering capillary pressure terms in the formulation ─ this difficulty was overcome by using an iterative secant method described later in Section 5.5.

Once the pressure field has been resolved, the pressure gradients operating across pore elements are used to compute local flow rates that are subsequently used to determine

the filling events that control changes in fluid occupancy. Here, the interface between phases is considpterered sharp and well defined and a multiple pore filling algorithm is used to update the menisci in each pore at the oil-water interface, making possible the simulation of concurrent menisci movements occurring at high rates (an important consideration when modelling viscous fingering phenomena).

We note that the incompressible nature of the fluids used in our simulations and the fact that the pressure equations are based on mass conservation, ensure that we inject the correct amount of fluid at each time step.

Finally, a clustering technique is used to identify the defending phase pores that are no longer connected to the outlet and are considered trapped.

As we can see in the high level flow chart shown in Figure 5.8, the time-stepping process is repeated until a stopping condition is reached. This condition allows the user to choose the stage at which the simulation should stop either after attaining a fixed saturation value, reaching breakthrough, performing a fixed number of steps, or injecting a fixed pore volume of the invading phase.

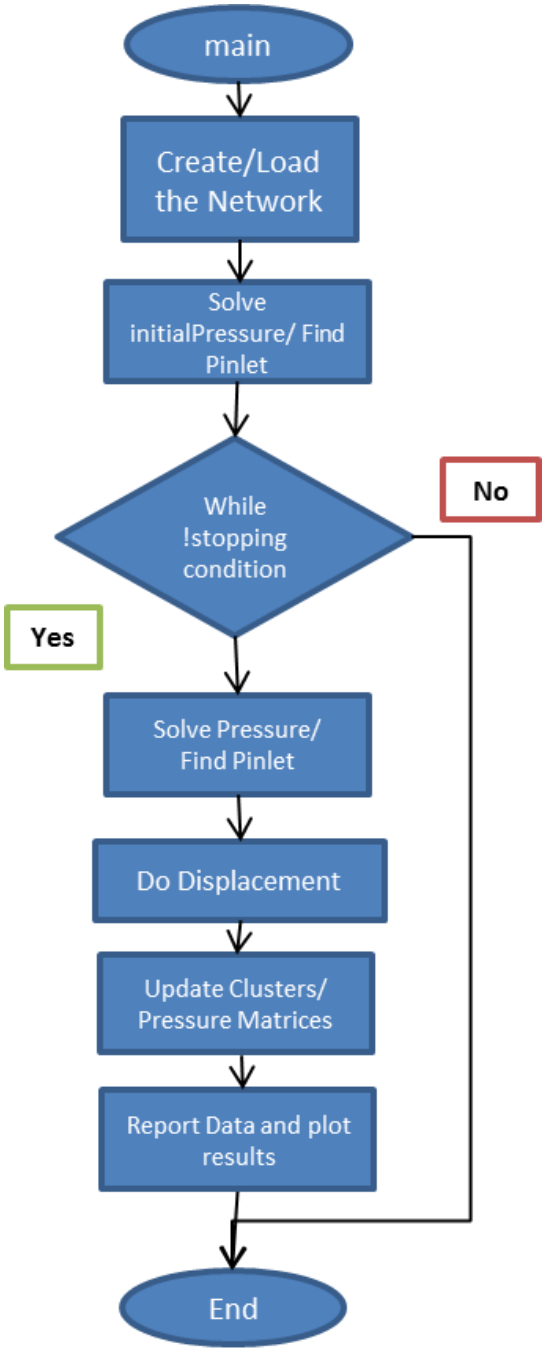

Figure 5.8: simplified flow chart of the developed dynamic model

5.4. NETWORK CREATION

Initially, a pore network is built that closely resembles the void space in a given rock, modelled as a number of interconnected pore elements ("pores") that form a three dimensional lattice representing the tortuous channels that permeate the rock fabric. Although the model has been developed in a way that allows us to build very general pore topologies, we have chosen to limit the current study to a model that makes no distinction between pore bodies and pore throats. Instead, we use an abstract approach named the "3Rs approach". The geometrical shape of the pore element itself is considered to be of secondary importance; instead it is the consequent behaviour of the system that is really important. This behaviour is the result of the net capillary entry pressure, conductance and volume of the pores. So, we consider that each pore element has three effective "radii"; one defines the capillary entry pressure (Rcap), another characterises the pore volume (Rvol), and a third governs the pore conductivity (Rcond).

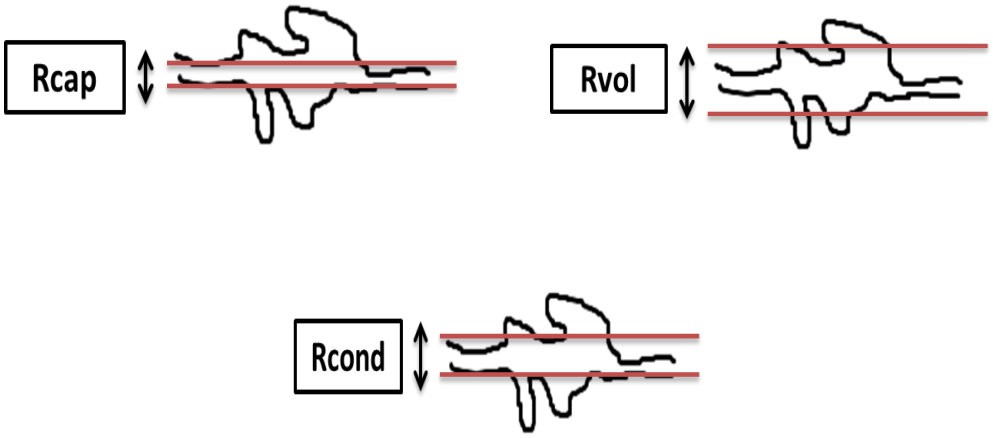

Figure 5.9: illustrating the 3Rs approach.

Furthermore, Rvol and Rcond can themselves be considered dependent on Rcap (Figure 5.9) and as a consequence, the volume and conductance of each pore element can be calculated as follows:

$$\begin{cases} \boldsymbol{V = A\pi \mathrm{Rcap}^{\nu} L 10^{(6\nu-12)}} \\ \boldsymbol{g = B\frac{\pi}{8}\frac{\mathrm{Rcap}^{\lambda} 10^{(6\lambda-24)}}{\mu L}} \\ \boldsymbol{\nu \in [0,3]; \lambda \in [1,4]} \end{cases} \quad (5.2)$$

where, A and B are volume and conductance pre-factors, Rcap the capillary entry radius, L the pore length, μ the viscosity, ν the volume exponent and λ the conductance exponent. For a network of cylinders, ν is equal to 2 and λ=4 making the relation between pressure gradients are local rates similar to Poiseuille's law.

The capillary radius and the coordination number statistical distributions are obtained from networks extracted are determined from rock images and, the exponents are determined by following the methodology of McDougall et al. (2002). The idea is to "*anchor"* the network model using relatively cheap, easily-acquired experimental mercury injection data. The experimental capillary pressure curves are first inverted to calculate the experimental *R-plot* using the equation:

$$R = \frac{2\,\sigma cos\theta}{P_c} \quad (5.3)$$

Although mercury/vacuum capillary pressure curves are often fairly structureless, their corresponding R-plots have been shown to be more structured (McDougall and Sorbie, 1994). The reason that R-plots generally exhibit more structure than semilog capillary pressure data lies in the fact that plotting of an inverse quantity has less of a smoothing effect than plotting logarithmically.

A typical R-plot exhibits the following characteristics: an initial decline due to limited initial accessibility of the mercury, a plateau region related to the spreading of the mercury cluster, and an inflection point (kink) at higher mercury saturations.

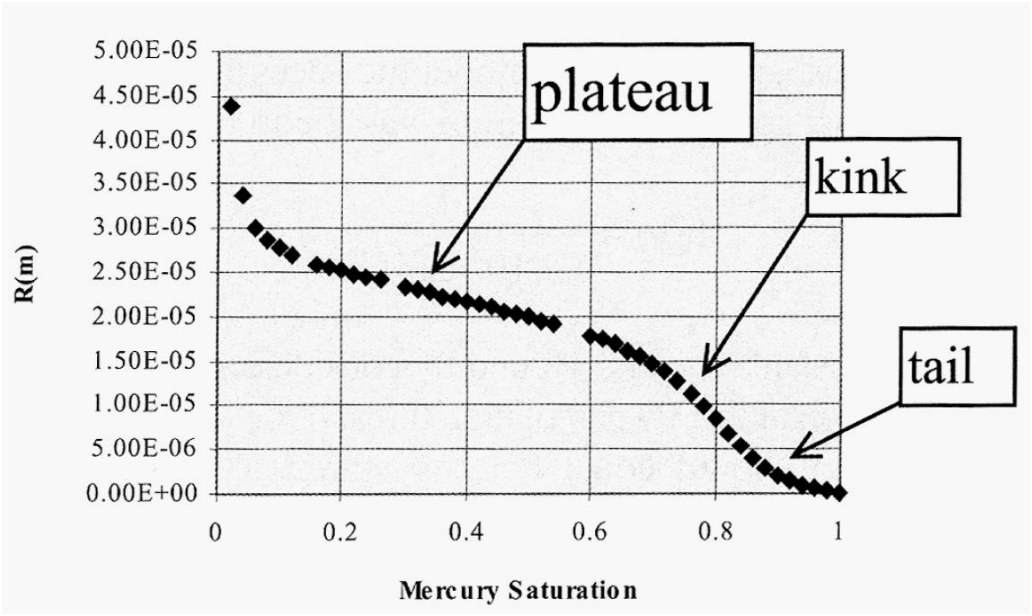

Figure 5.10: Schematic mercury intrusion data showing plateau, kink, and tail regions (McDougall et al., 2002).

The analytical equation can be used to calculate an analytical R-plot which are fitted to the experimental R-plot and used to determine the volume and conductance exponents, as shown Figure 5.11.

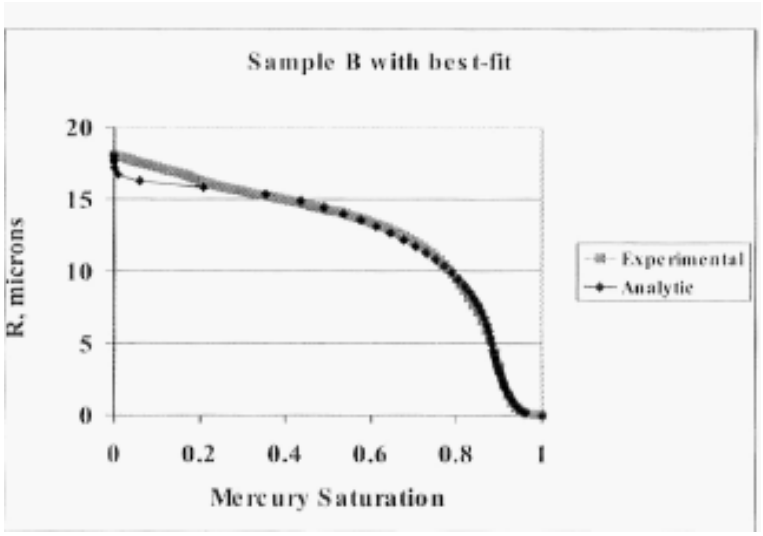

(a)

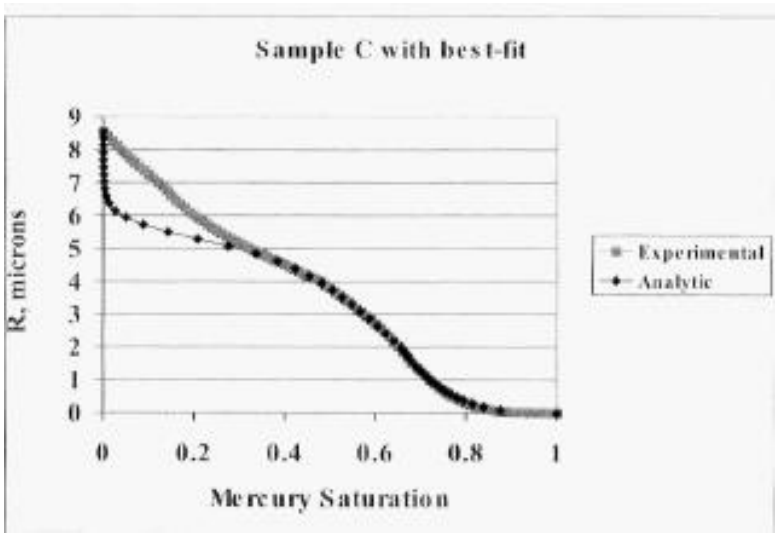

(b)

Figure 5.11: Two examples of fitting the analytical to the experimental R-plot (McDougall et al., 2002).

Initially a regular rectangular lattice of nodes is created and can subsequently be distorted if distortion is required, the nodal positions are slightly perturbed by a random amount proportional to the level of distortion (Figure 5.12). The new nodal coordinates are calculated as follows:

$$x_n = (i_n + 0.5 + 0.5\sigma u)\Delta x \quad -1 \leq i_n \leq n_x \tag{5.4}$$

$$y_n = (j_n + 0.5 + 0.5\sigma u)\Delta y \quad 0 \leq j_n < n_y \tag{5.5}$$

$$z_n = (k_n + 0.5 + 0.5\sigma u)\Delta z \quad 0 \leq k_n < n_z \tag{5.6}$$

where:

- n_x, n_y and n_z are the number of nodes in the x, y and z directions and are fixed in the input file by the user;
- $\Delta x, \Delta y$ and Δz are the average distance between two points to be sampled respectively in the x, y and z directions and are calculated as the length of the network divided by the number of points in that direction;
- u is sampled from a uniform distribution within the interval (-1,1);
- σ is the distortion level fixed by the user and should be between 0 and 1.

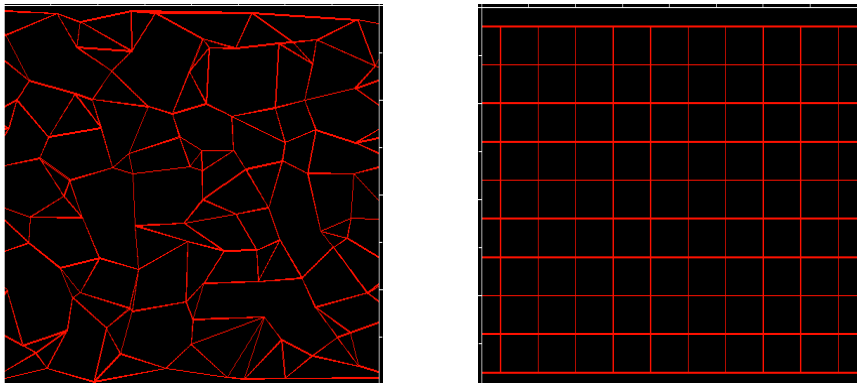

(a) **(b)**

Figure 5.12: Examples of distorted (a) and regular (b) networks

Once the node locations are found, we go on to connect them in the triangulation step by forming links: pairs (n_1, n_2) of integers each of which refer to the index of the network nodes linked by the pores. For regular networks, we use a simple algorithm that creates a fully connected regular network whilst, for the non-regular cases, we use a Delaunay algorithm that constructs triangles that maximise the smallest angle.

The Delaunay triangulation builds a highly connected network and so, some links need to be removed to ensure a physically realistic number of connections. Furthermore, the modelling framework offers the possibility to specify a statistical distribution of nodal coordination numbers (which refers to the number of pores connected to each node).

We define the degree of a node as the number of nodes connected to it and the less degree as the number of connections to nodes closer to the inlet.

Once the degree and less degree are calculated, each node is assigned a coordination number sampled from the coordination number statistical distribution. Initially, the degree and less degree of each node are computed and then, for each junction, a list of all the adjacent nodes is formed and the size of this list is compared with the coordination number assigned. If the list size is larger, some links have to be removed and we start by deleting the longest ones. However, we ensure that deleting the link

does not make the less degree of any node equal to zero and if it is the case, we move to the next longest link and continue until the degree is equal to the coordination number or until we run out of items in the list.

An example is presented here. Suppose that we have the situation of Figure 5.13 and we are assessing body 1 which has been assigned a coordination number equal to 3. Since the current coordination number is 4, we need to remove 1 link. So, we determine the longest link from body 1 which is the link (1, 2). However, by removing this link, the less-degree of body 2 will be zero (i.e. body 2 will not be connected to a body closer to the inlet than itself). As a consequence, we leave this link and move to the next longest link (from 1) which is (1, 3) which can be removed because body 3 maintains a connection to body 4 which is closer to the inlet and is done until the degree is equal to the coordination number or until we run out of items in the list.

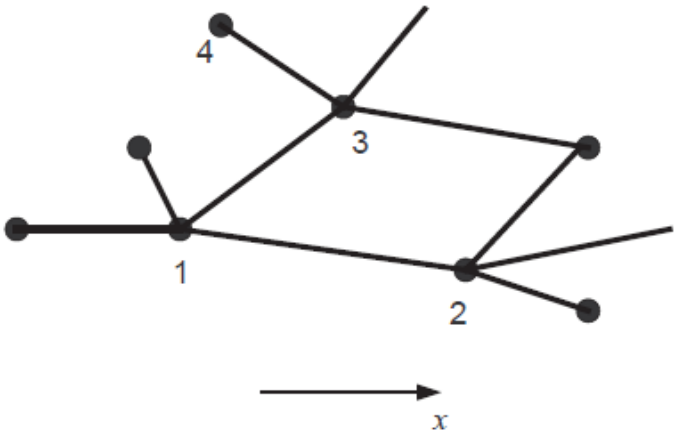

Figure 5.13: Example of how links are removed

This method aims to make sure that the network is well connected between the inlet and outlet and ensures that all nodes have at least one connection, otherwise numerical issues will occur while the pressure is solved.

Finally, the created links are transformed to pores which are assigned radii, conductances and volumes.

5.5. THE PRESSURE SOLVER

After building the pore network, fluid flows are simulated and these are clearly governed by local pressure gradients: consequently nodal pressures need to be computed in order to know how the fluids move over a given timestep.

In this section, we explain the methodology used to calculate the nodal pressures within the network and we use the simple networks presented in Figure 5.14 and Figure 5.15 to illustrate this. Both examples contain 8 nodes and 9 pores and there is a single inlet node (labelled 0) and a single outlet node (labelled 7).

We assume that the inlet pressure is equal to the differential pressure and that the outlet pressure is equal to zero, which is reasonable as only the pressure *differences* across the network are important.

Then, in order to have a faster and a more efficient solver, we make the entire problem non-dimensional which is possible because it is linear. This results in having an inlet pressure equal to 1 and an outlet pressure equal to zero at every time step. In the following discussion, we use uppercase letters to designate dimensional variables and lower case letters to denote non-dimensional values.

5.5.1. Single Phase Flow

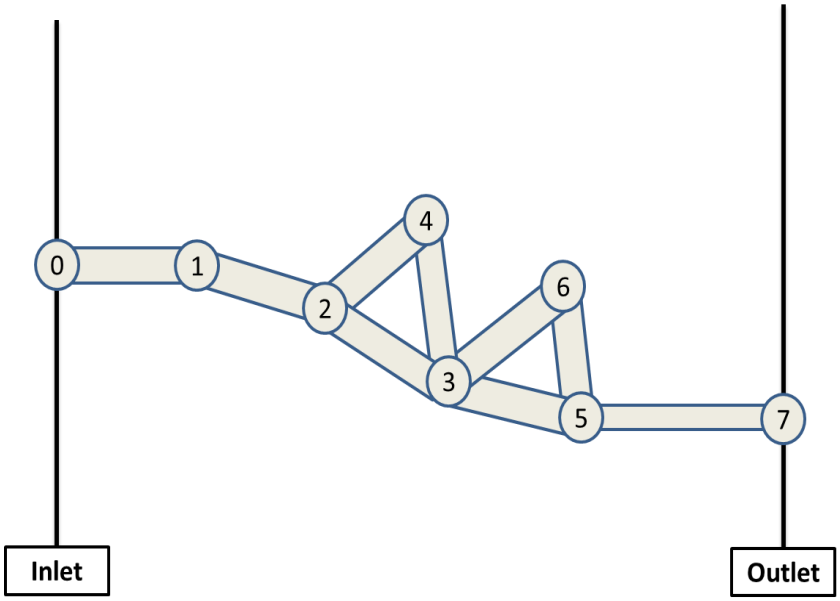

Figure 5.14: A simple network of water flow (white) from inlet to outlet

The pressure solver is based on the mass conservation equation. Simply, at every node *i* the flows going in and out are equal, so we can write:

$$\sum_{i,j} Q_{ij} = 0 \tag{5.7}$$

where Q_{ij} is the flow rate from node i to j .

In single phase flow, the flow rate between two nodes can be computed as follows:

$$Q_{ij} = G_{ij}(P_i - P_j) \tag{5.8}$$

where P_i is the pressure at node i, P_j is the pressure at node j and G_{ij} is the conductance of the pore linking nodes i and j, calculated using Poiseuille Law for a cylindrical pore element as follows:

$$G_{ij} = \frac{\pi {R_{ij}}^4}{8\mu L_{ij}} \tag{5.9}$$

R_{ij} and L_{ij} are respectively the radius and the length of the throat connecting nodes i and j.

If we consider the setup of Figure 5.14, we write after using the dimensional form of the mass conservation equation at node 2:

$$G_{12}(P_2 - P_1) + G_{23}(P_2 - P_3) + G_{24}(P_2 - P_4) = 0 \tag{5.10}$$

As discussed previously, we wish to work with non-dimensional variables and so, we define the non-dimensional nodal pressures and non-dimensional conductances as:

$$g_{ij} = \frac{G_{ij}}{G_s} \tag{5.11}$$

$$p_i = \frac{P_i}{P_{inlet}} \tag{5.12}$$

where P_{inlet} is the inlet pressure and G_s is the conductance scale defined as:

$$G_s = \frac{\pi {L_s}^3}{8\mu_s} \tag{5.13}$$

where L_s is the length scale (usually taken as the smallest radius in the network) and μ_s is the viscosity scale (chosen as the largest viscosity of the flowing phases).

Dividing equation (5.10) by G_s and P_{inlet} results in the non-dimensional form of the mass conservation equation:

$$(g_{12} + g_{23} + g_{24})p_2 - g_{12}p_1 - g_{23}p_3 - g_{24}p_4 = 0 \tag{5.14}$$

After considering the mass conservation equation in an interior node (node2), we go on to write it for nodes connected to the boundaries: node 1 (connected to the inlet) and node 5 (connected to the outlet). Using the same methodology described previously and considering that the non-dimensional inlet pressure is equal to 1 and the outlet pressure is equal to zero, we can write the following equations:

$$(g_{01} + g_{12})p_1 - g_{12}p_2 = g_{01} \tag{5.15}$$

$$(g_{57} + g_{56} + g_{35})p_5 - g_{56}p_6 - g_{35}p_3 = 0 \tag{5.16}$$

Notice that the RHS of Equation (5.15) is non-zero whilst the RHS of Equations (5.14) and (5.16) are zeros. Now, if we consider the mass conservation equation at every node in the network, solving for the spatial distribution of the pressure field becomes equivalent to solving the linear system:

$$G * p = q \tag{5.17}$$

where G is the coefficient matrix of dimensionless conductances, p is the column vector of dimensionless nodal pressures and q is the column vector of boundary conditions – corresponding to the dimensionless rates at the inlet pores. For the example of Figure 5.14, the pressure matrices and vectors are the following:

$$G = \begin{pmatrix} g_1 & -g_{12} & 0 & 0 & 0 & 0 \\ -g_{12} & g_2 & -g_{23} & -g_{24} & 0 & 0 \\ 0 & -g_{23} & g_3 & -g_{34} & -g_{35} & -g_{36} \\ 0 & -g_{24} & -g_{34} & g_4 & 0 & 0 \\ 0 & 0 & -g_{35} & 0 & g_5 & -g_{56} \\ 0 & 0 & -g_{36} & 0 & -g_{56} & g_6 \end{pmatrix}, \text{p=} \begin{pmatrix} p_1 \\ p_2 \\ p_3 \\ p_4 \\ p_5 \\ p_6 \end{pmatrix} \text{ and q=} \begin{pmatrix} g_{01} \\ 0 \\ 0 \\ 0 \\ 0 \\ 0 \end{pmatrix}$$

where we have defined:

$$\begin{pmatrix} g_1 \\ g_2 \\ g_3 \\ g_4 \\ g_5 \\ g_6 \end{pmatrix} = \begin{pmatrix} g_{01} + g_{12} \\ g_{12} + g_{23} + g_{24} \\ g_{23} + g_{34} + g_{35} + g_{36} \\ g_{24} + g_{34} \\ g_{35} + g_{56} + g_{57} \\ g_{56} + g_{36} \end{pmatrix}$$

Such a system can be solved using several methods. However, it is important to have an accurate solution to prevent mass conservation issues appearing. In this work, we use Cholesky decomposition to solve the system for 2D networks and Conjugate Gradient solver coupled with an Incomplete Cholesky Preconditioner to solve the problem for 3D networks.

Whilst the single phase flow model just described can be useful for several applications such as absolute permeability calculations or tracer injection simulations (dispersion test), dynamic pore network models are mostly useful for multiphase flow simulations.

5.5.2. Two Phase Flow

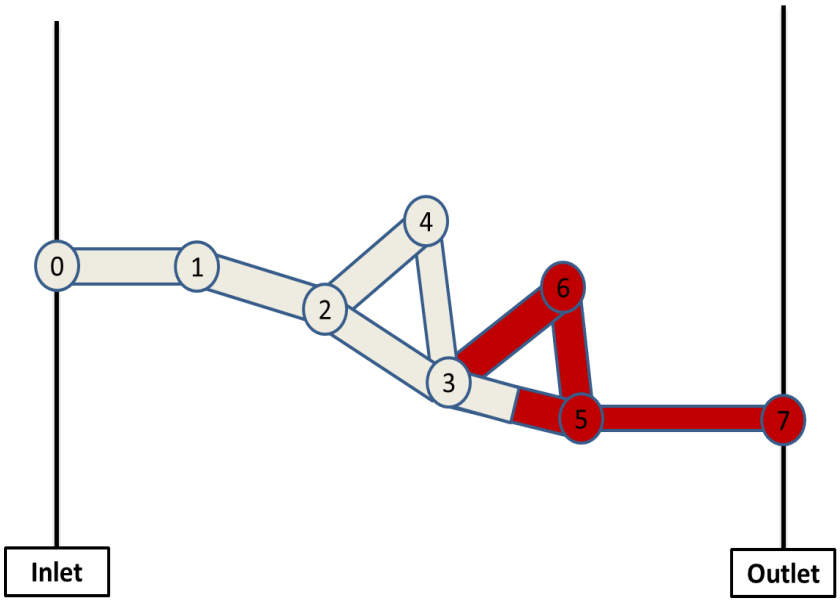

Figure 5.15: A simple network of water injection (white) in to oil (red)

In two phase flow, the flow within a pore situated at the interface separating wetting and nonwetting phases must account for the capillary pressure drop across that interface, and so we now have:

$$\begin{cases} Q_{ij} = G_{ij}(P_i - P_j + P_c) \text{ if } P_i - P_j > -P_c \\ Q_{ij} = 0 \; if \; P_i - P_j \leq -P_c \end{cases} \tag{5.18}$$

where the capillary entry pressure is defined using a simple Young-Laplace law as:

$$P_c = \frac{2\sigma cos\theta}{R} \tag{5.19}$$

Here σ is the interfacial tension, θ is the contact angle ($\theta = 180°$ for a strongly oil wet system) and R is the radius of the pore throat. It should be noticed that the capillary entry pressure is negative for an oil wet system.

After writing the non-dimensional mass conservation equation for node 3 (Figure 5.15) we have:

$$\begin{aligned} (g_{23} + g_{34} + g_{35} + g_{36})p_3 - g_{23}p_2 - g_{34}p_4 - g_{35}p_5 - g_{36}p_6 \\ = C_s * g_{35} * \left(-\frac{cos\theta 35}{r35}\right) + C_s * g_{36} * \left(-\frac{cos\theta 36}{r36}\right) \end{aligned} \tag{5.20}$$

where C_s is the *capillary scale* defined as $C_s = \frac{2\sigma}{P_{inlet} L_s}$,

Note that the RHS of Equation (5.20) now includes a new term representing the effect of the capillary entry pressure, making the matrix form of the problem as follows:

$$G * p = q_b + C_s q_c \tag{5.21}$$

For the example of Figure 5.14 , the pressure matrices and vectors now became::

$$G = \begin{pmatrix} g_1 & -g_{12} & 0 & 0 & 0 & 0 \\ -g_{12} & g_2 & -g_{23} & -g_{24} & 0 & 0 \\ 0 & -g_{23} & g_3 & -g_{34} & -g_{35} & -g_{36} \\ 0 & -g_{24} & -g_{34} & g_4 & 0 & 0 \\ 0 & 0 & -g_{35} & 0 & g_5 & -g_{56} \\ 0 & 0 & -g_{36} & 0 & -g_{56} & g_6 \end{pmatrix} \quad , \quad \text{p=} \begin{pmatrix} p_1 \\ p_2 \\ p_3 \\ p_4 \\ p_5 \\ p_6 \end{pmatrix} \quad , \quad q_b = \begin{pmatrix} g_{01} \\ 0 \\ 0 \\ 0 \\ 0 \\ 0 \end{pmatrix} \quad \text{and}$$

$$q_c = \begin{pmatrix} 0 \\ 0 \\ g_{35} * \left(-\frac{cos\theta 35}{r35}\right) + g_{36} * \left(-\frac{cos\theta 36}{r36}\right) \\ 0 \\ g_{35} * \left(\frac{cos\theta 35}{r35}\right) \\ g_{36} * \left(\frac{cos\theta 36}{r36}\right) \end{pmatrix}$$

where we have defined:

$$\begin{pmatrix} g_1 \\ g_2 \\ g_3 \\ g_4 \\ g_5 \\ g_6 \end{pmatrix} = \begin{pmatrix} g_{01} + g_{12} \\ g_{12} + g_{23} + g_{24} \\ g_{23} + g_{34} + g_{35} + g_{36} \\ g_{24} + g_{34} \\ g_{35} + g_{56} + g_{57} \\ g_{56} + g_{36} \end{pmatrix}$$

q_b and q_c are respectively the column vector of boundary conditions (corresponding to the non-dimensional rates at the inlet pores), and the capillary effects column vector (representing the capillary effects at the fluids interface).

We note that the second equation in (5.18) is a capillary pressure control that means that only the nonwetting invading phase can displace the defending wetting phase – we do not consider counter current imbibition events here. Hence, pores having $P_i - P_j \leq -P_c$

are effectively "*closed"* pores. This assumption has been used in several previous drainage dynamic network models (Lenormand et al., 1988, Blunt and King, 1991, Singh and Mohanty, 2003) and will be discussed further in the next section.

Unfortunately, simply solving the pressure field after setting the inlet pressure of such closed pores to zero is not as straightforward as it may initially appear. It is clear that ($P_i - P_j$) cannot be known before solving the pressure field and the pressure solution itself depends upon the distribution of closed throats selected, which in turn depends upon comparisons between capillary entry pressures and viscous pressure drops. So how should we proceed?

Blunt and King (1991) and Singh and Mohanty (2003) used an implicit pressure explicit saturation methodology to solve this problem. However, this method may lead to numerical problems at low rates and it becomes very difficult to simulate the invasion percolation like regime (Singh and Mohanty, 2003). Singh and Mohanty (2003) used a pseudo-percolation method below a threshold capillary number equal to 10^{-6}: at each time step, the throat with the highest *"potential"* is opened and the pressure is computed again to calculate the local rates. However, this methodology can also be criticized; as the transition between different regimes happens at different rates for different viscosity ratios and, for extra heavy oil, the effects of viscous forces may be important even at low capillary numbers (Lenormand et al. (1988)). To avoid these issues and to develop a rule free model, where the flow is totally controlled by the pressure gradients, we use the method described below.

The solution to this problem is as follows: (i) initially do not close any pores and solve for the pressure field, (ii) identify closed pores based upon the calculated pressure distribution and capillary entry conditions, (iii) re-solve the pressure field, (iv) iterate (ii)-(iii) until we obtain consistency between the pressure solution and the flowing network of open pores.

5.6. CLOSED PORES

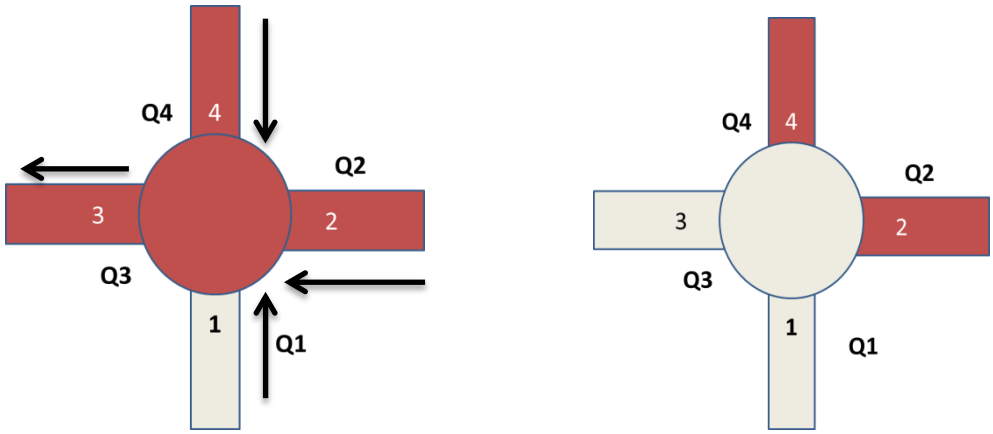

(a) **(b)**

Figure 5.16: A simple example of pore invasion highlighting the importance of closing negative net entry pressure pores. The arrows here are representing the flow directions.

The best way to understand why the flow in pores characterized by a negative net entry pressure ($\Delta P_{net} = P_i - P_j + P_c$) has to be zero, is to consider the simple example shown in Figure 5.16.

The non-wetting phase: water (white) is invading oil filled, oil-wet pores (red). After solving the pressures in the network, the local rates in the pores are computed and the flow directions determined. However, we should bear in mind that the pressure solver does not distinguish between the phases and as a consequence, we may have a situation similar to the one of Figure 5.16 (a), where both oil and water are flowing towards the node (flow directions are shown in the figure using arrows). We assume that, in such a situation, water will invade the pore having a positive net entry pressure; however, this is insufficient as a mass conservation error may occur in this case and inaccurate local rates can be calculated. Using the mass conservation equation we are able to write:

$$Q3 = Q1 - Q2 - Q4 \tag{5.22}$$

This results in having $Q3 > Q1$ whilst Q3 should be equal to Q1 to conserve the mass of the water phase. This issue can be solved by "*closing"* counter-current pores 2 and 4 and changing their conductance to zero in the pressure matrices (in reality we set the conductance to a very small value but not to zero to avoid numerical issues with the solver). Then, we perform a new pressure solution to have a consistent local rate in pore 3.

If the counter-current imbibition pores are not closed, not only will a mass conservation error occur, but the flow paths will also be very affected, as we can see in Figure 5.17 (where we compared simulations of a set of micromodel experiments from the litterature (Lenormand et al., 1988) before and after closing the counter-current pores). These experiments were performed at several injection rates using fluids giving an unfavourable viscosity ratio M=55555. At the lowest rates, capillary fingering was observed in the experiments and in the simulations with closed counter-current pores, whereas the displacement became stable and the water saturations at breakthrough were much higher when these pores were not closed. Furthermore, at the highest rate, whilst the tree shape of the fingers was reproduced when the counter-current pores were closed, the simulations exhibited thicker fingers when this was not done.These results suggest that, in order to reproduce the same flow regimes observed experimentally, it is important to close counter flow pores when solving the pressure field.

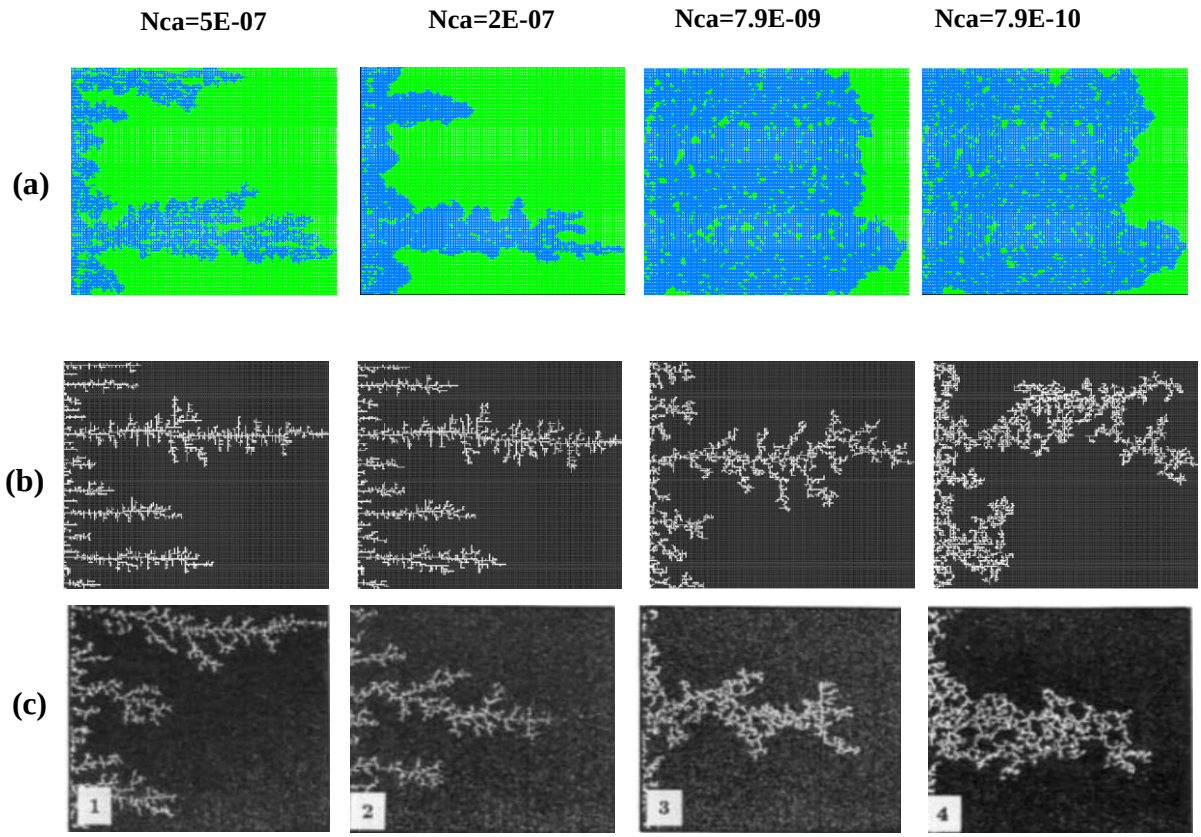

Figure 5.17: A comparison between experimental saturation path at breakthrough and simulated ones performed using a viscosity ratio M=55555 and several injection rates. (a) represents a set of simulations performed without closing the counter flow pores, (b) represents a set of simulations performed after closing counter flow pores and (c) represent the experimental results of Lenormand et al. (1988).

5.7. COUPLING RATE AND INLET PRESSURE

Our simulator provides the possibility of performing both constant differential pressure and constant flux simulations. However, the latter adds another level of complexity to the problem, the *dimensional* inlet pressure is not known *a priori* and a scaling is required once a *dimensionless* pressure field has been calculated. The procedure used to calculate the time-dependent inlet pressure in constant flux simulations is described next.

5.7.1. Single phase flow

Calculating single phase flow is relatively easy because of the linearity between the inlet pressure and the injection/production rate. Initially, the pressure is solved (with boundary conditions P_{in}=1, P_{out}=0) and the non-dimensional rate at the outlet is computed using:

$$q = \sum_{i \in O} \sum_{j \in NB_i} g_{ij}(p_j - p_i) \tag{5.23}$$

where :

- O= {outlet pore bodies} and $NB_i = \{body\ j; j\ is\ a\ neighbour\ of\ node\ i\}$;
- g_{ij}: is the non-dimensional conductance of the throat connecting bodies i and j;
- p_i and p_j: are the non-dimensional pressures at nodes i and j.

Now, the *dimensional* rate at the outlet can be written as:

$$Q = G_s P_{inlet} q \tag{5.24}$$

where G_s is the conductance scale defined earlier as $G_s = \frac{\pi {L_s}^3}{8\mu_s}$

For constant rate simulations, the dimensional rate $Q = Q_{target}$ is fixed by the user and so the dimensional inlet pressure can be found straightforwardly from $P_{inlet} = \frac{Q}{G_s q}$

5.7.2. Two phase flow

In 2-phase flow, the inlet pressure corresponding the target rate is once again not known in advance. Furthermore, the relationship between the inlet pressure and the rate at the outlet is no longer linear when capillary pressure is taken into account (as the value of the inlet pressure actually affects the distribution of pores that are available for displacement).

In order to address this issue, an iterative Secant Method was used to find P_{inlet} satisfying $Q(P_{inlet}) = Q_{target}$

At each iteration, the following steps are followed:

We calculate the inlet pressure at the kth+1 iteration from:

$$P_{inlet\ k+1} = P_{inlet\ k} - (P_{inlet\ k} - P_{inlet\ k-1}) \frac{(Q(P_{inlet\ k}) - Q_{target})}{(Q(P_{inlet\ k}) - Q(P_{inlet\ k-1}))} \tag{5.25}$$

Using this inlet value, the pressure field is then computed, the corresponding rate is calculated, closed pores are identified and their conductances are set to zero. The pressure is then re-solved under the new conditions. If newly closed/opened pores are identified, they are closed/opened and the pressure field is calculated once again – the procedure is repeated until all closed/open pores are identified and the rate at the outlet is consistent with the target injection rate.

This method can be made faster by carefully choosing $P_{inlet\,k}$ and $P_{inlet\,k-1}$ in the first iteration. One of the starting points is the previous step inlet pressure, which is generally close to the current solution. The second point is found by calculating a fast approximate solution via a modified version of the secant method described previously. Only the pores satisfying $|P_c| > P_{inlet}$ are closed and such pores can be determined before solving the pressure. As a consequence, we calculate relatively fast an approximate solution which is not "*correct"* as it does not consider all the pores that need to be closed but that represents a good approximation and is considered as the second starting point of the secant method described earlier in this section. If the starting points of the algorithm are chosen properly, the inlet pressure corresponding to the target injection rate, as well as the pressure solution and the onset of closed/open pores is generally found in one or two iterations.

As discussed in Chapter 4 the assumption of considering that there is a flow between two nodes only if the pressure is higher than the threshold capillary entry pressure is not new was used in several dynamic PNM (Lenormand et al (1988), Dias and Payatakes (1986), Koplik and Lasseter (1985) and Blunt and King (1990)). The main difference between all these models is the way to solve this non-Linear problem. Blunt and King (1990) used IMPES method, Lenormand et al (1988) used a relaxation technique to solve the pressure field, and Koplik and Lasseter (1985) used a trial technique were they investigated all the possible combinations of elementary displacements. The main difference between our model and these models is the way we identified the pore elements having a zero flow and the way we coupled the injection rate with the inlet pressure. The second difference is the void space representation we used the 3Rs approach in our model and these authors used volumeless throats and pore bodies without resistance. Finally, in our model we were tracking the meniscus and considering the capillary pressure even when the pore element is partially filled. However, in the model of Lenormand et al (1988) the capillary pressure was considered only as an entry condition and once the meniscus is inside a pore element the capillary pressure was not considered in the flow equations.

5.8. MULTIPLE-PORE FILLING

Once the nodal pressures are computed, we go on to fill the pores and update the menisci using a multiple pore filling algorithm. First, we loop through the throats situated at the interface and, for every throat; a net driving pressure ΔP_{net} is calculated:

$$\Delta P_{net} = P_i - P_j + P_c \tag{5.26}$$

If the net driving pressure is positive, water will be able to invade that pore and the time required to completely invade it is computed as:

$$t = \frac{V_{pore}(1 - S_w)}{\Delta P_{net} G_{ij}} \tag{5.27}$$

where S_w is the water saturation in that pore and V_{pore} is the volume of the pore.

The minimum filling time t_{min} across the entire network is found, the pore having the shortest filling time is completely invaded with water, and menisci are updated in all other pores having $t > t_{min}$ (Figure 5.18).

The water saturation is updated in each pore element and the new water saturation is computed from:

$$S_{w\,new} = S_{w\,old} + \frac{t_{min} * \Delta P_{net} * G_{ij}}{V_{pore}} \tag{5.28}$$

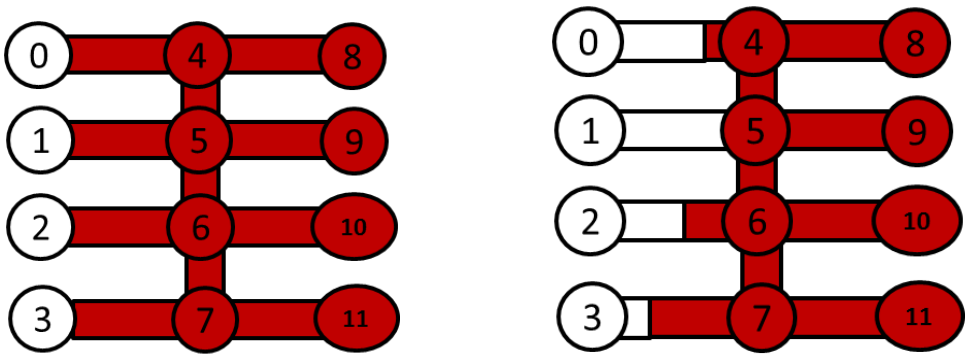

(a) **(b)**

Figure 5.18: An example illustrating the multiple filling algorithm in a case where water (white) invades oil filled pores. (a) represents the pores occupancy before the invasions and (b) shows the fluids distributions after the invasions.

5.9. CLUSTERING ALGORITHM

Clustering is an important process in pore network models as it helps in identifying the defending phase pores that are not connected to the outlet (and are considered trapped). Most of the pore network models published in the literature (Al-Futaisi and Patzek, 2003, Piri and Blunt, 2005, McDougall, 1994) use a Hoshen-Kopelman (Hoshen and Kopelman, 1976) algorithm or a slightly modified version of this method to label the clusters. This algorithm needs to do a loop through all the pores in the network at least once at every time step. For our model, we do not need to do clustering from scratch at every time step and it is sufficient to track the *changes* in the clusters after each invasion

and update the existing clusters. This is computationally more efficient and allows us to perform larger simulations.

At the beginning of the simulation, the oil phase forms one cluster. Then, after a new water invasion, 3 possible scenarios may occur (Figure 5.19):

Separating an existing oil cluster: In this case, the water invasion divides an existing oil cluster into two new clusters. To see whether we are in this situation we check if there is any oil path linking the old oil cluster after the new water invasion using a *Brute force algorithm*. If no alternative path is found, we split the old oil cluster into 2 new clusters.

Extending water cluster only: In this case, an alternative oil path exists linking the pre-existing oil cluster, the water cluster is extended by adding the newly invaded pore and keeping the same labelling in the oil cluster.

Joining a water cluster: In this situation, the water phase joins a pre-existing water phase cluster and, the 2 water clusters are merged, forming one water cluster.

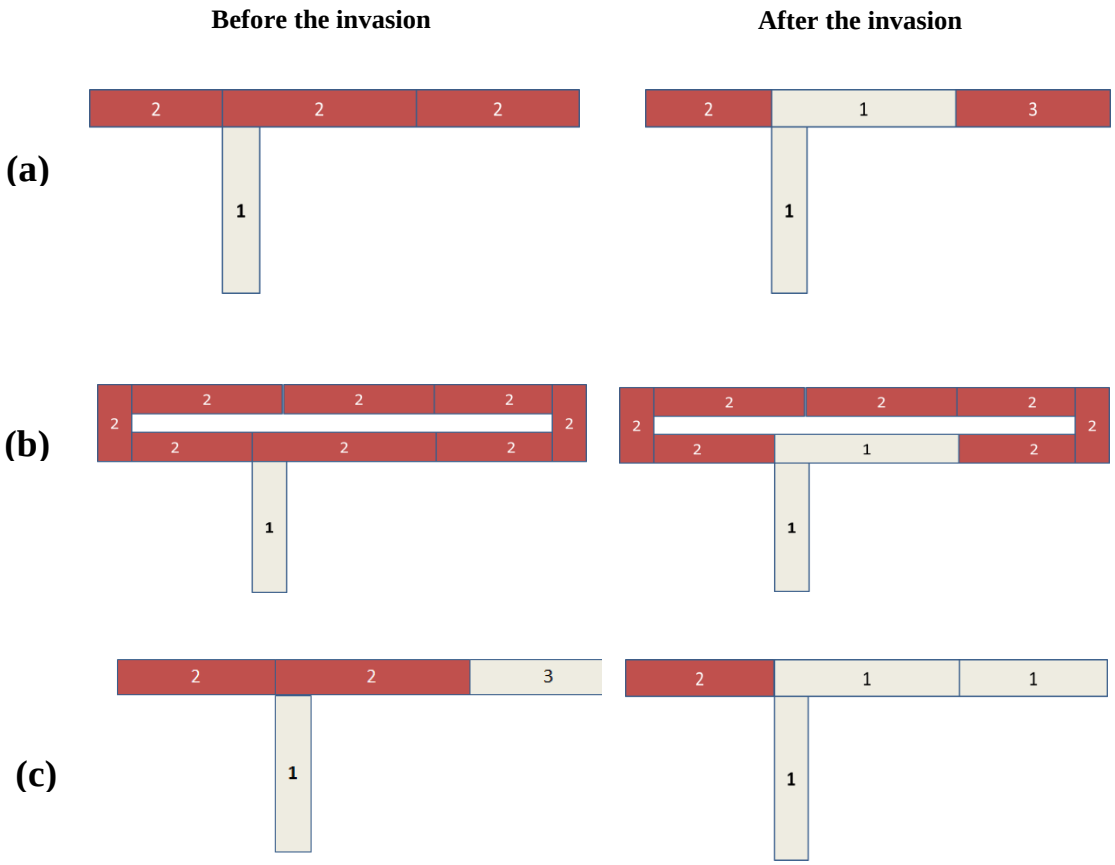

Figure 5.19 : Different scenarios to update clusters: Separating an existing oil cluster (a), Extending water cluster only (b) and joining a water cluster (c).

After updating the clusters, we check to see if new oil clusters are formed; if this is the case we do a *Brute force* check to verify if they are connected to the outlet. Otherwise, they are considered trapped and the conductances of all the corresponding pores are set to zero.

Chapter 6: Model validation

6.1. INTRODUCTION

Having built the dynamic drainage model, we now go on to validate it against available experimental data. As a first test, a network was constructed to simulate the micromodel experiments reported in the ground-breaking paper of Lenormand et al. (1988) ─ the experiments are first described and compared against the simulations from the model. This serves as a useful benchmarking exercise and should provide additional confidence in our modelling approach if our model is able to reproduce the same flow regimes as those observed in the experiments.

6.2. DESCRIPTION OF THE EXPERIMENTS

We begin this chapter with a brief review of a series of micromodel experiments undertaken by Lenormand and co-workers in the late 1980s.

Lenormand et al. (1988) fabricated transparent micromodels by means of a newly developed moulding technique using transparent polyester resin and a photographically etched mould. Etched ducts with rectangular cross-section were situated inside the resin and this constituted the 2D analogue of the pore space. The micromodels (15cm*13.5 cm) had regular etched networks with a coordination number equal to 4 and the bonds had a uniform pore size distribution with varying radii between 115μm and 345μm. An example of these micromodels is presented in Figure 6.1.

Lenormand et al. (1988) used a wide variety of fluids in their experiments:

- Coloured aliphatic oils with viscosities varying from 0.32 cP to 1000 cP were generally used as wetting phases (except for experiments using mercury and air);
- Glucose aqueous solutions with viscosities varying from 1 cP to 4700 cP were used as the non-wetting phase with oil;
- Air was used as a non-wetting phase with oil and as a wetting phase with mercury;
- Mercury was always a non-wetting fluid and its high surface tension and low viscosity (1.55 cP) enabled experiments with very low capillary numbers to be performed.

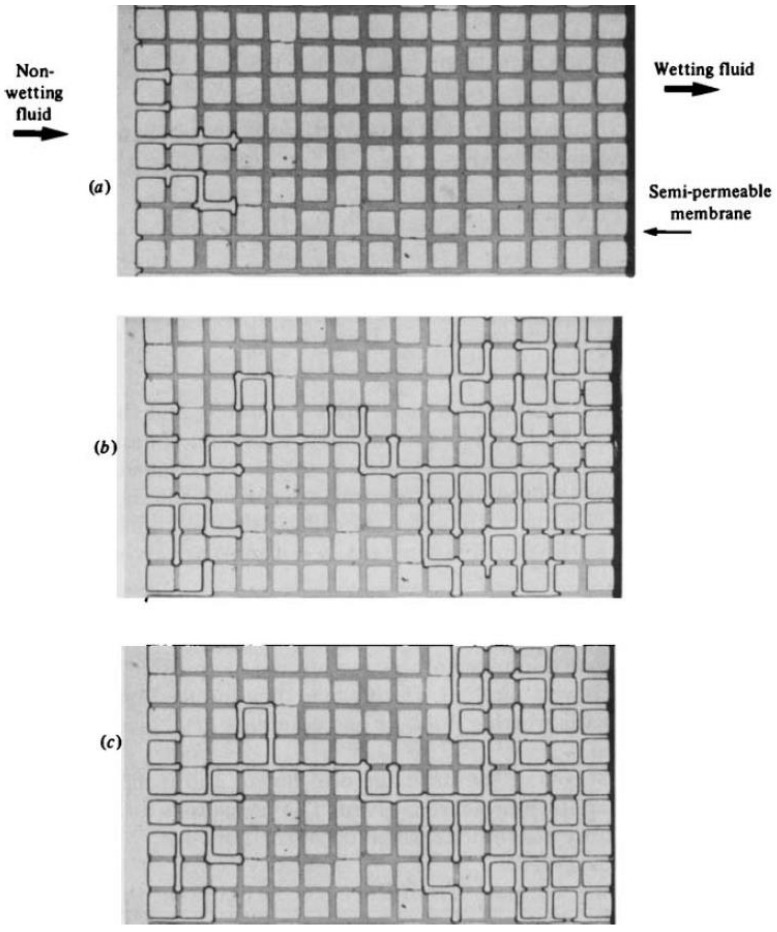

Figure 6.1: An example of the networks used by Lenormand et al. (1988). The non-wetting fluid is injected at the left of the picture (Lenormand et al., 1983).

An extensive range of different fluid combinations and flow rates were used in order to investigate the different flow regimes over a wide range of viscosity ratios and capillary numbers. Table 6.1 summarizes the various fluid combinations considered. In this table, Hg, W, O, H and A denote mercury, glucose aqueous solution, oil, hexane, and air respectively.

In all cases, the non-wetting phase was injected using a constant flow rate syringe pump and the models were horizontal to avoid gravitational effects.

Experiment	μ invading (cP)	μ defending (cP)	σ (dyne/cm)	M(μdef/μinv)	Nca
A-O 1	0.018	1000	20	5.56E+04	5.01E-07
A-O 2	0.018	1000	20	5.56E+04	2.00E-07
A-O 3	0.018	1000	20	5.56E+04	7.94E-09
A-O 4	0.018	1000	20	5.56E+04	7.94E-10
Hg-O 1	1.55	1000	370	6.45E+02	7.94E-07
Hg-O 2	1.55	1000	370	6.45E+02	1.58E-07
Hg-O 3	1.55	1000	370	6.45E+02	2.51E-08
Hg-O 4	1.55	1000	370	6.45E+02	2.51E-09
Hg-O 5	1.55	1000	370	6.45E+02	3.98E-10
Hg-O 6	1.55	100	410	6.45E+01	7.94E-07
Hg-O 7	1.55	100	410	6.45E+01	1.58E-07
Hg-O 8	1.55	100	410	6.45E+01	2.51E-08
Hg-O 9	1.55	100	410	6.45E+01	2.51E-09
Hg-O 10	1.55	100	410	6.45E+01	3.98E-10
Hg-O 11	1.55	5.6	450	3.61E+00	7.94E-07
Hg-O 12	1.55	5.6	450	3.61E+00	1.58E-07
Hg-O 13	1.55	5.6	450	3.61E+00	2.51E-08
Hg-O 14	1.55	5.6	450	3.61E+00	2.00E-09
Hg-O 15	1.55	5.6	450	3.61E+00	3.98E-10
Hg-H 1	1.55	0.32	470	2.06E-01	1.00E-05
Hg-H 2	1.55	0.32	470	2.06E-01	6.31E-07
Hg-H 3	1.55	0.32	470	2.06E-01	2.00E-08
Hg-H 4	1.55	0.32	470	2.06E-01	2.00E-09
Hg-A 1	1.55	0.018	480	1.16E-02	3.98E-05
Hg-A 2	1.55	0.018	480	1.16E-02	7.94E-06
Hg-A 3	1.55	0.018	480	1.16E-02	1.26E-06
Hg-A 4	1.55	0.018	480	1.16E-02	7.94E-09
W-O 1	570	5.6	14.5	9.82E-03	1.00E-01
W-O 2	570	5.6	14.5	9.82E-03	1.00E-03
W-O 3	570	5.6	14.5	9.82E-03	1.58E-04
W-O 4	570	5.6	14.5	9.82E-03	6.31E-06
W-O 5	4700	5.6	14.5	1.19E-03	1.26E-01
W-O 6	4700	5.6	14.5	1.19E-03	7.94E-03
W-O 7	4700	5.6	14.5	1.19E-03	2.51E-03
W-O 8	4700	5.6	14.5	1.19E-03	3.98E-04

Table 6.1: Fluids properties and capillary numbers of the different micromodel experiments (Lenormand et al., 1988).

6.3. COMPARISONS BETWEEN EXPERIMENTS AND SIMULATIONS

In this section, we design a network model that mimics the experimental set-up described in Lenormand paper ─ the primary aim here is to check if the developed simulator is able to reproduce the same flow regimes as those observed in the laboratory.

As seen in Figure 6.1, the micromodel topology is very close to a bond-only network ─ there are no large pore bodies surrounded by narrow pore throats, and so our bond model seems appropriate. The pore radii were assigned stochastically from the reported experimental pore size distributions and the experimental fluid properties and injection rates were used as inputs for the simulations. *We stress here that there was no attempt to history match the experimental observations* – the inputs to the model were simply those reported in the published paper (Table 6.1).

6.3.1. Simulation of experiments with favourable viscosity ratio

Several experiments were performed using a favourable viscosity ratio and we now compare qualitatively the saturation maps at breakthrough in both experiments and simulations.

At low rates, an invasion percolation like pattern was obtained and this displacement is controlled by the capillary entry pressures of the pores at the interface between the invading and defending fluids ─ the largest pores having the lowest capillary entry pressure are invaded first. This regime is characterised by invasions happening in all directions (even towards the inlet in some cases) and this leads to the occurrence of loops that can trap large quantities of oil. This behaviour was reproduced by the simulator as shown in Figures 6.2 and 6.3. These figures also show that an increase in rate reduced the frequency of loop formation, resulting in less trapped fluid and better sweep efficiency. At high rates, the displacements became stable ─ the interface between the fluids became flat and very small volumes of the defending fluid were trapped. It should be noticed that for all the simulations with a favourable viscosity

ratio, very good qualitative agreement was found and all the flowing regimes were reproduced by the simulator (Figures 6.2, 6.3, 6.4 and 6.5). However, we should bear in mind that the network is only statistically equivalent to the experimental micromodel and we do not know the exact radius of each physical pore. As a consequence, we should not expect to match the exact displacement paths in the simulations (only the regime).

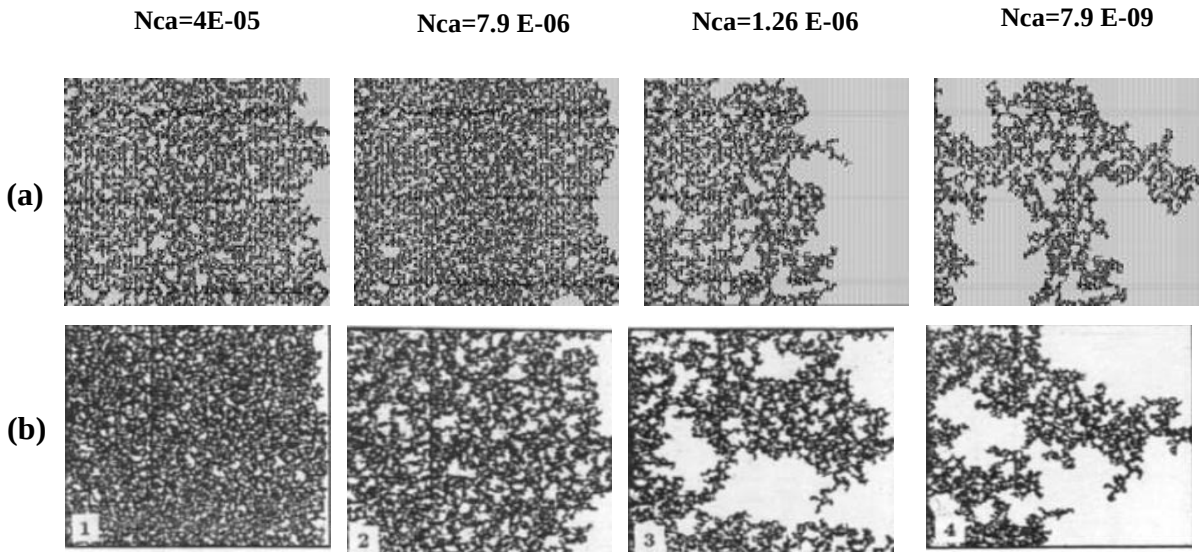

Figure 6.2 : Comparison between (a) simulations and (b) experiments of Mercury (Black) displacing air (white) (viscosity ratio M=0.0111).

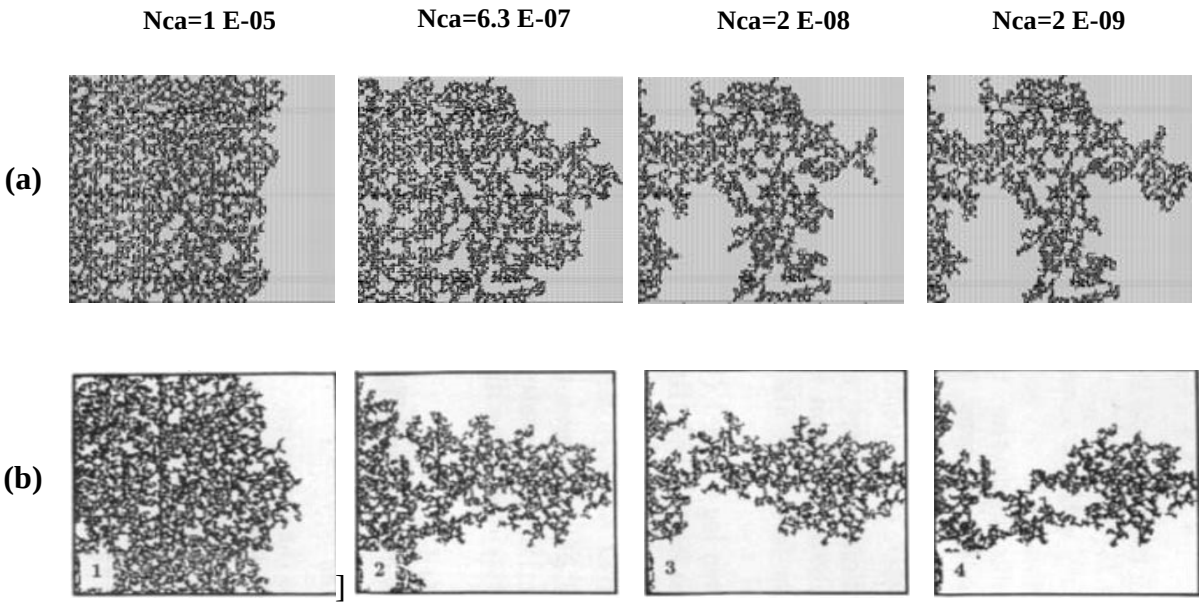

Figure 6.3: Comparison between (a) simulations and (b) experiments of Mercury (black) displacing hexane (white) (viscosity ratio M=0.2).

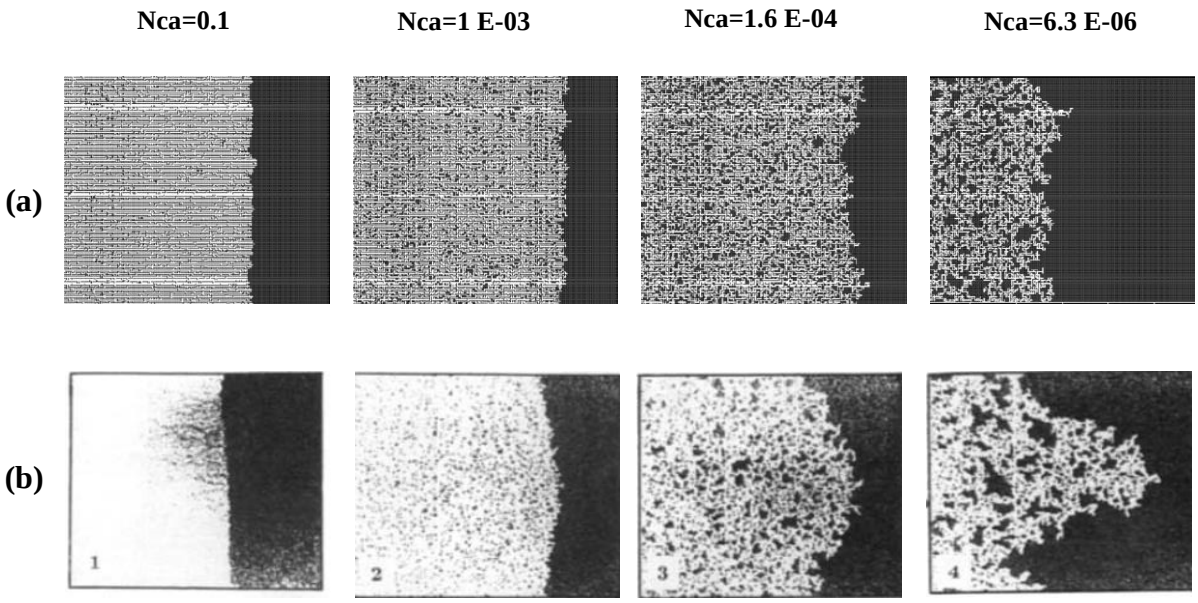

Figure 6.4: Comparison between (a) simulations and (b) experiments of Glucose solution (white) displacing oil (black) (viscosity ratio M=0.0098).

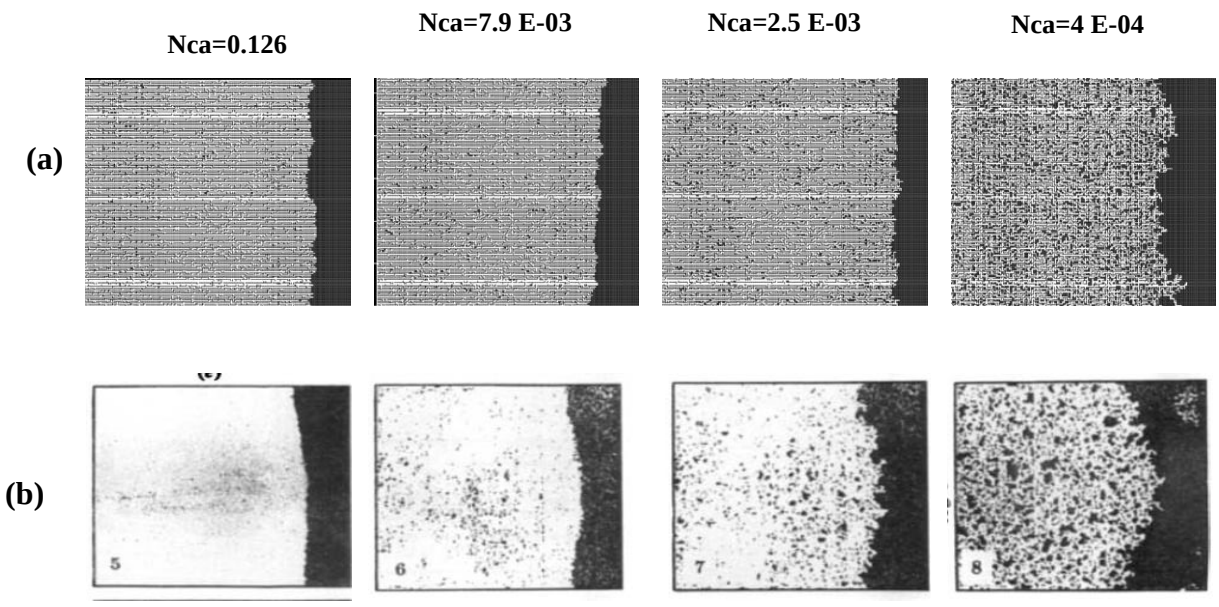

Figure 6.5: Comparison between (a) simulations and (b) experiments of Glucose solution (white) displacing oil (black) (viscosity ratio M=0.001).

6.3.2. Experiments with adverse viscosity ratio

In the unfavourable viscosity ratio experiments, the flow regimes observed were very different from the favourable viscosity ratio cases. Again, at low rates, capillary fingering was obtained and an invasion percolation like pattern was observed (with the occurrence of loops trapping large volumes (Figures 6.7, 6.8 and 6.9)). However, as the injection rate increased, the fingers became thinner and sharper until a clear viscous fingering regime was reached at high rates (Figure 6.6). In this regime, elongated tree shaped fingers were formed that grew towards the outlet leading to a very poor sweep efficiency at breakthrough.

Figure 6.10 shows the different stages of viscous finger initiation and growth ─ we notice an excellent qualitative agreement between the simulations and the experiments. In both cases, several fingers were initiated, with some subsequently growing faster and leaving the other instabilities behind.

Once again, a very good agreement was found with the experiments and all of the observed flow regimes were reproduced over a wide range of viscous ratios and capillary numbers (Figures 6.6 -6.10). Note again, however, that we are not expecting to reproduce the fingers at precisely the same locations as observed in the experiments, as we are only reproducing the network stochastically.

6.4. CONCLUSIONS

In this chapter, our model was tested against 35 micromodel experiments from the literature and excellent agreement has been found with all the experimental data. All of the observed flowing regimes (stable displacement, viscous fingering and capillary fingering) were reproduced as well as the transitions between them. No tuning parameters were required to reproduce the laboratory observations: the parameters reported in the experimental papers were simply used as inputs for the simulation.

Although the Lenormand experiments were performed nearly three decades ago, it appears that the only published model that has been able to reproduce the displacement

regimes of all the experiments reported in that paper is the one developed during this study (Regaieg et al 2014). This gives us additional confidence in our in-silico approach and we next go on to apply this framework to the simulation of slab scale experiments of water injection into heavy oil.

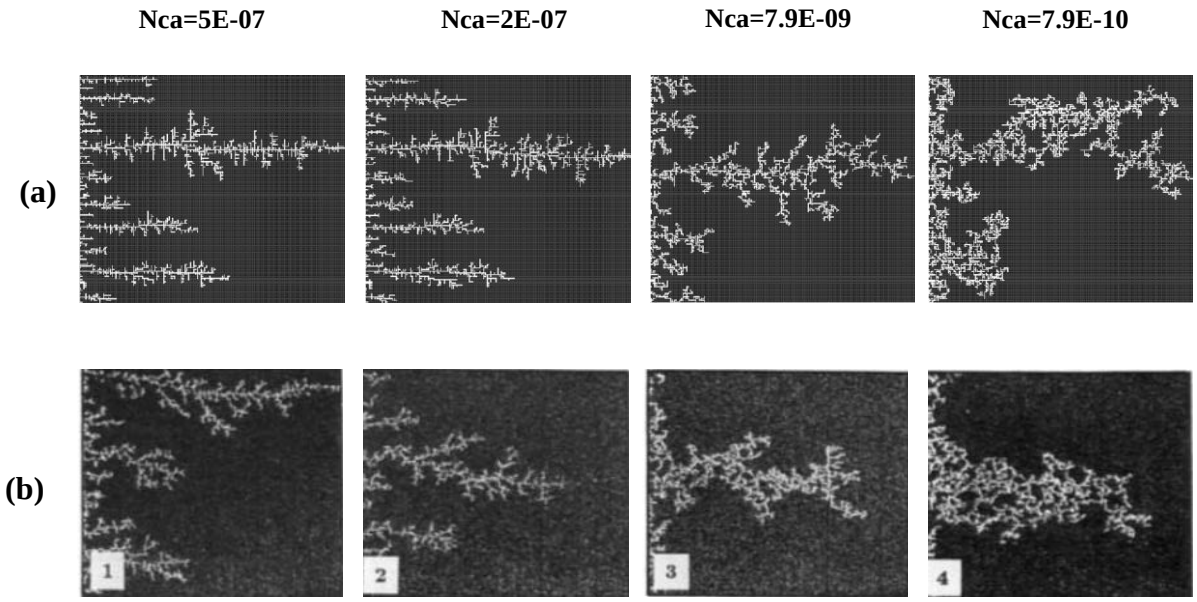

Figure 6.6 : Comparison between (a) simulations and (b) experiments of Air (white) displacing heavy oil (viscosity ratio M=55555).

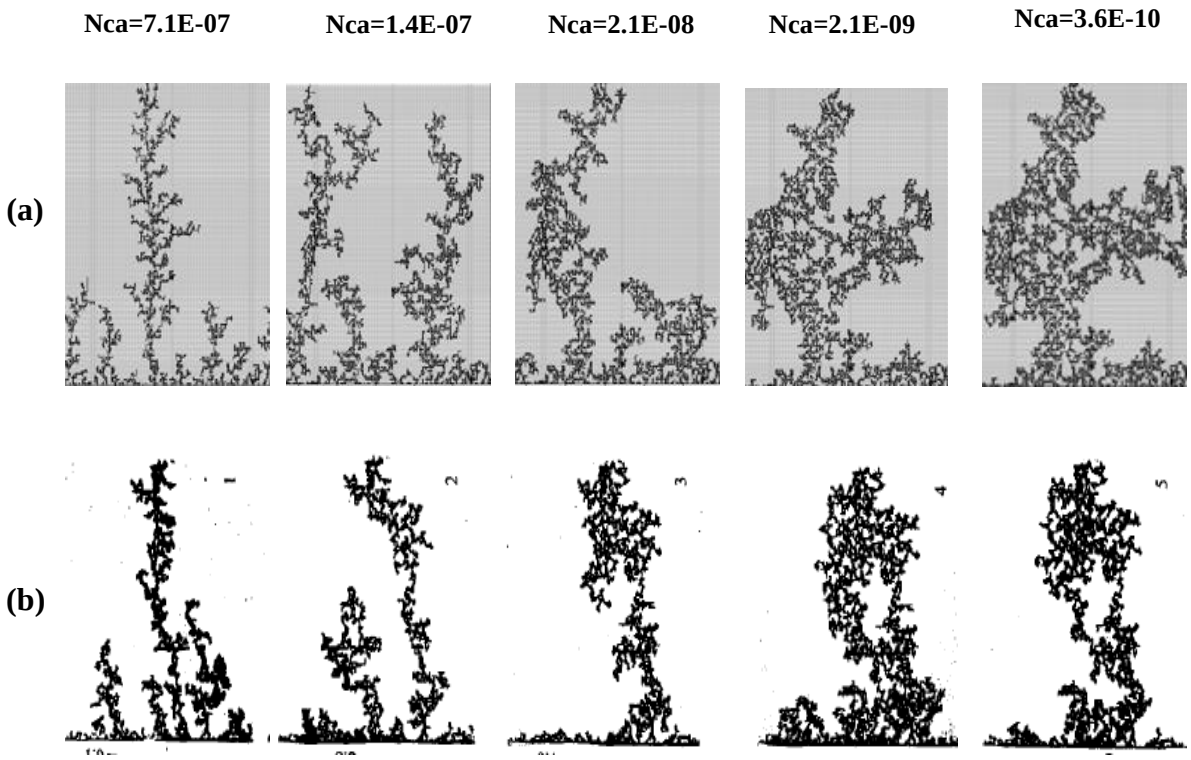

Figure 6.7: Comparison between (a) simulations and (b) experiments of Mercury (black) displacing oil (white) (viscosity ratio M=645).

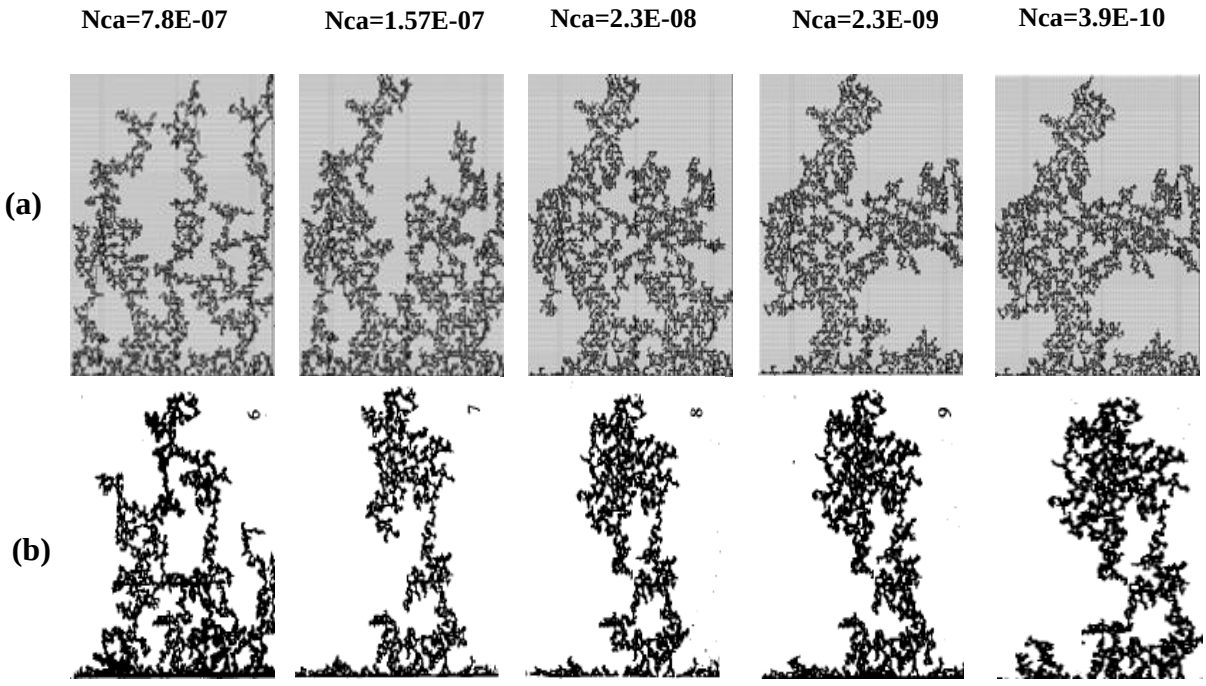

Figure 6.8 : Comparison between (a) simulations and (b) experiments of Mercury (black) displacing oil (white) (viscosity ratio M=64.5).

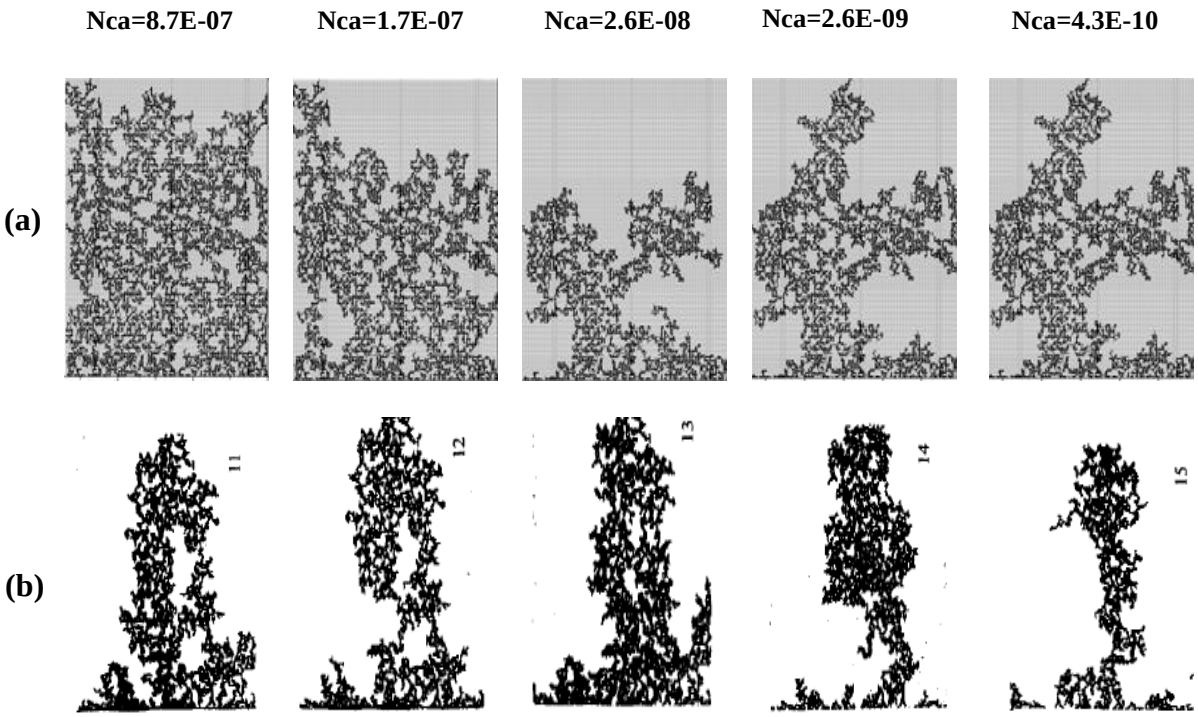

Figure 6.9: Comparison between (a) simulations and (b) experiments of Mercury (black) displacing oil (white) (viscosity ratio M=3.6).

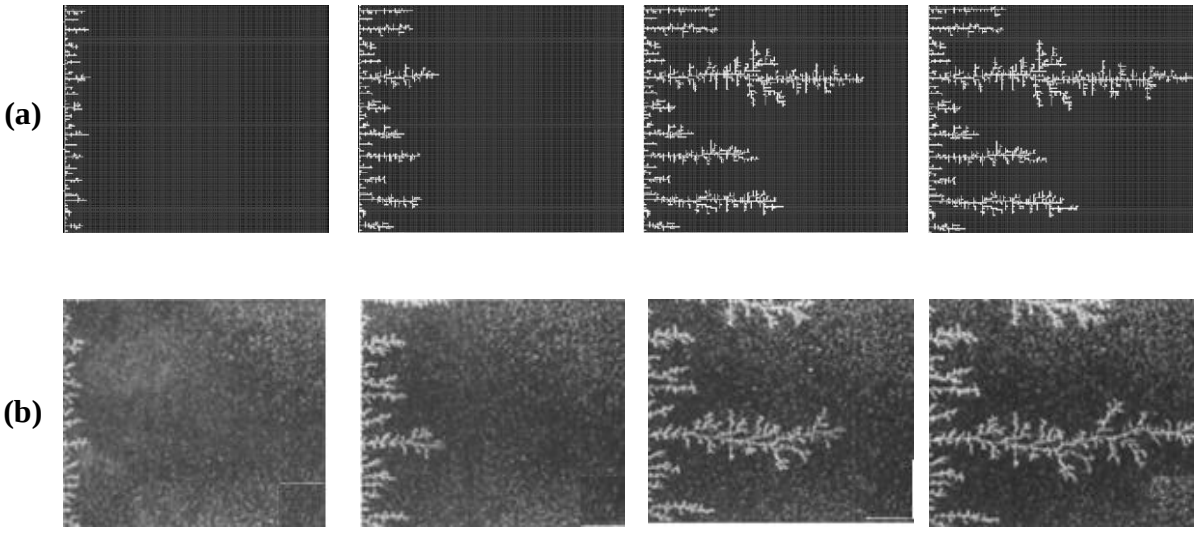

Figure 6.10 : Different stages of displacement of a heavy oil by air during (a) the simulation and (b) the experiment (viscosity ratio M=55555).

Chapter 7: Slab scale simulations of waterflooding experiments in heavy oil

7.1. INTRODUCTION

Although thermal methods have been popular and successfully applied in heavy oil recovery, they are often found to be uneconomic or impractical. Therefore, alternative production protocols are being actively pursued and an interesting option is water and/or polymer flooding. Such a technique has been successfully tested in laboratory investigations, where oil recovery was found to be much higher than expected (Bondino et al., 2011, Skauge et al., 2012).

However, despite encouraging results, these experimental studies showed that the mechanisms governing water displacing extra heavy oil are still poorly understood. This means that the optimization of this process for eventual field applications is still problematic and, ideally, a combination of experimental and simulation efforts should be put in place.

As we have seen in Chapter 2, conventional reservoir simulators are not able to accurately simulate viscous fingering during immiscible displacements because they fail to take into account pore scale mechanisms that govern these instabilities. Furthermore, whilst previous pore network simulators have had some success in simulating viscous fingering phenomena, most of the published studies have been performed at a very small scale (Joekar-Niassar and Hassanizadeh (2012)).

We have presented in Chapter 5 a newly developed pore network model that is highly efficient and able to reproduce viscous fingering phenomena. This simulator has subsequently been validated against various micromodel experiments (Chapter 6) where we demonstrated its ability to simulate all the observed flowing regimes and the transitions between them.

In this chapter, we go on to carry out a range of slab-scale (30cm x 30cm) simulations and compare them against the corresponding experimental observations of Skauge et al. (2012). Reproducing these experiments represents a first step in building a better understanding of the physics behind water displacing extra heavy oil. We start by describing the experiments themselves.

7.2. DESCRIPTION OF THE EXPERIMENTS

A number of experiments involving water and polymer injection into extra heavy oil have been performed recently using 30cm x 30cm x 2cm slabs of Bentheimer sandstone (precise details of the experimental procedures adopted can be found in (Skauge et al., 2012)). The Bentheimer slabs used in the study were relatively homogenous in nature, with a porosity of approximately 24% and permeability of around 2.5 Darcies, and were installed vertically into an X-ray scanner after having been sealed with epoxy resin. The densities of the oil and water were very close to one another and, as a consequence, the displacements were considered to be unaffected by gravitational instabilities.

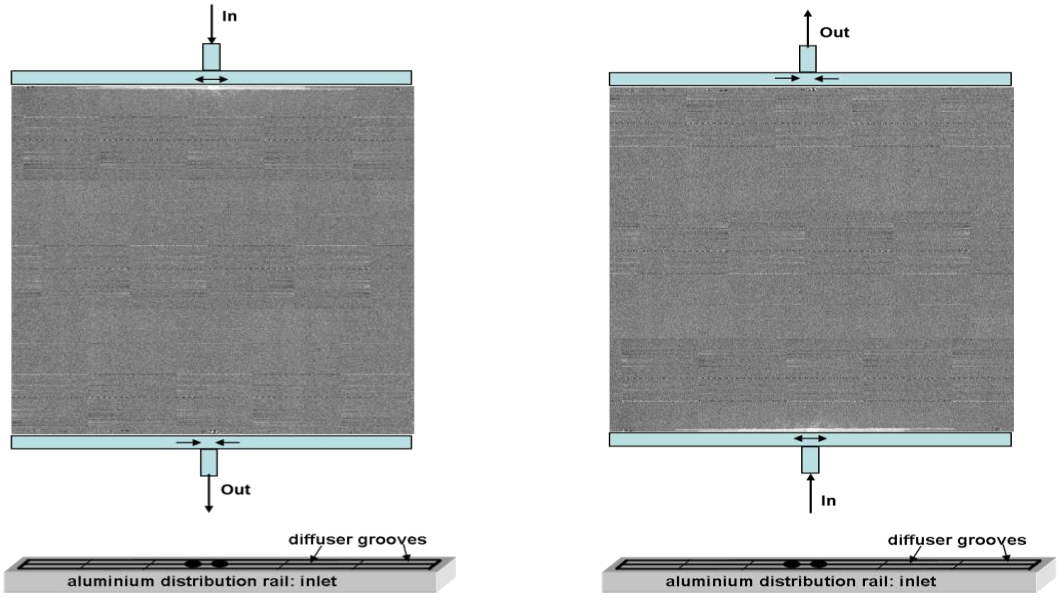

(a) (b)

Figure 7.1: Boundary conditions used in (a) E2000 and (b) E7000 experiments

Rail distributors were installed along the inlet and outlet edges of the slabs (Figure 7.1), with each rail having a central injection/production point and a groove to distribute the fluids across the entire inlet/outlet cross section. Each rock was dried at 80°C, vacuum saturated with 7g/l NaCl brine, and then oil was injected. The slab was subsequently aged for 3 weeks at 50°C. Two water injection experiments were reported: (i) experiment E7000, using 7000 cP oil with brine injected from the bottom of the slab, and (ii) experiment E2000, where 2000 cP oil was used and injection was performed from the top of the slab.

E7000 was characterised by an early water breakthrough after 0.04 PV injected, followed by a rapidly-increasing water-cut that reached 90% after 0.6 PV. After 2.3 PV injected, 20% of the OOIP had been recovered and, at the end of the waterflood (5.1 PV), this had increased to 26.4% – the water cut at this late stage was very high (~99%). Similar early water breakthrough behaviour was observed in the E2000 experiment

(0.043 PV injected) but the oil recovery was substantially higher (28.5% of oil had been recovered after 2.3 PV injected versus 20% for E7000).

The displacement regime during the waterflooding was similar in both experiments (as inferred from X-ray data) and examples of the patterning from both experiments are shown in Figures 7.2 and 7.3. Initially, sharp viscous fingers were observed and these grew rapidly towards the outlet edge of the slab. The fingers appeared more dendritic in the E7000 experiment and some instabilities were seen to propagate faster than others, preventing the growth of some of the smaller fingers (Figure 7.2 and Figure 7.3). Following water breakthrough, fingers throughout the slab appeared to thicken and coalesce, forming broad water channels and leading to an improvement in sweep efficiency.

Figure 7.4 compares the oil recovery, water cut and differential pressures measured in both experiments. We observe a better recovery in E2000 experiment, a lower water cut and a lower differential pressure.

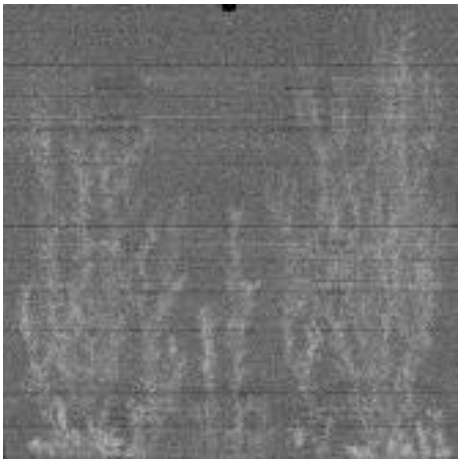

0.028 PV inj

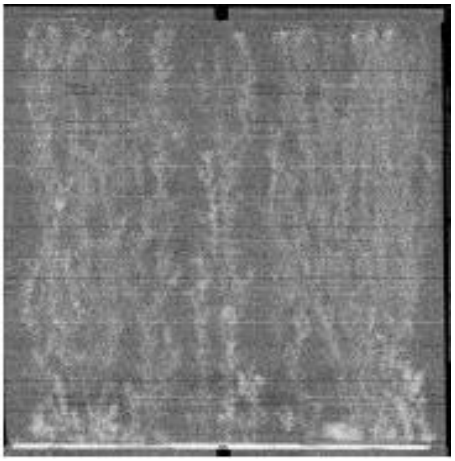

0.04 PV inj

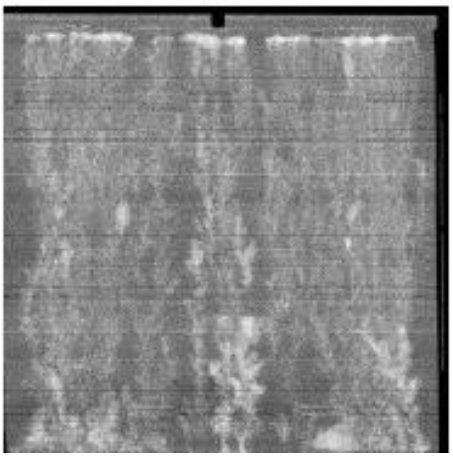

0.24 PV inj

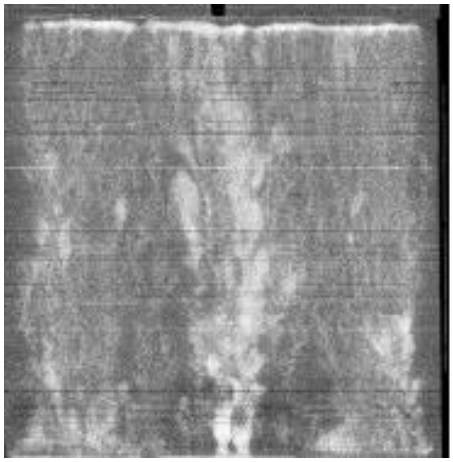

0.72 PV inj

Figure 7.2: X-Ray images of saturation maps of E7000 experiment for different injected pore volumes (Skauge et al., 2012). The water (white) is injected from the bottom to displace the oil (black).

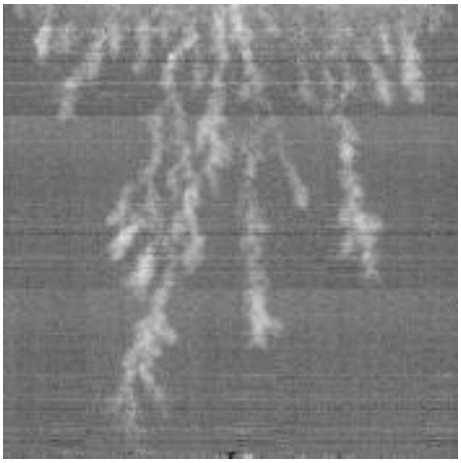

0.038 PV inj

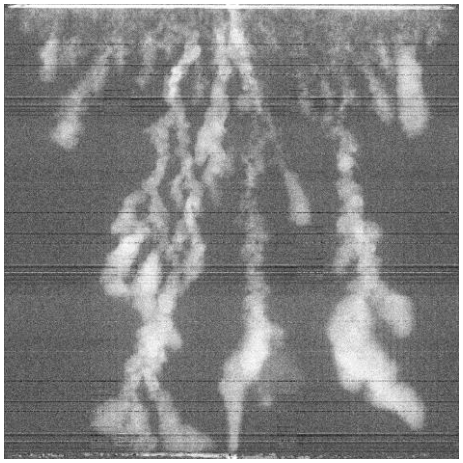

0.14 PV inj

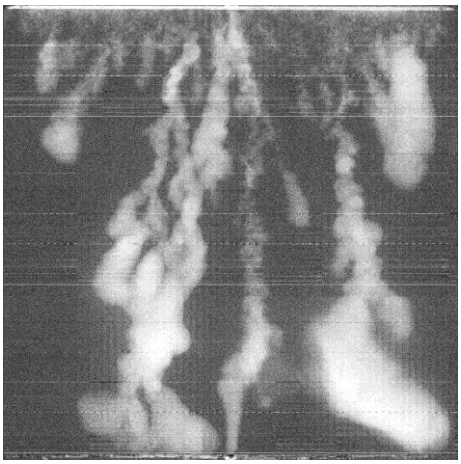

0.39 PV inj

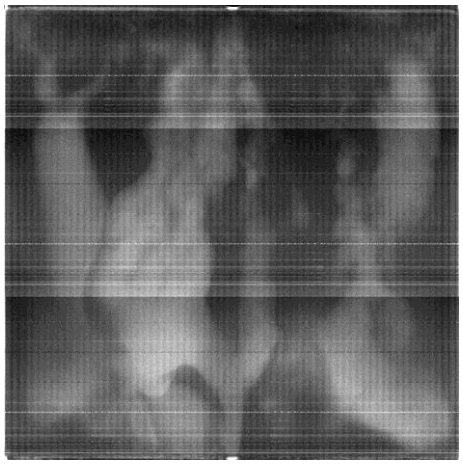

2.26 PV inj

Figure 7.3: X-Ray images of saturation maps of E2000 experiment for different injected pore volumes (Skauge et al., 2012). The water (white) is injected from the bottom to displace the oil (black).

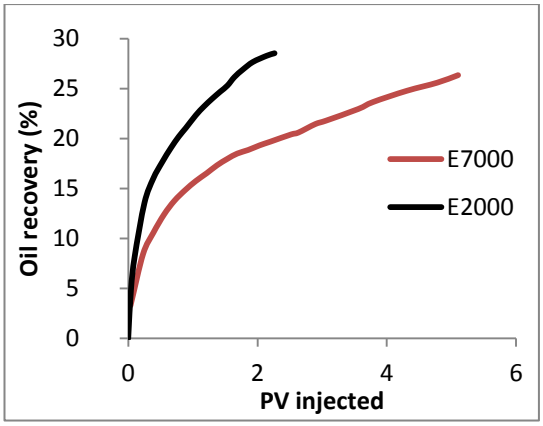

(a)

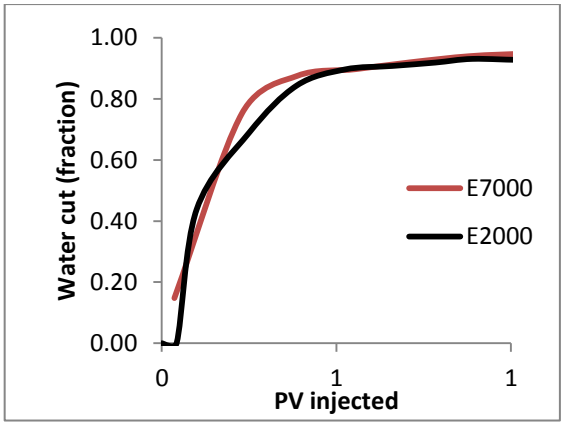

(b)

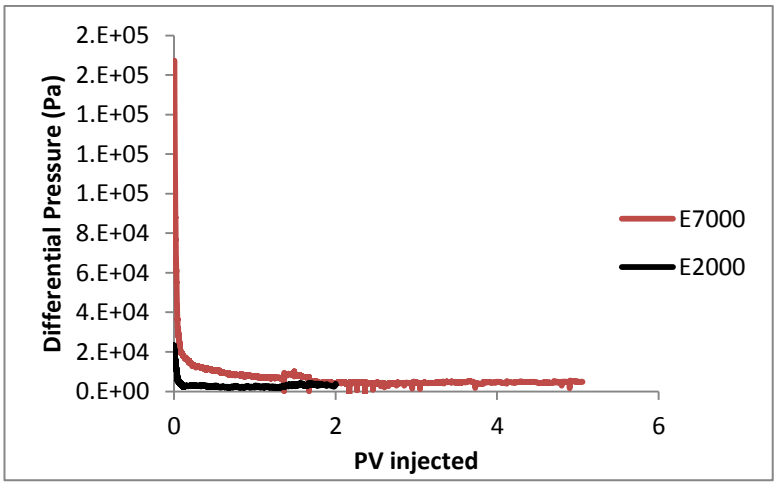

(c)

Figure 7.4: Comparison between (a) Oil Recovery, (b) Water cut and (c) Differential Pressure in E2000 and E7000 experiments.

7.3. SLAB SCALE SIMULATIONS

A series of slab scale simulations has been performed using rock/fluid data and injection protocols corresponding to those characterising the E7000 and E2000 experiments. We have restricted ourselves at present to large-scale 2D simulations in order to focus on finger morphology and development – consideration of the third dimension is conceptually straightforward but computationally expensive. However, performing 2D simulations requires appropriate scaling of the injection rate and this will now be discussed.

7.3.1. Capillary number in two dimensional simulations

The capillary number describes the ratio of viscous to capillary forces acting during two-phase flow in porous media and is generally defined as:

$$\mathrm{Nca} = \frac{Q\mu_{displacing}}{\sigma A} \tag{7.1}$$

where Q is the injection rate, A is the cross section of the inlet injection face, σ is the interfacial tension and $\mu_{displacing}$ is the viscosity of the displacing phase.

However, in 2D simulations, the cross sectional area of the medium (*A*) is not well defined. To avoid this issue, the definition has been adapted here to 2D systems by simply considering the total *flux* of invading fluid. By ensuring that the 2D network receives the same flux of fluid as the 3D experiments, their capillary numbers should be equivalent. In fact, Figure 7.5 shows two sets of simulations performed using the same viscosity ratio (M=7000) and different injection rates. The first set was performed using a 2D network and the second using a 3D network: the figure shows the water saturation at breakthrough plotted against capillary number. Whilst the same behaviour was obtained in both cases, the water saturation at breakthrough was lower in the 3D case at high capillary numbers, (corresponding to viscous fingering), which was as expected due to the difference in the dimensionality between the two cases.

In addition, Figure 7.6 compares two sets of 3D and 2D simulations having the same capillary number showing that the same flow regimes were obtained at the same capillary numbers for both 2D and 3D runs.

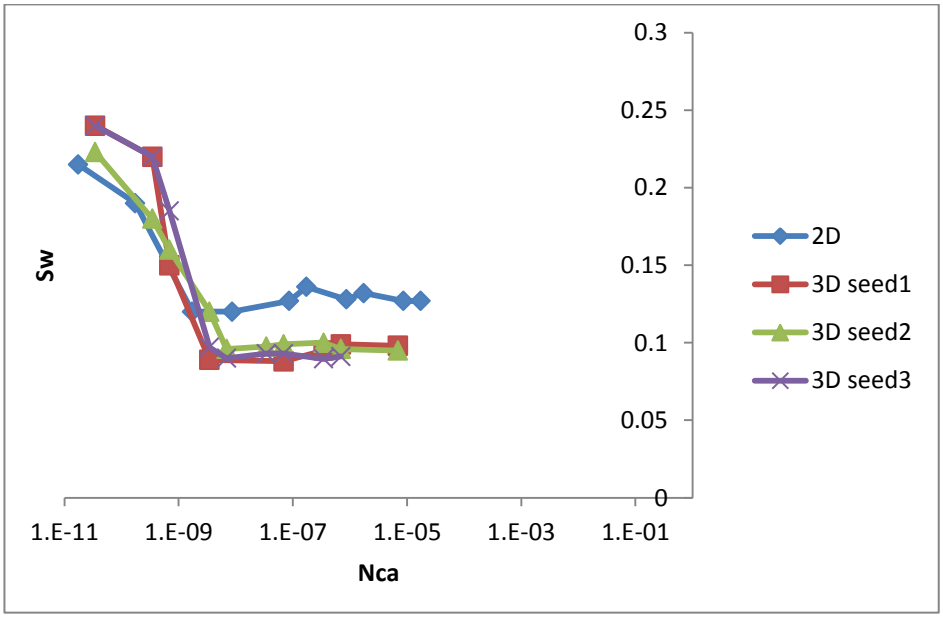

Figure 7.5: Water saturation at breakthrough for several capillary number values. In this figure two sets of simulations are presented: a 2D case (blue) and a 3D case using 3 seeds (red, green and purple). The viscosity ratio was equal to M=7000 for both sets of simulations.

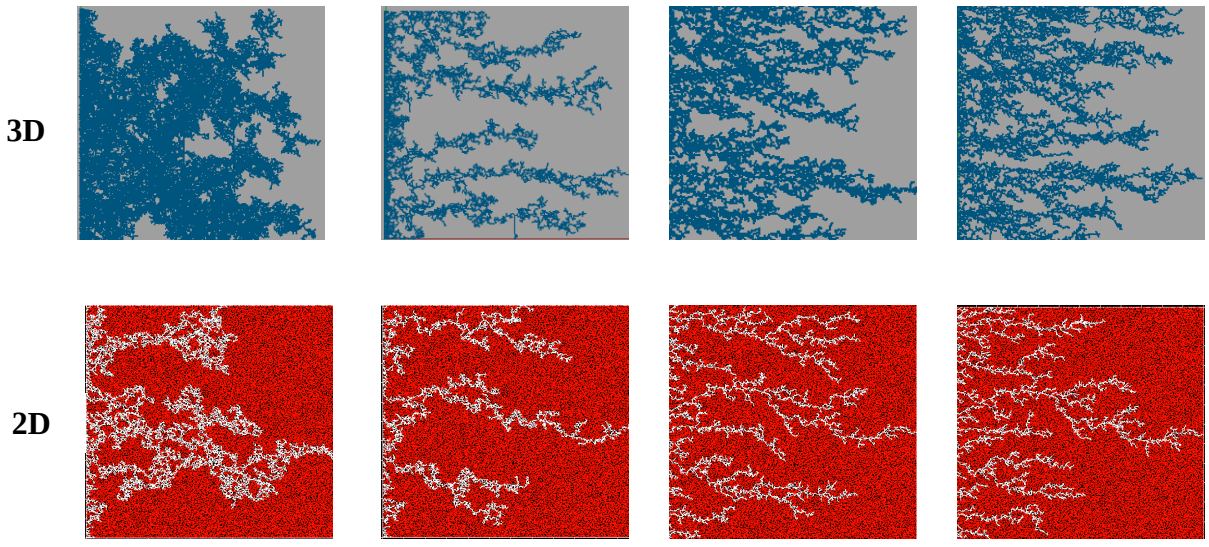

(a) (b) (c) (d)

Figure 7.6: comparison between 2D and 3D simulations for M=10 and the same capillary number: (a) Nca=3.86E-11, (b) Nca=3.86E-08, (c) Nca=3.86e-07 and (d) Nca=1.54E-06.

7.3.2. Simulation input

The first step in applying our modelling approach to the slab scale experiments consists of building a representative pore network that corresponds to the experimental porous medium. To this end, a network has been extracted from Bentheimer rock images and used to obtain the statistical distributions of the coordination number, throat radii and average distance between two connecting nodes. A capillary radius was assigned to each pore element using the statistical distribution of the throats obtained from the extracted network, and pre-factors and exponents corresponding to pore conductance and volume (equation (5.1)) were found by matching the permeability and the porosity of the rock.

The final network (1500*1500 nodes) comprises 3,400,000 pores which, to our knowledge, is the largest network that has ever been used in published dynamic pore network studies (more details of previously published dynamic models can be found in Chapter 4). Whilst the simulator is relatively fast, simulations at this scale still require a long running time, especially if we are interested in post-breakthrough behaviour. Hence, it is important to ascertain the frequency of pressure solution required to maintain accuracy, whilst not causing prohibitive run times. Figure 7.7 presents a set of simulations performed for unfavourable viscosity ratio in a 1000*1000 network containing 1,500,000 pore elements. It can be seen that reducing the pressure solution frequency from every pore filling event to every 50 events does not have a major impact on the flow regime or on the location of viscous fingers. We consequently choose to solve the pressure every 50 steps in the slab scale simulations to speed up the simulations (of course background checks using more frequent pressure solution were carried out throughout the work).

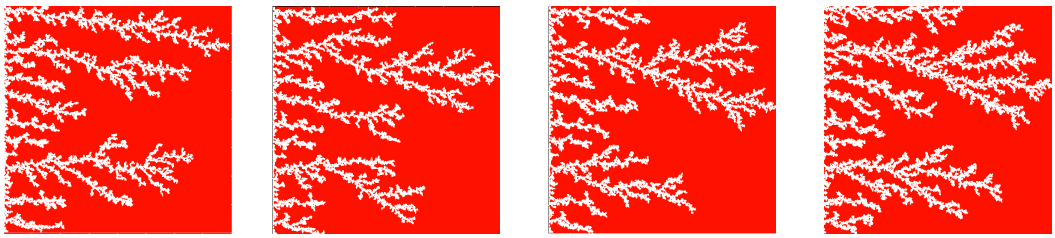

(a) (b) (c) (d)

Figure 7.7: Effect of changing the pressure solution frequency on the saturation map at breakthrough for M=2000 and Nca=7E-09 (a) pressure is solved at every step, (b) pressure is solved every 5 steps, (c) pressure is solved every 10 steps and (d) pressure is solved every 50 steps.

7.3.3. Simulation results

The E7000 and E2000 slab scale simulations performed using our dynamic model exhibit fingering behaviours that are very similar to those observed in the experiments. Initially, several sharp fingers were formed near the inlet of the networks with some subsequently growing faster and inhibiting the development of the shorter upstream instabilities left behind (Figure 7.8). These fingers had a fern-like shape and were oriented in the direction of the global pressure gradient. The instabilities exhibited more branches during E7000 simulation and breakthrough occurred earlier compared with E2000 case. It should be noticed that the water saturations at breakthrough were higher than the experimental values which was an expected result due the two dimensional nature of the simulations (Figure 7.9).

PV inj=0.011

PV inj=0.034

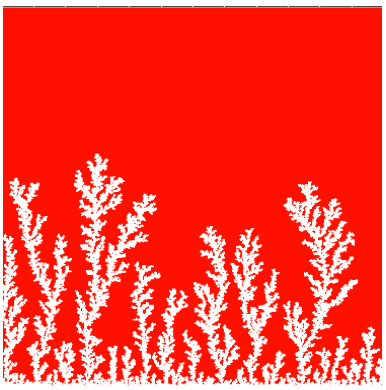

PV inj=0.06

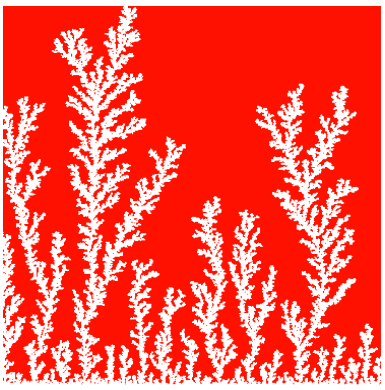

PV inj=0.09

Figure 7.8: Different stages of viscous fingering initiation and growth in E7000 simulation for different pore volumes injected.

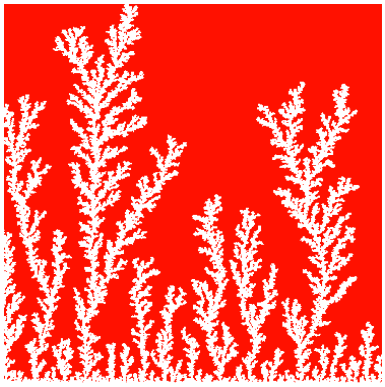

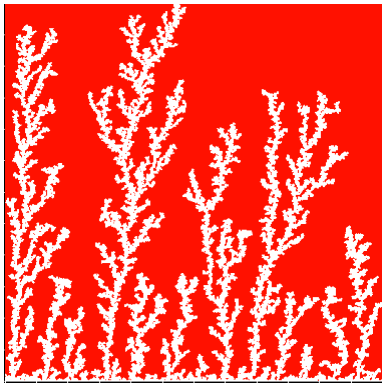

PV inj=0.089

PV inj=0.094

(a)

(b)

Figure 7.9: Comparison between (a) E7000 and (b) E2000 simulations at breakthrough

The simulated differential pressures behaved in a similar way to those observed in the experiments (Figure 7.10 and Figure 7.11). Initially, the pressure drop was high in both simulations and experiments, then, as the invading fluid advanced, the differential pressure decreased ─ expected as a result of the adverse viscosity ratio. We highlight that the pressure dropped faster in the experiments because of the lower water saturation at breakthrough, which is due to the difference in dimensionality between the experiments and the simulations (even though the 2D and 3D capillary numbers were matched). After breakthrough, the differential pressures fell further, reaching a plateau. Although the pressure drop post-breakthrough was seen to stabilize faster in the 2D simulations, both experimental and simulated plateau values were close. Moreover, Figure 7.14 shows that the recovery was higher in the E2000 simulation, which is qualitatively the same behaviour observed in the experiments (Figure 7.4).

In both E2000 and E7000 cases, sharp viscous fingers were reproduced and, following breakthrough, the simulations exhibited behaviours similar to those observed experimentally (Figure 7.12 and Figure 7.13). First, the upstream fingers grew towards

the outlet and some degree of finger thickening was observed. This is confirmed by Figure 7.15, which represents the water invasions *after* breakthrough at different stages of the E7000 simulation. This figure essentially represents the changes between the saturation map at breakthrough and later stages of the simulation. We can clearly see that the new water invasions occurred primarily around the tips of previous instabilities that had not yet reached the outlet. After several fingers reached the outlet, the water started to spread in all directions, resulting in further finger thickening and the emergence of broad water channels as a result of coalescing fingers. Of course, throughout this particular work, we must be aware that direct visual comparisons between our 2D simulations and 3D slab experiments is difficult. We must always bear in mind that X-ray data are essentially 2D composites of 3D scans.

As we have seen in Chapter 2, several researchers used the linear stability analysis to predict the stability of the displacements. We calculate the critical wavelength and the stability number corresponding to our simulations (and defined in Chapter 2). The results are shown in table

	E7000	**E2000**
Critical wavelength (λ_c)	6E-04 m	1.13E-03 m
Instability number (I_{sr})	4.36E4	1.23E4

Table 7.1: Critical wavelength and instability number in E2000 and E7000 experiments

In both E7000 and E2000, the critical wavelength was smaller than the width of the network and the instability number was higher than the critical value for rectangular section core (which is equal to π^2) which predicts the occurrence of viscous fingering and this was observed both the simulations and the experiments.

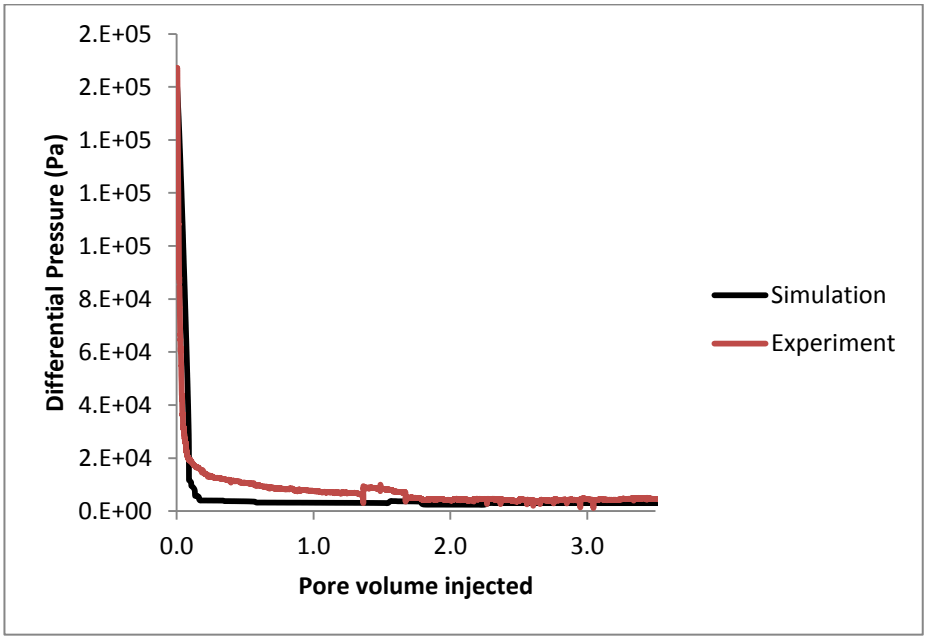

Figure 7.10: Comparison between the experimental (red) and simulated (black) differential pressure in E7000 experiment.

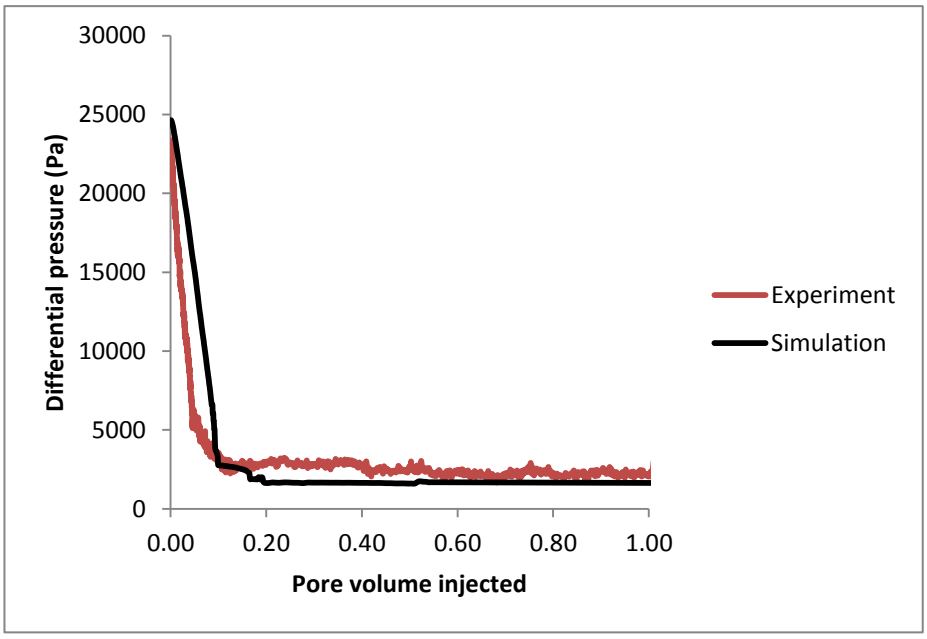

Figure 7.11: Comparison between the experimental (red) and simulated (black) differential pressure in E2000 experiment.

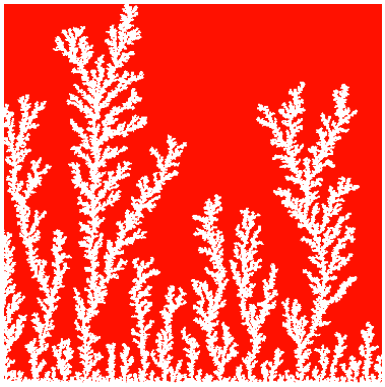

PV inj=0.089

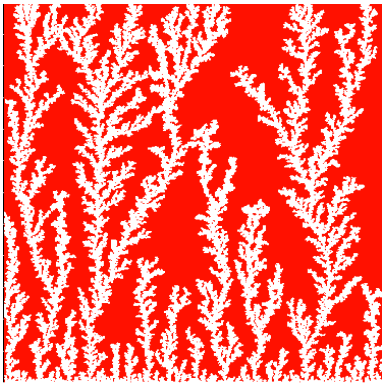

PV inj=0.72

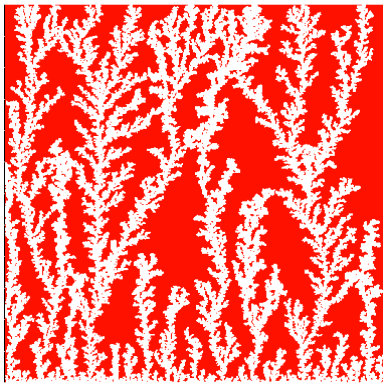

PV inj=3

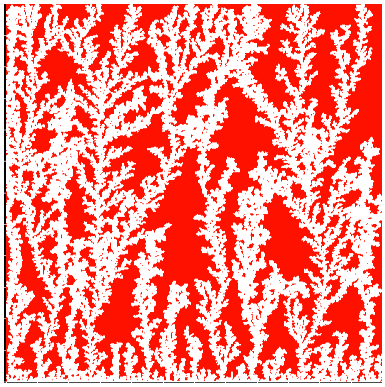

PV inj=6

Figure 7.12: Saturation maps from E7000 simulation for different injected pore volumes.

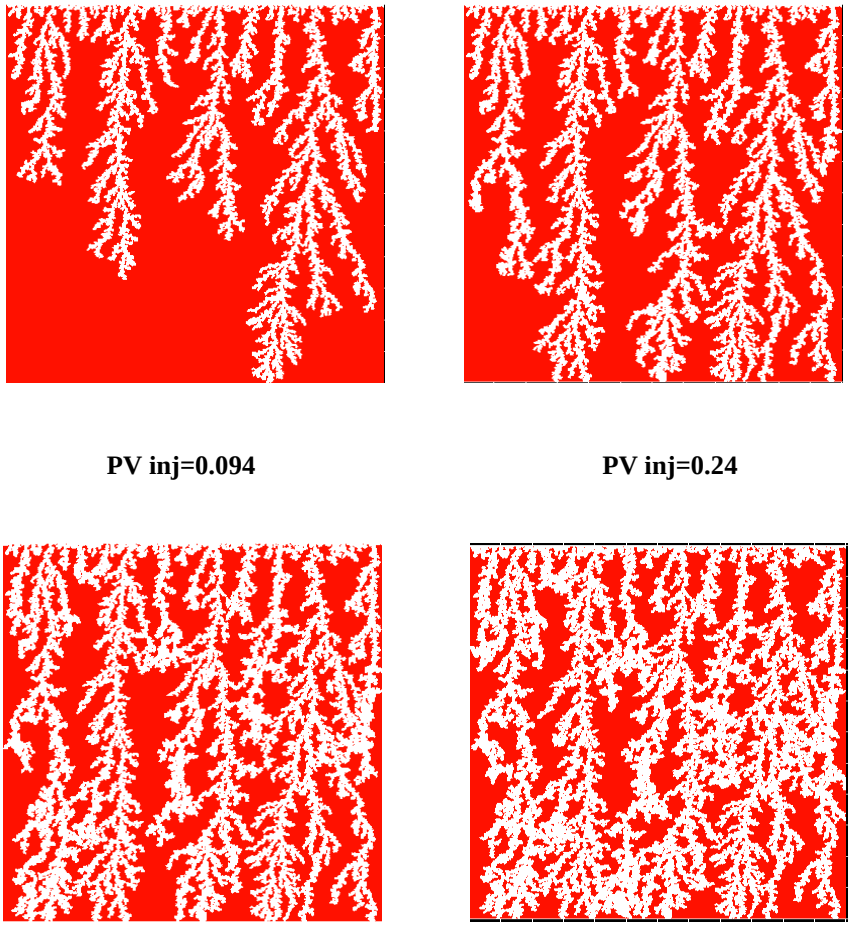

Figure 7.13: Saturation maps from E2000 simulation for different injected pore volumes.

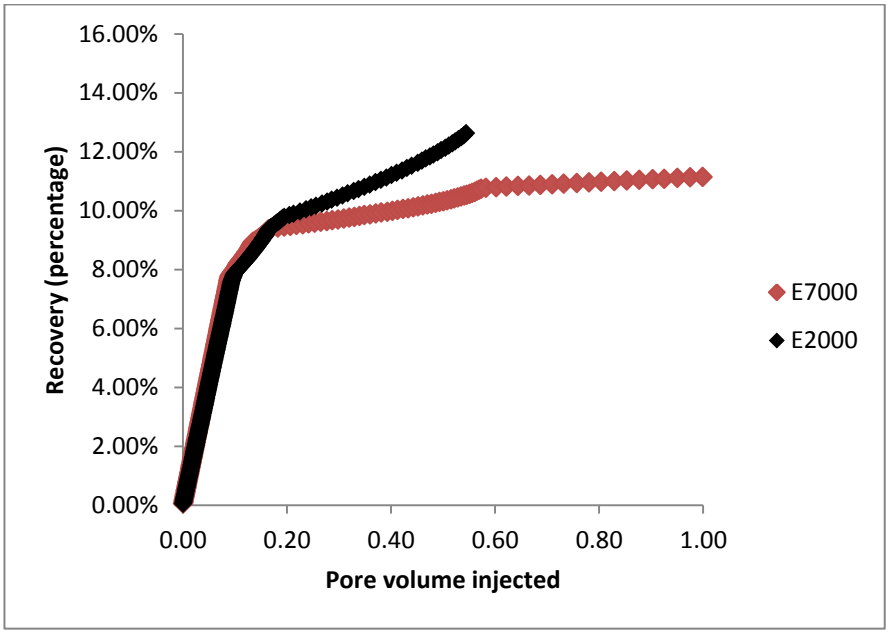

Figure 7.14: Comparison between the recovery in E7000 and E2000 simulations

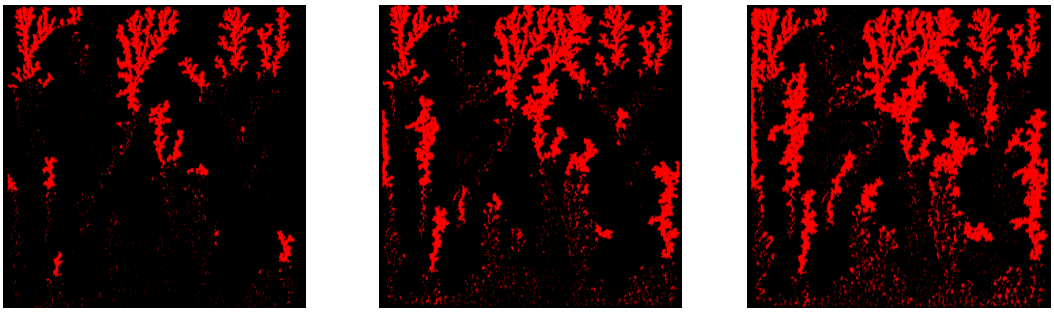

PV inj=0.72 **PV inj=3** **PV inj=6**

Figure 7.15: Location of the water invasions occurred after BT (red) at different stages of the simulation of experiment E7000

7.4. CONCLUSIONS

In this chapter, our new unsteady state drainage model has been applied to simulate slab scale waterflooding into extra heavy oil experiments. Initially, several sharp fingers were formed near the inlet of the network, with some subsequently growing faster and inhibiting the development of the shorter instabilities left behind. Whilst fingers were dendritic before breakthrough, the instabilities upstream started to thicken and merge, forming water broaden channels after breakthrough. This behaviour is qualitatively similar to that observed in the laboratory studies and is reproduced for the first time to our knowledge.

The simulated differential pressure behaviours were also similar to those observed experimentally. Moreover, the simulation of the experiment involving the least heavy oil gave higher oil recovery, which is also in agreement with the laboratory results.

Of course, we should not expect to reproduce fingers in identical spatial locations (our network is constructed stochastically) and we should also bear in mind that our simulations were performed in 2D systems because 3D networks would be computationally too costly. It is true that the the X-ray data are essentially 2D composites of 3D scans leading to the observation of a superposition of several viscous fingers (situated each in a 2D layer) as what seems to be one digitation. Our simulations showed that even in a 2D case we could observe finger thickening. If we now consider a 3D system composed of several 2D layers, in each layer the viscous fingers will start to thicken and if we do a projection of the water saturation (similar to the way the water saturation was imaged in the experiments) we see a " higher degree of finger thickening" which is only due to a visual effect.

Nevertheless, given the relatively simple modelling approach adopted here, our model performs well against the available experimental data by simulating the behaviour of instabilities before breakthrough and by reproducing the finger swelling phenomenon observed post-breakthrough. This allows us to present a hypothesis of why finger thickening is observed experimentally post water breakthrough, and is the focus of the following chapter of the thesis.

Chapter 8: An Explanation of finger thickening during unstable drainage floods

8.1. INTRODUCTION

The recovery of heavy oil by water-flooding involves the displacement of a highly viscous fluid by a less viscous fluid and this often results in the occurrence of so-called viscous fingering, which can be highly detrimental for oil recovery. The fingering causes early water breakthrough and, as a consequence, poor sweep efficiency. However, some recent laboratory studies have suggested that, under certain circumstances, water-flooding into extra-heavy oil (with viscosity up to 7000 cP) could actually result in higher than expected oil recovery (Bondino et al, 2011; Skauge et al, 2012; Skauge et al 2013). X-ray imaging of fluid fronts during these experiments has highlighted a finger swelling mechanism that has not been previously reported and the causes of this behaviour – as well as the physics involved in such displacements – have not been explained to date.

In the previous chapter, the developed dynamic pore network model has proved to be able to simulate qualitatively the experiments of Skauge et al. (2012) and to reproduce the finger swelling phenomenon. In this chapter, this tool is used to propose a physical explanation for the causes of finger thickening following water breakthrough. Finally, we use our approach to study the effects of varying core length, rock wettability, and injection rate upon the finger swelling phenomenon.

8.2. PROPOSED PHYSICAL EXPLANATION OF THE FINGER THICKENING PHENOMENON

In order to avoid any artefact that could be caused by reducing the frequency of the pressure solution, new sets of simulations are performed here using smaller networks. 1000*1000 networks are created and the capillary number and viscosity ratios of the E2000 and E7000 experiments are matched and the pressure is solved at *every* time step. These simulations are named respectively E2000_mod and E7000_mod.

Figure 8.1 shows that, initially several sharp viscous fingers were initiated and some instabilities were seen to propagate faster than others, preventing the growth of some of the smaller fingers. Following water breakthrough, fingers throughout the network appeared to thicken and coalesce, forming broad water channels and improving the sweep efficiency.

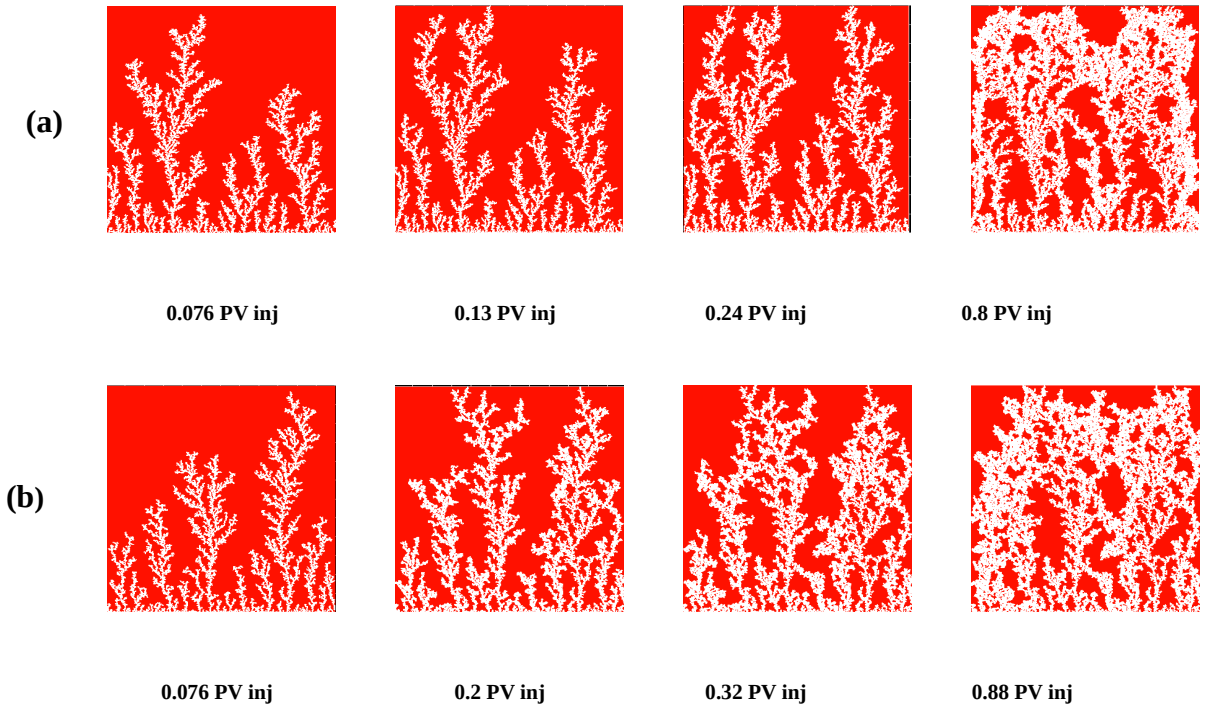

Figure 8.1: E7000_mod and E2000_mod simulations of waterflooding into heavy oil using viscosity ratios equal to (a) 7000 and (b) 2000. The capillary number is equal to 6.9 E-09 in both simulations.

If we examine the differential pressure of E7000_mod and E2000_mod simulations (Figure 8.2), we notice that it was high at the start of the simulations ─ hence, viscous pressures were much stronger than capillarity initially, leading to the occurrence of sharp and dendritic fingers. After water breakthrough, the differential pressure dropped across the system resulting in a reduction of the influence of viscous forces and an increase in the importance of capillary forces. Furthermore, when we examine the pressure profile of E2000_mod more closely at breakthrough (Figure 8.3), we notice that the highest pressure gradients occurred around the perimeters of fingers situated upstream of the outlet face of the network. This not only accelerated the growth of these instabilities towards the outlet but also caused some degree of finger thickening –a result of the increasing importance of the capillary forces on the displacement. This is confirmed by Figure 8.4, which represents the area that was swept after breakthrough (the red colour represents the new area swept post-breakthrough). We can clearly see that the new water invasions were occurring primarily around the tips of previous instabilities that had not yet reached the outlet. After several fingers reached the outlet, the inlet pressure dropped further and reached a plateau. At this stage of the water-flood, the viscous pressures that were driving the water towards the outlet became even smaller. This led to a further increase of the impact of the capillary forces on the displacements – pores having a lower capillary resistance were more likely to be filled first. Thus, water began to spread in all directions – the fingers thickened further and broad channels emerged as a result of coalescing fingers.

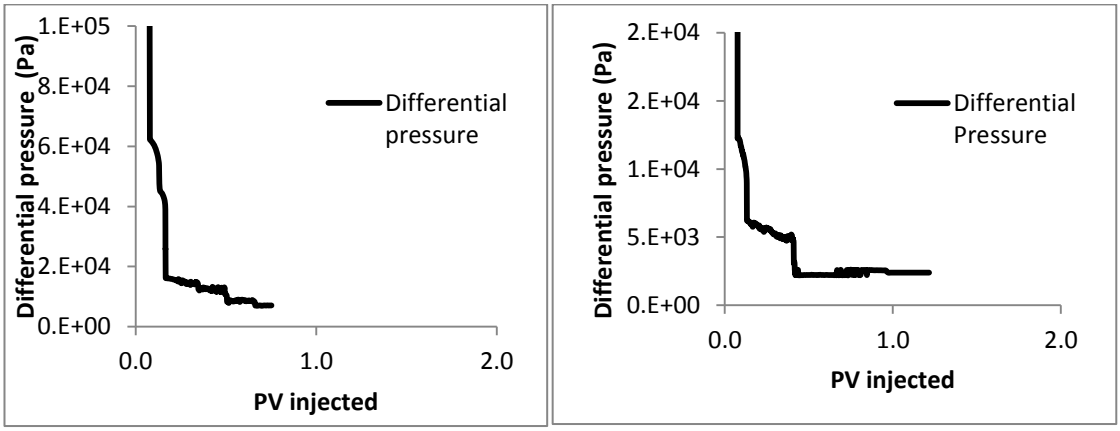

(a) (b)

Figure 8.2: Differential pressure in (a) E7000_mod and (b) E2000_mod simulations. The pressure drop starts high and then drops as the invading phase grows towards the outlet. After breakthrough, the differential pressure drops further and reaches a plateau.

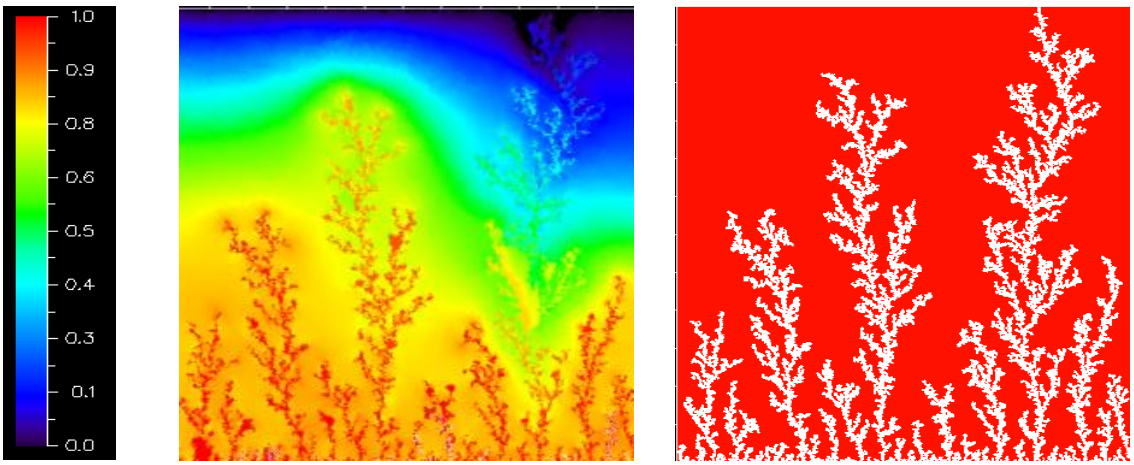

(a) **(b)**

Figure 8.3: (a) Pressure field and (b) saturation path in E2000_mod simulation. Note that the pressure drops in the spanning finger and that the highest pressure gradients are at the tip of the upstream instabilities.

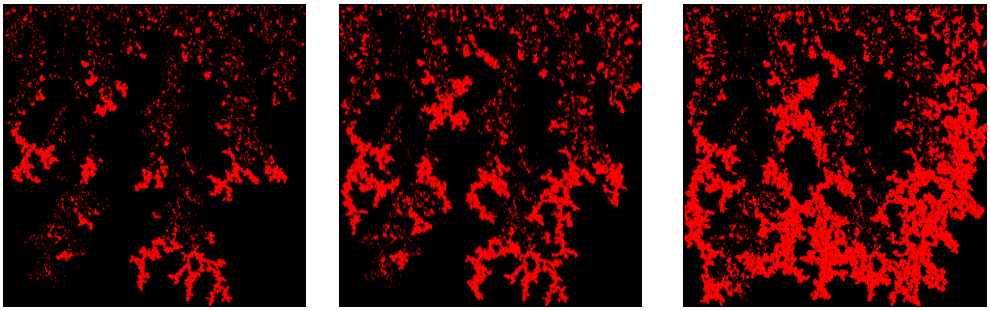

0.2 PV inj **0.32 PV inj** **0.88 PV inj**

Figure 8.4: Location of the new water invasions occurred after BT (red) at different stages of the simulation E2000_mod.

In light of these results, we propose that the finger thickening phenomenon is primarily caused by a drop in differential pressure through the formation of sample-spanning fingers at breakthrough, resulting in the highest local pressure gradients after breakthrough being associated with the tips of upstream fingers that have not yet reached the outlet. This makes the flow less viscous dominated, resulting in an increased impact of capillary forces, which leads to finger growth in all directions.

In order to have a better understanding of the finger swelling phenomenon, we now go on to examine the impact of varying a number of system variables on finger development and thickening. In order to reduce computational runtimes, we choose to use 5cm x 30cm simulations (corresponding to 250*1500 networks) for these sensitivities.

8.3. IMPACT OF CORE LENGTH ON FINGER THICKENING

The first sensitivity focuses on system length and several simulations were performed to investigate the effect of core length on finger thickening behaviour. The experimental conditions of E7000 were used (using a scaled injection rate of Q= 0.005 cc/hr that matched the experimental flux) and a weakly oil wet condition was assumed throughout (θ=100º). For network lengths equal to 30 cm and 15 cm, finger thickening was clearly

observed (Figure 8.6) and the plateau differential pressure post water breakthrough remained higher than the mean capillary entry pressure characterising the underlying network for the duration of the flood (Figure 8.5) (calculated using Young-Laplace's law as $P_c = \frac{2\sigma cos\theta}{\bar{R}}$ where $\bar{R}$ is the mean pore radius in the network).

For a system length equal to 7.5 cm, the pressure drop reached a plateau value very close to the mean capillary entry pressure of the network up until 4.5 PV injection. During this time, the perimeter pores of upstream fingers began to thicken and grow until reaching the outlet. When a second finger reached the outlet, the pressure drop decreased further, falling below the mean capillary entry pressure in the network – shortly after this second pressure reduction, finger swelling ceased. An even shorter network (3.25 cm) exhibited equally interesting behaviour. In this case, the differential pressure fell below the mean capillary entry pressure in the network as soon as the water reached the outlet. Here, *no* finger thickening behaviour was observed post-breakthrough.

These results show that finger thickening occurs when the pressure drop at the plateau stage is higher than the mean capillary entry pressure of the underlying pore structure. As a consequence, this suggests that the length of the core is an essential parameter in determining the extent of the finger thickening phenomenon. In fact, short cores may not be able to maintain a differential pressure high enough to cause finger swelling at all. Furthermore, the longer the core is, the higher the differential pressure required to maintain a fixed injection rate – consequently, for long cores, the pressure drop at the plateau stage is more likely to be higher than the mean capillary entry pressure and finger thickening is therefore more likely to occur.

.

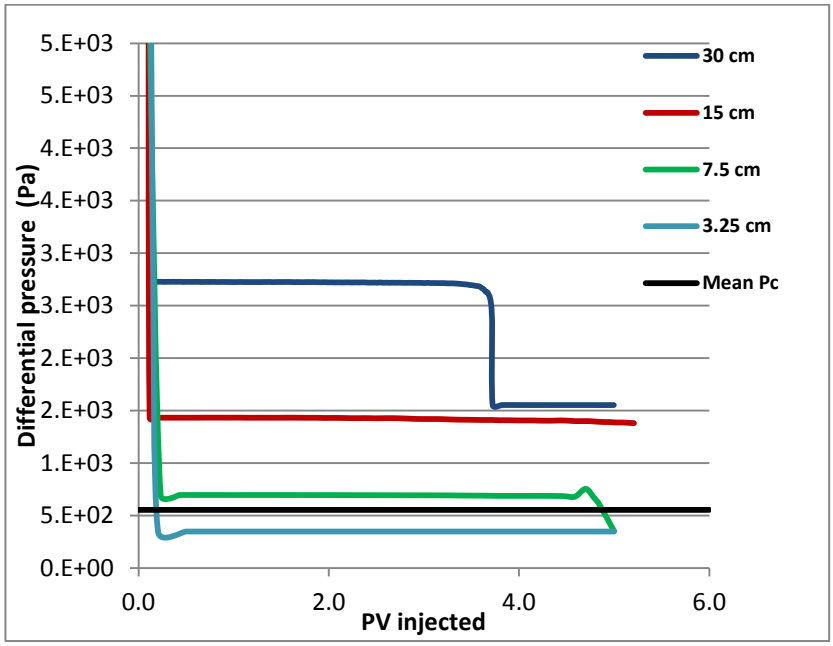

Figure 8.5: The differential pressure simulated for different networks lengths and the Mean Pc in the network (calculated using Young-Laplace's law and the average pore radius in the network). In this set of simulations: Q=0.005 cc/hr , Nca= 6.9 E-09, theta=100° and μoil=7000 cP.

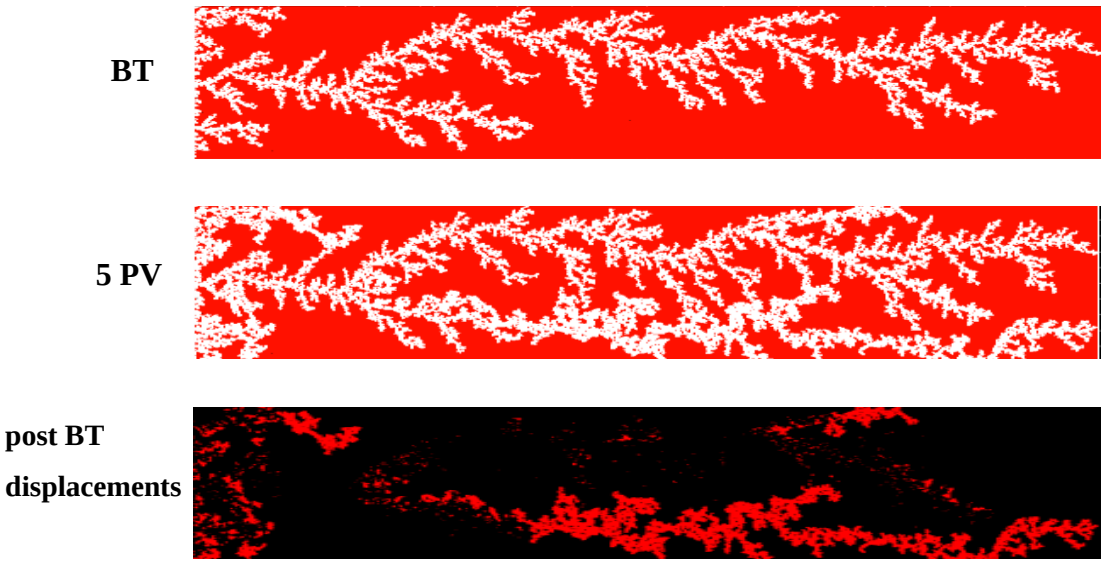

(a)

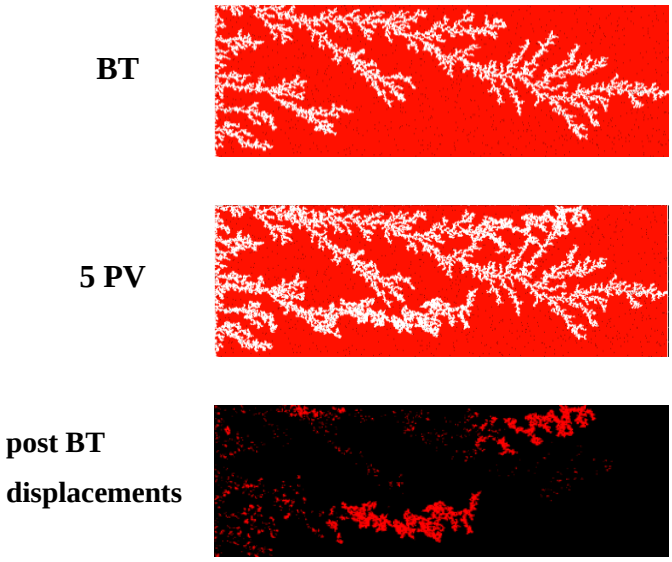

(b)

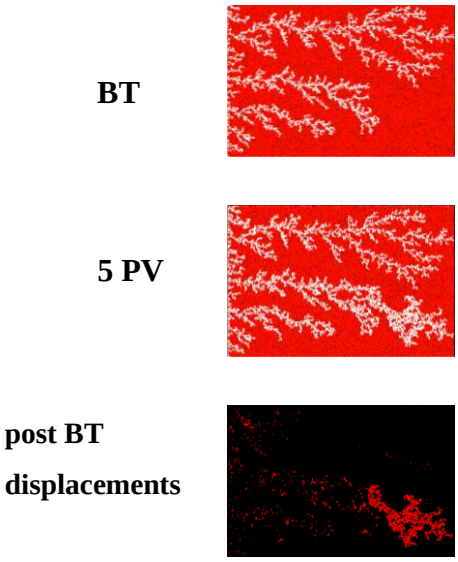

(c)

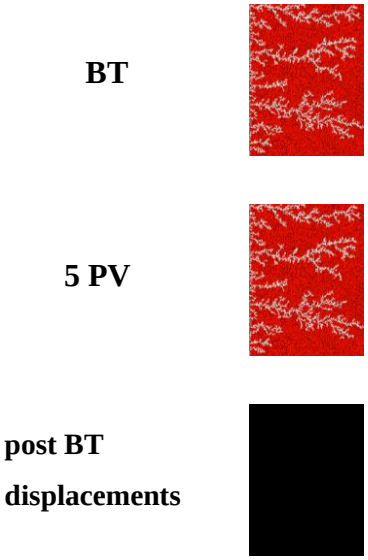

(d)

Figure 8.6: The saturation path at BT, the saturation path after BT(5PV) and the water invasions occurring after BT(5PV) for simulations with different network lengths: (a) 30cm, (b)15 cm, (c) 7.5 cm , (d) 3.25 cm. In this set of simulations: Q=0.005 cc/hr , Nca= 6.9 E-09 and theta=100° and μoil=7000 cP .

8.4. IMPACT OF WETTABILITY ON FINGER THICKENING

Simulations were performed using the experimental conditions of E7000 (Q= 0.005 cc/hr) under two different wettability scenarios: a strongly oil-wet case (θ=170°) and a weakly oil-wet case (θ=100°). The stabilised value of the pressure drop corresponding to the strongly oil-wet case was found to be lower than the mean capillary entry pressure in the network, while for the weakly oil-wet case the opposite was true (Figure 8.7). We find that finger thickening is predicted only for the weakly oil-wet case (Figure 8.8) – for the strongly oil-wet case, the saturation path did not change after water breakthrough. This can be explained as follows: a lower contact angle reduces the mean capillary entry pressure in the network and, as a consequence, the differential pressure now lies above this value and so capillary entry criteria can still be satisfied. These results again show that, to have finger thickening, the pressure drop across the system at the plateau stage of the flood should be higher than the average capillary pressure characterizing the network.

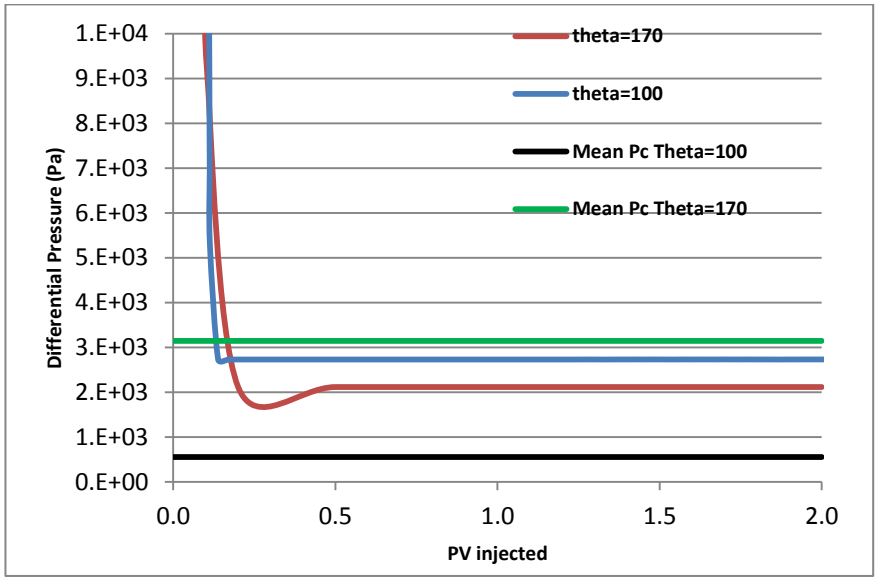

Figure 8.7: Comparison between the differential pressures in two simulations with different contact angles: theta=100 (blue) and theta=170 (red).The Mean Pc in the network (calculated using Young-Laplace's law and the Mean pore Radius in the network). In this set of simulations: Q=0.005 cc/hr, Nca= 6.9 E-09 and L=30 cm.

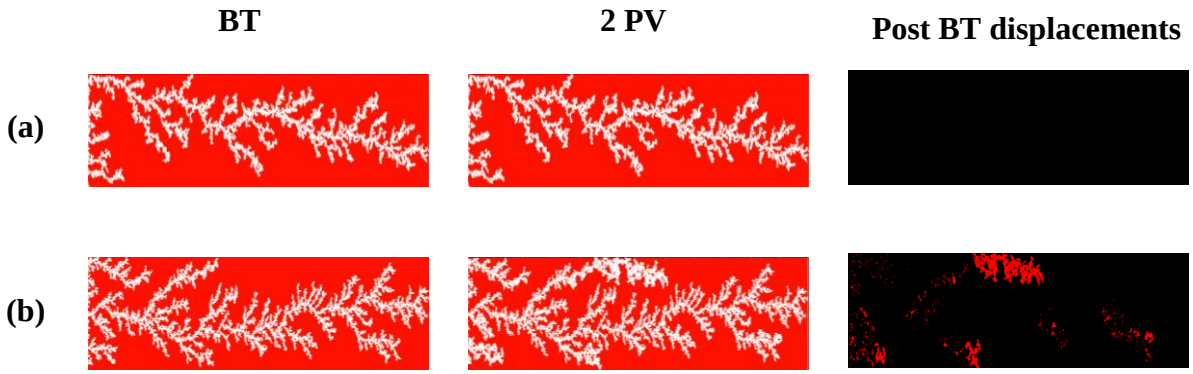

Figure 8.8: The saturation path at BT, the saturation path after BT (2 PV) and the water invasions occurred after BT (2 PV) for simulations with different contact angles: (a) theta=170 and (b) theta=100. In this set of simulations: Q=0.005cc/hr, Nca= 6.9 E-09, L=30 cm and μoil=7000 cP.

8.5. IMPACT OF INJECTION RATE ON FINGER THICKENING

Two simulations were performed using the rock/fluid conditions of E7000 at two different injection rates Q_1=0.005 cc/hr and Q_2=0.05 cc/hr (note that the scaled experimental rate corresponds to Q=0.005 cc/hr). The wettability scenario considered was a strongly oil-wet case (θ=170°). We find that the simulated pressure drop for the low rate simulation fell below the mean capillary entry pressure in the network (Figure 8.9), whereas for the high rate it remained higher than the mean capillary entry pressure throughout. Figure 8.10 shows that the phenomenon of finger thickening only occurred during the high rate simulation, in line with our earlier hypothesis.

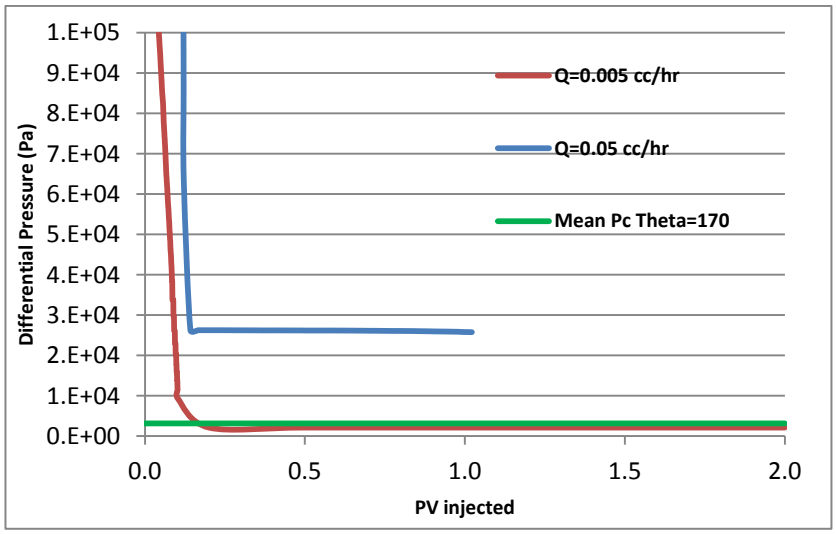

Figure 8.9: Comparison between the differential pressures in two simulations with different injection rates: Q=0.005 cc/hr and Q=0.05 cc/hr. The Mean Pc was calculated using the average pore radius in the network. In these simulations theta=170 and L=30 cm.

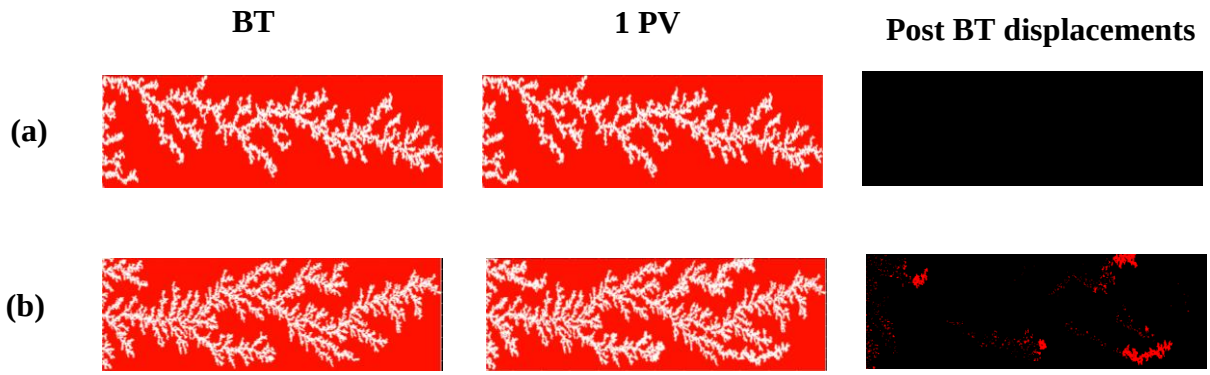

Figure 8.10: The saturation path at BT, the saturation path after BT (1 PV) and the water invasions occurred after BT (1 PV) for simulations with different injection rates: (a) Q=0.005 cc/hr and (b) Q=0.05 cc/hr. In these simulations theta=170°, L=30 cm and μoil=7000 cP.

8.6. Conclusions

In this chapter, the new model was again used to simulate water injection into extra heavy oil simulations. Before breakthrough, dendritic viscous fingers were obtained, whilst post breakthrough, highly dendritic water fingers were seen to thicken and coalesce, forming braided water channels and improving sweep efficiency. This behaviour is qualitatively similar to that observed in the laboratory studies.

Now, for the first time to our knowledge, a physical explanation is presented for finger swelling during drainage experiments. We propose that the finger thickening behaviour is due to the rapid changes in pressure drop that follow the breakthrough of water fingers and to the fact that the highest pressure gradients after breakthrough are found primarily at the tips of the upstream fingers. We suggest that the pressure drop at the plateau stage of the flood should be higher than the mean capillary entry pressure characterising the sample to observe this phenomenon.

Finally, we indicated that core length, wettability and injection rate are all important parameters affecting the finger thickening behaviour. Indeed, increasing the length of

the core, using a higher injection rate and/or having a more neutral wet condition all increase the potential for finger swelling.

Chapter 9: Influence of different system parameters on waterflooding in porous media

9.1. INTRODUCTION

In previous chapters, we have seen that the new model has been able to simulate viscous fingering as well as post-breakthrough finger swelling behaviour in the context of two slab-scale experimental studies. This allowed us to propose a physical explanation for the causes of this phenomenon and we proposed that the finger thickening behaviour is due to the rapid changes in pressure drop that follow water breakthrough.

In this chapter, we present a further, more general investigation into the effects of different system parameters – injection rate, viscosity ratio, wettability and core length – upon the displacement regime, front stability and oil recovery. We start by examining the flow regimes before breakthrough and go on to study the post-breakthrough behaviour, taking the conditions of the Skauge et al (2014) experiments as a base case and investigating the effects of several system parameters on oil recovery. This provides us with valuable information that can be useful for the optimization of waterflooding processes for eventual field applications.

9.2. PRE-BREAKTHROUGH BEHAVIOUR

9.2.1. Rate and viscosity ratio effects

We start by investigating the effects of viscosity ratio and capillary number on the flow regime and sweep efficiency up to water breakthrough. The parameters used for this part of the study have been chosen to mimic Bentheimer rock and the wettability was considered as nearly oil-wet (in line with the simulations reported in chapters 7 and 8).

The simulations were performed using 2D networks representing a 7.5cm x 7.5 cm rock sample. Although it is entirely feasible to run a limited number of 3D studies, we have chosen to use 2D equivalents to enable a larger number of sensitivities to be performed whilst keeping runtimes reasonable. In fact, we have seen in Chapter 6 that at identical capillary numbers, the same flow regime is obtained in both 2D and 3D simulations.

Figure 9.1 shows a set of simulations done at different injection rates with matched viscosity fluids. At low rates (Nca=4.6E-12 and Nca=4.6E-11), an invasion percolation like pattern is obtained and the displacements are controlled by the capillary entry pressures of the pores at the interface ─ the largest pores having the lowest capillary entry pressure are invaded first ─ and is characterised by invasions happening in all directions (even towards the inlet in some cases). This leads to the formation of network scale looped fingering situations that can trap large quantities of oil. Figure 9.1 also shows that an increase in rate reduced the frequency of the occurrence of these loops resulting in less trapped oil and better sweep efficiency. At high rates (Nca=4.6E-07), the displacement became stable ─ the interface between the fluids became flat and very small volumes of oil were trapped.

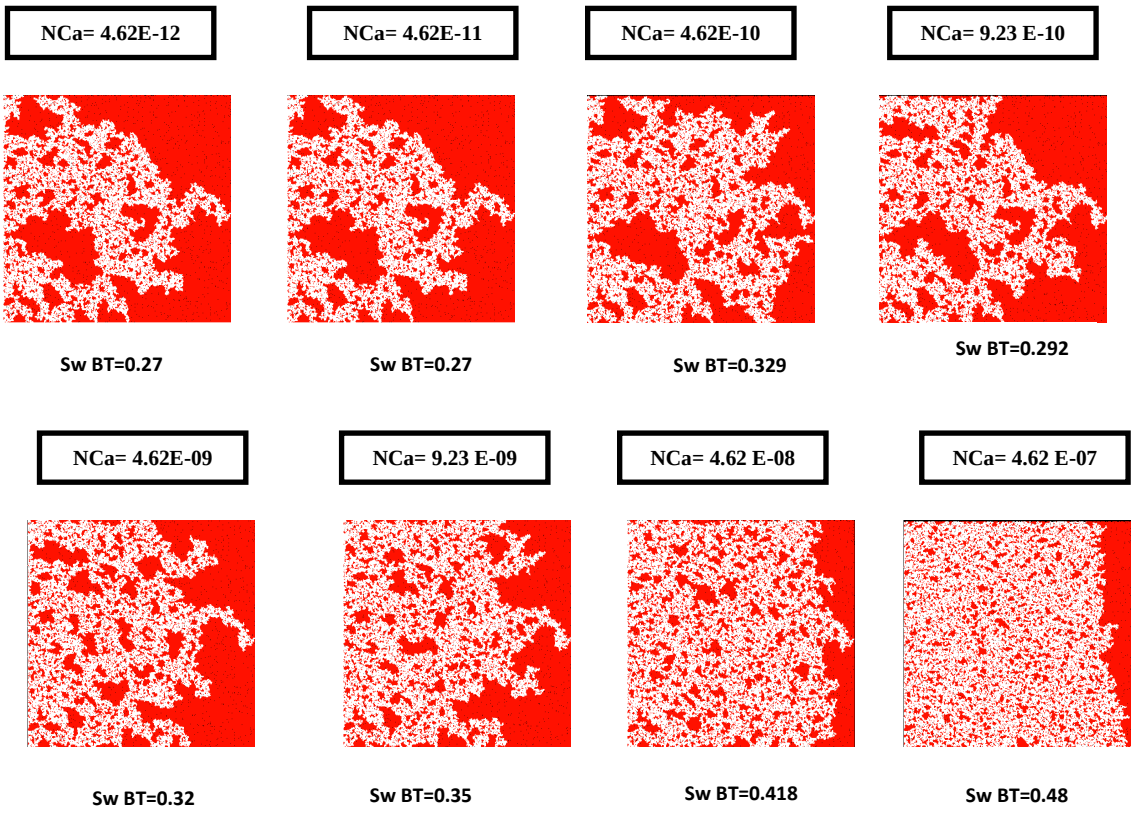

Figure 9.1: Simulations showing the capillary number effect on waterflooding of a Bentheimer surrogate (7.5*7.5cm) for a favourable viscosity ratio M=1.

Snapshots at breakthrough for several *adverse* viscosity ratios and different injection rates are shown in Figure 9.2. As expected, at low rates, capillary fingering was seen to dominate for all viscosity ratios and an invasion percolation-like pattern emerged in all cases. For viscosity ratios equal to 7000, 500 and 100, the initially thick capillary fingers were seen to become thinner as the injection rate increased, tending to a viscous fingering regime at high rates. In this regime, fern-shaped fingers are formed that grow towards the outlet leading to a very poor sweep efficiency. The simulations show that the finger shape is sensitive to the viscosity ratio and, for the same capillary number; the instabilities became more dendritic and sparse for more viscous oils. *In addition, we observed that the transition between capillary and viscous fingering regimes occurs at lower injection rates for waterfloods involving heavier oil.*

The simulations with a viscosity ratio equal to 10 (Figure 9.2 (d)) exhibit an interesting phenomenon. Initially, at low rates, an invasion percolation like pattern characterised by a high degree of trapped oil was obtained. At intermediate rates, however, a more

efficient displacement pattern emerged and increased recovery occurred at the border between the capillary-dominated and viscous fingering regimes (see Figure 9.8). At these intermediate rates, both the capillary and viscous forces are of comparable magnitudes. This can be explained by the fact that: (i) compared to the capillary dominated regime, the inlet pressure is relatively high and so more pores are accessible to the invading water, but (ii) the viscous pressures are not strong enough to cause fingering instabilities. Hence, a highly efficient displacement regime is obtained. The plots in Figures 9.7, 9.8 and 9.9 suggest that *the higher the viscosity ratio, the narrower the capillary number window for efficient displacement.*

Although the breakthrough recovery versus capillary number plots in Figures 9.3-9.8 are somewhat noisy, they mostly exhibit non-monotonic behaviour. We note that similar non-monotonic recovery behaviour was previously reported by Wang et al. (2012), who presented micromodel experiments involving two phase displacements with a viscosity ratio equal to 17.5. They observed a 20% increase in recovery at breakthrough between capillary and viscous dominated regimes (Figure 9.9).

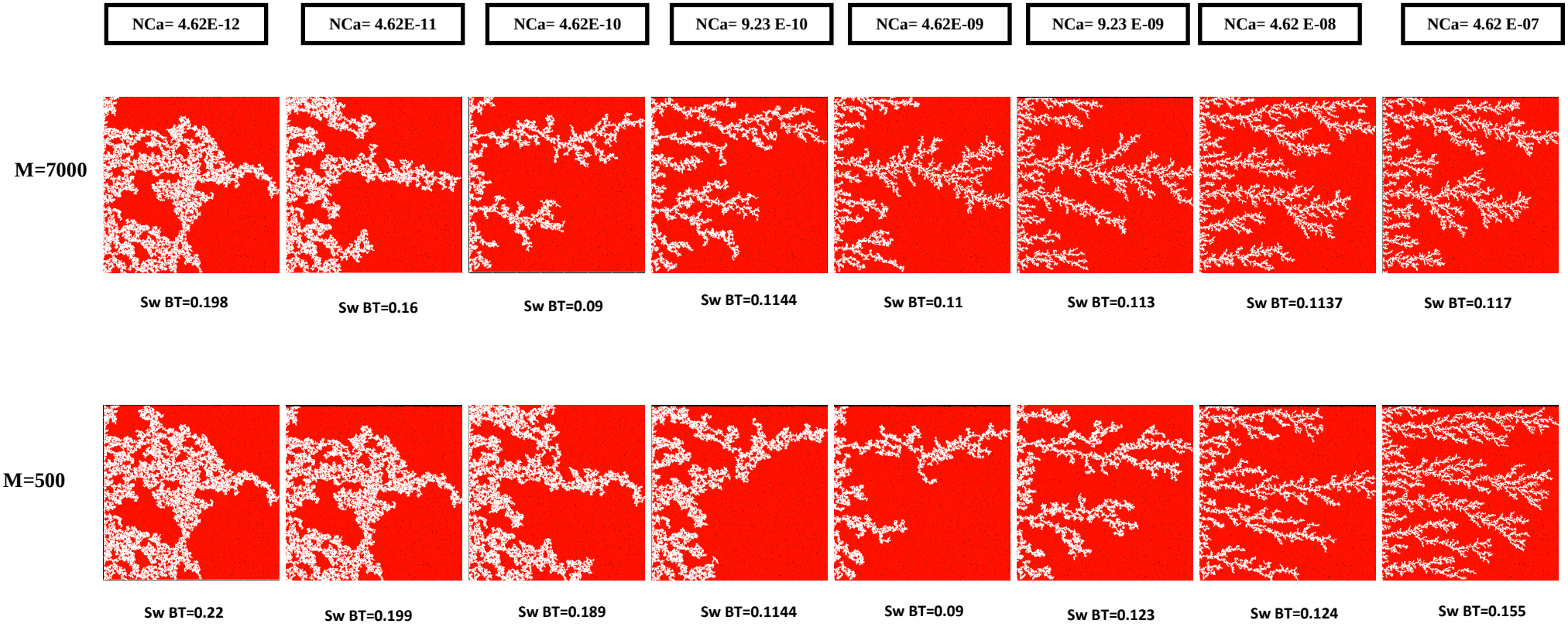
NCa= 4.62E-12
NCa= 4.62E-11
NCa= 4.62E-10
NCa= 9.23 E-10
NCa= 4.62E-09
NCa= 9.23 E-09
NCa= 4.62 E-08
NCa= 4.62 E-07
M=7000
Sw BT=0.198
Sw BT=0.16
Sw BT=0.09
Sw BT=0.1144
Sw BT=0.11
Sw BT=0.113
Sw BT=0.1137
Sw BT=0.117
M=500
Sw BT=0.22
Sw BT=0.199
Sw BT=0.189
Sw BT=0.1144
Sw BT=0.09
Sw BT=0.123
Sw BT=0.124
Sw BT=0.155

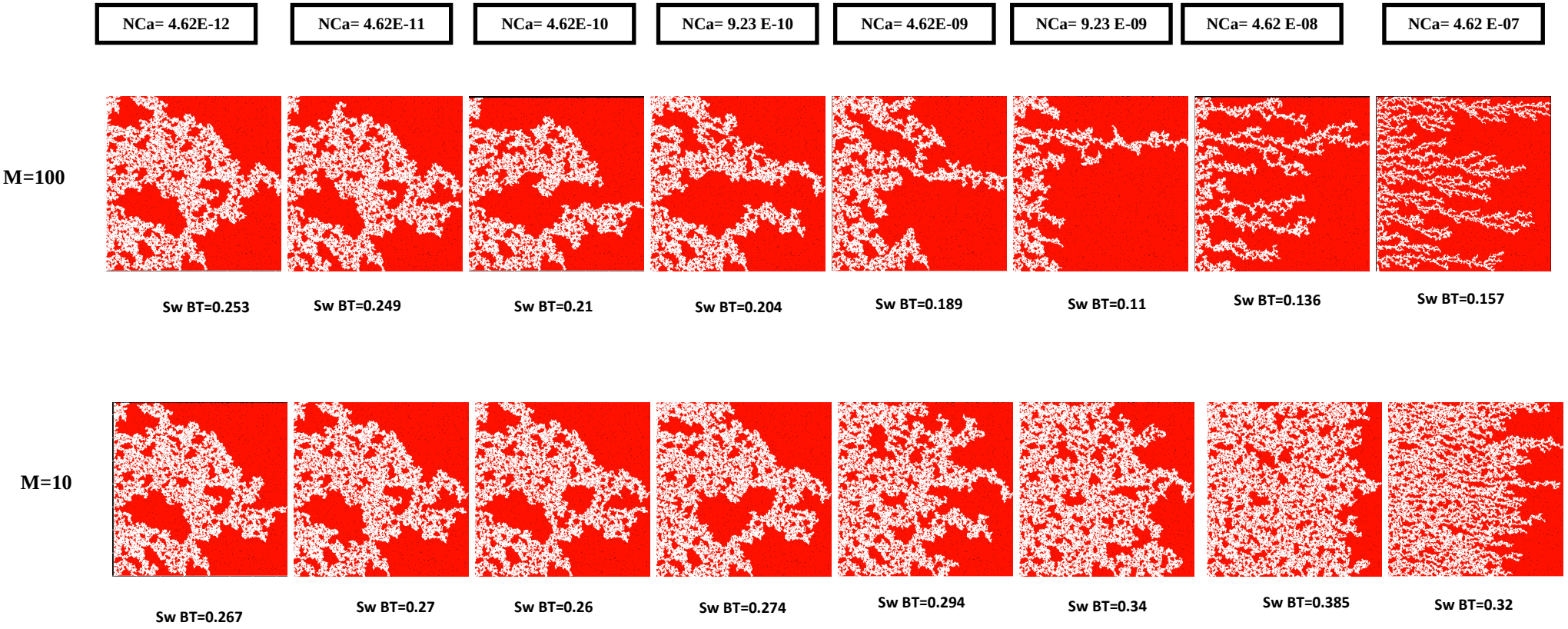

Figure 9.2: Simulations showing the capillary number effect on waterflooding of a Bentheimer surrogate (7.5*7.5cm) for various unfavourable viscosity ratios: (a) M=7000, (b) M=500, (c) M=100, and (d) M=10.

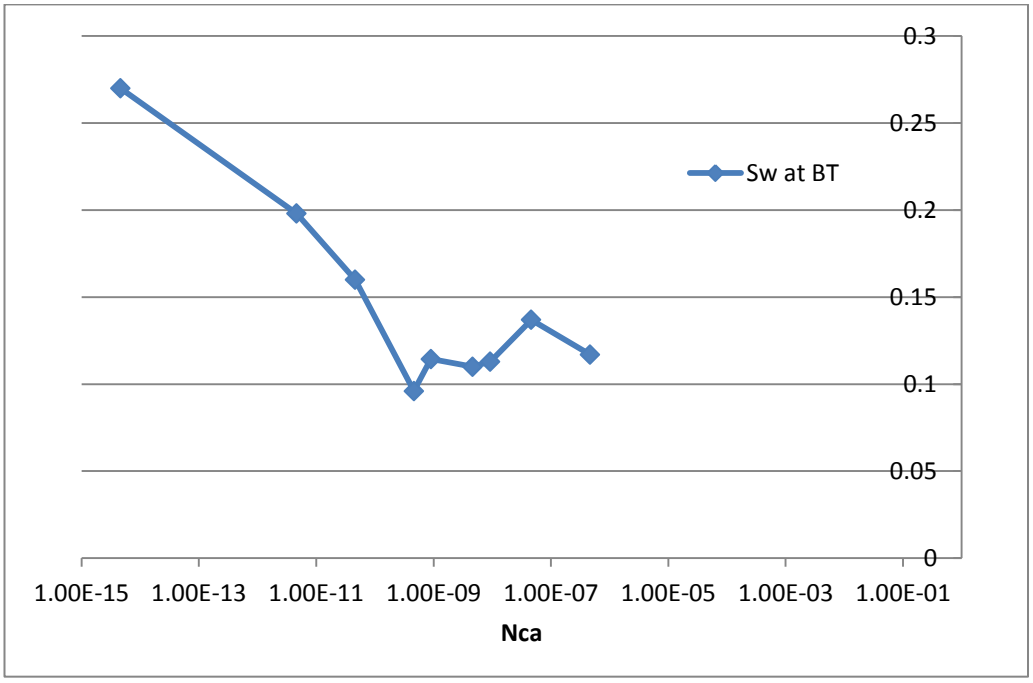

Figure 9.3: The fraction of the invading phase saturation at breakthrough for a viscosity ratio M=7000.

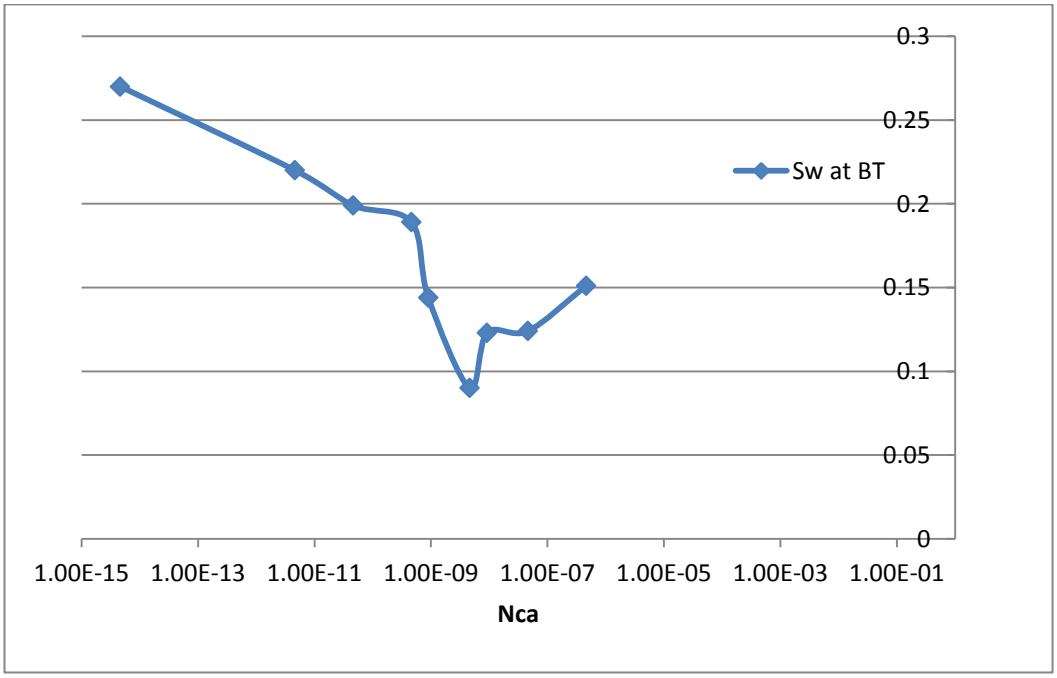

Figure 9.4: The fraction of the invading phase saturation at breakthrough for a viscosity ratio M=500.

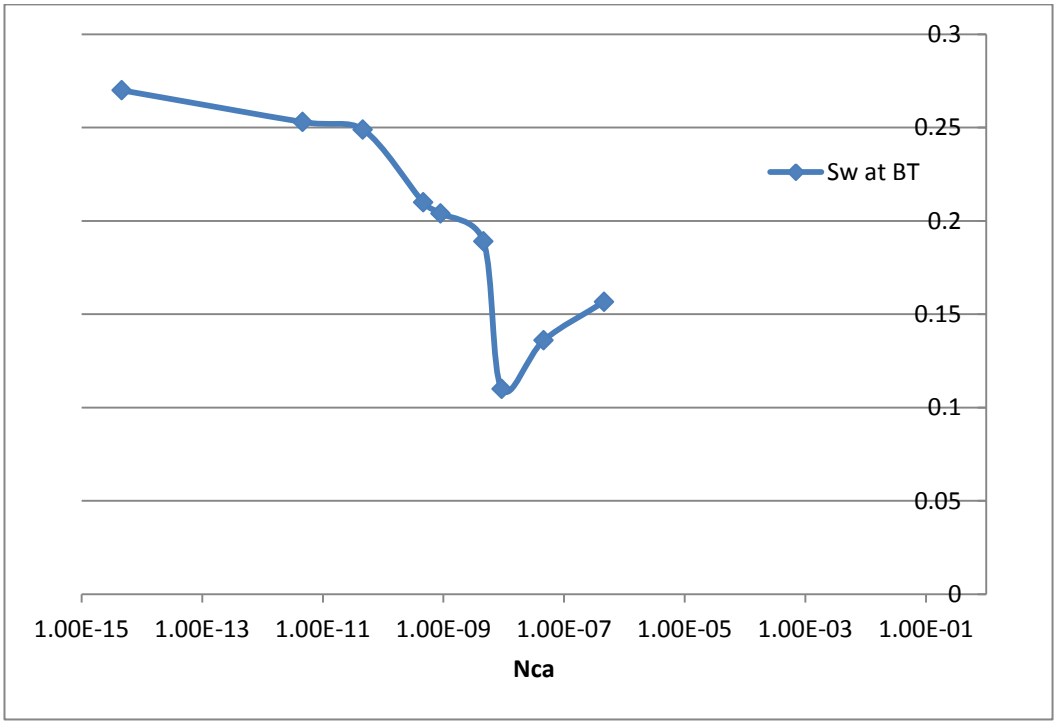

Figure 9.5: The fraction of the invading phase saturation at breakthrough for a viscosity ratio M=100.

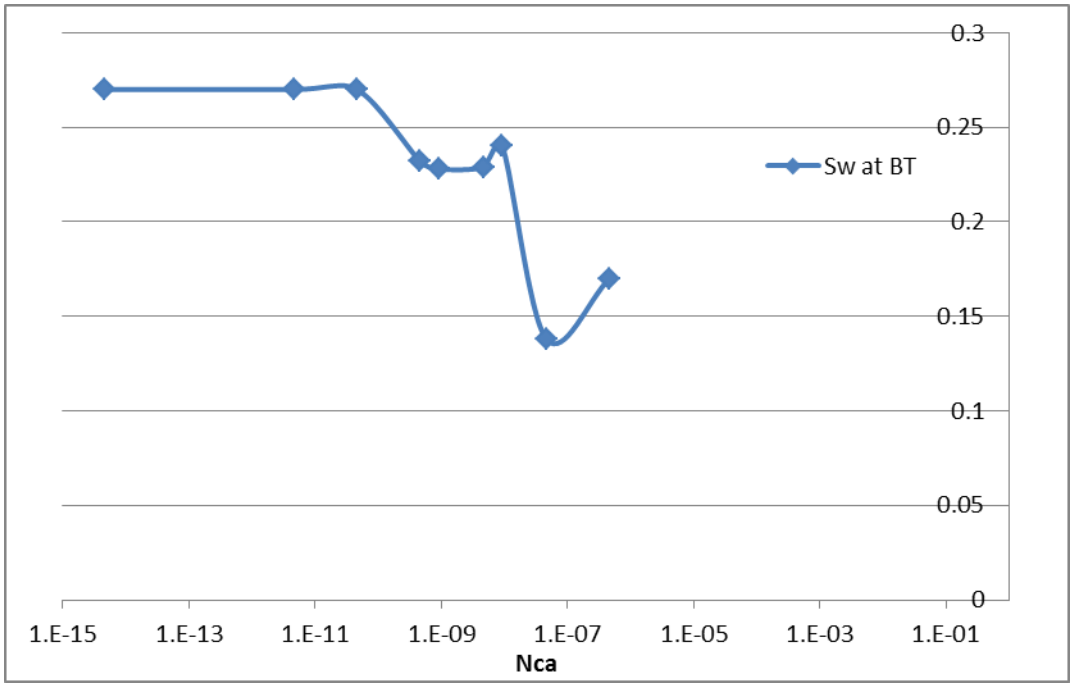

Figure 9.6: The fraction of the invading phase saturation at breakthrough for a viscosity ratio M=50.

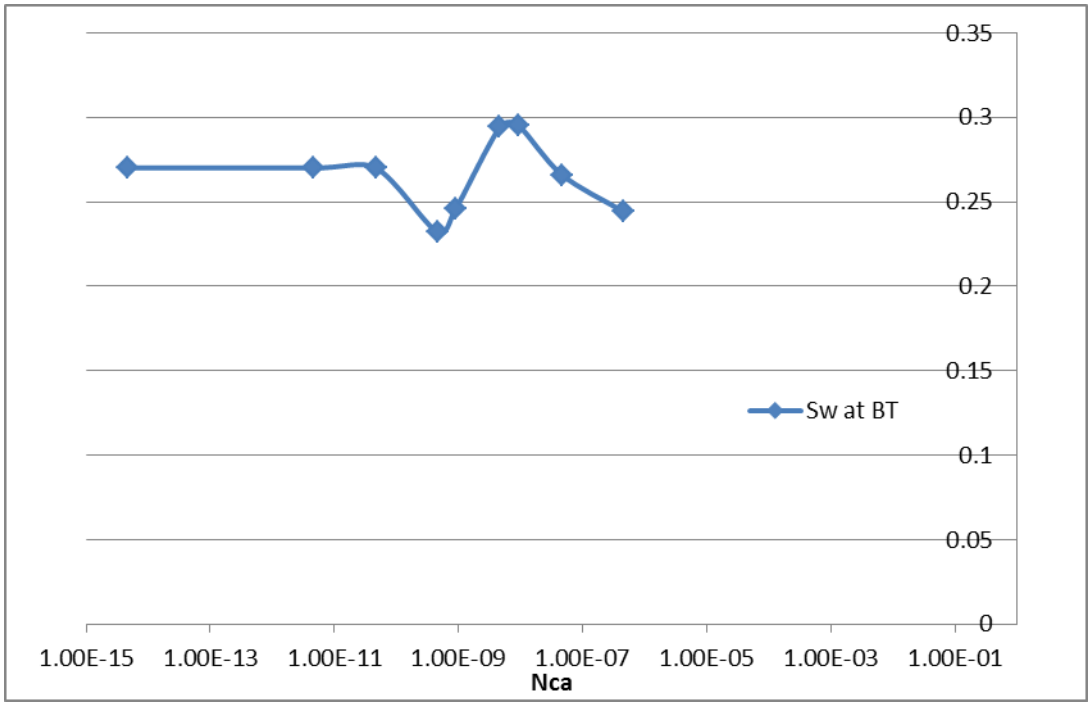

Figure 9.7: The fraction of the invading phase saturation at breakthrough for a viscosity ratio M=20.

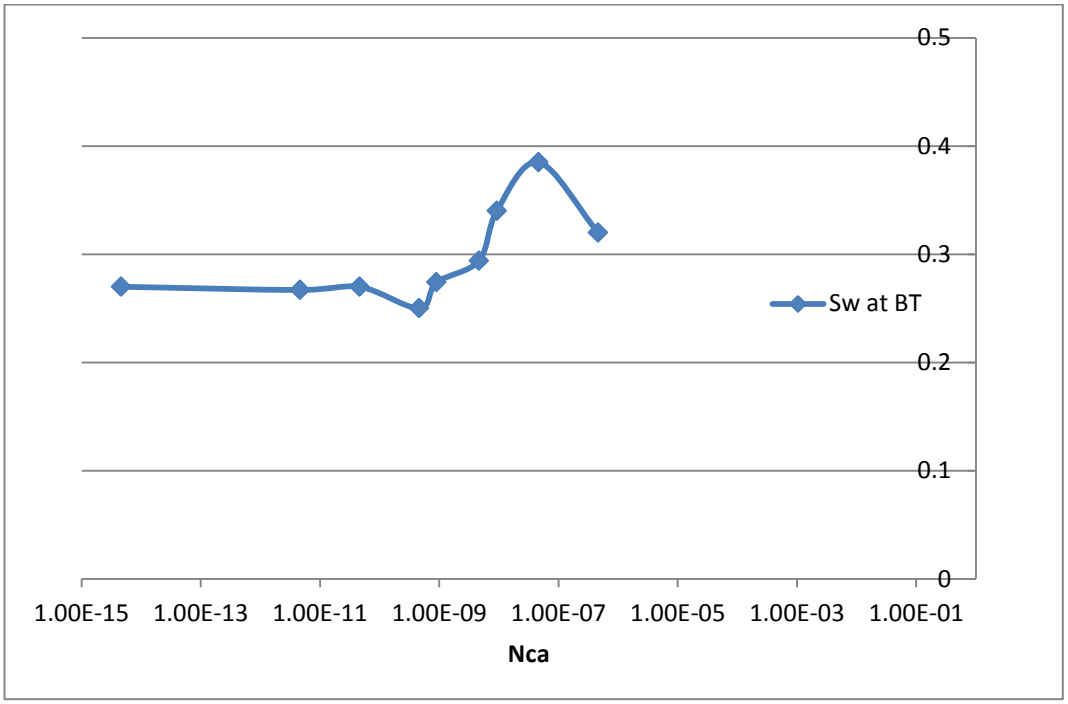

Figure 9.8: The fraction of the invading phase saturation at breakthrough for a viscosity ratio M=10.

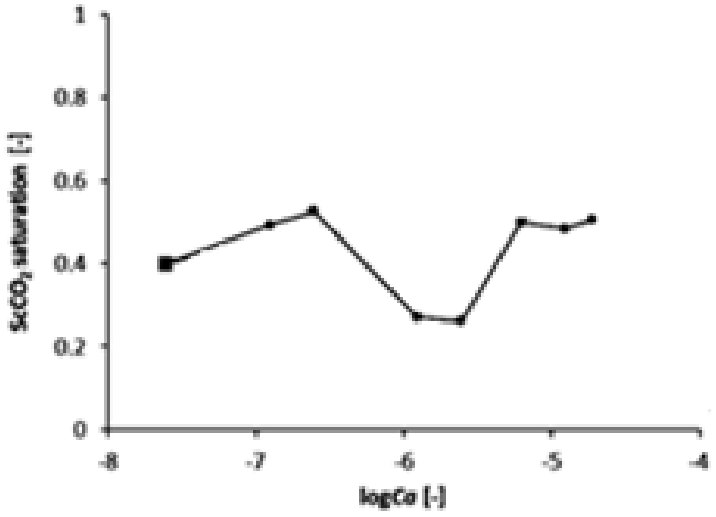

Figure 9.9: The fraction of the invading phase saturation at breakthrough observed during experiments (Wang et al., 2012) for M=17.5

In a recent paper, Skauge et al. (2014), performed waterflooding experiments using Bentheimer outcrop slabs (15cm*15cm). An X-ray imaging technique was used to visualize displacements and to determine the underlying flow mechanisms for a series of parameters combinations involving various viscosity ratios for a fixed capillary number (6.9E-09). The advantage of using slabs for this type of experiment is that it approximates a 2D system that is easier to monitor and visualize in real time.

A series of simulations have been performed to model these experiments. We have shown previously (Chapter 7) that we are able to reproduce the experimental behaviour at the full slab scale (30cm*30cm) for M=7000 and M=2000. However, in order to reduce computational runtimes, we now choose to use 5cm x 15cm models corresponding to 250*750 network. The network was built using the same methodology explained in Chapter 7 and the same wettability scenario was assumed (weakly oil wet).

The simulation of the first Skauge et al. (2014) experiment with a viscosity ratio M=5.1, showed the initiation of thick viscous fingers at early stages (Figure 9.10). However, these fingers later merged, forming a stable front with good sweep efficiency. This regime looks similar to the highly efficient displacement regime described earlier in this section and observed at the transition between capillary and viscous dominated flows for displacements involving adverse (but not very high) viscosity ratios. Whilst the displacement front initially remained flat in the simulation, some wider channels were seen to develop later and propagate faster towards the outlet. This occurred when the front had reached about 2/3 of the length of the slab (Figure 9.10 PV inj=0.277). Figure 9.12 shows a comparison with the corresponding experiment, which exhibits similar behaviour. Furthermore, the saturations at breakthrough were high in both experiment and simulation and were respectively equal to 0.46 and 0.4 – although the saturation images show that there was more trapping in the simulation, this is to be expected as a result of the two dimensional nature of the simulations that makes trapping easier. We must also remember that the experimental images are “stacks” of 2D sectional images.

In our simulation of the experiment with a viscosity ratio equal to 66 cP (Figure 9.11), thick viscous fingers were seen to merge forming water channels as the water advanced.

One of the channels reached the outlet faster than the others in both simulation and experiment ─ water saturation at breakthrough was relatively high and was equal respectively to 0.38 in the experiment and 0.27 in the simulation (see Figure 9.13 for a comparison).

As the viscosity ratio increased, the fingers started to become thinner and the water saturation at breakthrough lower. This behaviour was observed in both experiments and simulations with viscosity ratios equal to 412 and 616 (Figure 9.14 and Figure 9.15).

These simulations represent another test to check the ability of our simulator to reproduce qualitatively the same flow regimes observed experimentally. Again, the simulator proved capable of simulating the same flow regimes obtained in the laboratory studies.

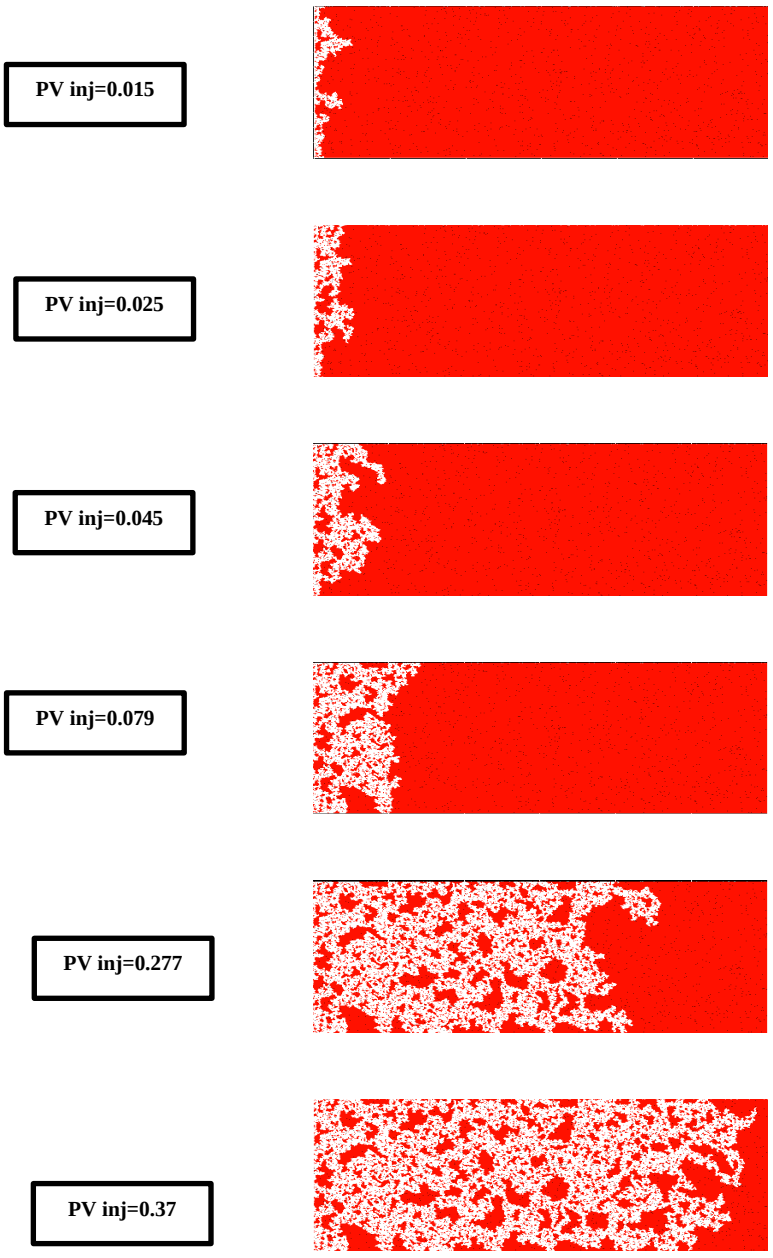

Figure 9.10: Saturation maps at different pore volumes injected during a waterflooding simulation of Bentheimer rock. The viscosity ratio was equal to 5.1 and the capillary number was 6.9 E-09.

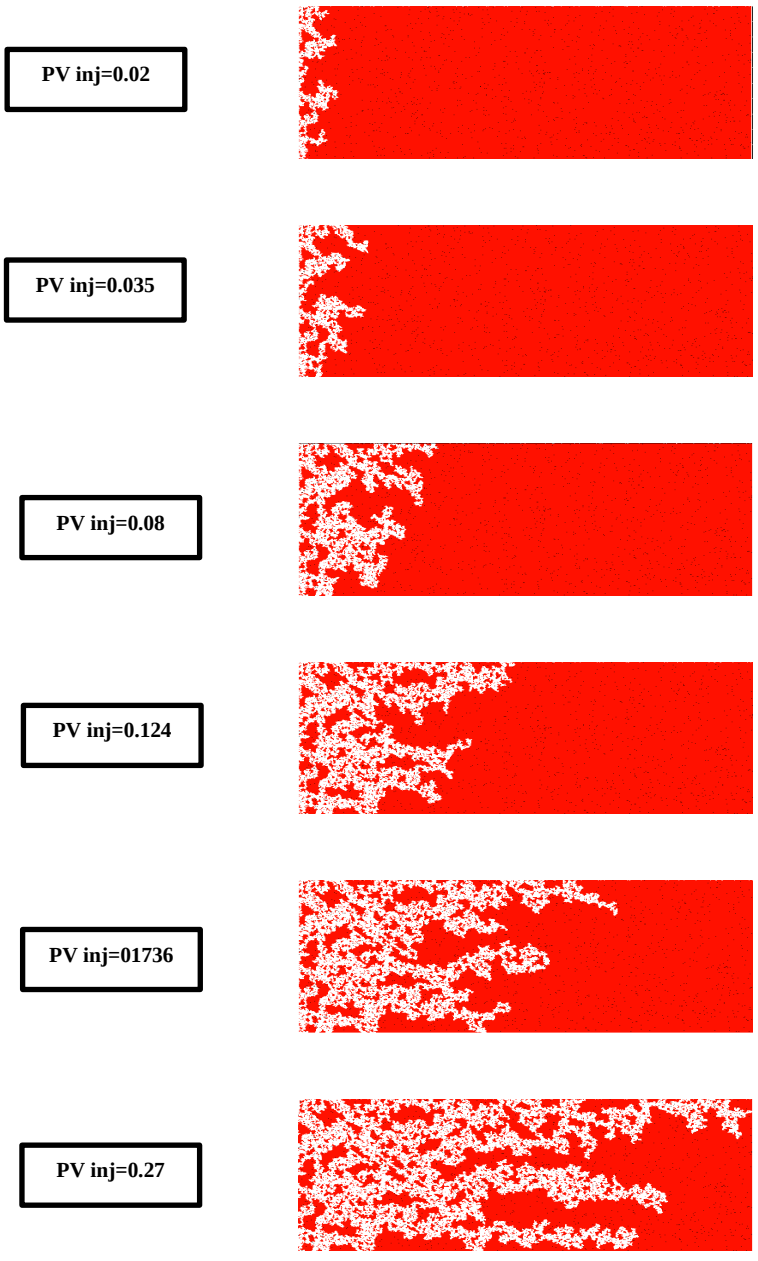

Figure 9.11: Saturation maps at different pore volumes injected during a waterflooding simulation of Bentheimer rock . The viscosity ratio was equal to 66 and the capillary number was 6.9 E-09.

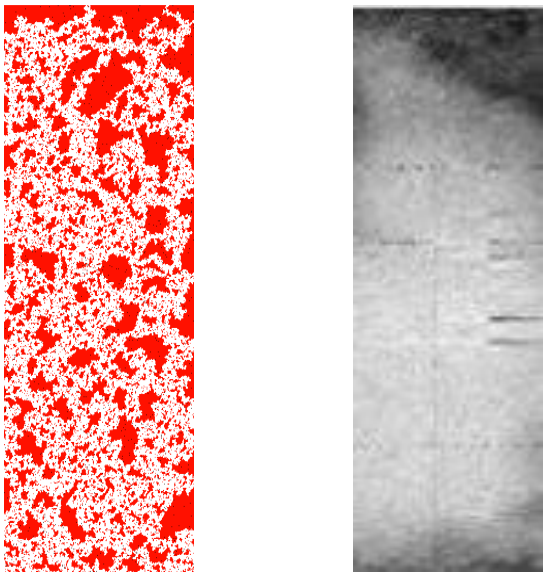

(a) **(b)**

Sw at BT=0.4 **Sw at BT =0.46**

Figure 9.12: Comparison between (a) simulated and (b) experimental saturation maps at breakthrough during waterflooding of a Bentheimer rock using fluids with a viscosity ratio M=5.1. The experimental results were taken from Skauge et al (2014).

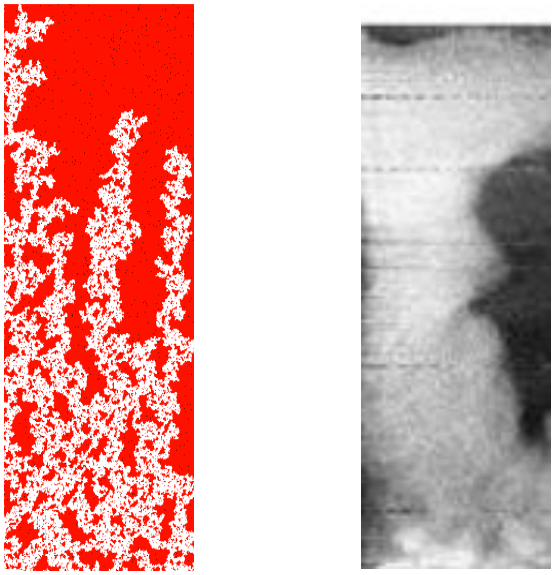

(a) **(b)**

Sw at BT=0.27 **Sw at BT=0.38**

Figure 9.13: Comparison between (a) simulated and (b) experimental saturation maps at breakthrough during waterflooding of a Bentheimer rock using fluids with a viscosity ratio M=66. The experimental results were taken from Skauge et al (2014).

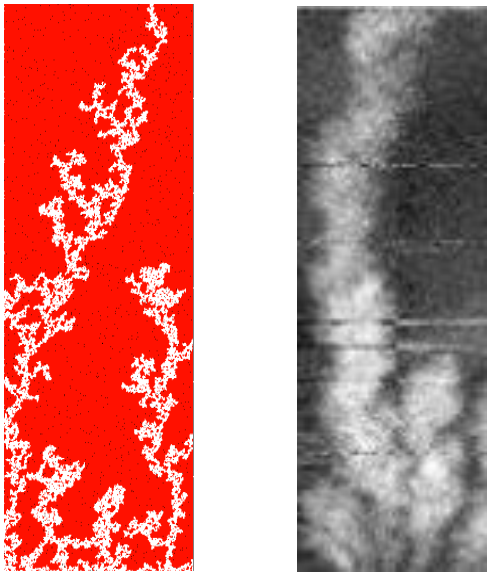

(a) **(b)**

Sw at BT=0.14 **Sw at BT =0.148**

Figure 9.14: Comparison between (a) simulated and (b) experimental saturation maps at breakthrough during waterflooding of a Bentheimer rock using fluids with a viscosity ratio M=412. The experimental results were taken from Skauge et al (2014).

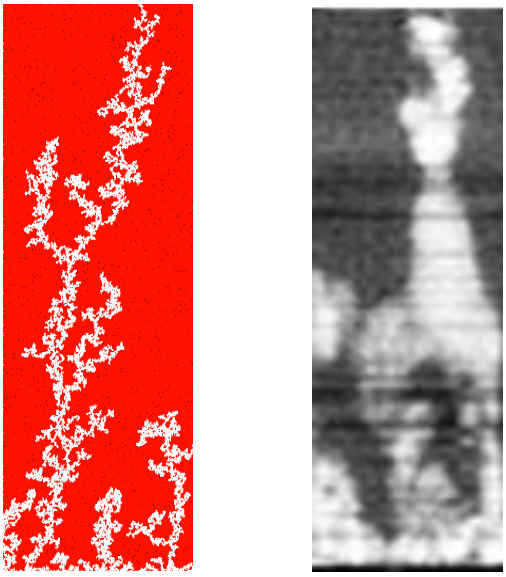

(a) **(b)**

Sw at BT=0.11 **Sw at BT=0.08**

Figure 9.15: Comparison between (a) simulated and (b) experimental saturation maps at breakthrough during waterflooding of a Bentheimer rock using fluids with a viscosity ratio M=616. The experimental results were taken from Skauge et al (2014).

9.2.2. Wettability effect

Several simulation sets were performed to investigate the general effect of wettability on oil recovery at breakthrough. The same network generated to mimic Bentheimer rock in the previous section is used in all the simulations and, in all sets, we start with a strongly oil wet system and then repeat the simulation using progressively lower contact angles (i.e. tending towards a more neutrally-wet condition).

It is commonly believed (Morrow, 1990, Jadhunandan and Morrow, 1995, Hirasaki et al., 2011) that optimal oil recovery is obtained at neutral wet or mixed wet conditions. These studies have generally focussed on conventional oils and our numerical simulations are consistent with this behaviour. Figure 9.16 shows a simulation in a 7.5cm *7.5cm Bentheimer surrogate for M=1 – we see that a decrease in the contact angle to intermediate wet conditions simply reduces the capillary forces and thus the flow becomes more viscous-dominated and the front becomes more stable (the water saturation at breakthrough increases from 24% for θ=180° to 56% for θ=90°).

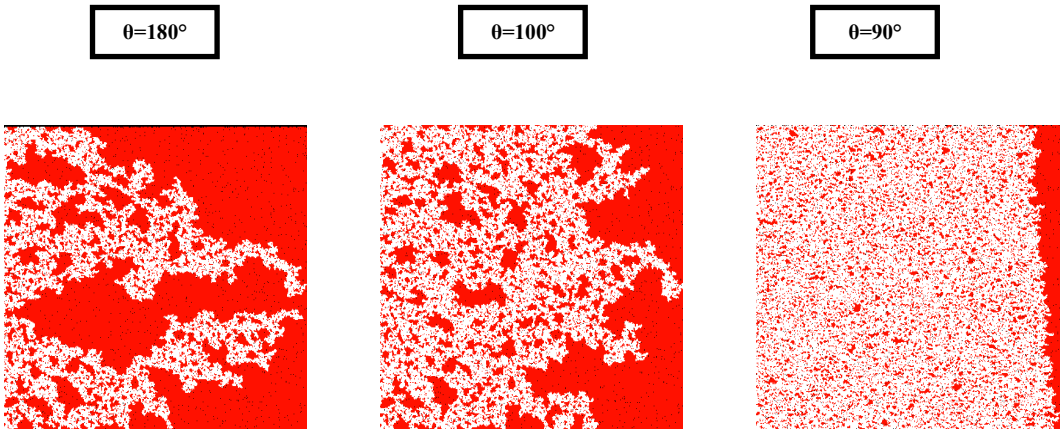

Figure 9.16: Contact angle effect on waterflooding of a Bentheimer surrogate (7.5*7.5cm). M=1 and NCa=9.23 E-09.

However, the behaviour becomes very different for heavier oils. In Figure 9.17 (M=100), we can see that when the system approaches intermediate-wet conditions, viscous fingering rapidly takes over, resulting in a decrease in recovery at breakthrough from 24% to 17%.

Similar behaviour was observed for M=7000 (Figure 9.18). In this case, reducing the contact angle resulted in the emergence of thinner fingers and as a result a decline in recovery at breakthrough. Here, the capillary forces act to stabilise the water front only under strongly oil-wetting conditions, preventing the initiation of instabilities.

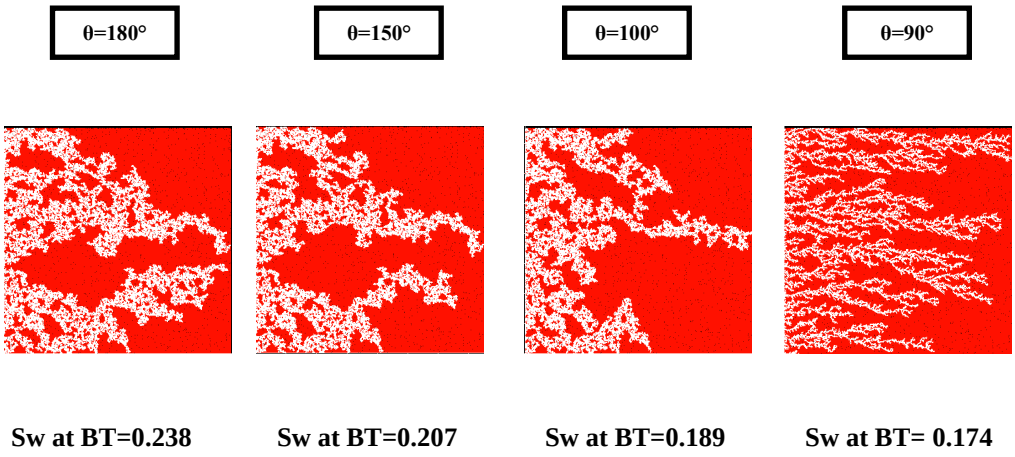

Figure 9.17: Contact angle effect on waterflooding of a Bentheimer surrogate (7.5*7.5cm). M=100 and NCa=4.62E-09.

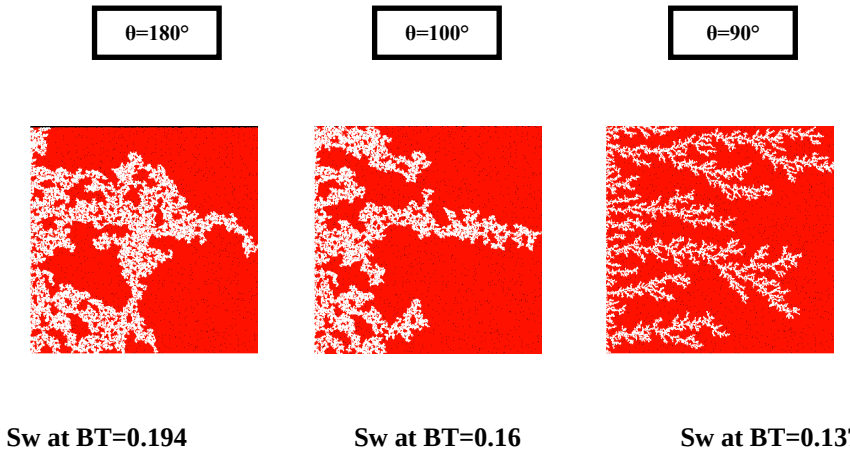

Figure 9.18: Contact angle effect on waterflooding of a Bentheimer surrogate (7.5*7.5cm). M=7000 and NCa=4.62E-11.

We conclude this discussion with an example of how a change in wettability can also force a system into the highly efficient displacement regime described earlier. The M=10 case (Figure 9.19) exhibits this interesting behaviour. Here, a decrease in contact angle from 180° to 100° increased oil recovery by 7%. This is due to the fact that the initial rate was low and so, for a strongly oil-wet system, the flow regime was capillary dominated. A decrease in the contact angle (and hence the capillary forces) shifted the flow regime into the highly efficient window that we have described earlier in this chapter.

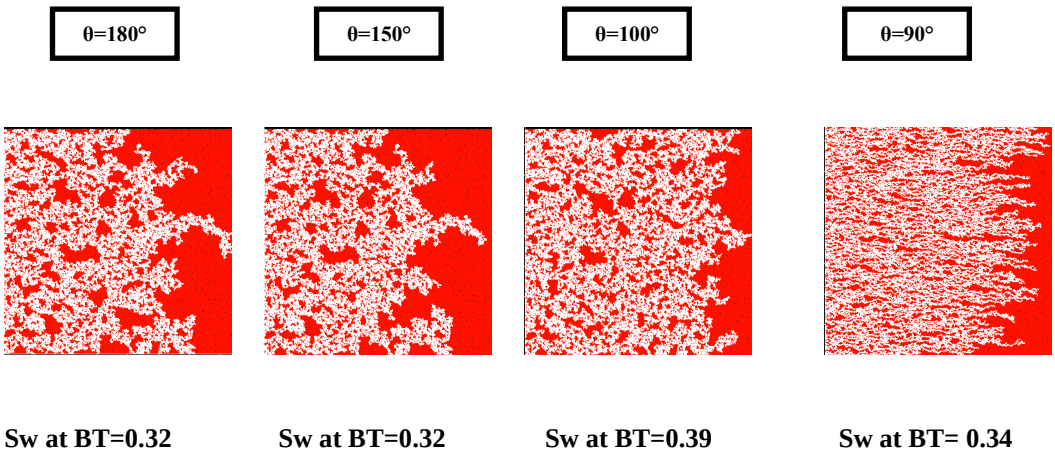

Figure 9.19: Contact angle effect on waterflooding of a Bentheimer surrogate (7.5*7.5cm). M=10 and NCa=4.62E-08.

To summarize, we see that wettability is an important parameter affecting the recovery of heavy oil. Indeed, a relatively small change in the contact angle can result in a large change in oil recovery and this effect becomes more significant when we are close to the intermediate wetting state. For example, for M=10, a decrease in the contact angle by 10° reduced the oil recovery by 5% at breakthrough, whilst for M=1 a similar change in the contact angle increased the oil recovery at breakthrough by 21%. However, we should bear in mind that a change of wettability can also have an effect on film flow that is not modelled in our simulator and therefore this effect is not captured by our model.

9.2.3. Core length effect

Several simulation sets were performed to investigate the effect of core length on oil recovery at breakthrough. An irregular network of bonds was used in these simulations with a mean pore radius equal to 25μm, an average coordination number in 2D equal to 3 and average bond length equal to 300 μm. Starting with low injection rates and then increasing the injection flux, we compare the flow regimes obtained for two networks with lengths equal to 12cm and 6cm respectively. The viscosity ratio was set equal to 7000. Figure 9.20 shows that for all the simulations, the same flow regime was obtained in the short and in the longer network. This suggests that, *before breakthrough*, the network length does not affect the emergent flow regime.

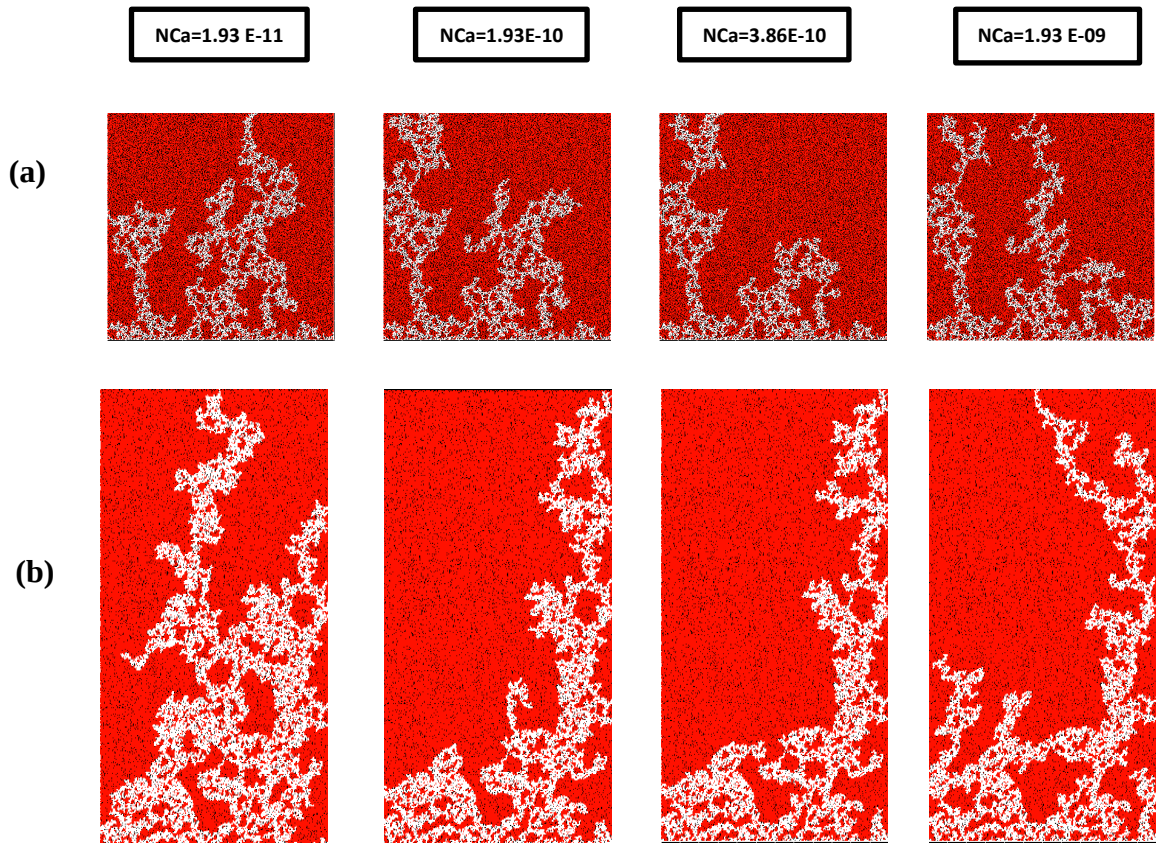

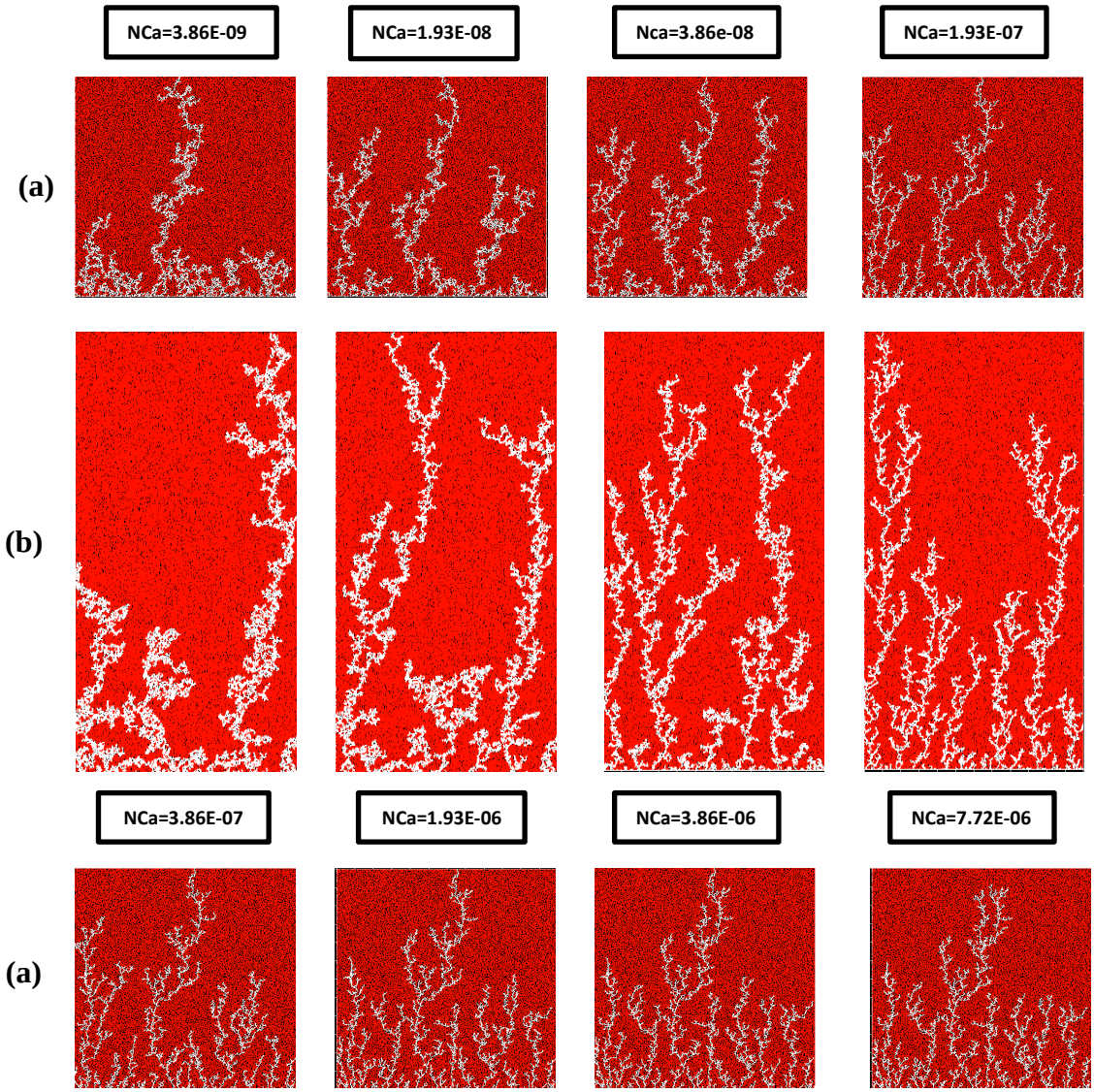
NCa=3.86E-09
NCa=1.93E-08
Nca=3.86e-08
NCa=1.93E-07
(a)
(b)
NCa=3.86E-07
NCa=1.93E-06
NCa=3.86E-06
NCa=7.72E-06
(a)

(b)

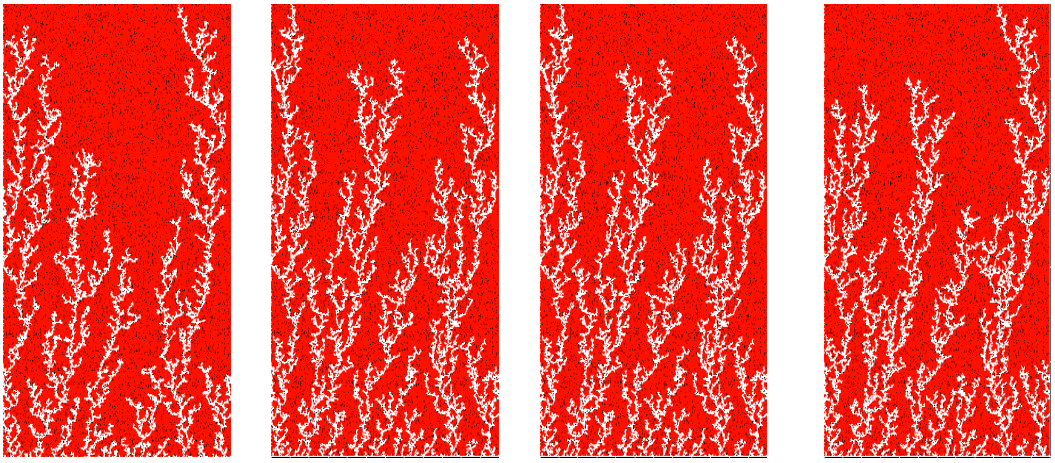

Figure 9.20: Comparison between simulations performed using different network lengths 6cm*6cm (a) and 12cm*6cm (b). The viscosity ratio was equal to 7000 and several capillary numbers were considered.

9.3. POST-BREAKTHROUGH BEHAVIOUR

Having studied the flow behaviour until breakthrough, we now go on to investigate the flow mechanisms after breakthrough. Such mechanisms may be especially important for extra heavy oil where water breakthrough occurs at very low saturations.

We have seen in Chapter 8 that, under some conditions of injection rate, wettability and core length, there is no extra oil recovery after breakthrough ─ the injected water flows only through the spanning fingers. We have also demonstrated that recovery after breakthrough can be extended for longer times if the flow rate is higher, cores are longer and wetting conditions are more neutral. In this section, we will examine post-breakthrough behaviour.

First, we check our post-breakthrough behaviour against the Skauge et al. (2014) experiments. Considering first the displacement involving fluids with a viscosity ratio M=66, we see that, in both experiment and simulation, thick viscous fingers were initiated and then merged to form thick water channels as the water advanced (Figure 9.21). One of these thick fingers reached the outlet faster than the others in both simulation and experiment, and the water saturation at breakthrough was relatively high (equal to 0.38 in the experiment and 0.27 in the simulation). Following breakthrough, the thick fingers left behind the main front continued to grow towards the outlet,

recovering more oil – again, this behaviour was exhibited in both experiment and simulation.

For displacements involving heavier oils (M=412 and M=616 shown in Figures 9.22 and 9.23 respectively), the fingers were thinner than those observed in the M=66 case and the water saturation at breakthrough lower. After breakthrough, all fingers started to thicken and some of the upstream fingers continued to grow towards the outlet. The simulation behaviour was in good agreement with the experimental observations.

These simulations represent a base case and will be used subsequently to check the effect of changing one of the system parameters (injection rate, wettability and core length) upon the flow regimes and oil recovery.

(a)

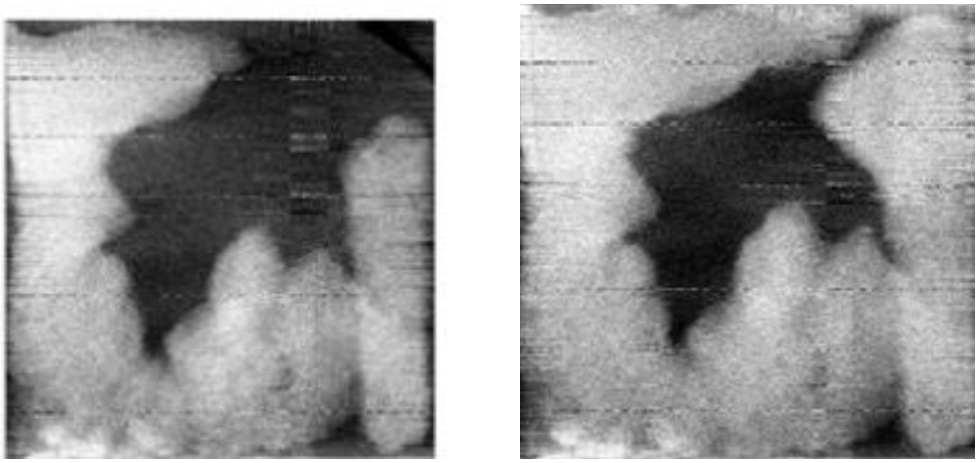

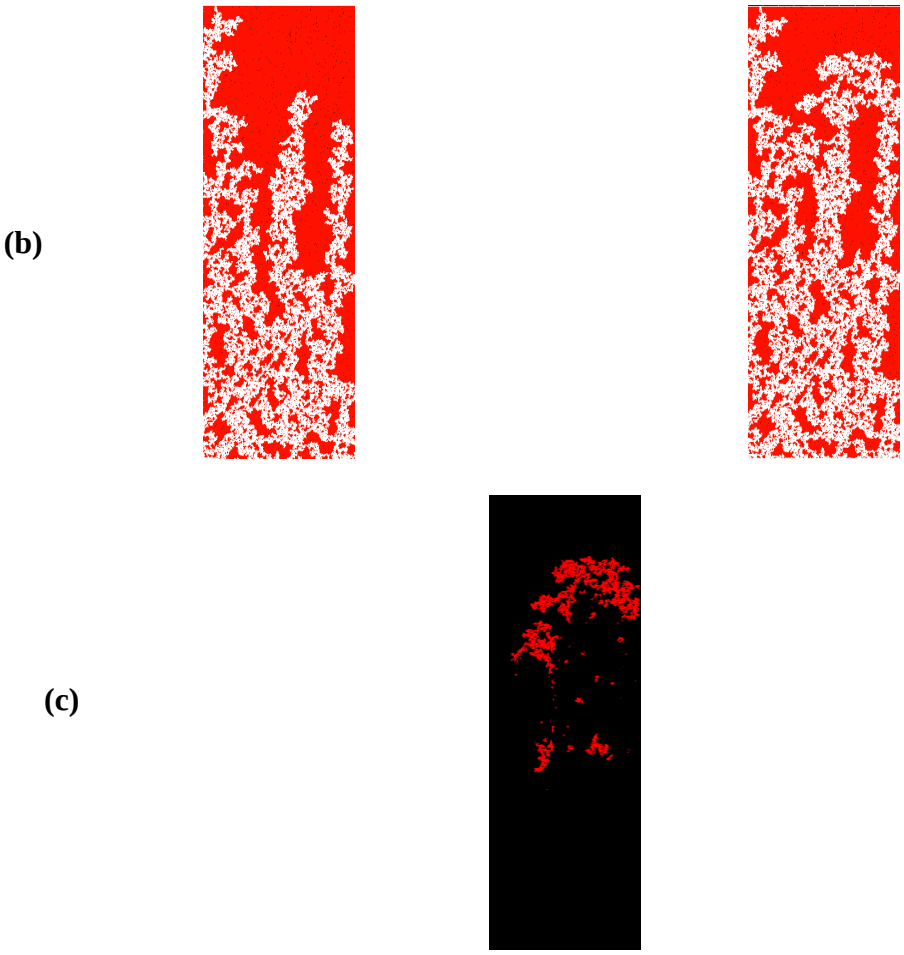

Figure 9.21: Comparison between (a) simulated and (b) experimental saturation maps at breakthrough and after 1PV injected during waterflooding of a Bentheimer rock using fluids with a viscosity ratio M=66. (c) Location of the new water invasions occurred after BT (red) at 1 PV injected. The experimental results were taken from Skauge et al (2014).

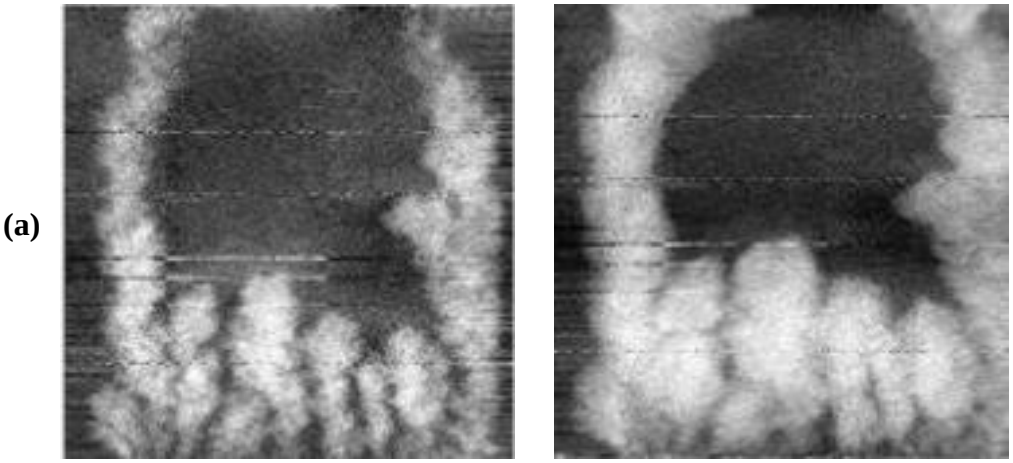

(b)

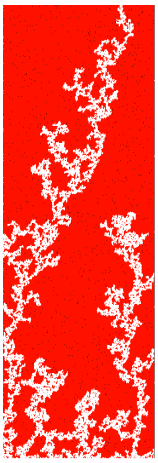

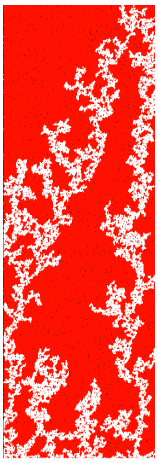

(c)

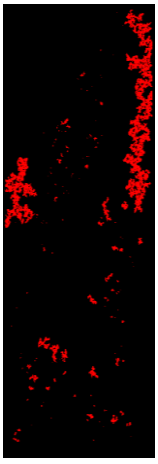

Figure 9.22: Comparison between simulated (a) and experimental (b) saturation maps at breakthrough and after 1PV injected during waterflooding of a Bentheimer rock using fluids with a viscosity ratio M=412. (c) Location of the new water invasions occurred after BT (red) at 1 PV injected. The experimental results were taken from Skauge et al (2014).

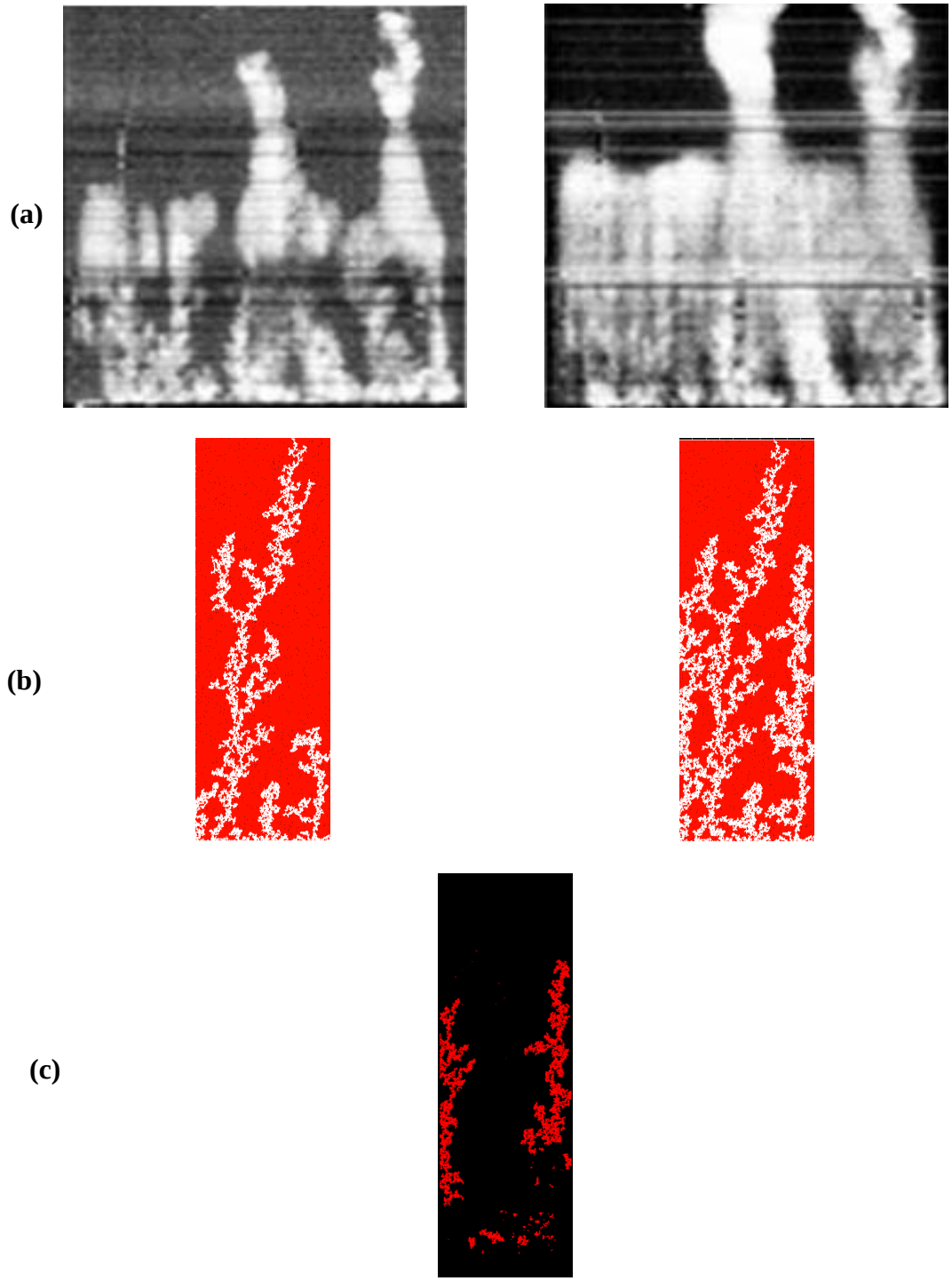

Figure 9.23: Comparison between simulated (a) and experimental (b) saturation maps at breakthrough and after 1PV injected during waterflooding of a Bentheimer rock using fluids with a viscosity ratio M=616. (c) Location of the new water invasions occurred after BT (red) at 1 PV injected. The experimental results were taken from Skauge et al (2014).

9.3.1. Rate and viscosity ratio effects

Several simulation sets were performed to investigate the effect of injection rate on oil recovery after breakthrough. The first set (Figure 9.24) represents a case with a viscosity ratio M=66 and weakly oil conditions. At the lowest rate, thick fingers were obtained prior to breakthrough, leading to high water saturation at breakthrough ─ hence, the main recovery mechanism was the development of the thick fingers. However, as the rate increased, the fingers became thinner and the water saturation at breakthrough smaller. In these cases, most of the oil was recovered by the growth of the fingers left behind; some finger thickening was observed for the medium rate but almost no thickening was seen at the highest rate. An increase in the injection rate decreased the recovery after roughly 0.25 PV of injection, as we can see in Figure 9.25.

Heavier oils (M=616 and M=7000) exhibited different flow behaviour, as shown in Figures 9.26-9.29, which represent different sets of simulations performed using weakly oil wet conditions at different injection rates. For a viscosity ratio equal to 616 (Figure 9.26), viscous fingering was observed even at the lowest rate considered, resulting in early water breakthrough and extensive oil recovery post-breakthrough. However, at the high rate more viscous instabilities were observed, resulting in a higher recovery at breakthrough. After breakthrough, two different recovery mechanisms were evident: (i) at the low rate the upstream fingers were seen to thicken and grow slightly towards the outlet, (ii) at the high rate, the upstream fingers remained thin and continued to grow towards the outlet. Figure 9.27 shows that an increase in the injection rate improves the oil recovery for this viscosity ratio.

The simulations involving fluids with a viscosity ratio equal to 7000 again showed low water saturation at breakthrough; and this saturation did not vary considerably after changing the injection rate (Figure 9.28). Like the previous case, most of the recovery occurred post breakthrough. At the lowest rate, the instabilities were seen to thicken and grow towards the outlet. However, as the rate increased, the thickening was less noticeable and more fingers were seen growing towards the outlet as a result of the high viscous forces. Furthermore, the recovery was better for higher rates, as can be seen in Figure 9.29.

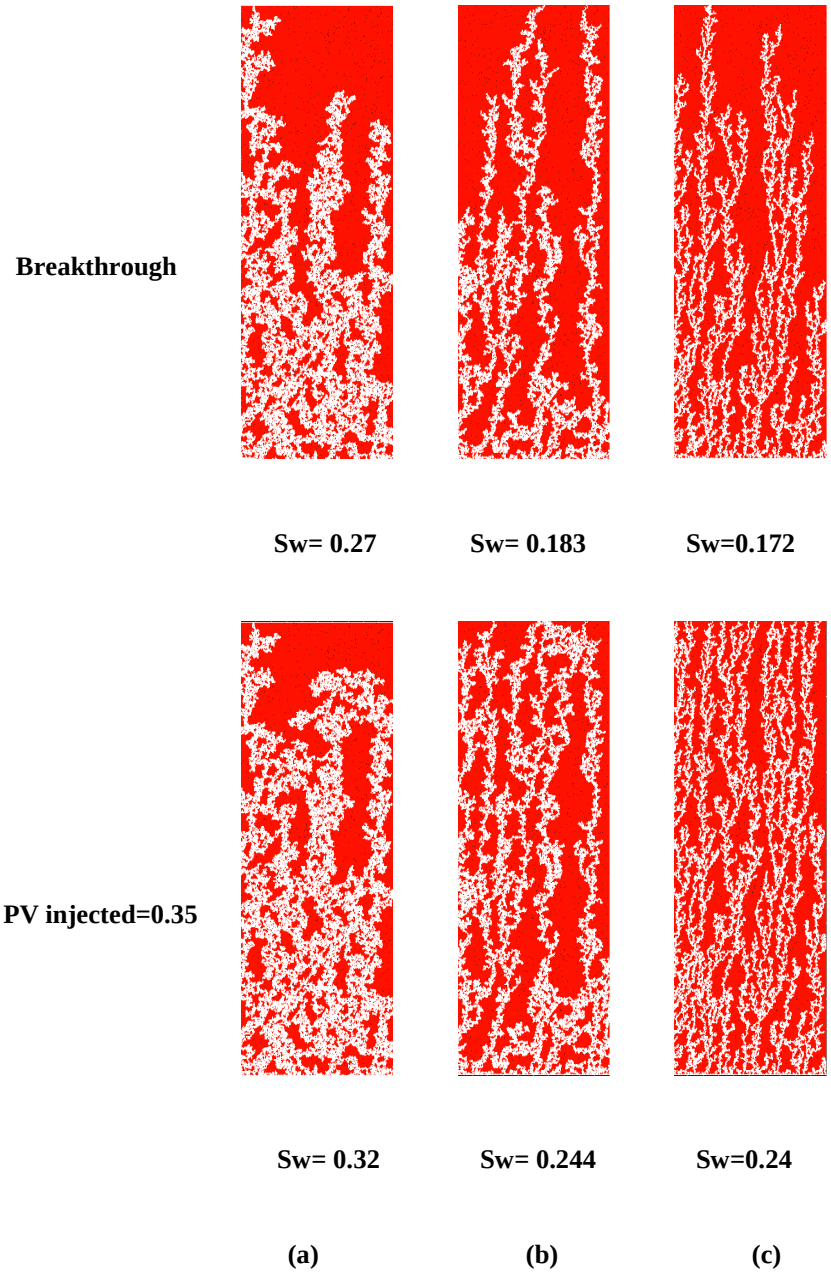

Figure 9.24: Comparison between simulations performed in Bentheimer surrogate (5*15 cm) at several injection rates: (a) Q1= 0.005 cc/hr (Nca= 6.9E-9), (b) Q2= 0.05 cc/hr (Nca=6.9 E-08) and (c) Q3= 0.5 cc/hr (Nca=6.9 E-07). In this case the viscosity ratio was equal to 66.

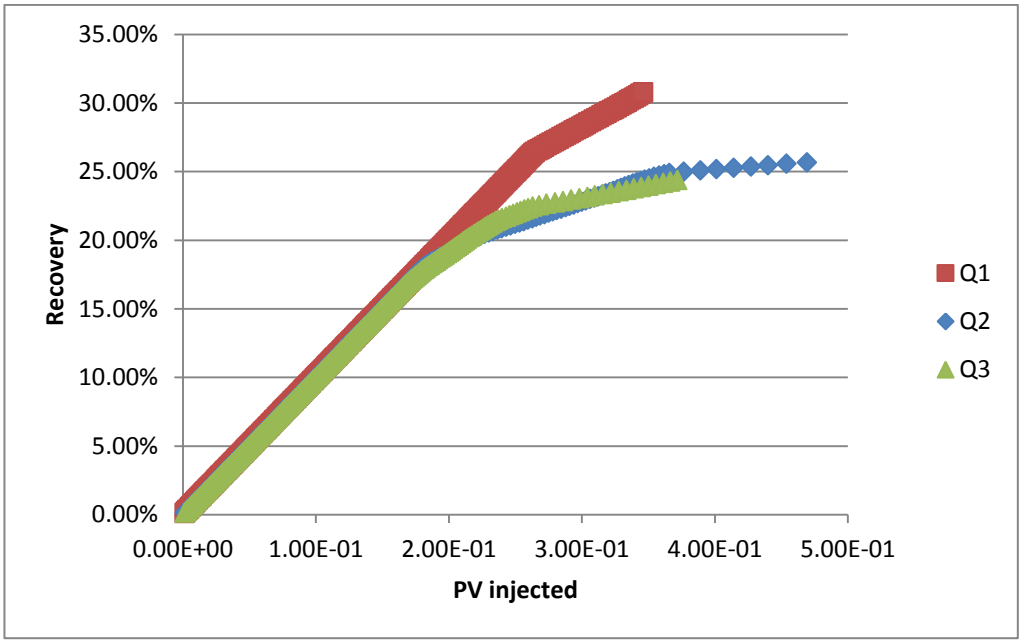

Figure 9.25: Comparison between oil recovery in simulations performed in Bentheimer surrogate (5*15 cm) at several injection rates: Q1= 0.005 cc/hr (Nca= 6.9E-9) , Q2= 0.05 cc/hr (Nca=6.9 E-08) and Q3= 0.5 cc/hr (Nca=6.9 E-07) . In this case the viscosity ratio was equal to 66.

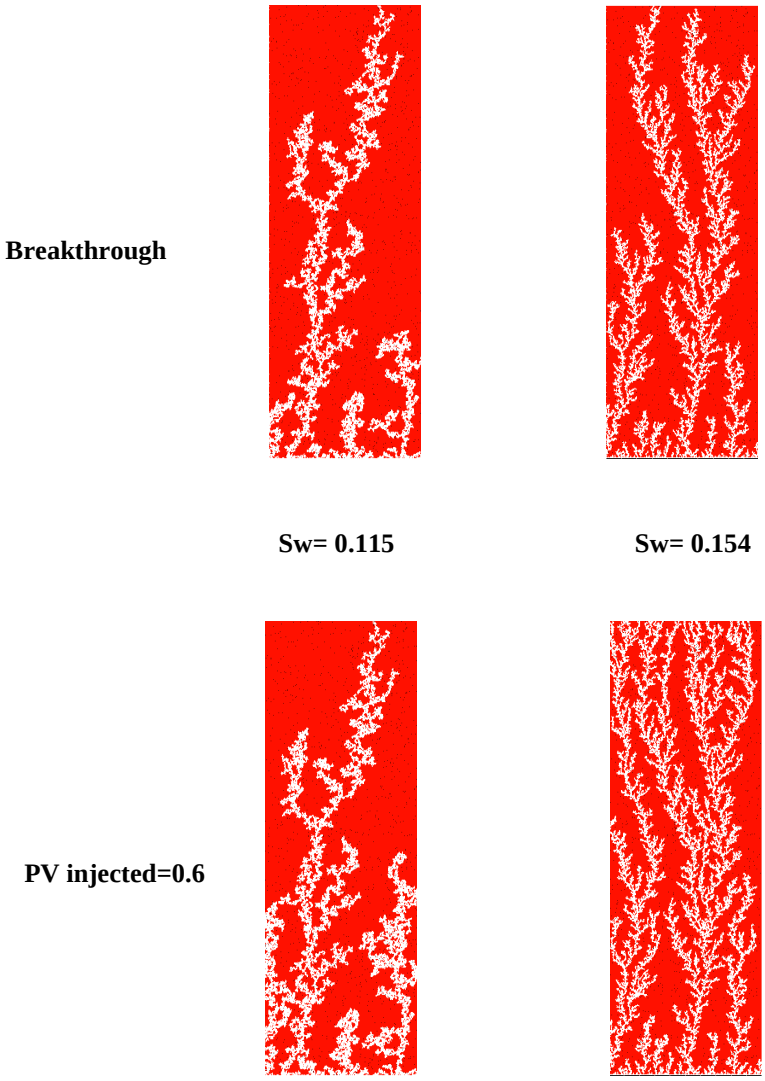

Figure 9.26: Comparison between simulations performed in Bentheimer surrogate (5*15 cm) at several injection rates: (a) Q1= 0.005 cc/hr (Nca= 6.9E-9) and (b) Q3= 0.5 cc/hr (Nca=6.9 E-07). In this case the viscosity ratio was equal to 616.

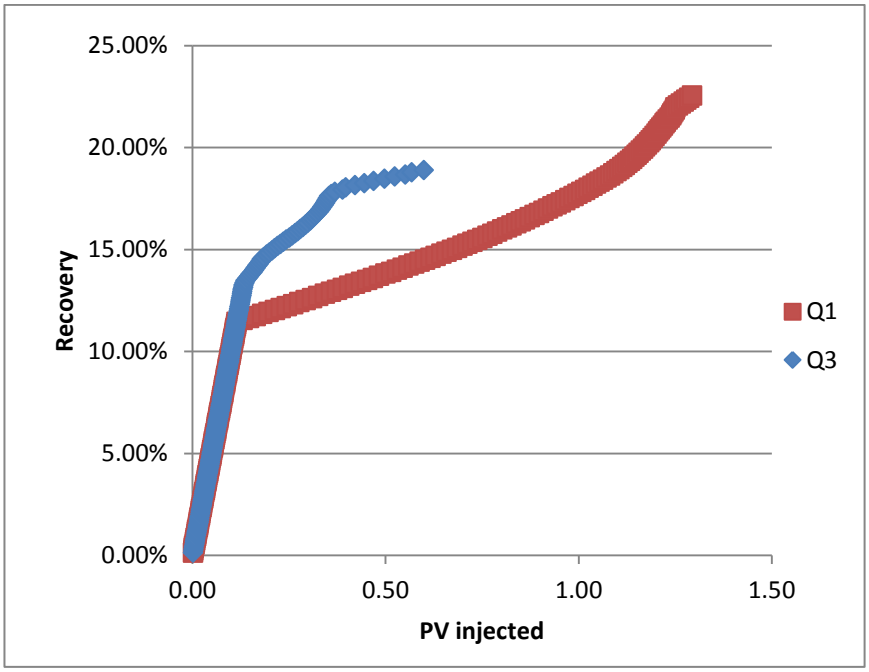

Figure 9.27: Comparison between oil recovery in simulations performed in Bentheimer surrogate (5*15 cm) at several injection rates: Q1= 0.005 cc/hr (Nca= 6.9E-9) and Q3= 0.5 cc/hr (Nca=6.9 E-07) . In this case the viscosity ratio was equal to 616.

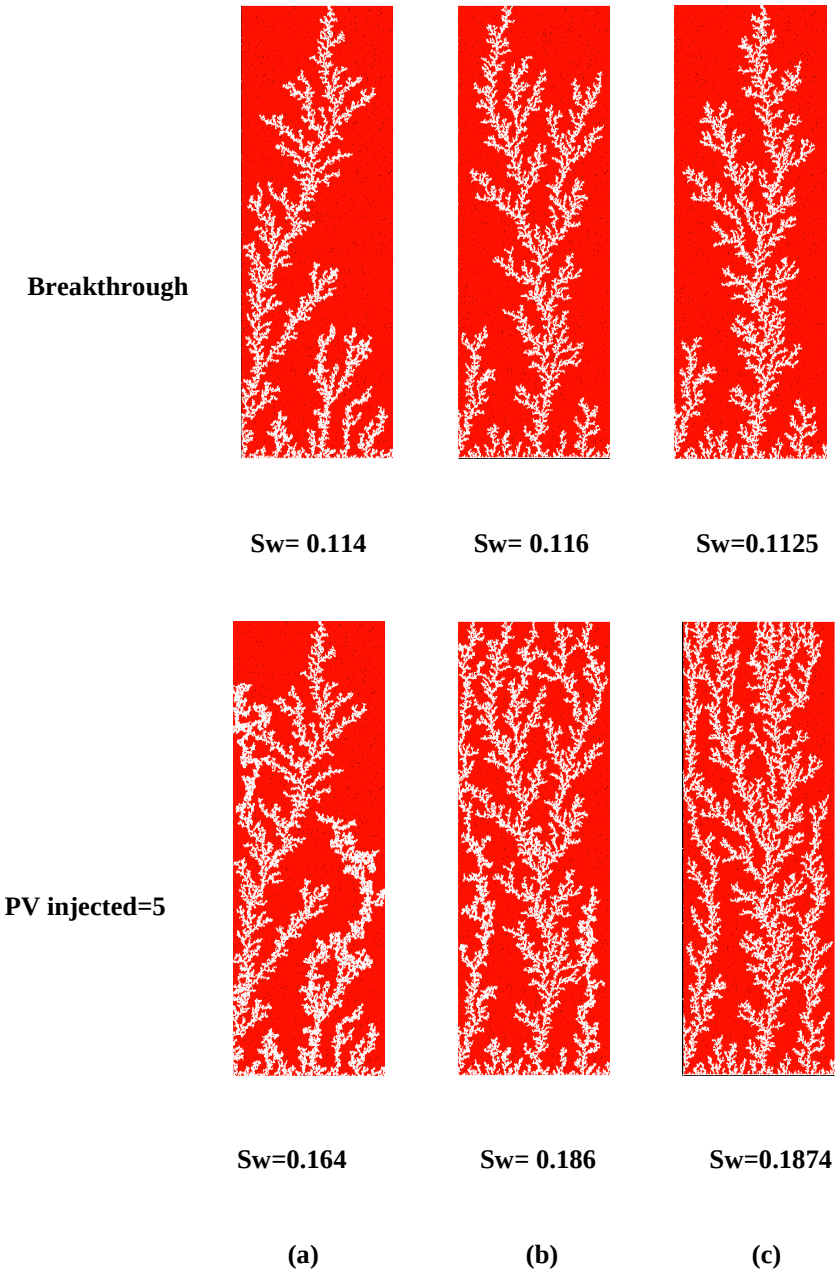

Figure 9.28: Comparison between simulations performed in Bentheimer surrogate (5*15 cm) at several injection rates: (a) Q1= 0.005 cc/hr (Nca= 6.9E-9), (b) Q2= 0.05 cc/hr (Nca=6.9 E-08) and (c) Q3= 0.5 cc/hr (Nca=6.9 E-07). In this case the viscosity ratio was equal to 7000 and the network was weakly oil wet.

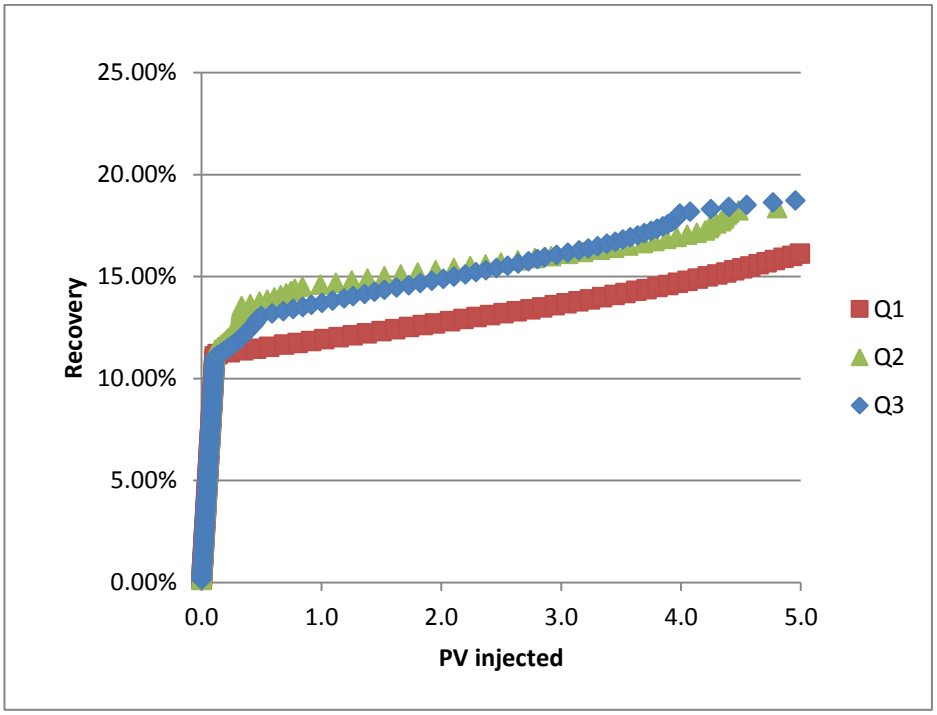

Figure 9.29: Comparison between oil recovery in simulations performed in Bentheimer surrogate (5*15 cm) at several injection rates: Q1= 0.005 cc/hr (Nca= 6.9E-9) , Q2= 0.05 cc/hr (Nca=6.9 E-08) and Q3= 0.5 cc/hr (Nca=6.9 E-07) . In this case the viscosity ratio was equal to 7000 and the network was weakly oil wet.

9.3.2. Wettability effect

A number of simulations were performed to investigate the effect of wettability on oil recovery after breakthrough in a 5 cm*15 cm Bentheimer surrogate ─ in all sets, we compare two wettability scenarios: strongly oil wet and weakly oil wet cases.

The first set represents a case with a viscosity ratio equal to 7000 and a capillary number Nca=6.9 E-08. Figure 9.30 shows that sharp viscous fingers were observed in both considered wettability scenarios, resulting in early water breakthrough and extensive oil recovery post-breakthrough. After breakthrough, two different recovery mechanisms were observed: (i) in the strong oil wet case the upstream fingers were seen to thicken and grow slightly towards the outlet, (ii) in the weakly oil wet case, however, the upstream fingers remained thin and simply continued to grow towards the outlet. Figure 9.31 shows that the displacement involving the weakly oil-wet system gave higher recovery.

Figure 9.32 represents a case at the same capillary number Nca=6.9 E-08 but a different viscosity ratio. In the strongly oil wet case, thick fingers were obtained before breakthrough leading to high water saturation at breakthrough. Hence the main recovery mechanism in this case was the development of the thick fingers. In the weakly oil wet case, the fingers were thinner and the water saturation at breakthrough smaller. Here, most of the oil was recovered by the growth of thin fingers towards the outlet (although a small degree of finger thickening was also observed). Figure 9.39 shows that, in contrast to the M=7000 case, the displacement involving the weakly oil wet network gave *lower* recovery at equivalent injected pore volumes.

These results clearly demonstrate that wettability is an important parameter that can affect the oil recovery and the flow regime considerably. Changing the wettability towards more neutral wet conditions changes the balance between the viscous and capillary forces towards a more viscous dominated regime and this effect is similar to the behaviour observed after an increase in the injection rate. *Having a more neutral wet condition can lead to an increase or a decrease in oil recovery depending upon the viscosity ratio of the fluids.* Again, we should remember that a change of wettability can

have an effect on film flow that is not modelled in our simulator and therefore this effect is not captured by our model.

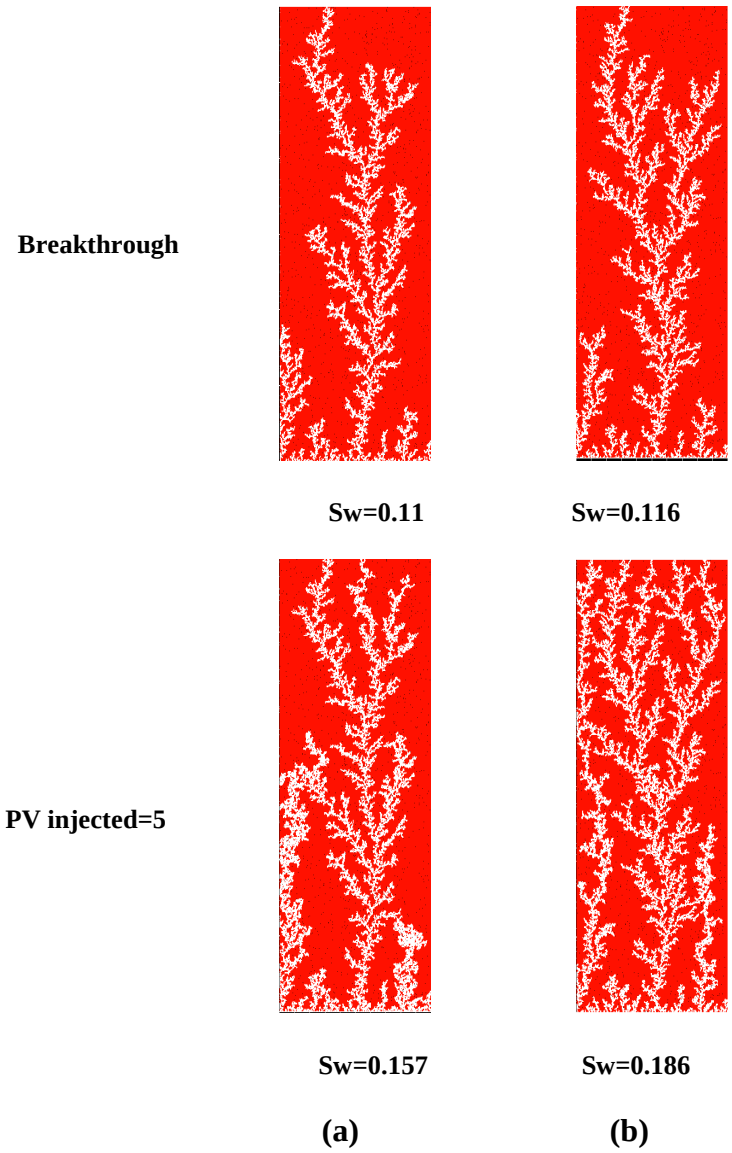

Figure 9.30: Comparison between simulations performed in Bentheimer surrogate (5*15 cm) at different wettability scenarios: (a) a strongly oil wet case (θ=180°)and (b) a weakly oil wet case (θ=100°)). In this case the viscosity ratio was equal to 7000 and the capillary number was equal to Nca=6.9E-08.

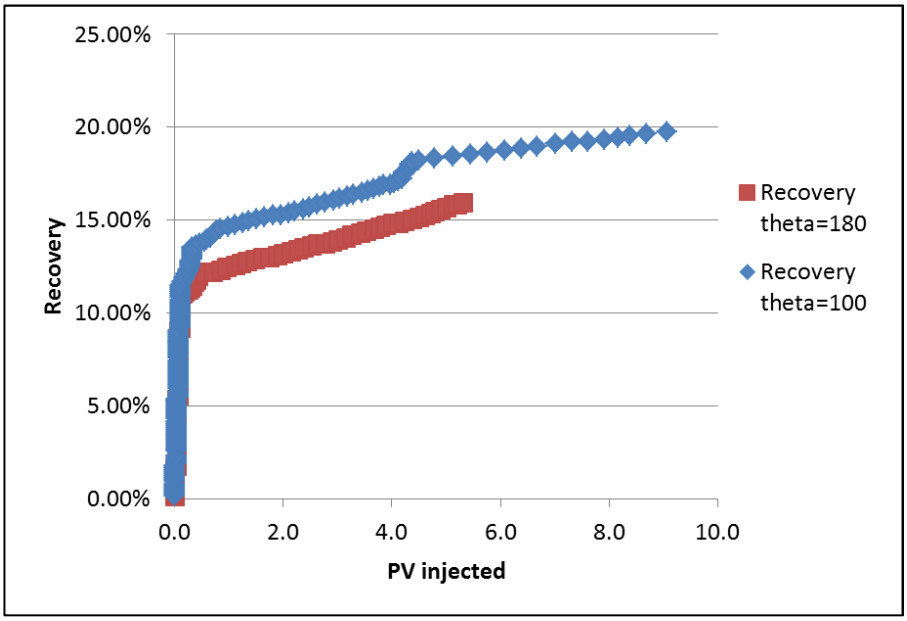

Figure 9.31: Comparison between the oil recovery in simulations performed in Bentheimer surrogate (5*15 cm) at different wettability scenarios. In this case the viscosity ratio was equal to 7000 and the capillary number was equal to Nca=6.9E-08.

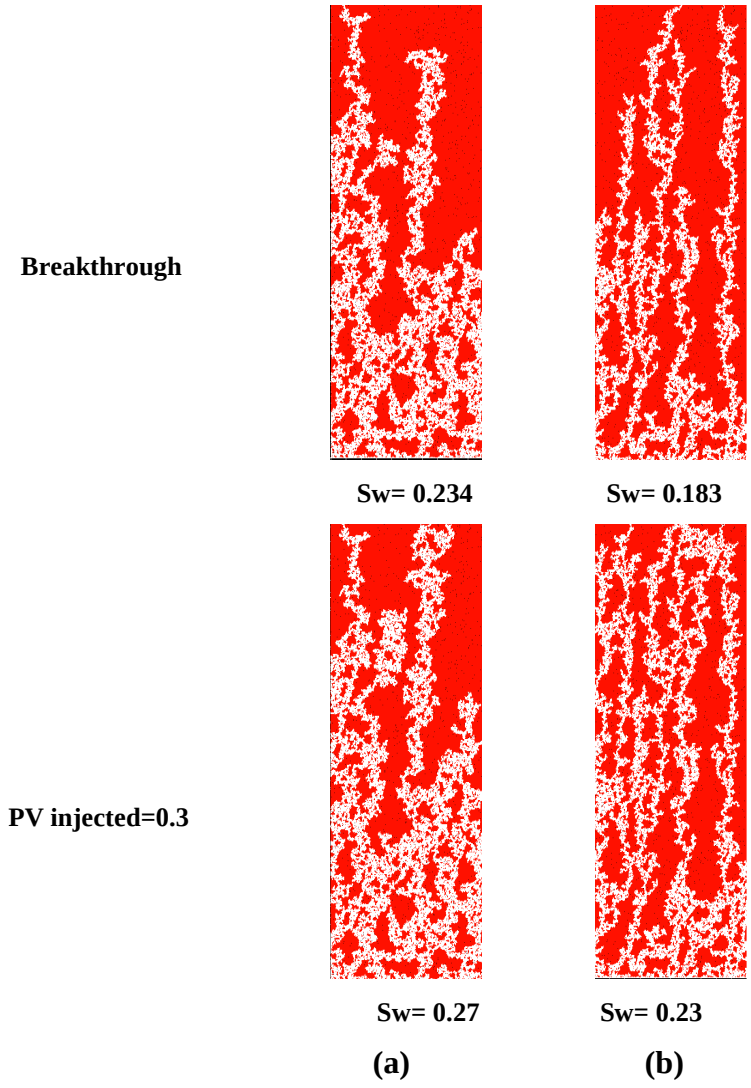

Figure 9.32: Comparison between simulations performed in Bentheimer surrogate (5*15 cm) at different wettability scenarios: (a) a strongly oil wet case (θ=180°) and (b) a weakly oil wet case (θ=100°)). In this case the viscosity ratio was equal to 66 and the capillary number was equal to Nca=6.9E-08.

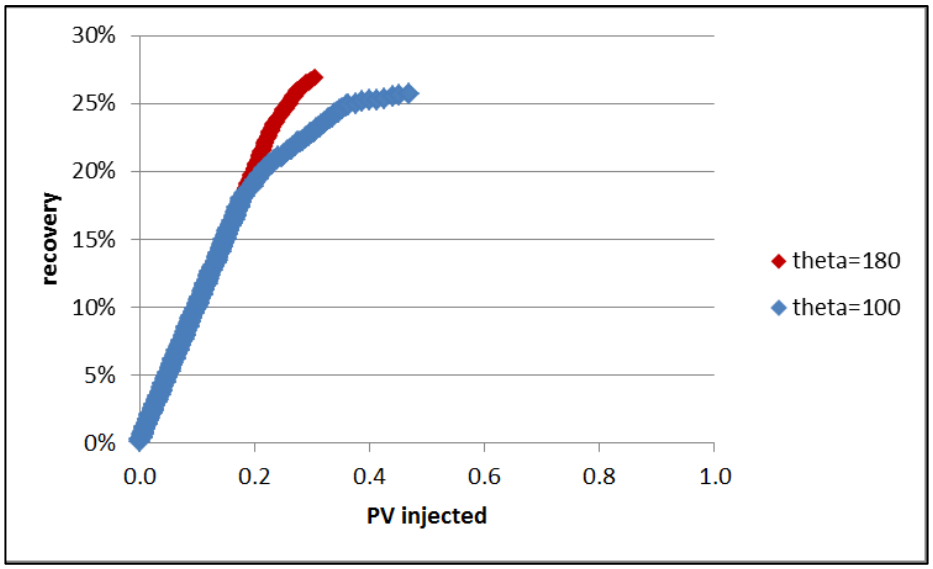

Figure 9.33: Comparison between the oil recovery in simulations performed in Bentheimer surrogate (5*15 cm) at different wettability scenarios. In this case the viscosity ratio was equal to 66 and the capillary number was equal to Nca=6.9E-08.

9.3.3. Core length effect

We investigate the impact of system length upon the flow behaviour post breakthrough. Two 2D networks corresponding to rocks with dimensions equal to 5 cm * 7.5 cm and 5 cm * 15 cm are considered and in all the simulations a weakly oil wet condition was assumed throughout (θ=100^o).

Figures 9.36 – 9.42 show the results of simulations at several rates for a displacement with a viscosity ratio equal to 7000. In all cases, although the same flow regime was obtained in the short and long systems, the number of viscous instabilities was seen to be higher in the shorter network. When we compare the oil recovery curves, we see that for all cases, while the recovery was faster in the shorter core, the oil recovery catches up in the longer core after injecting 4-5 pore volumes ─ the *final* recovery is similar in all cases.

Figure 9.41 and Figure 9.42 present the results of simulations done to investigate the effects of system length for a less viscous oil (M=66) and at a capillary number equal to 6.9 E-09. For the longest network, thick fingers were obtained initially that then merged, forming water channels as the simulations continued. For the shorter system, the thick fingers reaching the outlet were initiated faster and this resulted in lower water saturation at breakthrough (20% for the short network and 27% for the longer one). After reaching the outlet, some water started flowing through the spanning fingers, thus reducing the sweep efficiency. The oil recovery plots show that more oil was recovered for the longer system, which is opposite to the behaviour observed for the extra heavy oil (M=7000).

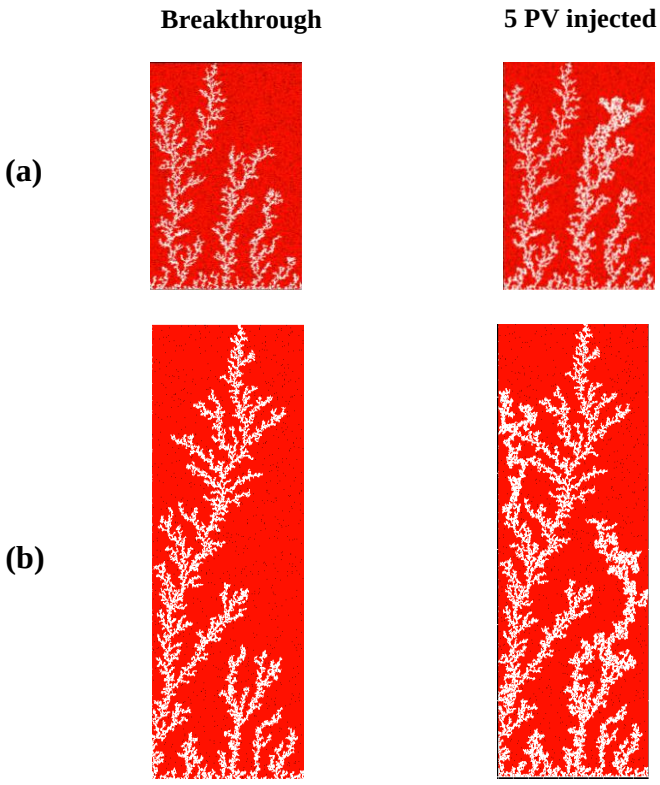

Figure 9.34: Comparison between the saturation maps in two simulations performed in networks having different lengths: (a) 5cm*7.5 cm network and (b) 5 cm*15 cm network. The viscosity ratio was equal to 7000 in this set and the capillary number was equal to 6.9 E-09.

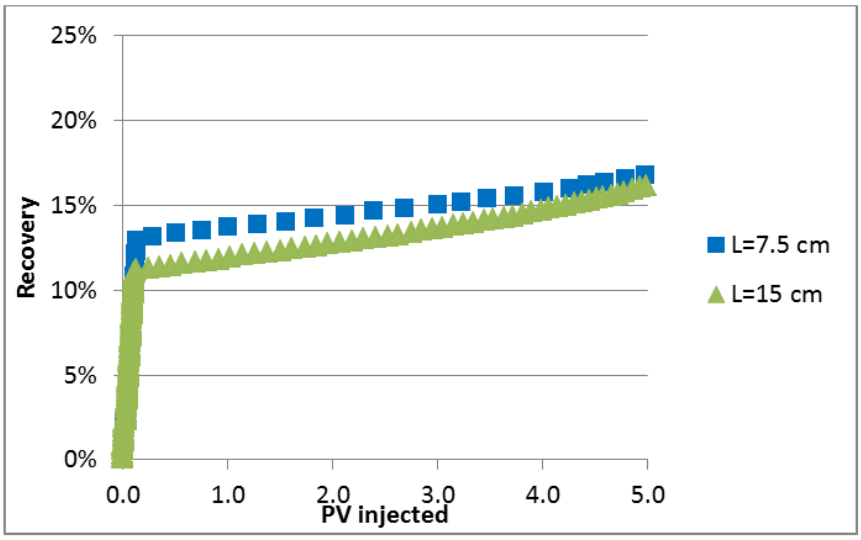

Figure 9.35 Comparison between the oil recovery in two simulations performed in networks having different lengths: 5cm*7.5 cm network and 5 cm*15 cm network. The viscosity ratio was equal to 7000 in this set and the capillary number was equal to 6.9 E-09.

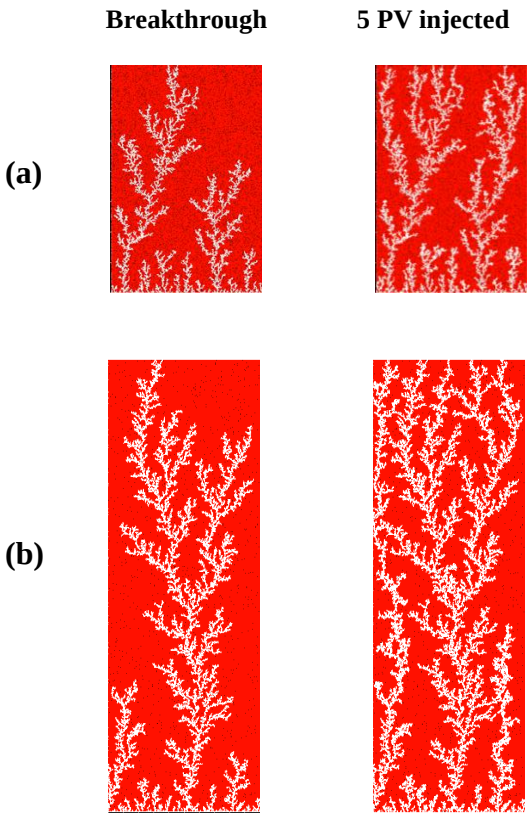

Figure 9.36: Comparison between the saturation maps in two simulations performed in networks having different lengths: (a) 5cm*7.5 cm network and (b) 5 cm*15 cm network. The viscosity ratio was equal to 7000 in this set and the capillary number was equal to 6.9 E-08.

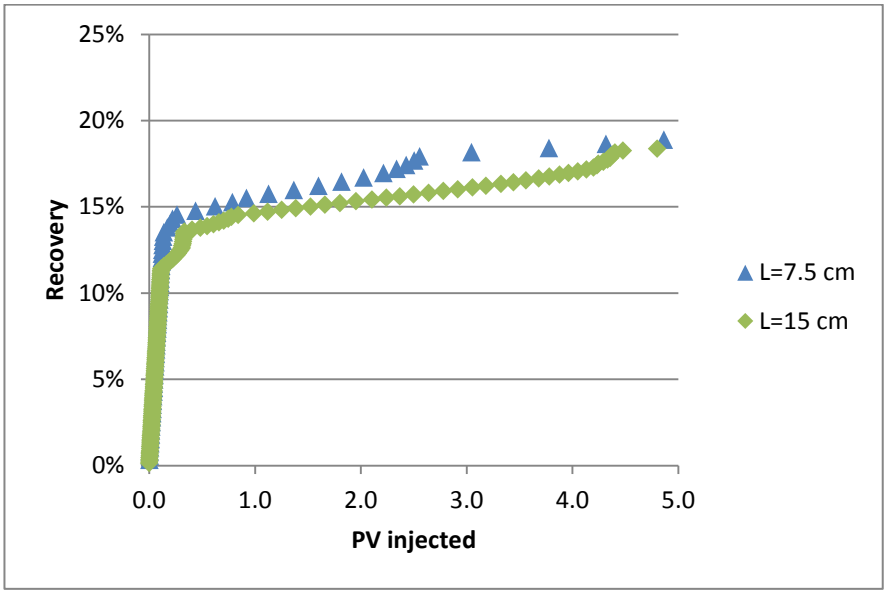

Figure 9.37: Figure 9.38 Comparison between the oil recovery in two simulations performed in networks having different lengths: 5cm*7.5 cm network and 5 cm*15 cm network . The viscosity ratio was equal to 7000 in this set and the capillary number was equal to 6.9 E-08.

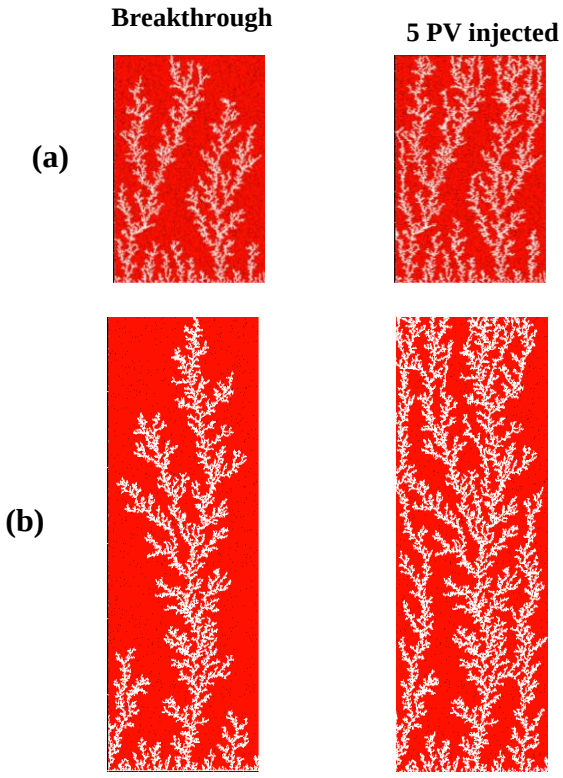

Figure 9.39: Comparison between the saturation maps in two simulations performed in networks having different lengths: (a) 5cm*7.5 cm network and (b) 5 cm*15 cm network. The viscosity ratio was equal to 7000 in this set and the capillary number was equal to 6.9 E-07.

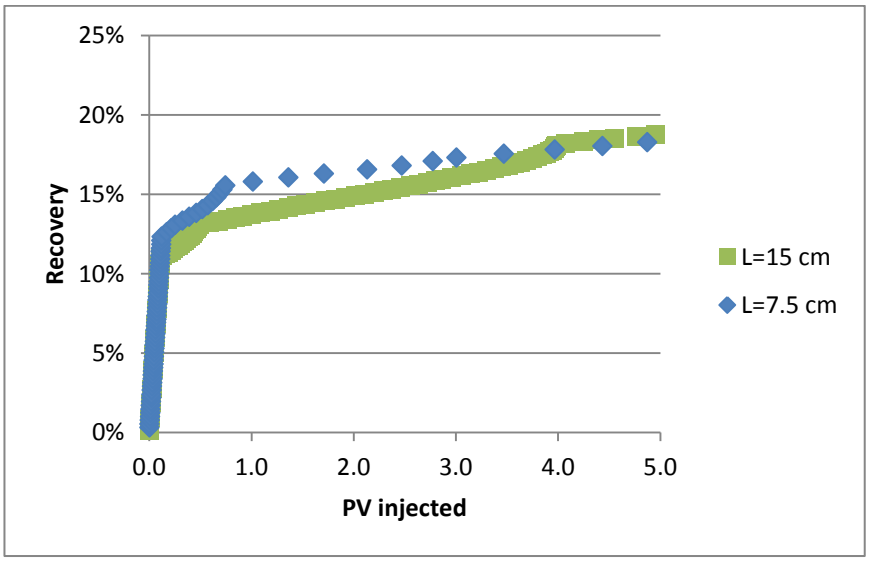

Figure 9.40: Comparison between the oil recovery in two simulations performed in networks having different lengths: 5cm*7.5 cm network and 5 cm*15 cm network . The viscosity ratio was equal to 7000 in this set and the capillary number was equal to 6.9 E-07.

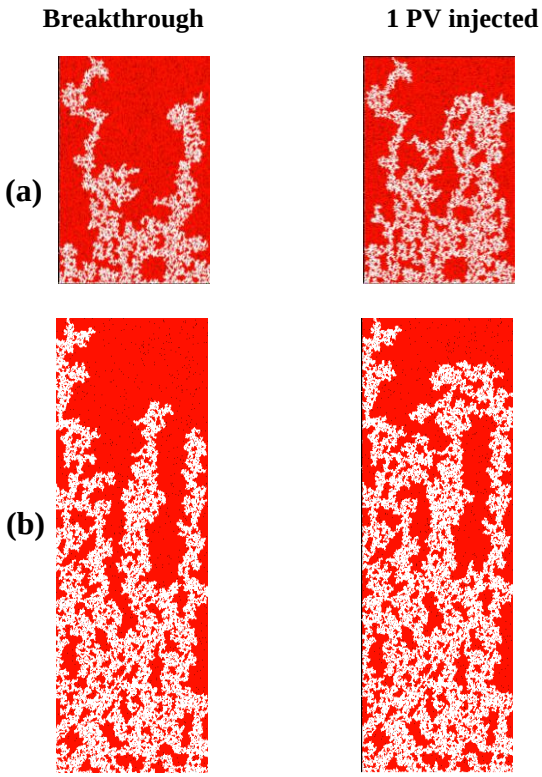

Figure 9.41: Comparison between the saturation maps in two simulations performed in networks having different lengths: (a) 5cm*7.5 cm network and (b) 5 cm*15 cm network. The viscosity ratio was equal to 66 in this set and the capillary number was equal to 6.9 E-09.

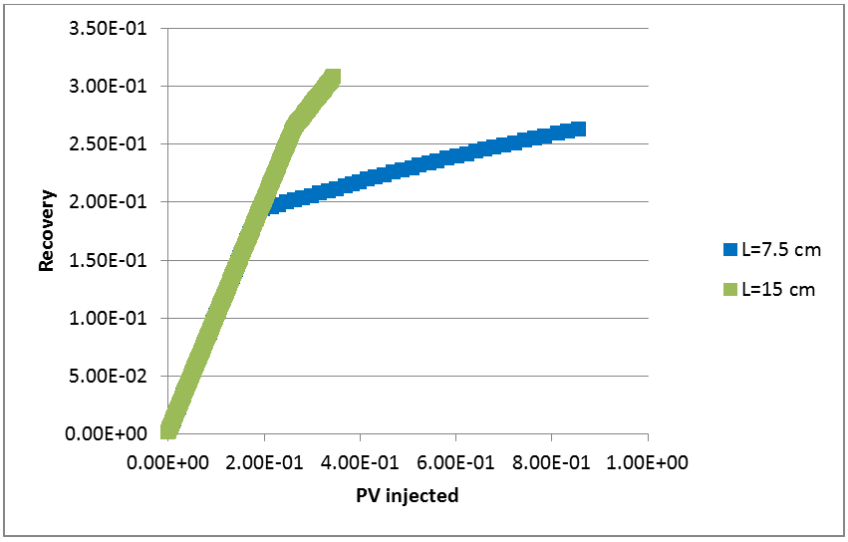

Figure 9.42: Comparison between the oil recovery in two simulations performed in networks having different lengths: 5cm*7.5 cm network and 5 cm*15 cm network. The viscosity ratio was equal to 66 in this set and the capillary number was equal to 6.9 E-09.

9.4. CONCLUSIONS

Chapter 9 has presented an investigation of some of the effects of injection rate, viscosity ratio, wettability and core length on the flow behaviour before and after water breakthrough. The following conclusions can be drawn.

9.4.1. Before breakthrough behaviour

Rate and viscosity ratio effect:

At low rates and *favourable* viscosity ratio, a capillary fingering regime is obtained and loops grow in all directions, trapping large volumes of oil. As the flow rate increases, less trapping occurs and the displacement front becomes flatter until reaching the stable displacement regime characterized by a high recovery and small volumes of trapped fluid.

For an *adverse* viscosity ratio, a capillary fingering regime is obtained at low rates. As the injection rate is increased, the water saturation at breakthrough begins to decrease in most cases and the fingers become thinner. At high rates, a viscous fingering regime results. The transition to a viscous fingering regime occurs at lower rates for high viscosity ratios. For a fixed injection rate, the instabilities are sharper for higher viscosity ratios.

At intermediate rates and adverse (but not very high) viscosity ratios, a more efficient displacement regime emerges ─ increased recovery occurs at the border between the capillary-dominated and viscous fingering regimes. At these intermediate rates, both the capillary and viscous forces are of comparable magnitudes. Consequently, (i) compared to the capillary dominated regime, the inlet pressure is relatively high and so more pores are accessible to the invading water, but (ii) the viscous pressures are not strong enough to cause fingering instabilities. As a consequence, a highly efficient displacement regime is obtained and plots of the water saturation at breakthrough suggest that the

higher the viscosity ratio, the narrower the capillary number window for efficient displacement.

Wettability effect:

Wettability is an important parameter governing constant rate waterfloods of heavy oils and a change of wettability can completely change the emergent flow regime. Hence a small change in wettability can have a large impact on oil recovery – this is especially true as the system approaches neutral wet conditions.

The commonly-held idea that recovery is higher at intermediate wet conditions could be questioned for heavy oils: in our case this was actually shown to be the worst wettability scenario for recovery. For intermediate and high injection rates, a decrease in the contact angle (from oil wet towards more neutral conditions) generally results in a decrease in oil recovery at breakthrough. At low injection rates, however, a decrease in contact angle can considerably improve oil recovery. The range of capillary numbers over which this phenomenon occurs narrows as the oil viscosity becomes higher.

Core length effect:

Simulations suggest that the same flow regime before breakthrough is obtained in experiments performed using different core lengths under the same experimental conditions.

9.4.2. Post breakthrough behaviour

The code was able to simulate the same flow regimes as those observed in Skauge et al. (2014) and the conditions of their experiments were used as base cases for our post-breakthrough study. The simulations were generally in agreement with the laboratory study and the flow regimes and the recovery mechanisms were similar to those observed in the experiments.

Rate and viscosity ratio effect:

The rate effect on the post-breakthrough behaviour changes for different adverse viscosity ratio. In displacements characterized by a viscosity ratio M=66, thick water channels are observed at low rates leading to a high oil recovery at breakthrough. In this case, an increase in rate makes these channels thinner and decreases the recovery at breakthrough as well as the overall recovery after an equal number of injected pore volumes.

For heavier oils (M=616 and M7000), viscous fingering is observed even at low rates. After breakthrough, upstream fingers are seen to thicken and propagate slowly towards the outlet at low rates, whilst, at high rates, more fingers grow towards the outlet and the thickening behaviour is limited. In this case, an increase in injection rate improves the recovery.

Wettability effect:

Wettability is an important parameter that can affect oil recovery and flow regime considerably. Changing the wettability towards a more neutral wet condition changes the balance between the viscous and capillary forces towards a more viscous dominated regime. This effect is similar to the behaviour observed after an increase in injection rate. Having a more neutral wet condition can lead to an increase or a decrease of the oil recovery depending upon the viscosity ratio of the fluids.

Core length effect:

Herce again, the impact of core length was different according to the oil viscosity. In displacements with a viscosity ratio M=66, increasing the length of the core increased the recovery. However, for heavier oil (M=7000), the number of viscous instabilities was seen to be greater in the shorter network. Although the recovery is faster in the shorter core, the oil recovery catches up in the long core case after injecting ~ 5 pore volumes: the ultimate recovery was found to be similar in both cases.

Chapter 10: Unsteady state relative permeability

10.1. INTRODUCTION

In multiphase flow, fluids such as oil, brine and gas compete for the same flow paths resulting in an additional resistance to the flow. This additional resistance can be described by normalizing permeabilities with respect to a base permeability for each of the flowing phases. As a result, we can introduce the concept of relative permeability which is, by definition, a measure of the ability of a porous medium to conduct a given fluid when one or more other fluids are present. Furthermore, Darcy's law can be extended to the flow of more than a single fluid within the pore space by considering the relative permeability of each phase.

Having a good estimate of relative permeability is crucial for estimating the flow of reservoir fluids. The main laboratory procedures to measure relative permeability are unsteady state and steady state techniques.

In steady-state methods, both phases (oil and water, gas and oil, or gas and water) are injected simultaneously at constant rates. Injection continues until a steady state regime is reached, as indicated by a constant pressure drop across the system and constant saturations. This stage corresponds to one point on the relative permeability curve of each phase. This is then followed by repeating the same procedure after changing the flow rates of each phase and continuing this procedure until the whole relative permeability curve can be constructed.

In unsteady-state methods, only one phase is injected at either a constant flow rate or a constant pressure drop. Throughout the injection, the pressure drop and production of phases are measured and the relative permeabilities are calculated from the measured data by an analytical method or with a history matching technique.

After studying the effects of different system parameters upon the saturation maps and recovery in the previous chapter, we now investigate the effects of these system parameters on the corresponding unsteady-state relative permeability curves for displacements involving heavy and extra heavy oil. Finally, we perform a fractional flow/Buckley-Leverett calculation to compute the macroscopic saturation fronts at a series of times (PVs) both before and after breakthrough (BT).

10.2. THEORETICAL BACKGROUND

To find oil and water relative permeabilities, unsteady state methods are often used because of their simplicity. A small linear core is usually saturated with water and then oil is injected until an irreducible water saturation is reached. This is followed by wateflooding, during which the differential pressure and cumulative production are measured.

Buckley and Leverett (1941) developed a theory for a linear, immiscible, one dimensional displacement, in which the total flow rate is constant in every cross section. The theory is founded on the conservation of mass principle and determines the velocity of a plane of constant water saturation moving through a linear system, such as a core in a water flood test. The Buckley-Levrett equation can be written as follows:

$$\frac{df_w}{dS_w}\frac{\partial S_w}{\partial x} = \frac{A\emptyset}{q}\frac{\partial S_w}{\partial t} \tag{10.1}$$

Where:

S_w, f_w and Ø are respectively the water saturation, the fraction of water flowing out of the core and the porosity of the core. A and q are respectively the cross-sectional area to flow and the water injection rate.

Welge (1952), using Buckley-Leverett displacement theory, presented a method to obtain the average saturation behind the shock front, which is useful in determining the

oil recovery. He produced the necessary basis to enable one to calculate relative permeability ratios. Assuming that relative permeability is solely a function of saturation, Welge developed the following relationships in order to calculate the relative permeability ratio:

$$f_o = \frac{\overline{S_w} - S_{w2}}{Q_i} \tag{10.2}$$

and

$$f_o = \frac{1}{\frac{kr_w}{kr_o}\frac{\mu_o}{\mu_w} + 1} \tag{10.3}$$

where:

f_o is the fractional volume of oil flowing from the core outlet

$\overline{S_w}$ is the average saturation of the displacing fluid

S_{w2} is the saturation of the displacing fluid at the core outlet

Q_i is the cumulative pore volumes of the water injected

kr_o and kr_w are the relative permeability of oil and water

μ_o and μ_w are the viscosity of oil and water

Johnson et al. (1959) extended the work of Welge to permit the calculation of individual relative permeabilities. This procedure is often referred to as the JBN method. The

equation which follows was also based on non-capillary Buckley Leverett frontal displacement theory:

$$f_o = \frac{d(\frac{1}{Q_i I_r})}{d(\frac{1}{Q_i})} \tag{10.4}$$

where: I_r is the relative injectivity describing the intake capacity and calculated as:

$$I_r = \frac{{}^{q}/_{\Delta p}}{({}^{q}/_{\Delta p})^{initial}}$$

q is the total volumetric flowrate and Δp is the differential pressure

Jones and Roszelle (1978) continued the work of Johnson and co-authors and presented a graphical technique, which makes the relative permeability calculation much more simple and accurate than the previous method. This method works for both constant pressure and constant injection rate simulations. Two plots are needed: (i) average non-wetting phase saturation versus the pore volume injected of the invading phase (Figure 10.1) and (ii) the effective viscosity versus the pore volume injected (Figure 10.2).

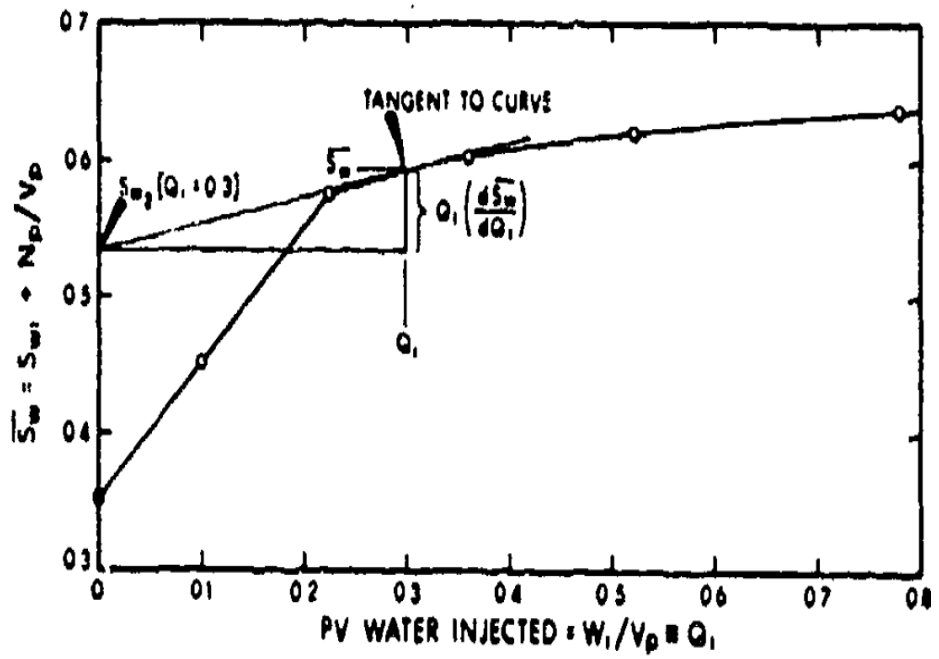

Figure 10.1: An example of the plot of average saturation as a function of pore volume of water injected (Jones and Roszelle, 1978).

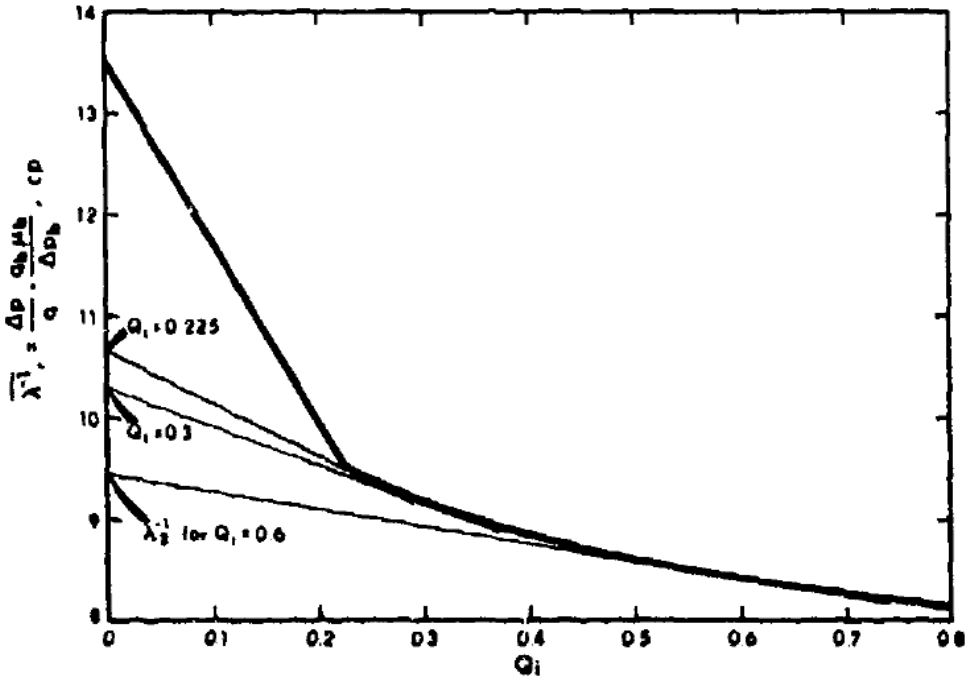

Figure 10.2: An example of the plot of average effective viscosity as a function of pore volume of water injected (Jones and Roszelle, 1978).

First, the average water saturation is calculated as a function of the injected pore volume Q_i :

$$\overline{S_w} = S_{wi} + \frac{N_p}{V_p} \tag{10.5}$$

The average saturation can be plotted as a function of the injected pore volume and then the tangent can be drawn for a particular Q_i (Figure 10.1). The intercept value is the saturation at the outlet and is equivalent to the Welge equation (Welge, 1952).

$$S_{w2} = \overline{S_w} - Q_i \frac{d\overline{S_w}}{d\, Q_i} \tag{10.6}$$

Now the fractional flow of oil is equal to the slope of the tangent line in Figure 10.1 at any pore volume injected meaning that the fractional flow of oil can be calculated from the average and intercept saturations:

$$f_{o2} = (\overline{S_w} - S_{w2})/\, Q_i \tag{10.7}$$

Moreover, the fractional water saturation can be calculated as follows:

$$f_{w2} = 1 - f_{o2} \tag{10.8}$$

The next step in the procedure is to calculate the average effective viscosity λ^{-1} , which is found by comparing $\Delta p/q$ measured during the waterflood with the single phase flow value ($\Delta pb/qb$)

So,

$$\overline{\lambda^{-1}} = \mu_b \frac{\Delta p/q}{\Delta pb/qb} \tag{10.9}$$

where: μ_b is the viscosity of the fluid used to find the absolute permeability;

qb is the rate used to calculate the permeability;

Δpb is the pressure drop measured in the permeability calculations.

After plotting the average effective viscosities versus the cumulative pore volume of water injected, calculating the tangent to the average viscosity curve at a particular point allows us to calculate the value of the effective viscosity ${\lambda_2}^{-1}$ which is simply the intercept of the tangent (Figure 10.2). The equation corresponding to the tangent construction is:

$${\lambda_2}^{-1} = \overline{\lambda^{-1}} - Q_i \frac{d\overline{\lambda^{-1}}}{d\, Q_i} \tag{10.10}$$

Finally, the relative permeability of each phase can be computed as:

$$k_{rw} = \frac{\mu_w f_{w2}}{\lambda_2^{-1}} \tag{10.11}$$

$$k_{ro} = \frac{\mu_w f_{o2}}{\lambda_2^{-1}} \tag{10.12}$$

10.3. METHODOLOGY

For our unsteady state relative permeability calculations, a three dimensional network of pore elements (20*20*20) was built (Figure 10.3) and was used for two phase displacements simulations. Production data were then generated from the simulations ─ differential pressure, oil recovery and water cut ─ and these were then used to calculate unsteady state relative permeabilities (Figure 10.4) with the JBN (Johnson et al., 1959) analytical method or a modified version (Jones and Roszelle, 1978).

The JBN and Jones and Roszelle methods provide convenient means for calculating the relative permeability curves from oil production and total fluid production data. The methods also require additional data such as the measured flow rates of each fluid and the pressure drop across the network. This data must be smooth and continuous in its overall trend because these methods require differentiation of either the total flow rate or the pressure drop. Therefore, we perform an exponential smoothing to the production data using Microsoft Excel software prior to their use in the analytical calculations.

Although, the JBN and Jones and Roszelle methods are equivalent, the Jones and Roszelle technique is easier to use and gives a more accurate evaluation of relative permeability. Furthermore, Figure 10.4 shows an example of relative permeability calculation from the same production data and confirms that both methods give similar results. As a consequence, we use the Jones and Roszelle technique for all the unsteady state relative permeability calculations performed in this chapter.

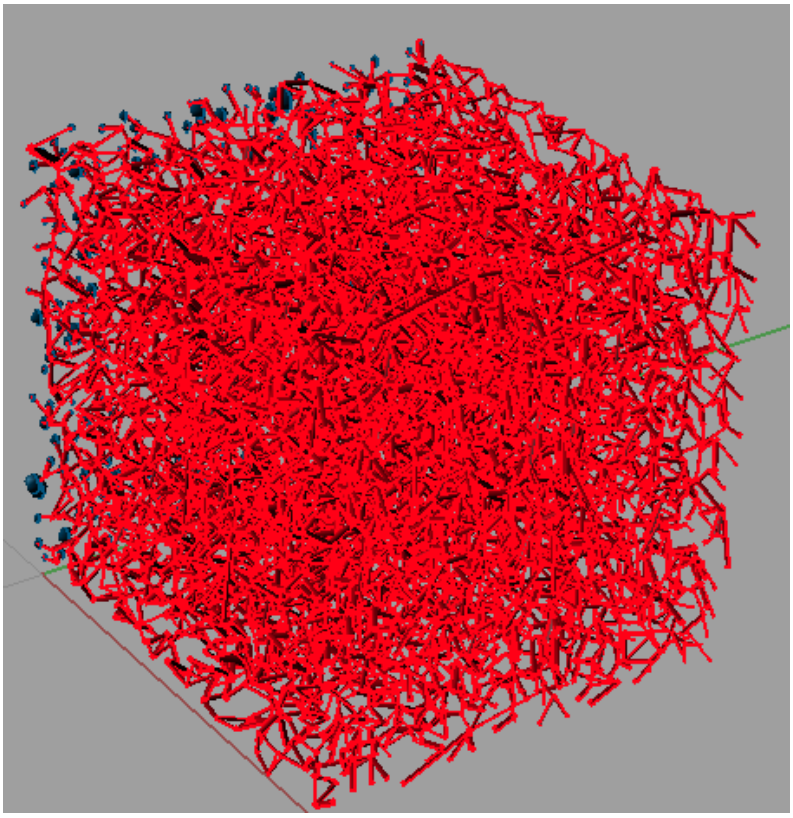

Figure 10.3: A three dimensional cubic network used in the relative permeability simulations

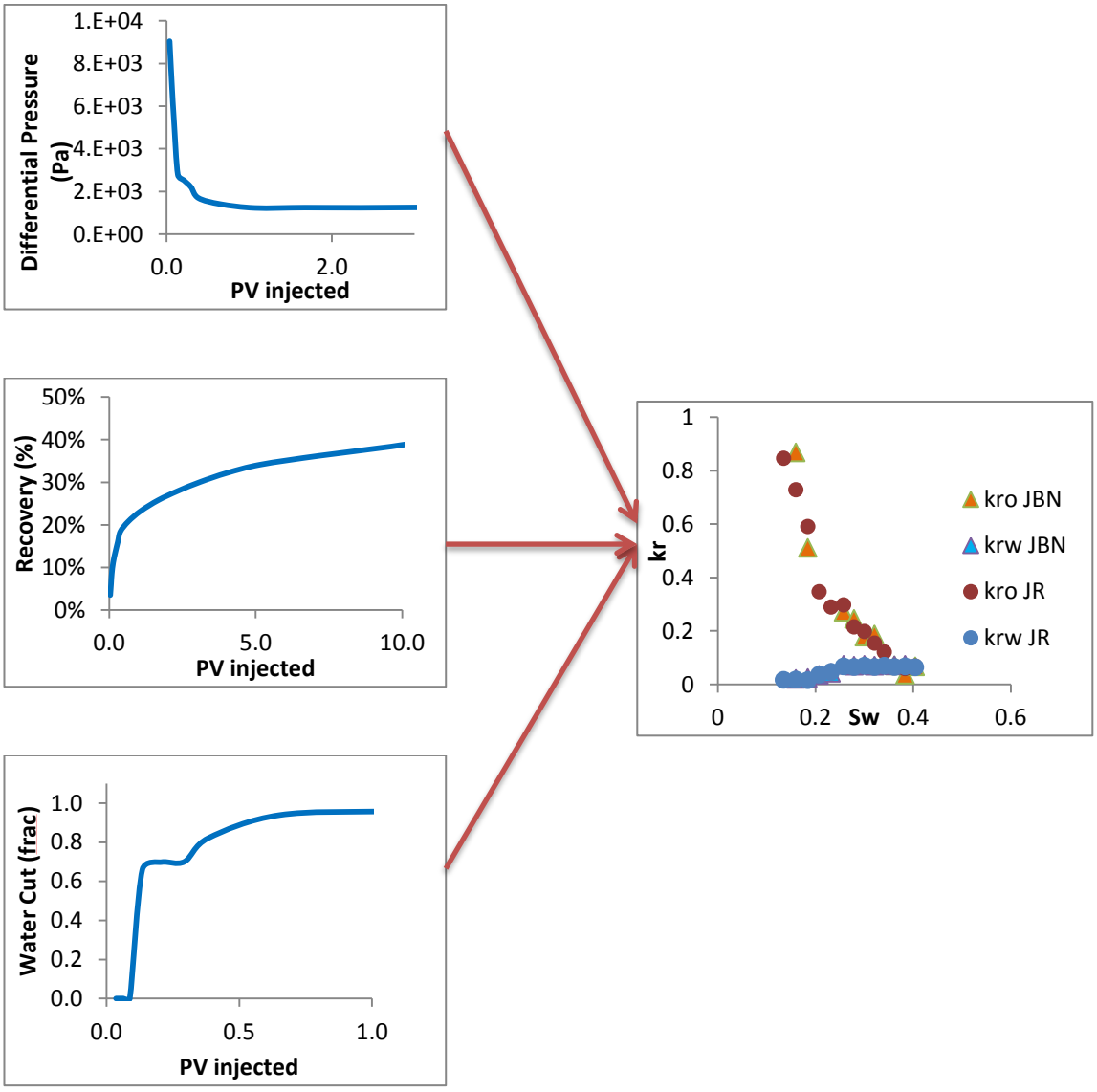

Figure 10.4: The methodology used to generate relative permeability curves. These data correspond to a simulation with a viscosity ratio equal to 100 and a capillary number equal to 8.7E-08.

10.4. INJECTION RATE EFFECT ON UNSTEADY STATE RELATIVE PERMEABILITY

Several authors have investigated the effects of injection rate on unsteady state relative permeability.

Lefebvre du Prey (1973) performed several waterflooding experiments using artifical porous media: teflon (strongly oil wet), alumina (strongly water wet) and stainless steel (that may have intermediate wettability for some fluid combinations). The effect of injection rate upon the unsteady relative permeability sets (computed with the JBN method) was then investigated. It was observed that, as the capillary number/injection rate increases, the relative permability of both phases increased.

Maini et al. (1990) performed water flooding experiments in sand packs and used viscous oil (M=405 and M=12). Then, they calculated unsteady state relative permeability using a history matching technique. They found that the unsteady-state relative permeability sets were rate dependent and that, an increase in the injection rate resulted in an increase in the relative permeability of both phases.

Henderson et al. (1996) performed gas and condensate displacements and calculated unsteady state relative permeability using the Longeron (1980) analytical method which is developed for displacements involving fluids having a low interfacial tension. They found that, the unsteady-state relative permeability sets are rate dependant and that an increase in the injection rate results in an increase in relative permeability of both phases.

Furthermore, several authors have investigated the effects of injection rate and viscosity ratio upon relative permeability using dynamic pore network models. Blunt and King (1990, 1991) used a drainage pore network model to generate relative permeability sets for a range of rates. They used Darcy's law to calculate the relative permeability sets at different stages of the simulation and found the relative permeability to be sensitive to the capillary number and viscosity ratio ─ they observed that, at the same saturation, the relative permeability of the defending phase increased if the injection rate increased

(Figure 10.5). However, both increasing and decreasing trends were observed in the invading phase relative permeability.

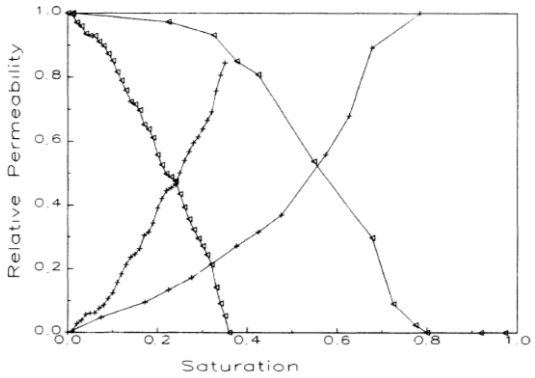

Figure 10.5: Effect of capillary number on relative permeability. The curves in the left are for a capillary dominated flow and those on the right represent a viscous fingering case with M=10 (Blunt and King, 1990)

Singh and Mohanty (2003) simulated drainage displacements for different viscosity ratios and capillary numbers and computed relative permeability using Darcy's law in thin slices of the porous domain. At high capillary numbers, the relative permeability curves exhibited a linear shape, whilst, at low rates, they had a non-linear form. They observed that, for a unit viscosity ratio, increasing the capillary number increased the relative permeability of both wetting and non-wetting fluids. This behaviour was consistent with the experimental results of Lefebvre du Prey (1973) as shown in Figure 10.6.

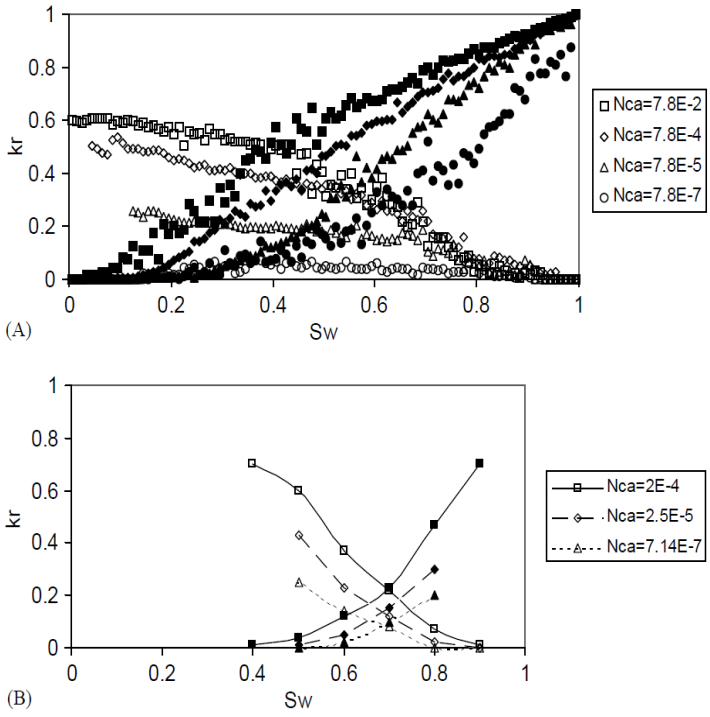

Figure 10.6: Effect of capillary number on relative permeability sets for a displacement with unit viscosity ratio for: (A) simulations performed with dynamic pore network model (Singh and Mohanty, 2003) (B) Experimental study for a strongly oil wet waterfloods (Lefebvre du Prey, 1973)

Other researchers have developed dynamic *imbibition* network models to investigate the effect of system parameters on relative permeability. Constantinides and Payatakes (1996) built a model that takes into account the dynamics of ganglia. They observed that, at the same saturation, the relative permeability of both phases increased at a higher rate.

Returning now to the new simulations developed as part of this work, Figure 10.7 shows a set of unsteady state relative permeability curves from runs performed using the same network, wettability and viscosity ratio (equal to 7000) but different injection rate. Increasing the rate from 0.1 cc/hr to 1 cc/hr increased the relative permeability of the oil and the relative permeability of water. However, increasing the rate from 1 cc/hr to 10 cc/hr did not have a noticeable effect on the relative permeability curves.

A similar behaviour was observed in simulations involving different viscosity ratios: M=500 (Figure 10.8) and M=100 (Figure 10.9).

These results suggest that, an increase in rate may result in an increase in the relative permeability of both phases, which is consistent with the trend observed in most of the experimental and numerical studies presented earlier. However, a range of rates and viscosities could be found for which the relative permeability is insensitive to a change of rate.

Two important factors should be considered to better understand this increase of relative permeability at high rates. First, as the rate increases, the flow becomes less stable leading to the occurrence of viscous fingering whereby instabilities develop and grow towards the outlet. As a result, the water phase affects the flow of oil less than it would in the capillary dominated regime. Thus, the relative permeability of both phases increases as they tend to segregate and have separate flow paths.

The second factor to take into account is the size of the pores filled by each phase. At low rates, water invades the larger pores first, and most of the small pores remain oil filled. However, as the rate increases, more small pores are filled with water and more large pores remain oil filled. This results in a decrease in the relative permeability of water, which has the opposite effect of that associated with the first factor (the flow paths are segregated at high rates) and explains the limited increase in the relative permeability of water at high rates. However, having more large pores filled with oil increases the relative permeability to oil, which amplifies the increase of relative permeability caused by the first factor.

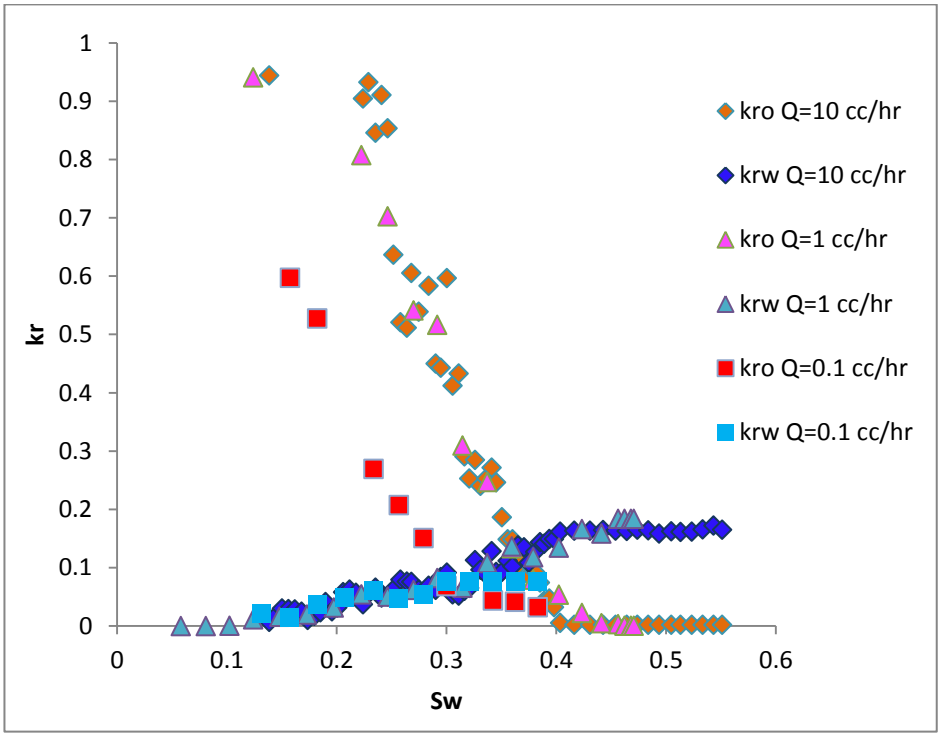

Figure 10.7: Unsteady state relative permeability sets for a viscosity ratio M=7000 and different injection rates.

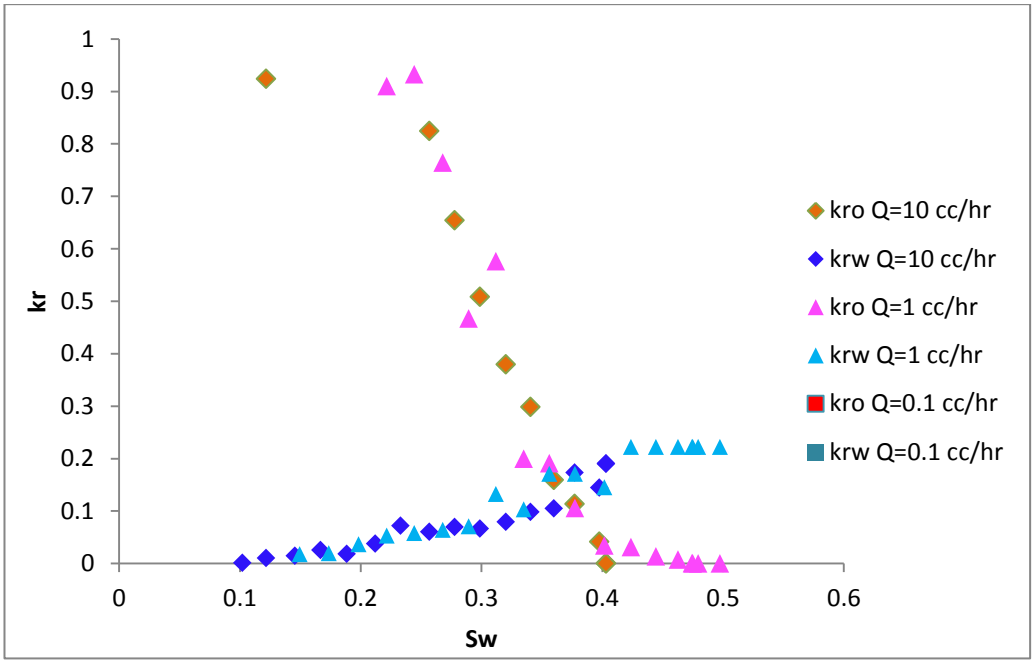

Figure 10.8: Unsteady state relative permeability sets for a viscosity ratio M=500 and different injection rates.

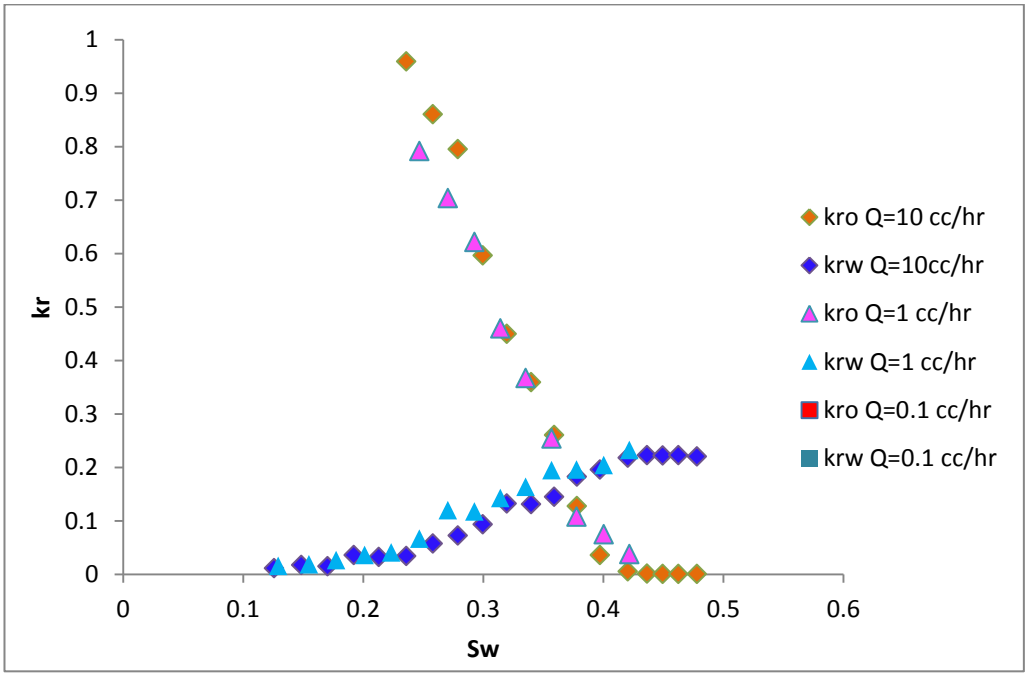

Figure 10.9: Unsteady state relative permeability sets for a viscosity ratio M=100 and different injection rates.

10.5. VISCOSITY RATIO EFFECT ON UNSTEADY STATE RELATIVE PERMEABILITY

Several researchers have been interested in studying the viscosity ratio effect upon unsteady state relative permeability.

Richardson (1957) performed steady and unsteady-state relative permeability measurements during water flooding experiments where the viscosity of the oil used was equal to 151 cP and 1.8 cP. They found good agreement between both methods and obtained the same relative permeability sets from oils having different viscosities ─ they concluded that relative permeability does not depend on viscosity ratio.

In contrast, the study of Lefebvre du Prey (1973) discussed in section 10.3, showed that the viscosity had a profound effect on relative permeability ─ the higher the viscosity of one of the phases is, the lower the relative permeability of the other.

Wang et al. (2006) studied unsteady-state relative permeability for heavy and extra heavy oils and considered fluids with viscosity ratios varying from 430 cP to 13550 cP. They performed imbibition experiments and used a history matching technique to calculate the relative permeability sets. They observed that, for the range of rates and viscosities considered, the relative permeability of both oil and water phases were lower for higher viscosity ratios.

Singh and Mohanty (2003) performed a pore network modelling study to investigate the effect of viscosity ratio on relative permeability. They built a dynamic drainage model and found that the relative permeability of the wetting phase decreased as the viscosity ratio increased (Figure 10.10).

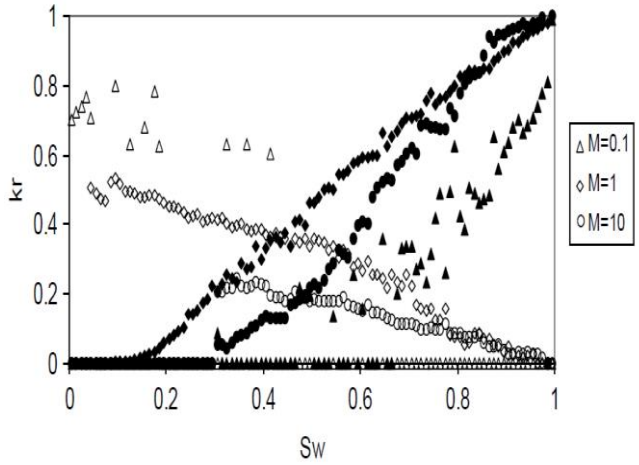

Figure 10.10: The effect of viscosity on drainage relative permeability for Nca=7.8E-4 (Singh and Mohanty, 2003).

From these reported situations, it is clear that no general consensus exists. Therefore, we perform a number of simulations with different viscosity ratios using our new pore network model to gain a better idea concerning this effect.

Figure 10.11, Figure 10.12 and Figure 10.13 represent three sets of relative permeability data generated from the new model at the same rate but using different viscosity ratios.

In Figure 10.11, the viscosity ratio did not have an effect on the relative permeabilities at this rate for viscosity ratios varying from 50 to 7000. However, Figure 10.12 and Figure 10.13 show a different behaviour. Here, an increase in the viscosity ratio decreased the relative permeabilities and this effect was more pronounced at higher rates.

These results show that, an increase in viscosity ratio generally results in a decrease in both relative permeabilities which is consistent with the studies of Wang et al 2006 and Singh and Mohanty (2003). However, a range of viscosities and rates could be found where the relative permeability appears to be insensitive to a change in viscosity ratio, which is in agreement with the experimental study of Richardson (1957). Hence, our modelling approach is able to reconcile these apparently contradicting studies.

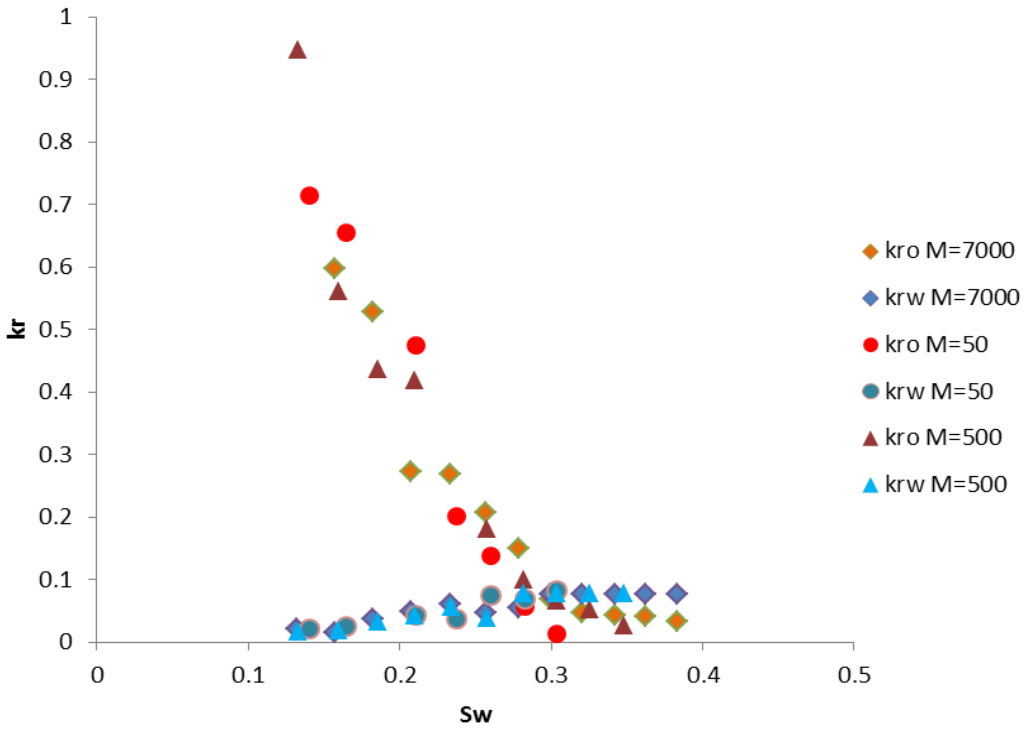

Figure 10.11: Relative permeability sets for different viscosity ratios and similar injection rate Q=0.1 cc/hr (Nca= 8.7E-08).

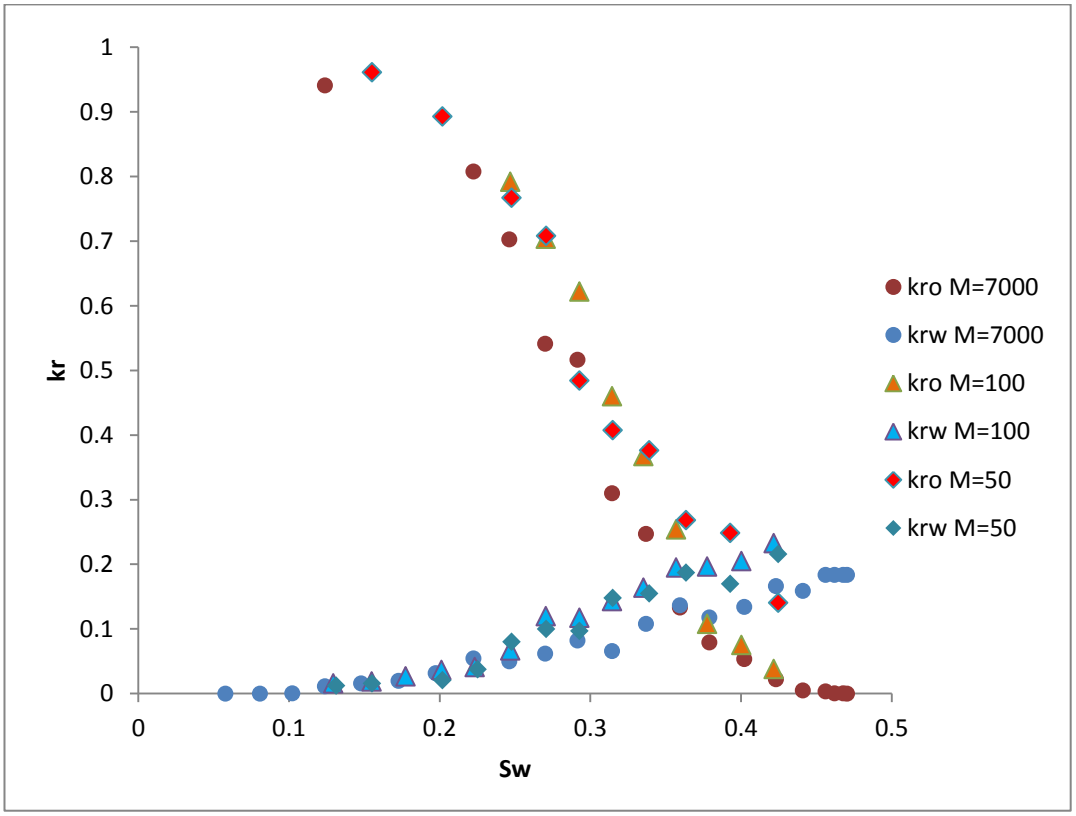

Figure 10.12: Relative permeability sets for different viscosity ratios and similar injection rate Q=1 cc/hr (Nca=8.7E-07).

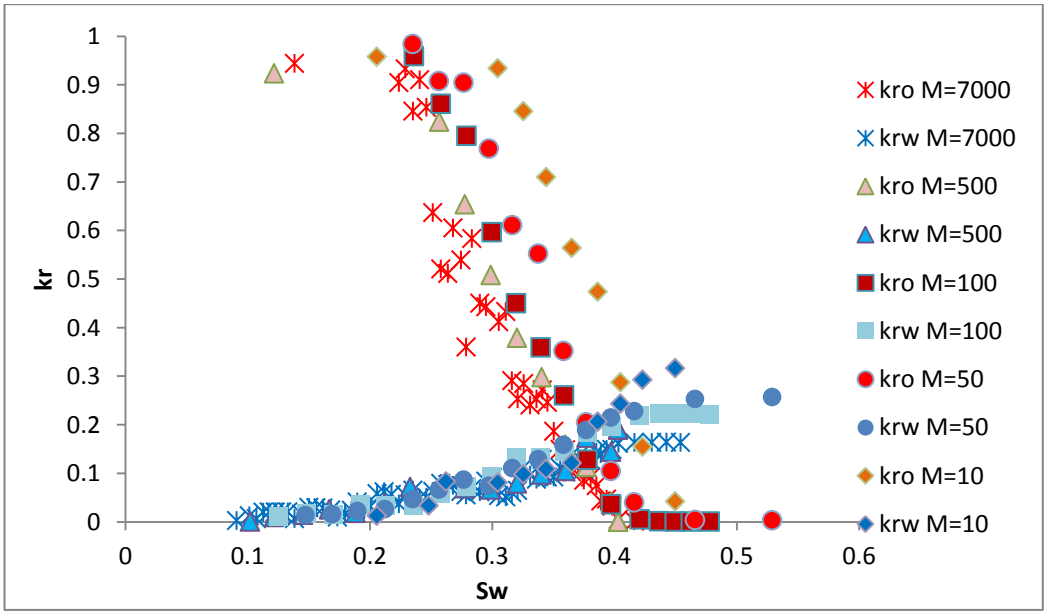

Figure 10.13: Relative permeability sets for different viscosity ratios and similar injection rate Q=10 cc/hr (Nca= 8.7E-06).

10.6. WETTABILITY EFFECT ON UNSTEADY STATE RELATIVE PERMEABILITY

In this section, we study the effect of wettability on unsteady state relative permeability by comparing relative permeability sets from strongly and weakly oil wet cases.

Owens and Archer (1971) performed gas-oil and water-oil displacements using fired samples of Sandstone and oil with viscosities equal to 26 cP and 1.7 cP. The wettability of the samples was changed using a chemical in order to have different wettability scenarios and the production data of these displacements was used to calculate the unsteady state relative permeability using JBN method. Results showed that, as the contact angle goes towards a more water wet scenario, the relative permeability of the oil increases whilst the relative permeability of the water decreases.

Although not specifically a wettability study, some insight into modified capillary entry criteria can be informed from McDougall et al. (1997) , who reported on the effects of interfacial tension (IFT) on gas oil relative permeability using an unsteady state pore network simulator. They calculated unsteady state relative permeability from production data using a modified version of Jones and Roszelle method (Jones and Roszelle, 1978) and found that a decrease of IFT results in a marked increase of the gas relative permeability but a very small change in the oil relative permeability (Figure 4.8). This behaviour was observed in both constant rate and constant pressure drop simulations. Considering that the effect of the wettability is taken into account in the simulator only in the capillary entry pressure calculation, one should expect that a decrease of IFT should have a similar effect as going from strongly oil wet conditions towards neutral wettability.

In order to investigate this, several simulation sets were performed where the wettability of the pore network was varied. Figure 10.14 represents simulations that were performed using a viscosity ratio equal to 7000, different wettability scenarios (strongly oil-wet and weakly oil-wet cases) and several injection rates. At an injection rate of 0.1 cc/hr, decreasing the contact angle towards neutral-wet conditions increased the relative permeability of oil (consistent with Owens and Archer (1971) and the numerical study

of McDougall et al. (1997)). However, at higher rates the wettability did not have an effect on relative permeability.

Figure 10.15 shows the relative permeabilities obtained from a similar set of simulations but using a lighter oil (M=50 cP). Again, decreasing the contact angle towards neutral wet conditions increased the relative permeability of oil. This increase occurred at all the rates studied but was more significant at the lowest injection flux.

These results show that decreasing the contact angle from a strongly oil-wet condition towards a neutral-wet state results in an increase of the relative permeability of oil, which is again in agreement with the experimental study of Owens and Archer (1971) ─ only a small change was observed in the relative permeability of the water. However, for very viscous oils, a range of rates was found where the relative permeability is *insensitive* to a change of wettability.

Two important factors should be considered in order to understand this increase in relative permeability at neutral-wet conditions. First, as the contact angle decreases from strongly oil-wet towards neutral-wet, the flow becomes less stable, leading to the occurrence of viscous fingering, with instabilities growing towards the outlet. As a result, the water phase has less of an effect on the flow of oil than in capillary dominated regime. Thus, the relative permeability of both phases increases because, in viscous fingering regime, they tend to segregate and have separate flow paths.

The second factor to take into account is the size of the pores filled by each phase. At strongly oil-wet conditions, water is more likely to invade the larger pores first and most of the smaller pores remain oil filled. However, as the contact angle decreases, more small pores are filled with water and more large pores become oil filled. This has the effect of *decreasing* the relative permeability of water ─ the opposite effect to the first factor (the flow paths are segregated at high rates) ─ and this explains the limited increase in the relative permeability of water. However, having more large pores filled with oil increases the relative permeability of oil which *amplifies* the increase of relative permeability cause by the first factor.

It should be reiterated that this behaviour is no longer valid if the injection rates and viscosity ratios are high. In such cases, viscous fingering regimes occur and the flow paths are already separated under strongly oil-wet conditions (meaning that decreasing the contact angle towards more neutral-wet conditions does not have a major effect on relative permeability, see Figure 10.14).

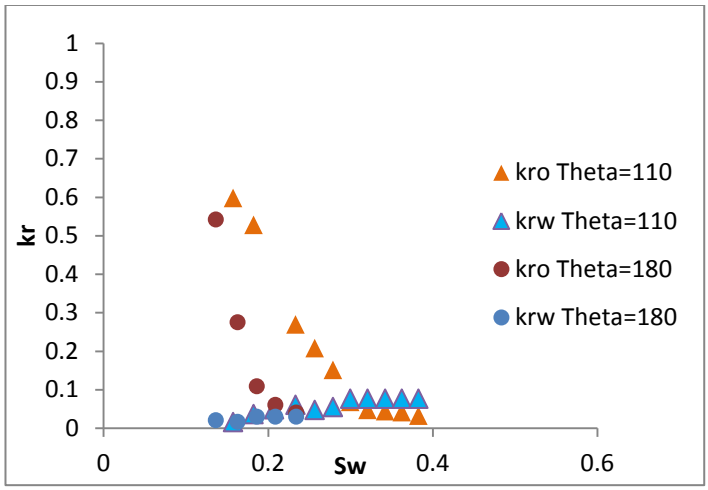

(a)

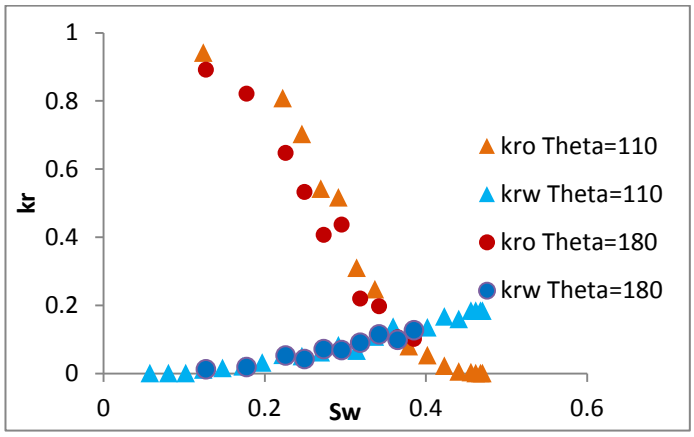

(b)

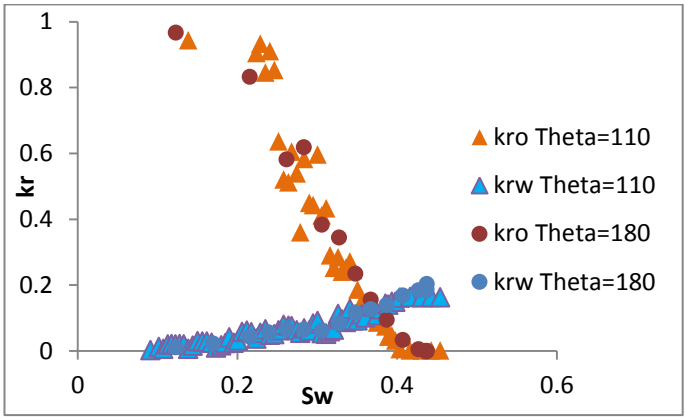

(c)

Figure 10.14: Relative permeability sets for M=7000 and different wettability scenarios (strongly oil wet and weakly oil wet cases). Different injection rates were considered Q=0.1 cc/hr (Nca=8.7 E-08) (a), Q=1 cc/hr (Nca=8.7 E-07) (b) and Q=10 cc/hr (Nca=8.7 E-06) (c).

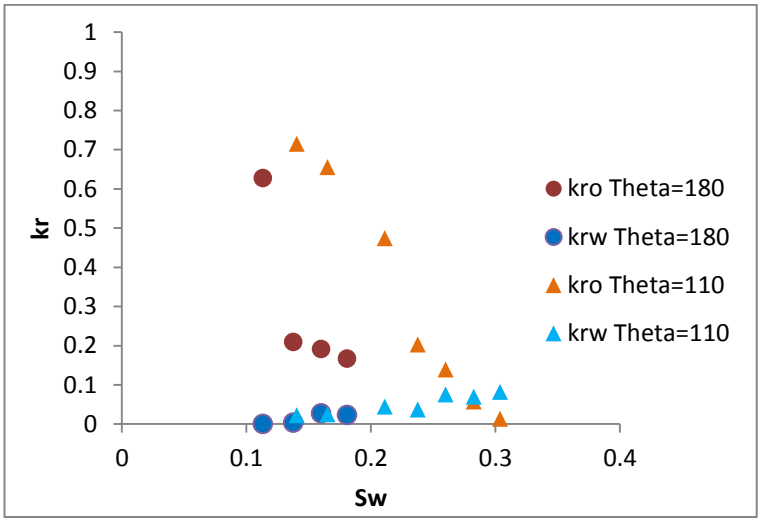

(a)

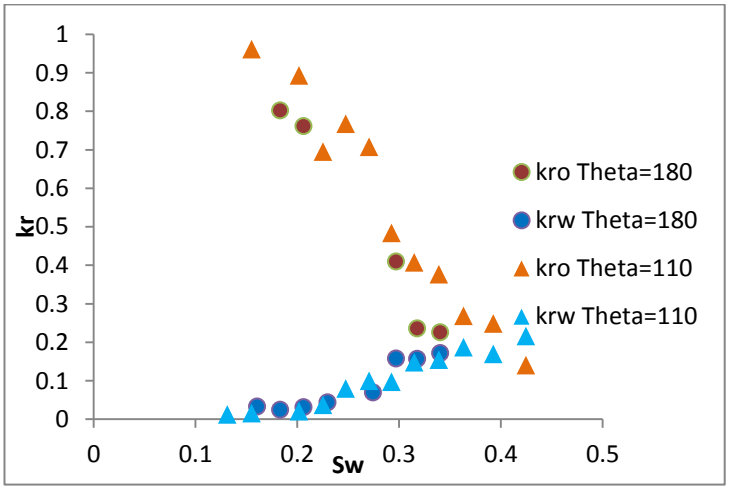

(b)

Figure 10.15: Relative permeability sets for M=50 and different wettability scenarios (strongly oil wet and weakly oil wet cases). Different injection rates were considered Q=0.1 cc/hr (Nca=8.7 E-08) (a) and Q=1 cc/hr (Nca=8.7 E-07) (b) .

10.7. SATURATION PROFILE

In this section, we propose to plot saturation profiles of several simulations performed at the same injection rate (1 cc/hr) and using several viscosity ratios (M=50, M=100 and M=7000). Buckley Levrett equation (10.13) can be integrated and used to plot the saturation profiles from the fractional flow curves computed in the simulations. These can then be used to give an idea about the evolution of the invading phase distribution at several stages of the simulations.

Figures 10.16, 10.17 and 10.18 show that the extra recovery happening throughout the length of the network and no oil bank was observed in these saturation profiles which is consistent with our observation of the finger thickening phenomenon that was occurring at the periphery of the already developed fingers and was leading to the extra oil recovery post breakthrough.

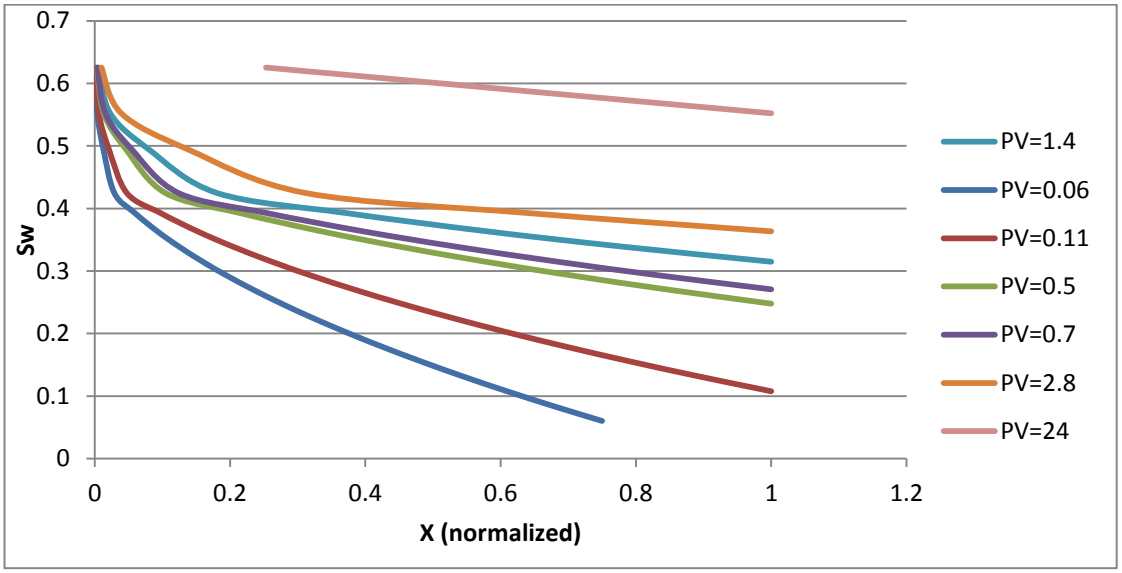

Figure 10.16: Saturation profiles at several pore volumes injected for a simulation with a viscosity ratio M=50 and at an injection rate Q=1cc/hr.

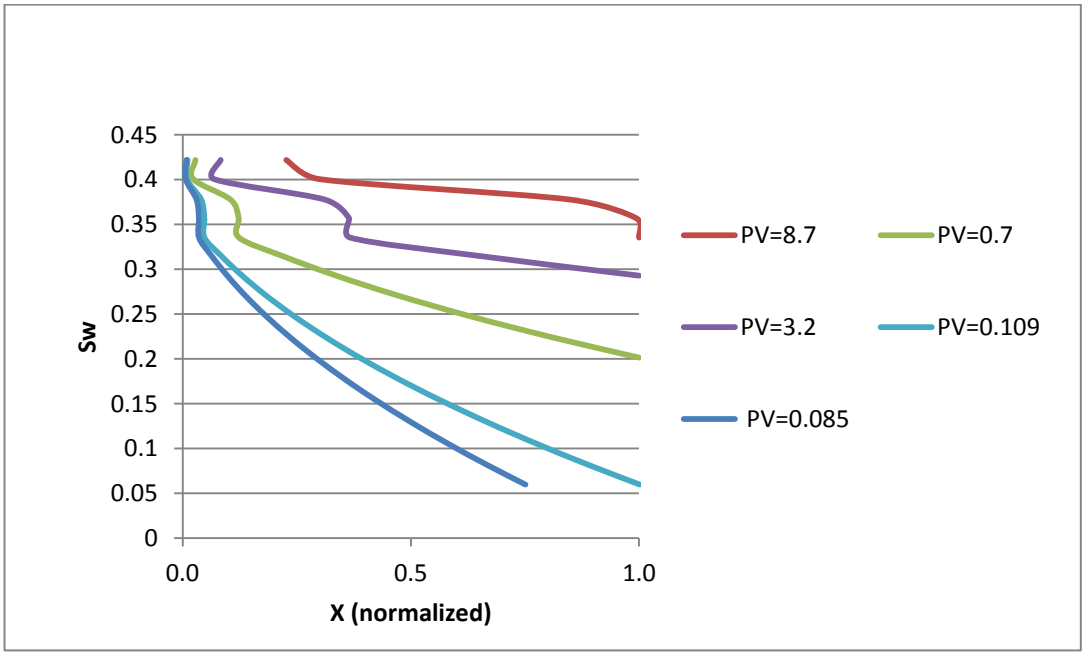

Figure 10.17: Saturation profiles at several pore volumes injected for a simulation with a viscosity ratio M=100 and at an injection rate Q=1cc/hr.

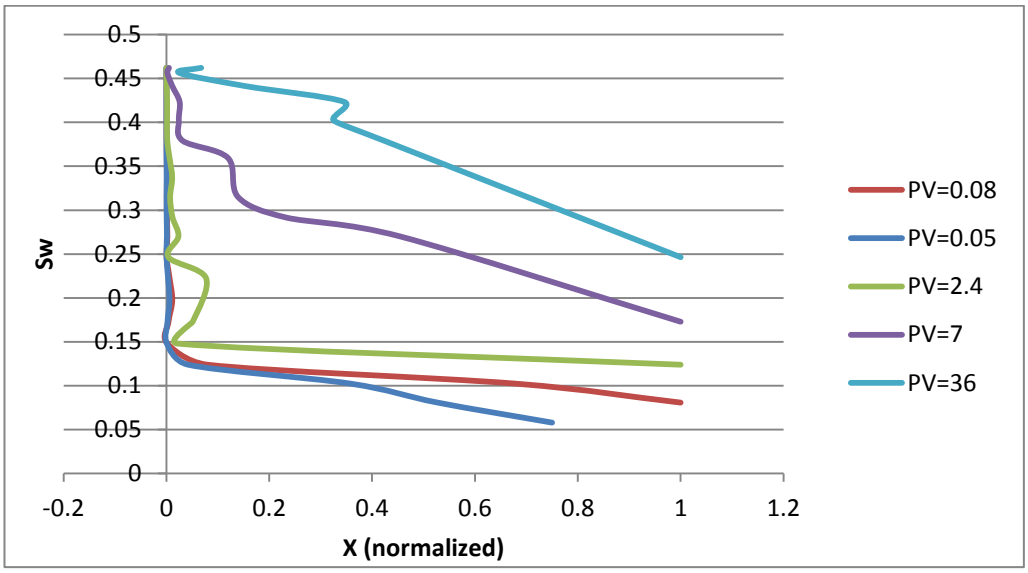

Figure 10.18: Saturation profiles at several pore volumes injected for a simulation with a viscosity ratio M=7000 and at an injection rate Q=1cc/hr.

10.8. CONCLUSIONS

In this chapter, the model has been used to investigate the effects of injection rate, viscosity ratio and wettability on unsteady-state relative permeability. The relative permeability was found to be sensitive to these parameters and the following behaviours were observed:

- An increase in rate may result in an increase in the relative permeability of both phases. However, a range of rates and viscosities could be found for which the relative permeability is insensitive to a change in rate;
- An increase in viscosity ratio may result in a decrease of relative permeability. However, once again, a range of viscosities and rates could be found where the relative permeability is insensitive to a change in viscosity;
- Decreasing the contact angle from a strongly oil-wet condition towards neutral-wet results in an increase of the relative permeability to oil but no significant change was observed in the relative permeability of the water. For very viscous

oils, a range of rates was found where the relative permeability is insensitive to a change of wettability from strongly oil-wet conditions towards neutral-wet.

These findings were in agreement with the published experimental investigations and show that, in order to have meaningful unsteady-state relative permeability sets, measurements should be made under conditions similar to those found in a reservoir in terms of fluid properties, displacement velocity and rock wettability.

Chapter 11: Conclusions and future work

11.1. CONCLUSIONS

The flow in porous media is governed by the competition between viscous and capillary forces. Whilst these pore scale phenomena completely determine the flow regime, they are not explicitly taken into account by the classical reservoir simulators. As a consequence, in some situations, reservoir simulators are unable to reproduce certain flow behaviours observed experimentally, such as viscous fingering phenomena (Riaz et al., 2007). The motivation of the present work is to overcome this issue by applying a pore scale modelling technique (pore network modelling) to simulate slab experiments at the appropriate scale.

Our extensive review of the literature pertaining to viscous fingering in immiscible displacements during Chapter 2 revealed that viscous fingering is a complex phenomenon that depends upon various rock/fluid parameters. Although several attempts have been made in the past to simulate such instabilities, most of the models reported to date have been too simplistic or have been applied at a too small scale.

One of the most successful techniques applied to viscous fingering simulation has been the pore network modelling approach. A literature review of the different approaches used to generate statistically representative pore networks or to recreate the pore space from rock images was presented in Chapter 3. Following this, the different ways to simulate multiphase flow in such networks was presented and the main applications of quasi-static models reviewed.

Chapter 4 went on to give particular focus to the published *dynamic* pore network modelling studies. The main challenges and issues faced by the researchers in this area were presented and the main applications of these models were summarized. Whilst

these dynamic simulators were found to be very useful in giving physically-based insights into a range of physical phenomena, most of them were applied at a very small scale due to computational limitations and unrealistic running for core scale application.

In Chapter 5 we presented a newly developed fully dynamic drainage pore network model that includes an iterative approach to enable capillary pressure to be taken into account when solving for the global pressure field. In addition, we included a time-dependent pressure drop in the formulation that allowed us to model fixed injection rate experiments reported in the literature. Furthermore, the developed simulator was fast enough to simulate waterfloods in slab-type systems at the scale of tens of centimetres.

The model has been tested against 35 micromodel experiments from the literature (Lenormand et al., 1988) and Chapter 6 discusses the various results. In all cases, an excellent agreement has been found with the experimental data. All the various flow regimes (stable displacement, viscous fingering and capillary fingering) were reproduced, as well as the transition between them, without requiring any tuning.

Being able to simulate all of the flow regimes of the Lenormand experiments gave us increased confidence about our in-silico approach and we went on to apply this model to the simulation of slab scale experiments of water injection into heavy oil in (Chapter 7). Initially, several sharp fingers were formed near the inlet of the network, with some subsequently growing faster and inhibiting the development of the shorter instabilities left behind. Whilst fingers were dendritic before breakthrough, the instabilities upstream started to thicken and merge, forming water broaden channels after breakthrough. This behaviour is qualitatively similar to that observed in the laboratory studies and is reproduced for the first time to our knowledge. This allowed us to present a hypothesis of the causes of finger thickening behaviour observed experimentally post water breakthrough which was presented in chapter 8.

We proposed that the finger swelling is due to a rapid change in pressure drop after breakthrough and to the fact that the highest pressure gradients after breakthrough are found primarily at the tip of upstream fingers. We suggested that a necessary condition to have this phenomenon is that the differential pressure at the plateau stage of the flood

should be higher than the mean capillary entry pressure characterising the sample. Furthermore, we indicated that core length, wettability and injection rate, are all important parameters affecting the finger thickening behaviour. Indeed, increasing the length of the core, using a higher injection rate and/or having a more neutral wet condition all increase the potential for extra recovery after breakthrough.

Chapter 9 presents a sensitivity study of the effects of injection rate, viscosity ratio and wettability on the flow behaviour before and after breakthrough. The following conclusions can be drawn:

Rate and viscosity ratio effect:

- In displacements with a favourable viscosity ratio: at low rates, a capillary fingering regime is obtained and large volumes of oil are trapped. An increase of the injection rate results in a stable displacement and improved recovery;
- In displacements with an unfavourable viscosity ratio: at low rates, capillary fingering regime is obtained and as the rate increases, the fingers start to become thinner and the recovery at breakthrough decreases. Simulations at higher viscosity ratios were characterised by a transition to viscous fingering at lower rates and by more dendritic viscous instabilities;
- For displacements with adverse (but not very high) viscosity ratios, a more efficient displacement regime emerges and increased recovery occurs at the border between the capillary-dominated and viscous fingering regimes. This regime was predicted by our model and was observed in several experimental studies;
- Post-breakthrough behaviour is different for different viscosity ratios. In displacements at a viscosity ratio M=66, thick water channels are observed at low rates, leading to high oil recovery at breakthrough. In this case, an increase in the rate makes these channels thinner and decreases the recovery at breakthrough (as well as the overall recovery). For heavier oils (M=616 and M=7000), breakthrough occurs after very low PV injected and recovery mainly occurrs after breakthrough by the growth of the upstream fingers. The latter are seen to thicken and propagate slowly towards the outlet at low rates, whilst, at

high rates, more fingers grow towards the outlet and the thickening behaviour is limited. In this case, an increase in injection rate improves the recovery;

- The code was able to simulate the same flow regimes as were observed in the laboratory study of Skauge et al. (2014), in which they performed various waterfloods with different viscosity ratios. The simulations were generally in very good agreement with the laboratory study.

Wettability effect:

- A small change in wettability can change the flow regime dramatically and have a large impact on oil recovery – this is especially true as the system approaches neutral wet conditions;
- Neutral wet conditions lead to a very high water saturation at breakthrough for favourable viscosity ratio cases but they give the worst recovery at breakthrough for heavy oils;
- At low injection rates and adverse (but not very high) viscosity ratios, a decrease in contact angle can considerably improve oil recovery by switching the flow to a highly efficient regime;
- Changing the wettability towards a more neutral-wet condition changes the balance between the viscous and capillary forces towards a more viscous dominated regime and the effect on recovery is similar to that described after an increase in injection rate;

Core length effect:

- The same flow regime *before* breakthrough is obtained in simulations performed using different system lengths and the same experimental conditions;
- The *post*-breakthrough behaviour, however, is different according to the oil viscosity. In displacements with a viscosity ratio M=66, increasing the length of the core improves recovery. However, for heavier oil (M=7000), the number of viscous instabilities was seen to be higher in the shorter network and, whilst the recovery is faster in the shorter core, the oil recovery

catches up in the longer system after injecting ~ 5 pore volumes ─ the ultimate recovery was found to be similar in both cases.

Finally, in Chapter 10, the model was used to investigate the effects of injection rate, viscosity ratio and wettability on unsteady-state relative permeability. The relative permeability was found to be sensitive to these parameters and the following behaviours were observed:

- An increase in rate may result in an increase in the relative permeability of both phases. However, a range of rates and viscosities could be found for which the relative permeability was insensitive to a change of rate;
- An increase in viscosity ratio may result in a decrease of relative permeability. However, a range of viscosities and rates could be found where the relative permeability was insensitive to a change of viscosity;
- Decreasing the contact angle from a strongly oil-wet condition towards neutral-wet resulted in an increase in the relative permeability to oil but no significant change was observed in the relative permeability to water. For very viscous oils, a range of rates was found where the relative permeability was insensitive to a change in wettability.

These findings were in agreement with the published experimental investigations and they show that, in order to have meaningful unsteady-state relative permeability sets, measurements should be made under conditions similar to those found in a reservoir in terms of fluid properties, displacement velocity and rock wettability.

11.2. FUTURE WORK

The dynamic pore scale network simulator developed in this work may be used to a variety of future applications.

The first possibility is to add a solute to the water phase ─ examples include polymer, surfactant and salt ─ and modelling the dispersion and diffusion of its molecules inside the aqueous phase as well as the adsorption of these molecules by the rock.

For the case of polymer, the solution viscosity depends on the shear rate (because of the non-Newtonian nature of polymer solution) and on the concentration of the polymer solution. A feasibility study has already been performed for the polymer case and the preliminary results look promising. A very simplistic polymer model has been built considers only dispersion as the main displacement mechanism of polymer inside the aqueous phase (which should be the most important mechanism at high rates). The aqueous solution viscosity in each pore element was considered to be only dependent on polymer concentration following this simple equation:

$$\mu_{polymer\ solution}\,(cP) = 70 * \frac{C\ polymer\ pore}{C\ polymer\ injected} + 1$$

where $C\ polymer\ pore$ is the polymer concentration in the pore element and $C\ polymer\ injected$ is the concentration of the polymer solution injected.

A preliminary result is presented in Figure 11.1, initially a 0.1 PV waterflood simulation was performed with a viscosity ratio equal to 100, and this was followed by a polymer solution injection at the inlet. The waterflood exhibited a viscous fingering behaviour pre-polymer. However, when the polymer was added to the aqueous solution a more stable front was observed. This simplistic model shows that a more efficient displacement could be obtained once the polymer solution started to be injected.

Surfactant effects could also be modelled easily by changing the contact angle and the interfacial tension according to the intra-pore concentrations of the solution. Similarly, we could simulate the change of contact angle by low salinity waterflooding and investigate its effect on front stability and sweep efficiency.

Another interesting area for study would be to generalize this model to make it suitable for imbibition simulations. In this case, closing pores with counter current invasions is no longer a reasonable assumption and a more general mixing rule should be formulated. However, once this is tackled, more complex wettability scenarios could be considered, such as mixed wet and fractional wet cases. In addition, some interesting simulations could be performed that consider the *simultaneous* injection of water and oil

that will make the calculation of steady state relative permeability sets more realistic. Other application, such as ganglia formation and mobilization, could also be addressed.

Finally, this model could be generalized to enable the simulation of flow in more realistic networks extracted from pore images, as well as the addition of more complex pore geometries and sub-pore physical phenomena, such as film flow and snap off ─ issues that may be important for realistic imbibition simulations.

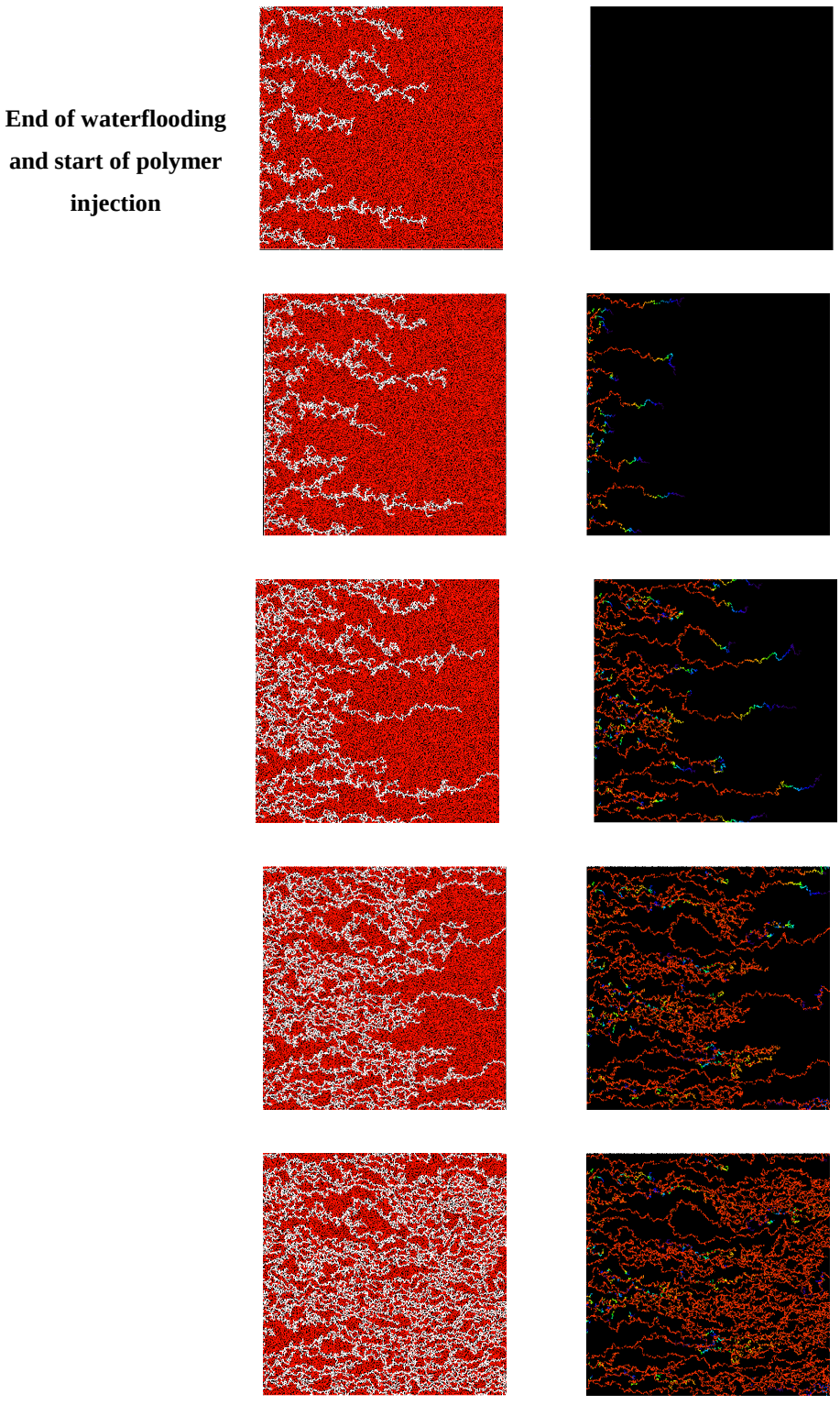

Figure 11.1: A waterflooding simulation followed by a polymer solution injection. The saturation maps (a) and the polymer concentrations in the network (red represents a concentration equal to the one of the injected polymer solution and blue a very low polymer concentration) (b) are plotted in this case. μoil =100 in this simulation.

ADLER, P., JACQUIN, C. & QUIBLIER, J. 1990. Flow in simulated porous media. *International Journal of Multiphase Flow,* 16**,** 691-712.

ADLER, P. M., JACQUIN, C. G. & THOVERT, J. F. 1992. The formation factor of reconstructed porous media. *Water Resources Research,* 28**,** 1571-1576.

AKER, E., MALOY, K. J. & HANSEN, A. 1998a. Simulating temporal evolution of pressure in two-phase flow in porous media. *Physical Review E,* 58**,** 2217-2226.

AKER, E., MALOY, K. J., HANSEN, A. & BATROUNI, G. G. 1998b. A two-dimensional network simulator for two-phase flow in porous media. *Transport in Porous Media,* 32**,** 163-186.

AL-DHAHLI, A. R., GEIGER, S. & VAN DIJKE, M. I. 2012. Three-phase pore-network modeling for reservoirs with arbitrary wettability. *Spe Journal,* 18**,** 285-295.

AL-FUTAISI, A. & PATZEK, T. W. 2003. Extension of Hoshen–Kopelman algorithm to non-lattice environments. *Physica A: Statistical Mechanics and its Applications,* 321**,** 665-678.

AL-GHARBI, M. S. & BLUNT, M. J. 2005. Dynamic network modeling of two-phase drainage in porous media. *Physical Review E,* 71.

AL-KHARUSI, A. S. & BLUNT, M. J. 2007. Network extraction from sandstone and carbonate pore space images. *Journal of Petroleum Science and Engineering,* 56**,** 219-231.

ARNS, C. H., BAUGET, F., LIMAYE, A., SAKELLARIOU, A., SENDEN, T., SHEPPARD, A., SOK, R. M., PINCZEWSKI, W., BAKKE, S. & BERGE, L. I. 2005. Pore-scale characterization of carbonates using X-ray microtomography. *SPE JOURNAL-RICHARDSON-,* 10**,** 475.

ARNS, C. H., KNACKSTEDT, M. A., PINCZEWSKI, W. V. & MARTYS, N. S. 2004. Virtual permeametry on microtomographic images. *Journal of Petroleum Science and Engineering,* 45**,** 41-46.

BAKKE, S. & ØREN, P.-E. 1997. 3-D pore-scale modelling of sandstones and flow simulations in the pore networks. *SPE JOURNAL-RICHARDSON-,* 2**,** 136-149.

BANAVAR, J. R., KOHMOTO, M. & ROBERTS, J. 1986. Aggregate models of pattern formation. *Physical Review A,* 33**,** 2065-2067.

BEHBAHANI, H. & BLUNT, M. J. Analysis of imbibition in mixed-wet rocks using pore-scale modeling. SPE Annual Technical Conference and Exhibition, 2004. Society of Petroleum Engineers.

BILGESU, H. I., ALI, M. W., AMINIAN, K. & AMERI, S. 2002. Computational Fluid Dynamics (CFD) as a Tool to Study Cutting Transport in Wellbores. Society of Petroleum Engineers.

BLUNT, M. & KING, P. 1990. MACROSCOPIC PARAMETERS FROM SIMULATIONS OF PORE SCALE FLOW. *Physical Review A,* 42**,** 4780-4787.

BLUNT, M. & KING, P. 1991. RELATIVE PERMEABILITIES FROM 2-DIMENSIONAL AND 3-DIMENSIONAL PORE-SCALE NETWORK MODELING. *Transport in Porous Media,* 6**,** 407-433.

BLUNT, M. J. 1997. Effects of heterogeneity and wetting on relative permeability using pore level modeling. *Spe Journal,* 2**,** 70-87.

BLUNT, M. J. & SCHER, H. 1995. PORE-LEVEL MODELING OF WETTING. *Physical Review E,* 52**,** 6387-6403.

BOGOYAVLENSKIY, V. A. 2001. Mean-field diffusion-limited aggregation: A "density" model for viscous fingering phenomena. *Physical Review E,* 64**,** 066303.

BOGOYAVLENSKIY, V. A. & CHERNOVA, N. A. 2000a. Diffusion-limited aggregation: A relationship between surface thermodynamics and crystal morphology. *Physical Review E,* 61**,** 1629.

BOGOYAVLENSKIY, V. A. & CHERNOVA, N. A. 2000b. Diffusion-limited aggregation: A revised mean-field approach. *Physical Review E,* 61**,** 5422-5428.

BONDINO, I., HAMON, G., KALLEL, W. & KACHUMA, D. Relative permeabilities from simulation in 3D rock models and equivalent pore networks: critical review and way forward. SCA2012-01, Proceedings of the International Symposium of the Society of Core Analysts, Aberdeen, Scotland, UK, 2012.

BONDINO, I., MCDOUGALL, S. R. & HAMON, G. 2009. A pore-scale modelling approach to the interpretation of heavy oil pressure depletion experiments. *Journal of Petroleum Science and Engineering,* 65**,** 14-22.

BONDINO, I., NGUYEN, R., HAMON, G., ORMEHAUG, P. A., SKAUGE, A. & JOUENNE, S. 2011. TERTIARY POLYMER FLOODING IN EXTRA-HEAVY OIL: AN INVESTIGATION USING 1D AND 2D EXPERIMENTS,

CORE SCALE SIMULATION AND PORESCALE NETWORK MODELS. *International Symposium of the Society of Core Analysts.* Austin, Texas, USA.

BORELLO, L., BONUCCELLI, M. & MORALE, G. 2007. The CFD Approach For The Risk Analysis Of A Blow-Out Event. Society of Petroleum Engineers.

BRYANT, S. & BLUNT, M. 1992. Prediction of relative permeability in simple porous media. *Physical Review A,* 46**,** 2004.

BRYANT, S. & RAIKES, S. 1995. Prediction of elastic-wave velocities in sandstones using structural models. *Geophysics,* 60**,** 437-446.

BRYANT, S. L., KING, P. R. & MELLOR, D. W. 1993a. Network model evaluation of permeability and spatial correlation in a real random sphere packing. *Transport in Porous Media,* 11**,** 53-70.

BRYANT, S. L., MELLOR, D. W. & CADE, C. A. 1993b. Physically representative network models of transport in porous media. *Aiche Journal,* 39**,** 387-396.

BUCHGRABER, M., CLEMENS, T., CASTANIER, L. M. & KOVSCEK, A. R. The displacement of viscous oil by associative polymer solutions. SPE Annual Technical Conference and Exhibition, 2009. Society of Petroleum Engineers.

BUCKLEY, S. & LEVERETT, M. 1941. Mechanism of fluid displacement in sands. *Trans. Aime,* 146.

CATES, M. E. 1986. Diffusion-limited aggregation without branching in the continuum approximation. *Physical Review A,* 34**,** 5007-5009.

CHEN, J. D. & WILKINSON, D. 1985. PORE-SCALE VISCOUS FINGERING IN POROUS-MEDIA. *Physical Review Letters,* 55**,** 1892-1895.

CHEN, S. & DOOLEN, G. D. 1998. Lattice Boltzmann method for fluid flows. *Annual Review of Fluid Mechanics,* 30**,** 329-364.

CHIN, J., BOEK, E. S. & COVENEY, P. V. 2002. Lattice Boltzmann simulation of the flow of binary immiscible fluids with different viscosities using the Shan-Chen microscopic interaction model. *Philosophical Transactions of the Royal Society of London Series a-Mathematical Physical and Engineering Sciences,* 360**,** 547-558.

CHUOKE, R. L., VAN MEURS, P. & VAN DER POEL, C. 1959. The Instability of Slow, Immiscible, Viscous Liquid-Liquid Displacements in Permeable Media. Society of Petroleum Engineers.

CLEMENS, T., TSIKOURIS, K., BUCHGRABER, M., CASTANIER, L. & KOVSCEK, A. 2013. Pore-Scale Evaluation of Polymers Displacing Viscous Oil-Computational-Fluid-Dynamics Simulation of Micromodel Experiments. *Spe Reservoir Evaluation & Engineering,* 16**,** 144-154.

COENEN, J., TCHOUPAROVA, E. & JING, X. Measurement parameters and resolution aspects of micro X-ray tomography for advanced core analysis. Proceedings of the international symposium of the society of core analysts, UAE.(SCA 2004-36), 2004.

CONSTANTINIDES, G. N. & PAYATAKES, A. C. 1996. Network simulation of steady-state two-phase flow in consolidated porous media. *Aiche Journal,* 42**,** 369-382.

DACCORD, G., NITTMANN, J. & STANLEY, H. E. 1986. Radial viscous fingers and diffusion-limited aggregation: Fractal dimension and growth sites. *Physical Review Letters,* 56**,** 336.

DAHLE, H. K. & CELIA, M. A. 1999. A dynamic network model for two-phase immiscible flow. *Computational Geosciences,* 3**,** 1-22.

DAHLE, H. K., CELIA, M. A. & HASSANIZADEH, S. M. 2005. Bundle-of-tubes model for calculating dynamic effects in the capillary-pressure-saturation relationship. *Transport in Porous Media,* 58**,** 5-22.

DIAS, M. M. & PAYATAKES, A. C. 1986a. NETWORK MODELS FOR 2-PHASE FLOW IN POROUS-MEDIA .1. IMMISCIBLE MICRODISPLACEMENT OF NONWETTING FLUIDS. *Journal of Fluid Mechanics,* 164**,** 305-336.

DIAS, M. M. & PAYATAKES, A. C. 1986b. NETWORK MODELS FOR 2-PHASE FLOW IN POROUS-MEDIA .2. MOTION OF OIL GANGLIA. *Journal of Fluid Mechanics,* 164**,** 337-358.

DICARLO, D. A. 2006. Quantitative network model predictions of saturation behind infiltration fronts and comparison with experiments. *Water Resources Research,* 42.

DING, W., WILLIAMS, J., KARANTH, D. & SOVANI, S. 2006. CFD application in automotive front-end design. SAE Technical Paper.

DIXIT, A. B., MCDOUGALL, S. R. & SORBIE, K. S. 1998. A Pore-Level Investigation of Relative Permeability Hysteresis in Water-Wet Systems.

DONG, B., YAN, Y. Y. & LI, W. Z. 2011. LBM Simulation of Viscous Fingering Phenomenon in Immiscible Displacement of Two Fluids in Porous Media. *Transport in Porous Media,* 88**,** 293-314.

DONG, H. & BLUNT, M. J. 2009. Pore-network extraction from micro-computerized-tomography images. *Physical Review E,* 80**,** 036307.

DONG, H., TOUATI, M. & BLUNT, M. J. Pore network modeling: analysis of pore size distribution of Arabian core samples. SPE Middle East Oil and Gas Show and Conference, 2007. Society of Petroleum Engineers.

DOORWAR, S. & MOHANTY, K. K. Viscous fingering during non-thermal heavy oil recovery. SPE Annual Technical Conference and Exhibition, 2011. Society of Petroleum Engineers.

DOORWAR, S. & MOHANTY, K. K. 2014. Extension of the dielectric breakdown model for simulation of viscous fingering at finite viscosity ratios. *Physical Review E,* 90**,** 013028.

DUNSMUIR, J. H., FERGUSON, S., D'AMICO, K. & STOKES, J. 1991. X-ray microtomography. *A new tool for the characterization of porous media, Pap. SPE,* 22860.

ENGELBERTS, W. F. & KLINKENBERG, L. J. 1951. Laboratory Experiments on the Displacement of Oil by Water from Packs of Granular Material. World Petroleum Congress.

ERDAL, F. M., SHIRAZI, S. A., SHOHAM, O. & KOUBA, G. E. CFD Simulation of Single-Phase and Two-Phase Flow in Gas-Liquid Cylindrical Cyclone Separators.

FANCHI, J. & CHRISTIANSEN, R. Applicability of fractals to the description of viscous fingering. SPE Annual Technical Conference and Exhibition, 1989. Society of Petroleum Engineers.

FATT, I. 1956. The network model of porous media.

FENWICK, D. H. & BLUNT, M. J. 1998. Three-dimensional modeling of three phase imbibition and drainage. *Advances in Water Resources,* 21**,** 121-143.

FERER, M., JI, C., BROMHAL, G. S., COOK, J., AHMADI, G. & SMITH, D. H. 2004a. Crossover from capillary fingering to viscous fingering for immiscible unstable flow: Experiment and modeling. *Physical Review E,* 70**,** 016303.

FERER, M., JI, C., BROMHAL, G. S., COOK, J., AHMADI, G. & SMITH, D. H. 2004b. Crossover from capillary fingering to viscous fingering for immiscible unstable flow: Experiment and modeling. *Physical Review E,* 70.

FERNÁNDEZ, J. F. & ALBARRÁN, J. M. 1990. Diffusion-limited aggregation with surface tension: Scaling of viscous fingering. *Physical Review Letters,* 64**,** 2133-2136.

FISCHER, U. & CELIA, M. A. 1999. Prediction of relative and absolute permeabilities for gas and water from soil water retention curves using a pore-scale network model. *Water Resources Research,* 35**,** 1089-1100.

FRETTE, V., FEDER, J., JØSSANG, T., MEAKIN, P. & MÅLØY, K. J. 1994. Fast, immiscible fluid-fluid displacement in three-dimensional porous media at finite viscosity contrast. *Physical Review E,* 50**,** 2881.

FUJII, K. 2005. Progress and future prospects of CFD in aerospace—Wind tunnel and beyond. *Progress in Aerospace Sciences,* 41**,** 455-470.

GARIK, P., RICHTER, R., HAUTMAN, J. & RAMANLAL, P. 1985. Deterministic solutions of fractal growth. *Physical Review A,* 32**,** 3156-3159.

GIELEN, T., HASSANIZADEH, S. M., LEIJNSE, A. & NORDHAUG, H. F. 2005. Dynamic Effects in Multiphase Flow: A Pore-scale Network Approach. *In:* DAS, D. B. & HASSANIZADEH, S. M. (eds.) *Upscaling Multiphase Flow in Porous Media.* Springer Netherlands.

GILJE, E. 2008. *Simulation of viscous instabilities in miscible and*

immiscible displacement. Master University of Bergen.

GUNSTENSEN, A. K., ROTHMAN, D. H., ZALESKI, S. & ZANETTI, G. 1991. Lattice Boltzmann model of immiscible fluids. *Physical Review A,* 43**,** 4320-4327.

HAGOORT, J. 1974. Displacement Stability of Water Drives in Water-Wet Connate-Water-Bearing Reservoirs.

HAMMOND, P. S. & UNSAL, E. 2012. A dynamic pore network model for oil displacement by wettability-altering surfactant solution. *Transport in Porous Media,* 92**,** 789-817.

HASSANIZADEH, S. M., CELIA, M. A. & DAHLE, H. K. 2002. Dynamic Effect in the Capillary Pressure-Saturation Relationship and its Impacts on Unsaturated Flow. *Vadose Zone Journal,* 1**,** 38-57.

HASSANIZADEH, S. M. & GRAY, W. G. 1990. MECHANICS AND THERMODYNAMICS OF MULTIPHASE FLOW IN POROUS-MEDIA INCLUDING INTERPHASE BOUNDARIES. *Advances in Water Resources,* 13**,** 169-186.

HASSANIZADEH, S. M. & GRAY, W. G. 1993. THERMODYNAMIC BASIS OF CAPILLARY-PRESSURE IN POROUS-MEDIA. *Water Resources Research,* 29**,** 3389-3405.

HELBA, A. A., SAHIMI, M., SCRIVEN, L. E. & DAVIS, H. T. 1992. Percolation Theory of Two-Phase Relative Permeability.

HELE-SHAW, H. 1898. Flow of water. *Nature,* 58**,** 520.

HENDERSON, G., DANESH, A., TEHRANI, D., AL-SHAIDI, S. & PEDEN, J. 1996. Measurement and correlation of gas condensate relative permeability by the steady-state method. *Spe Journal,* 1**,** 191-202.

HIRASAKI, G., MILLER, C. A. & PUERTO, M. 2011. Recent advances in surfactant EOR. *Spe Journal,* 16**,** 889-907.

HOMSY, G. M. 1987. Viscous fingering in porous media. *Annual Review of Fluid Mechanics,* 19**,** 271-311.

HOSHEN, J. & KOPELMAN, R. 1976. Percolation and cluster distribution. I. Cluster multiple labeling technique and critical concentration algorithm. *Physical Review B,* 14**,** 3438-3445.

HUANG, H., HUANG, J.-J. & LU, X.-Y. 2014. Study of immiscible displacements in porous media using a color-gradient-based multiphase lattice Boltzmann method. *Computers & Fluids,* 93**,** 164-172.

HUGHES, R. G. & BLUNT, M. J. 2000. Pore scale modeling of rate effects in imbibition. *Transport in Porous Media,* 40**,** 295-322.

JADHUNANDAN, P. P. & MORROW, N. R. 1995. Effect of Wettability on Waterflood Recovery for Crude-Oil/Brine/Rock Systems.

JERAULD, G. & SALTER, S. 1990. The effect of pore-structure on hysteresis in relative permeability and capillary pressure: pore-level modeling. *Transport in Porous Media,* 5**,** 103-151.

JIANG, Z., DIJKE, M., SORBIE, K. & COUPLES, G. 2013. Representation of multiscale heterogeneity via multiscale pore networks. *Water Resources Research,* 49**,** 5437-5449.

JIANG, Z., WU, K., COUPLES, G., VAN DIJKE, M., SORBIE, K. & MA, J. 2007. Efficient extraction of networks from three-dimensional porous media. *Water Resources Research,* 43.

JOEKAR-NIASAR, V. & HASSANIZADEH, S. M. 2011a. Effect of fluids properties on non-equilibrium capillarity effects: Dynamic pore-network modeling. *International Journal of Multiphase Flow,* 37**,** 198-214.

JOEKAR-NIASAR, V. & HASSANIZADEH, S. M. 2011b. Specific interfacial area: The missing state variable in two-phase flow equations? *Water Resources Research,* 47.

JOEKAR-NIASAR, V., PRODANOVIC, M., WILDENSCHILD, D. & HASSANIZADEH, S. M. 2010. Network model investigation of interfacial area, capillary pressure and saturation relationships in granular porous media. *Water Resources Research,* 46.

JOHNSON, E., BOSSLER, D. & BOSSLER, V. 1959. Calculation of relative permeability from displacement experiments.

JONES, S. & ROSZELLE, W. 1978. Graphical techniques for determining relative permeability from displacement experiments. *Journal of Petroleum Technology,* 30**,** 807-817.

KALAYDJIAN, F. 1987. A macroscopic description of multiphase flow in porous media involving spacetime evolution of fluid/fluid interface. *Transport in Porous Media,* 2**,** 537-552.

KANTOR, Y., WITTEN, T. A. & BALL, R. C. 1986. Quasicontinuum variants of diffusion-limited aggregation. *Physical Review A,* 33**,** 3341-3351.

KASSNER, K. & BRENER, E. 1994. Continuum description of noiseless diffusion-limited aggregation. *Physical Review E,* 50**,** 2161-2165.

KEBLINSKI, P., MARITAN, A., TOIGO, F. & BANAVAR, J. R. 1994. Continuum approach to diffusion-limited-aggregation type of growth. *Physical Review E,* 49**,** R4795-R4798.

KIM, T., HENSON, M. & LIN, M. C. A hybrid algorithm for modeling ice formation. Proceedings of the 2004 ACM SIGGRAPH/Eurographics symposium on Computer animation, 2004. Eurographics Association, 305-314.

KIM, T. & LIN, M. C. 2007. Fast animation of lightning using an adaptive mesh. *Visualization and Computer Graphics, IEEE Transactions on,* 13**,** 390-402.

KING, P. R. 1987. THE FRACTAL NATURE OF VISCOUS FINGERING IN POROUS-MEDIA. *Journal of Physics a-Mathematical and General,* 20**,** L529-L534.

KOPLIK, J. 1982. Creeping flow in two-dimensional networks. *Journal of Fluid Mechanics,* 119**,** 219-247.

KOPLIK, J. & LASSETER, T. J. 1985. 2-PHASE FLOW IN RANDOM NETWORK MODELS OF POROUS-MEDIA. *Society of Petroleum Engineers Journal,* 25**,** 89-100.

LAM, C. H. & HORVATH, V. K. 2000. Pipe network model for scaling of dynamic interfaces in porous media. *Physical Review Letters,* 85**,** 1238-1241.

LANGAAS, K. & YEOMANS, J. M. 2000. Lattice Boltzmann simulation of a binary fluid with different phase viscosities and its application to fingering in two dimensions. *The European Physical Journal B - Condensed Matter and Complex Systems,* 15**,** 133-141.

LEFEBVRE DU PREY, E. 1973. Factors affecting liquid-liquid relative permeabilities of a consolidated porous medium. *Society of Petroleum Engineers Journal,* 13**,** 39-47.

LENORMAND, R., TOUBOUL, E. & ZARCONE, C. 1988. NUMERICAL-MODELS AND EXPERIMENTS ON IMMISCIBLE DISPLACEMENTS IN POROUS-MEDIA. *Journal of Fluid Mechanics,* 189**,** 165-187.

LENORMAND, R. & ZARCONE, C. 1984. Role of roughness and edges during imbibition in square capillaries. *SPE J,* 13264.

LENORMAND, R., ZARCONE, C. & SARR, A. 1983. Mechanisms of the displacement of one fluid by another in a network of capillary ducts. *Journal of Fluid Mechanics,* 135**,** 337-353.

LEVINE, H. & TU, Y. 1992. Mean-field diffusion-limited aggregation and the Saffman-Taylor problem in three dimensions. *Physical Review A,* 45**,** 1044-1052.

LEVINE, H. & TU, Y. 1993. Theory of diffusion-limited growth. *Physical Review E,* 48**,** R4207-R4210.

LEWALLE, J., SINGH, K. M. & BAMBACHT, J. P. 1994. ANALYSIS OF THE WET PRESSING OF PAPER PULP. *International Journal of Multiphase Flow,* 20**,** 415-437.

LIANG, S. 1986. Random-walk simulations of flow in Hele Shaw cells. *Physical Review A,* 33**,** 2663-2674.

LIN, C. Y. & SLATTERY, J. C. 1982. Three-dimensional, randomized, network model for two-phase flow through porous media. *Aiche Journal,* 28**,** 311-324.

LINDQUIST, W. & VENKATARANGAN, A. 1999. Investigating 3D geometry of porous media from high resolution images. *Physics and Chemistry of the Earth, Part A: Solid Earth and Geodesy,* 24**,** 593-599.

LINDQUIST, W. B., LEE, S. M., COKER, D. A., JONES, K. W. & SPANNE, P. 1996. Medial axis analysis of void structure in three-dimensional tomographic images of porous media. *Journal of Geophysical Research: Solid Earth (1978–2012),* 101**,** 8297-8310.

LONGERON, D. G. 1980. Influence of Very Low Interfacial Tensions on Relative Permeability.

LØVOLL, G., JANKOV, M., MÅLØY, K., TOUSSAINT, R., SCHMITTBUHL, J., SCHÄFER, G. & MÉHEUST, Y. 2011. Influence of viscous fingering on dynamic saturation–pressure curves in porous media. *Transport in Porous Media,* 86**,** 305-324.

LOVOLL, G., MEHEUST, Y., MALOY, K. J., AKER, E. & SCHMITTBUHL, J. 2005. Competition of gravity, capillary and viscous forces during drainage in a two-dimensional porous medium, a pore scale study. *Energy,* 30**,** 861-872.

LØVOLL, G., MÉHEUST, Y., TOUSSAINT, R., SCHMITTBUHL, J. & MÅLØY, K. J. 2004. Growth activity during fingering in a porous Hele-Shaw cell. *Physical Review E,* 70**,** 026301.

LUCIA, F. J. 1999. *Carbonate reservoir characterization,* Springer.

MAI, A. & KANTZAS, A. 2009. Heavy oil waterflooding: effects of flow rate and oil viscosity. *Journal of Canadian Petroleum Technology,* 48**,** 42-51.

MAI, A. & KANTZAS, A. 2010. Mechanisms of heavy oil recovery by low rate waterflooding. *Journal of Canadian Petroleum Technology,* 49**,** 44-50.

MAI, A. T. & KANTZAS, A. Improved Heavy Oil Recovery by Low Rate Waterflooding. International Thermal Operations and Heavy Oil Symposium, 2008. Society of Petroleum Engineers.

MAINI, B., COSKUNER, G. & JHA, K. 1990. A Comparison Of Steady-State And Unsteady-State Relative Permeabilities Of Viscocities Oil And Water In Ottawa Sand.

MAJORS, P. D., LI, P. & PETERS, E. J. 1997. NMR Imaging of Immiscible Displacements in Porous Media.

MÅLØY, K. J., FEDER, J. & JØSSANG, T. 1985. Viscous fingering fractals in porous media. *Physical Review Letters,* 55**,** 2688.

MANDELBROT, B. B. 1967. How long is the coast of Britain. *Science,* 156**,** 636-638.

MANTHEY, S., HASSANIZADEH, S. M. & HELMIG, R. 2005. Macro-scale dynamic effects in homogeneous and heterogeneous porous media. *Transport in Porous Media,* 58**,** 121-145.

MAXWORTHY, T. 1987. The nonlinear growth of a gravitationally unstable interface in a Hele-Shaw cell. *Journal of Fluid Mechanics,* 177**,** 207-232.

MCDOUGALL, S., SALINO, P. & SORBIE, K. The Effect of Interfacial Tension Upon Gas-Oil Relative Permeability Measurements: Interpretation Using Pore-Scale Models. SPE Annual Technical Conference and Exhibition, 1997. Society of Petroleum Engineers.

MCDOUGALL, S. R. 1994. *The application of network modelling techniques to steady-and-unsteady-state multiphase flow in porous media.* PhD, Heriot Watt University.

MCDOUGALL, S. R., CRUICKSHANK, J. & SORBIE, K. S. 2002. Anchoring Methodologies for Pore-Scale Network Models: Application to Relative Permeability and Capillary Pressure Preduction. *PETROPHYSICS-HOUSTON-*, 43**,** 365-375.

MCDOUGALL, S. R. & SORBIE, K. S. 1993. The Combined Effect of Capillary and Viscous Forces on Waterflood Displacement Efficiency in Finely Laminated Porous Media. *SPE Annual Technical Conference and Exhibition.* Houston, Texas: 1993 Copyright 1993, Society of Petroleum Engineers, Inc.

MCDOUGALL, S. R. & SORBIE, K. S. 1995. The Impact of Wettability on Waterflooding: Pore-Scale Simulation.

MOGENSEN, K. & STENBY, E. H. 1998. A dynamic two-phase pore-scale model of imbibition. *Transport in Porous Media,* 32**,** 299-327.

MOORE, M. G., JUEL, A., BURGESS, J. M., MCCORMICK, W. & SWINNEY, H. L. 2002. Fluctuations in viscous fingering. *Physical Review E,* 65**,** 030601.

MORROW, N. R. 1990. Wettability and Its Effect on Oil Recovery.

NAUENBERG, M. 1983. Critical growth velocity in diffusion-controlled aggregation. *Physical Review B,* 28**,** 449-451.

NGUYEN, V. H., SHEPPARD, A. P., KNACKSTEDT, M. A. & PINCZEWSKI, W. V. 2006. The effect of displacement rate on imbibition relative permeability and residual saturation. *Journal of Petroleum Science and Engineering,* 52**,** 54-70.

NIEMEYER, L., PIETRONERO, L. & WIESMANN, H. J. 1984. Fractal Dimension of Dielectric Breakdown. *Physical Review Letters,* 52**,** 1033-1036.

NITTMAN, J., DACCORD, G. & STANLEY, M. 1985. Fractal growth of viscous fingers: quantitative characterization of a fluid instability phenomenon. *Nature,* 314**,** 391.

NORDHAUG, H. F., CELIA, M. & DAHLE, H. K. 2003. A pore network model for calculation of interfacial velocities. *Advances in Water Resources,* 26**,** 1061-1074.

OAK, M. Three-phase relative permeability of water-wet Berea. SPE/DOE Enhanced Oil Recovery Symposium, 1990. Society of Petroleum Engineers.

ODEH, A. S. 1959. Effect of Viscosity Ratio on Relative Permeability (includes associated paper 1496-G).

OHTA, S. & HONJO, H. 1991. Homogeneous and self-similar diffusion-limited aggregation including surface-diffusion processes. *Physical Review A,* 44**,** 8425-8428.

OKABE, H. & BLUNT, M. J. 2004. Prediction of permeability for porous media reconstructed using multiple-point statistics. *Physical Review E,* 70**,** 066135.

ØREN, P.-E. & BAKKE, S. 2002. Process based reconstruction of sandstones and prediction of transport properties. *Transport in Porous Media,* 46**,** 311-343.

ØREN, P.-E. & BAKKE, S. 2003. Reconstruction of Berea sandstone and pore-scale modelling of wettability effects. *Journal of Petroleum Science and Engineering,* 39**,** 177-199.

ØREN, P.-E., BAKKE, S. & ARNTZEN, O. J. 1998. Extending predictive capabilities to network models. *SPE JOURNAL-RICHARDSON-,* 3**,** 324-336.

OUTMANS, H. D. 1962. Nonlinear Theory for Frontal Stability and Viscous Fingering in Porous Media.

OWENS, W. & ARCHER, D. 1971. The effect of rock wettability on oil-water relative permeability relationships. *Journal of Petroleum Technology,* 23**,** 873-878.

PATERSON, L. 1984. Diffusion-Limited Aggregation and Two-Fluid Displacements in Porous Media. *Physical Review Letters,* 52**,** 1621-1624.

PATZEK, T. W. & SILIN, D. B. 2001. Shape factor and hydraulic conductance in noncircular capillaries I. One-phase creeping flow. *Journal of Colloid and Interface Science,* 236**,** 295-304.

PERKINS, T. K. & JOHNSTON, O. C. 1969. A Study of Immiscible Fingering in Linear Models.

PETERS, E. & CAVALERO, S. The fractal nature of viscous fingering in porous media. SPE Annual Technical Conference and Exhibition, 1990. Society of Petroleum Engineers.

PETERS, E. J. & FLOCK, D. L. 1981. The Onset of Instability During Two-Phase Immiscible Displacement in Porous Media. *Society of Petroleum Engineers Journal,* 21**,** 249-258.

PETERS, E. J. & HARDHAM, W. D. 1989. A Comparison of Unstable Miscible and Immiscible Displacements. Society of Petroleum Engineers.

PIETRONERO, L. & WIESMANN, H. 1988. From physical dielectric breakdown to the stochastic fractal model. *Zeitschrift für Physik B Condensed Matter,* 70**,** 87-93.

PIRI, M. & BLUNT, M. J. 2005. Three-dimensional mixed-wet random pore-scale network modeling of two- and three-phase flow in porous media. I. Model description. *Physical Review E,* 71**,** 026301.

PONS, M.-N., WEISSER, E., VIVIER, H. & BOGER, D. 1999. Characterization of viscous fingering in a radial Hele-Shaw cell by image analysis. *Experiments in fluids,* 26**,** 153-160.

QUIBLIER, J. A. 1984. A new three-dimensional modeling technique for studying porous media. *Journal of Colloid and Interface Science,* 98**,** 84-102.

RACHFORD, H. H., JR. 1964. Instability in Water Flooding Oil from Water -Wet Porous Media Containing Connate Water.

RIAZ, A., TANG, G.-Q., TCHELEPI, H. A. & KOVSCEK, A. R. 2007. Forced imbibition in natural porous media: Comparison between experiments and continuum models. *Physical Review E,* 75**,** 036305.

RIAZ, A. & TCHELEPI, H. A. 2006. Influence of relative permeability on the stability characteristics of immiscible flow in porous media. *Transport in Porous Media,* 64**,** 315-338.

RICHARDSON, J. G. 1957. The Calculation of Waterflood Recovery From Steady-State Relative Permeability Data.

ROBERTS, A. P. 1997. Statistical reconstruction of three-dimensional porous media from two-dimensional images. *Physical Review E,* 56**,** 3203.

ROMERO-ZERON, L., LI, L., ONGSURAKUL, S. & BALCOM, B. 2009. Visualization of waterflooding through unconsolidated porous media using magnetic resonance imaging. *Petroleum Science and Technology,* 27**,** 1993-2009.

ROMERO-ZERON, L., ONGSURAKUL, S., LI, L. & BALCOM, B. 2010. Visualization of the effect of porous media wettability on polymer flooding performance through unconsolidated porous media using magnetic resonance imaging. *Petroleum Science and Technology,* 28**,** 52-67.

RYAZANOV, A. V., VAN DIJKE, M. I. & SORBIE, K. S. Pore-network prediction of residual oil saturation based on oil layer drainage in mixed-wet systems. SPE Improved Oil Recovery Symposium, 2010. Society of Petroleum Engineers.

SAFFMAN, P. G. & TAYLOR, G. 1958. The Penetration of a Fluid into a Porous Medium or Hele-Shaw Cell Containing a More Viscous Liquid. *Proceedings of the Royal Society of London. Series A. Mathematical and Physical Sciences,* 245**,** 312-329.

SANDOW, S. & TRIMPER, S. 1993. Aggregation processes in a master-equation approach. *EPL (Europhysics Letters),* 21**,** 799.

SHEPPARD, A., SOK, R. & AVERDUNK, H. Improved pore network extraction methods. International Symposium of the Society of Core Analysts, 2005. 21-25.

SHEPPARD, A., SOK, R., AVERDUNK, H., ROBINS, V. & GHOUS, A. Analysis of rock microstructure using high-resolution X-ray tomography. Proceedings of the International Symposium of the Society of Core Analysts, 2006.

SILIN, D. & PATZEK, T. 2006. Pore space morphology analysis using maximal inscribed spheres. *Physica A: Statistical Mechanics and its Applications,* 371**,** 336-360.

SILIN, D. B., JIN, G. & PATZEK, T. W. 2003. Robust determination of the pore space morphology in sedimentary rocks. *Soc. Petrol. Eng*.

SINGH, M. & MOHANTY, K. K. 2003. Dynamic modeling of drainage through three-dimensional porous materials. *Chemical Engineering Science,* 58**,** 1-18.

SKAUGE, A., ORMEHAUG, P., VIK, B., FABBRI, C., BONDINO, I. & HAMON, G. Polymer Flood Design for Displacement of Heavy Oil Analysed by 2D-imaging. IOR 2013-From Fundamental Science to Deployment, 2013.

SKAUGE, A., ORMEHAUG, P. A., GURHOLT, T., VIK, B., BONDINO, I. & HAMON, G. 2012. 2-D Visualisation of Unstable Waterflood and Polymer Flood for Displacement of Heavy Oil. *SPE Improved Oil Recovery Symposium.* Tulsa, Oklahoma, USA: Society of Petroleum Engineers.

SKAUGE, T., VIK, B. F., ORMEHAUG, P. A., JATTEN, B. K., KIPPE, V., SKJEVRAK, I., STANDNES, D. C., ULEBERG, K. & SKAUGE, A. 2014. Polymer Flood at Adverse Mobility Ratio in 2D Flow by X-ray Visualization. Society of Petroleum Engineers.

SORBIE, K. & SKAUGE, A. Can network modeling predict two-phase flow functions. SCA2011-29, International Symposium of the Society of Core Analysts in Austin, TX, USA, 2011. 18-21.

STOKES, J., WEITZ, D., GOLLUB, J. P., DOUGHERTY, A., ROBBINS, M., CHAIKIN, P. & LINDSAY, H. 1986. Interfacial stability of immiscible displacement in a porous medium. *Physical Review Letters,* 57**,** 1718.

TAO, R., NOVOTNY, M. A. & KASKI, K. 1988. Diffusion-limited aggregation with surface tension. *Physical Review A,* 38**,** 1019-1026.

THOMPSON, K. E. 2002. Pore-scale modeling of fluid transport in disordered fibrous materials. *Aiche Journal,* 48**,** 1369-1389.

VALVATNE, P. H. & BLUNT, M. J. 2004. Predictive pore-scale modeling of two-phase flow in mixed wet media. *Water Resources Research,* 40.

VAN DAMME, H., OBRECHT, F., LEVITZ, P., GATINEAU, L. & LAROCHE, C. 1986. Fractal viscous fingering in clay slurries. *Nature,* 320**,** 731-733.

VAN DER MARCK, S. C., MATSUURA, T. & GLAS, J. 1997. Viscous and capillary pressures during drainage: Network simulations and experiments. *Physical Review E,* 56**,** 5675-5687.

VAN DIJKE, M. I. J. & SORBIE, K. S. 2006. Existence of fluid layers in the corners of a capillary with non-uniform wettability. *Journal of Colloid and Interface Science,* 293**,** 455-463.

VAN KATS, F. & EGBERTS, P. 1999. Simulation of three-phase displacement mechanisms using a 2D lattice-Boltzmann model. *Transport in Porous Media,* 37**,** 55-68.

VAN MEURS, P. 1957. The Use of Transparent Three-Dimensional Models for Studying the Mechanism of Flow Processes in Oil Reservoirs. Society of Petroleum Engineers.

VICSEK, T. 1992. *Fractal Growth Phenomena*, World Scientific.

VIZIKA, O., AVRAAM, D. G. & PAYATAKES, A. C. 1994. ON THE ROLE OF THE VISCOSITY RATIO DURING LOW-CAPILLARY-NUMBER FORCED IMBIBITION IN POROUS-MEDIA. *Journal of Colloid and Interface Science,* 165**,** 386-401.

WANG, J., DONG, M. & ASGHARI, K. Effect of Oil Viscosity on Heavy Oil-Water Relative Permeability Curves. SPE/DOE Symposium on Improved Oil Recovery, 2006. Society of Petroleum Engineers.

WANG, S. Y., HUANG, Y., PEREIRA, V. & GRYTE, C. C. 1985. Application of computed tomography to oil recovery from porous media. *Applied optics,* 24**,** 4021-4027.

WANG, Y., ZHANG, C., WEI, N., OOSTROM, M., WIETSMA, T. W., LI, X. & BONNEVILLE, A. 2012. Experimental Study of Crossover from Capillary to Viscous Fingering for Supercritical CO2–Water Displacement in a Homogeneous Pore Network. *Environmental Science & Technology,* 47**,** 212-218.

WELGE, H. J. 1952. A simplified method for computing oil recovery by gas or water drive. *Journal of Petroleum Technology,* 4**,** 91-98.

WITTEN JR, T. & SANDER, L. M. 1981. Diffusion-limited aggregation, a kinetic critical phenomenon. *Physical Review Letters,* 47**,** 1400.

WU, K., VAN DIJKE, M. I., COUPLES, G. D., JIANG, Z., MA, J., SORBIE, K. S., CRAWFORD, J., YOUNG, I. & ZHANG, X. 2006. 3D stochastic modelling of

heterogeneous porous media–applications to reservoir rocks. *Transport in Porous Media,* 65**,** 443-467.

XIA, B. & SUN, D.-W. 2002. Applications of computational fluid dynamics (cfd) in the food industry: a review. *Computers and Electronics in Agriculture,* 34**,** 5-24.

XIAO, R.-F., ALEXANDER, J. I. D. & ROSENBERGER, F. 1988. Morphological evolution of growing crystals: A Monte Carlo simulation. *Physical Review A,* 38**,** 2447-2456.

YIOTIS, A. G., PSIHOGIOS, J., KAINOURGIAKIS, M. E., PAPAIOANNOU, A. & STUBOS, A. K. 2007. A lattice Boltzmann study of viscous coupling effects in immiscible two-phase flow in porous media. *Colloids and Surfaces a-Physicochemical and Engineering Aspects,* 300**,** 35-49.

ZHANG, J.-H. & LIU, Z.-H. 1998. Study of the relationship between fractal dimension and viscosity ratio for viscous fingering with a modified DLA model. *Journal of Petroleum Science and Engineering,* 21**,** 123-128.

ZHOU, X., MORROW, N. & MA, S. 2000. Interrelationship of Wettability Initial Water Saturation Aging Time and Oil Recovery by Spontaneous Imbibition and Waterflooding. *Spe Journal,* 5**,** 199-207.

ZITHA, P. L., NGUYEN, Q. P., CURRIE, P. K. & BUIJSE, M. A. 2006. Coupling of foam drainage and viscous fingering in porous media revealed by X-ray computed tomography. *Transport in Porous Media,* 64**,** 301-313.